Alma Mater Studiorum - Università di Bologna

---

Dottorato di Ricerca in:

Meccanica e Scienze Avanzate dell'Ingegneria

Curriculum: Ingegneria delle Macchine e dei Sistemi Energetici

Ciclo XXVI

Settore Concorsuale di afferenza: 09/C1
Settore Scientifico disciplinare: ING-IND/08

# OPTIMAL SUPERVISORY CONTROL OF HYBRID VEHICLES

Presentata da:

Alberto Cerofolini

| Coordinatore: | Relatore: |
|---|---|
| Prof. Ing. Vincenzo Parenti Castelli | Prof. Ing. Davide Moro |

---

Esame Finale 2014

# Preface

The realization of my research activity was made possible by the contribution of many people who I'd wish to thank, in chronological order.

First, I'm very thankful to Prof. Ing. Davide Moro, who recognized my interest in the field of scientific research and gave me the chance to test my abilities during the years.

Then I would like to thank Prof. Ing. Nicolo Cavina, who assisted me closely during my entire work at the Department of Industrial Engineering (DIN) of the University of Bologna, always patiently listening and providing useful suggestions. His humble approach, despite his great knowledge of the subject, will always be an example of professionalism.

I'm very honored that I had the opportunity to work together with Ing. Mauro Rioli, who shared with me a part of his enormous expertise in almost every aspect of automotive design and research, as its successful career as racing and road vehicles designer clearly demonstrates. He taught me a great lesson about the role of engineers and researchers: one should never stop to imagine new concepts and always think out of the box, calling his own knowledge into question.

I would like to thank all the engineers working at the Advanced Research Department of IAV GmbH, especially Dipl. Ing. Oliver Dingel, Dr. Ing. Nicola Pini and Dr. Ing. Igor Trivic, for their professional and involved support during the common research projects.

I'm also very thankful to Prof. Dr. Lino Guzzella and Dr. Christopher Onder, who invited me as an Academic Guest in the IDSC (Institute of Dynamic Systems and Control) at ETH Zurich, during the last part of my PhD.

I thank all the colleagues at DIN and IDSC, for the nice moments spent together. A very special thanks goes to Ing. Giorgio Mancini and M.Sc. Tobias Nueesch.

Finally, I would like to thank all my family, for the great support and understanding.

*Modena, 16 Marzo 2014*

# Contents

# Abstract

Road vehicle legislation is becoming always more stringent about pollutant emissions, forcing automotive manufacturers to address the research towards more efficient and environmentally safe internal combustion engines, or to install complex and expensive after-treatment systems. Hybrid vehicles (HV), comprising a conventional Internal Combustion Engine (ICE) powertrain, and a secondary energy source to be converted into mechanical power as well, represent a well-established alternative to substantially reduce both fuel consumption and tailpipe emissions.

Several HV architectures are either being studied or already available on the market, strongly differing in terms of topology, hybridization ratio and nature of the adopted additional energy storage source, e.g. Mechanical, Electric, Hydraulic and Pneumatic Hybrid Vehicles. Among the others, Electric (HEV) and Mechanical (HSF-HV) parallel Hybrid configurations are examined throughout this Thesis, the first representing the most common and mature technology, the latter being a promising alternative, characterized by higher roundtrip energy conversion efficiency.

To fully exploit the HV potential, an optimal choice of the hybrid components to be installed must be properly designed, while an effective Supervisory Control must adopted. The term Supervisory Control or Energy Management System (EMS), is used to describe the way the different power sources are managed and how they interact. In the case studies treated in this work, regarding parallel HVs, it typically comprehends the Torque/Power split factor between thermal and secondary motor, ICE start/stop command and possibly the gear-shift strategy.

In many cases, Optimal Control Theory principles, e.g. Dynamic Programming (DP) and Pontryagin's Minimum Principle (PMP), can be applied as useful methodologies to define the best performance of a vehicle over a predefined mission, i.e. a homologation cycle. Then, real-time controllers can be derived starting from the obtained optimal benchmark results. However, the application of these powerful instruments requires a simplified and yet reliable and accurate model of the hybrid vehicle system. This can be a complex task, especially when the complexity of the system grows, i.e. a HSF-HV system assessed in this Thesis.

The first task of the following dissertation is to establish the optimal modeling approach for an innovative and promising mechanical hybrid vehicle architecture. It will be shown how the chosen modeling paradigm can affect the goodness and

the amount of computational effort of the solution, using an optimization technique based on DP.

The second issue that is here addressed concerns the control of pollutant emissions in a parallel Diesel-HEV. Focusing on Diesel engine-based hybrid vehicles, the $NO_x$ emissions are particularly relevant, since the highest $NO_x$ concentration corresponds to the engine operating points where the highest efficiency is attained. Moreover, the emissions level obtained under real world driving conditions is substantially higher than the usual result obtained in a homologation cycle. For this reason, an on-line control strategy capable of guaranteeing the respect of the desired emissions level, while minimizing fuel consumption and avoiding excessive battery depletion is the target of the corresponding section of the Thesis. The resulting controller has been experimentally validated by means of Hardware-in-the-Loop (HiL) test-bench experiments.

# List of Figures

# List of Tables

# Abbreviations - Nomenclature

| Acronym | Description |
|---|---|
| AMT | Automated Manual Transmission |
| APU | Auxiliary Power Unit |
| AST | Air Storage Tank |
| CF | Capacity Factor |
| CI | Compression Ignition |
| CVT | Continuously Variable Transmission |
| DP | Dynamic Programming |
| ECMS | Equivalent Consumption Minimization Strategy |
| EEMS | Equivalent Emissions Minimization Strategy |
| EMG | Electric Motor-Generator |
| EMS | Energy Management Strategy |
| EREV | Extended Range Electric Vehicle |
| EV | Electric Vehicle |
| FC | Fuel Consumption |
| FWD | Forward simulation |
| GB | Gearbox |
| GT | Gas Turbine |
| HCU | Hybrid Control Unit |
| HEV | Hybrid Electric Vehicle |
| HHV | Hydraulic Hybrid Vehicle |
| HiL | Hardware-in-the-loop |
| HMP | Hydraulic Motor-Pump |
| HPA | High Pressure Accumulator |
| HR | Hybridization Ratio |

| Acronym | Description |
|---|---|
| HSF-HV | High Speed Flywheel - Hybrid Vehicle |
| HV | Hybrid Vehicle |
| ICE | Internal Combustion Engine |
| ISG | Integrated Starter Generator |
| LPA | Low Pressure Accumulator |
| MPC | Model Predictive Control |
| $NO_x$ | Nitrogen Oxides |
| PE | Power Electronics |
| PHV | Pneumatic Hybrid Vehicle |
| PMC | Pneumatic Motor-Compressor |
| PMP | Pontryagin's Minimum Principle |
| PR | Pressure Ratio |
| PSD | Power Split Device |
| PSG | Planetary Gear Set |
| PSH | Pumped Storage Hydro (system) |
| PSO | Particle Swarm Optimization |
| QSS | Quasi Static Simulation |
| SI | Spark Ignition |
| SOC | State of Charge |
| TIT | Turbine Inlet Temperature |
| WOT | Wide Open Throttle |
| ZEV | Zero Emissions Vehicle |

| Symbol | Description | Unit |
|---|---|---|
| $A_f$ | Vehicle frontal area | [m$^2$] |
| $C$ | Optimal cost-to-go function | [J] or [kg] |
| $D$ | Vehicle distance | [km] |
| $E$ | Energy | [J] |
| $F$ | Force | [N] |
| $G$ | Final state cost | [J] |
| $H$ | Hamiltonian function | [J] or [kg] |
| $H_l$ | Fuel lower heat value | [J/kg] |
| $I$ | Current | [A] |
| $J$ | Cost functional | [J] or [kg] |
| $L$ | Cost function | [W] or [kg/s] |
| $P_j$ | Power of the $j$-th component | [W] |
| $Q$ | Battery charge | [C] or [Ah] |
| $R_i$ | Internal resistance of the battery | [Ω] |
| $S_j$ | State identifier of the $j$-th component | [-] |
| $T$ | Total duration of the control mission | [s] |
| $T_i$ | Time constant of the integrator component, PI controller | [s] |
| $T_j$ | Torque of the $j$-th component | [Nm] |
| $U$ | Voltage | [V] |
| $V$ | Volume | [m$^3$] |
| $V_{oc}$ | Open-circuit voltage | [V] |
| $c_r$ | Rolling friction coefficient | [-] |
| $c_d$ | Drag coefficient | [-] |
| $d$ | Vehicle distance | [km] |
| $g$ | Gravitational acceleration | [m/s$^2$] |
| $g_N$ | Final state cost | [J] of [kg] |
| $g_s$ | Selected gear number | [-] |
| $h$ | Water reservoir level height | [m] |
| $i_g$ | Total gear ratio | [-] |

| Symbol | Description | Unit |
|---|---|---|
| $k_f$ | HSF friction coefficient | [W/(rad/s)$^2$] |
| $k_p$ | Proportional gain, PI controller | [-] |
| $l_k$ | Instantaneous discrete cost function | [J] or [kg] |
| $m$ | Mass *j*-th component | [kg] |
| $\overline{m}$ | Distance-specific mass | [mg/km] |
| $m_v$ | Vehicle mass | [kg] |
| $\overset{*}{m}$ | Mass flow rate | [kg/s] |
| $r_w$ | Wheel radius | [m] |
| $s$ | Equivalence factor | [-] |
| $u$ / $u_j$ | Control inputs vector / *j*-th control input | [-] |
| $v$ | Vehicle speed | [m/s] |
| $w$ | Disturbances vector | [-] |
| $x$ / $x_j$ | State variables vector / *j*-th state | [-] |
| $\Theta$ | Inertia | [kgm$^2$] |
| $\alpha_t$ | Extended throttle | [%] |
| $\alpha_{NO_x}$ | $NO_x$ emissions equivalence factor | [-] |
| $\gamma$ | Road slope angle | [°] |
| $\varepsilon_{\Delta\omega}$ | Angular speed threshold | [rad/s] |
| $\eta_j$ / $\bar{\eta}_j$ | Efficiency / cycle-averaged efficiency *j*-th component | [-] |
| $\lambda$ | Co-state | [-] |
| $\xi$ | State-of-charge | [-] |
| $\rho_{air}$ | Air density | [kg/m$^3$] |
| $\tau$ | Transmission ratio | [-] |
| $\varphi_N$ | Penalty for the final state | [J] or [kg] |
| $\omega_j$ | Angular speed *j*-th component | [rad/s] |
| $\omega_j$ | Angular acceleration *j*-th component | [rad/s$^2$] |

*Ad Ura e Alba*

# 1. Introduction

In this Chapter the main goals of the research activity carried out during my PhD are clarified. Then the structure of the Thesis is explained in greater detail.

## 1.1 Motivation of the Thesis

Hybrid vehicles are nowadays considered one of the most promising technologies to reduce both fuel consumption and pollutant emissions of road cars.

To fully exploit their potential advantages, HV powertrains need to be optimized, solving the following different design problems:

- *Topology optimization*: the goal is here to find the best possible powertrain structure, e.g. series, parallel, etc.;
- *Parametric optimization*: for a given vehicle structure, find the best components and their optimal sizing;
- *Energy management optimization*: the target is to define the best supervisory control that allows achieving the target control objective.

Several studies treating one or more of the latter three problems can be found in literature. However, there are still some topics that could be enhanced to help improving the cited optimization techniques.

Among the various HV types, HEV and HSF-HV are characterized by some features that authorize to consider them the most prompt and advantageous technologies. On one hand, HEV can be regarded as a mature technology, already present on market from several years. On the other hand, HSF-HV or Mechanical hybrids in general, appear promising, if one considers that the stored secondary energy source does not involve energy conversion processes between sources of different nature, so that the overall round-trip efficiency can be considered higher.

Moreover, electrochemical accumulators still require some safety and disposal issues to be solved. Innovative topologies of these two kinds have been proposed in [188] for parallel HV frames and the advantages are proved with advanced simulation environments over a set of standard homologation cycles.

The first goal pursued by the present dissertation is to establish a benchmark of FE performance for the selected HV topologies. To achieve a similar target a QSS simulation framework needs to be established to apply a powerful algorithm of Optimal Control Theory that is DP. HEV models for DP simulation are already well-established in literature, while elaborate mechanical hybrid vehicles include a more complex dynamic that must be carefully analyzed to achieve reliable models. Throughout this dissertation, two distinct modeling approaches are presented, one more detailed and the other simplified, analyzing the benefits of each one in the field of FE-oriented optimization. This is done in Chapter 4.

The second objective of this work is again in the field of EMS optimization, especially regarding the problem of on-line control of $NO_x$ emissions for a diesel HEV. Even though diesel HEVs can be considered the best option to further reduce $CO_2$ emissions of road vehicles, some issues arise from the use of CI engines, resulting in more $NO_x$ and PM emissions, both harmful for human's health and the environment. $NO_x$ emissions are particularly critical, since the highest efficiency combustion conditions are favorable to the production of $NO_x$ emissions. Although some authors already designed some extended ECMS control algorithms to take into account pollutant emissions of HEVs, the resulting objective function is typically a weighted sum of one or more pollutants and fuel, where the weighting factors are constant values treated as tuning parameters. The results of the research activity discussed in the dedicated Chapter of this Thesis, is instead to design and validate a controller structure whose goal is to minimize fuel consumption while respecting emissions constraints and guaranteeing charge-sustaining conditions for the battery in real world driving conditions. This has been achieved by means of a near-optimal controller derived from PMP, capable of on-line adaptation of the weighting factor between $NO_x$ and FC.

Finally, a DP-based approach aimed at topology and parametric optimization of a complex hybrid structure is presented, focused on the most efficient choice of the input and state variables needed to describe the system and exploit its FE potential.

## 1.2 Structure of the Thesis

In Chapter 2, an overview of possible hybrid vehicle types is proposed, providing fundamental distinction rules based on commonly recognized features, such as hybridization ratio (HR), topology and alternative energy source type. Then, a classification of existent Supervisory Control strategies, necessary to contextualize the innovative contents of this work, is included in the final section.

Chapter 3 offers a detailed analysis of possible modeling approaches for a hybrid vehicle system, mainly distinguishing between QSS and FWD/dynamic paradigms, for both HEV and HSF-HV components.

In Chapter 4 the FE optimization methodologies for HVs are recalled, including some considerations about gearshift patterns and drivability issues. Then, the concluding section of this Chapter is devoted to illustrate the simulation results of the FE optimization routines developed for the selected hybrid technologies.

Chapter 5 presents a treatise on the development of an on-line controller for $NO_x$ emissions in a diesel-HEV. An innovative controller is derived from Optimal Control Theory (PMP), obtaining a near-optimal and causal structure, whose real-time on-board implementation is feasible. The simulation results have been experimentally validated by means of a HiL engine test-bench as shown in the conclusions of this section.

In Appendix A.1 a DP-based framework to optimize a complex serial/parallel hybrid system is depicted.

In Appendix A.2 DP is applied to a hybrid power system, consisting of a Pumped Storage Hydro unit (PSH), Gas Turbines (GT) and a wind farm. The results are compared to a causal heuristic strategy.

# 2. Hybrid Powertrains Design and Control

In this Chapter a brief overview of the main hybrid propulsion system technologies is presented. The main advantages of the implementation of such vehicles is introduced, later focusing on the architectures selected for the research carried out in this PhD project. Finally, a short recall of the main EMSs for HVs is provided in the concluding section.

## 2.1 Advantages of Hybrid Vehicles

An HV can be described as a vehicle in which a secondary energy storage system is added to a conventional fossil fuel ICE-based powertrain. In general, a HV includes an engine as fuel converter and one or more additional prime movers fed by a secondary energy source ([66]). There are multiple aspects of HV technology that allow these systems to attain a better FE, if compared to conventional vehicles ([110, 207]):

- Engine downsizing, while fulfilling constraints of maximum required power;
- Braking energy recuperation instead of dissipating it into heat, as with conventional friction brakes ([33, 56, 153]);
- Energy distribution optimization between primary and secondary energy sources, resulting in higher efficiencies of motors and higher round-trip efficiency (see [47]);
- Removal of idle FC by means of ICE start/stop system;
- Elimination of clutch slipping losses by ICE engagement only when speeds are synchronized.

Depending on the nature and impact of the hybrid technology on a given propulsion system, the advantage in terms of FE can be higher than 30% compared to ICE-based powertrains, as depicted in Figure 2.1 on NEDC homologation cycle, even though HVs tend to be about 10-30% heavier than conventional vehicles.

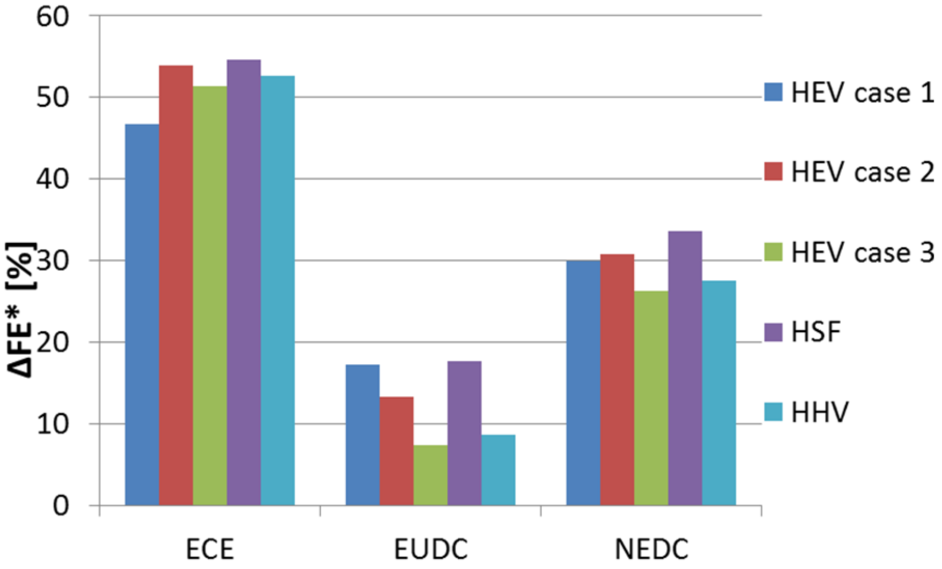

Figure 2.1: FC comparison of different pHV technologies for the European homologation cycles (source [47]).

The contribution of regenerative braking is highlighted in Figure 2.2 for the same HV technologies investigated in the previous figure, limited in this case to NEDC cycle simulations.

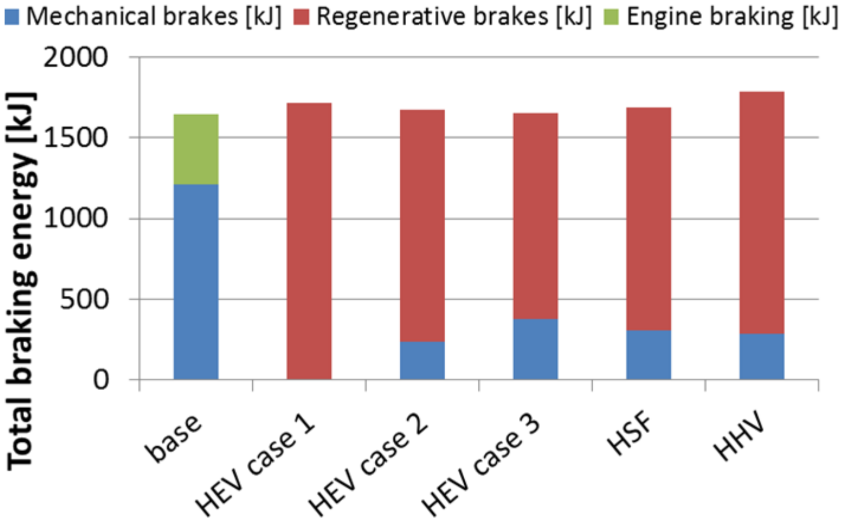

Figure 2.2: Distribution of Total braking Energy for the NEDC cycle for different HV technologies (source [47]).

An optimal design of the HV systems is a key factor to obtain the desired FE benefits, while fulfilling the required vehicle performances. The authors of [211, 24] propose a general methodology for the assessment of hybrid architectures. The most relevant parameters to define a HV are:

- System configuration: HV topology;
- Hybridization ratio HR (also known as Degree-of-Hybridization DoH);
- Secondary energy source.

In the next sections a compact classification, based on the latter criteria, is presented.

### 2.1.1 Hybridization Ratio

A general definition of HR can be expressed by the following equation:

$$HR = \frac{P_{s,max}}{P_{s,max} + P_{ICE,max}} \tag{2.1}$$

where $P_{s,max}$ represents the maximum power of the prime mover of the secondary energy storage system and $P_{ICE,max}$ is the maximum ICE power.

Since HEV is the most common and developed hybrid technology, a more detailed classification is available for those systems, where the alternative storage is the electrochemical energy of a battery:

- *Micro hybrid*: ICE-based powertrain equipped with a small electric motor, essentially used as Integrated Starter Generator (ISG). $HR \approx 5\%$;
- *Full hybrid*: pure electric drive is allowed and higher electric power levels are needed, often requiring high voltage and complex power electronics (PE). $HR \approx 30 - 45\%$;
- *Mild hybrid*: the size of the electric components is smaller and does not allow ZEV operation, at least at higher vehicle speeds (see [98, 15]). $HR \approx 10 - 15\%$;
- *Plug-in PHEV*: the battery can be recharged directly from the electric grid, therefore limitations due to charge-sustaining operation fall. $HR > 50\%$;
- *Extended-range electric vehicles EREV*: ICE is used only as Auxiliary Power Unit (APU). $HR \approx 90\%$.

Since HR is a key parameter for the HV design, defining the sizing of prime movers and thus guiding the choice of the installed components, several methodologies have been proposed in literature to tackle this task. In [174, 179, 181] DP is applied to solve the problem of the optimal choice of HR. The advantage of similar techniques is that the task of optimal components identification is decoupled from their optimal use on a specified control mission, since the solution provided by the DP algorithm already guarantees optimality. Further optimization techniques, such as Particle Swarm Optimization (PSO) have been proposed (see [51]) to calculate the optimal sizing, possibly coupled with a DP procedure.

## 2.2 Hybrid Vehicle Topologies

According to [37, 75] HV architectures can be classified into four main categories:

- Parallel hybrid;
- Series hybrid;
- Series/Parallel or Combined hybrid;
- Complex hybrid.

Details of these classes are given in the following sections.

### 2.2.1 Parallel Hybrid Vehicle (pHV)

Parallel HVs can be considered ICE-based vehicles with an additional secondary power path. The power distribution between the conventional and the hybrid path can be optimized, leading to an additional degree of freedom in fulfilling the driver's power demand.

Both prime movers can be sized independently for a selected fraction of the total vehicle maximum power. The schematics of two pHV with different HRs are shown in Figure 2.3 in case of a HEV. Since the engine is coupled to the drivetrain, the installation of a clutch cannot be avoided.

Thanks to the numerous operating modes allowed, this configuration can lead to a very high level of the average efficiency of both the machines propelling the vehicle ([86, 132]).

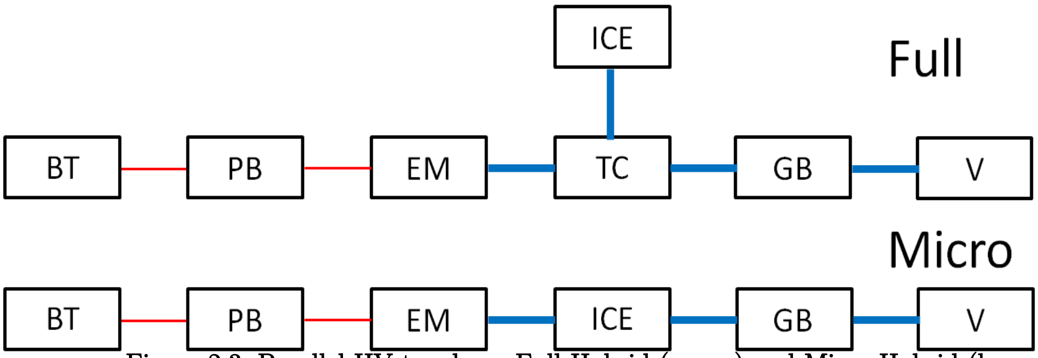

Figure 2.3: Parallel HV topology: Full-Hybrid (upper) and Micro-Hybrid (lower).

Figure 2.4 illustrates the typical operating modes of a pHEV. The two power flows can be combined in a generic "Torque Coupler" TC (although sometimes an additional clutch is installed) and the power balance can be controlled selecting the ratio $u_{ts}$ between secondary (electric) power and total requested power.

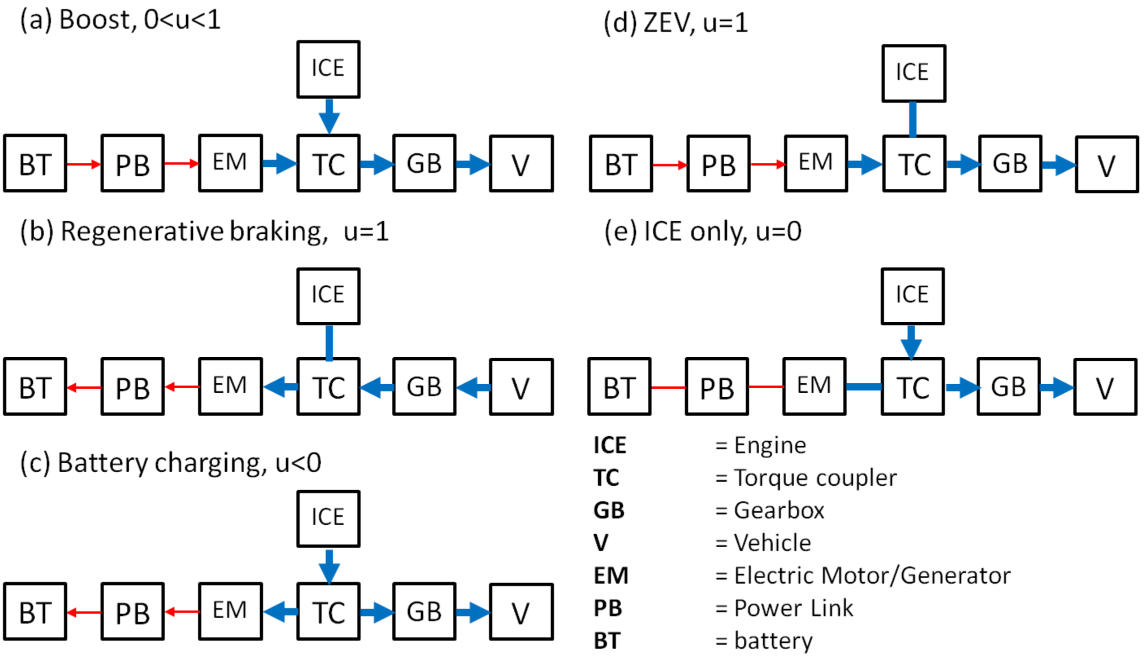

Figure 2.4: pHV operating modes.

During acceleration phases, ICE provides a fraction of the total power in the so-called *power assist*, while the rest comes from the additional machine ($0 < u_{ts} < 1$). During deceleration/braking operations, the secondary power path recuperates energy and stores it for later use ($u_{ts} = 1$). At light load, ICE can provide more power than requested from the driver's demand, therefore loading the additional energy storage system ($u_{ts} < 0$). In theory, depending on the HR, both pure ICE ($u_{ts} = 0$) and ZEV ($u_{ts} = 1$) are also possible.

### 2.2.2 Series Hybrid Vehicle (sHV)

Although the present section is referred to an HEV, it can be generally extended to other hybrid energy types, applying the same concepts. A Series HEV can be schematized as an EV, equipped with an APU to extend its electrical range. A schematic of such a hybrid system is illustrated in Figure 2.5.

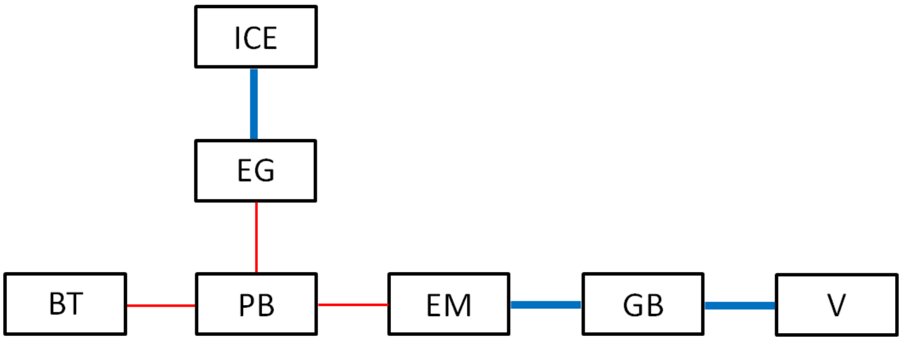

Figure 2.5: Series HV topology.

The sHEV is equipped with two electric machines; The EG is used to charge the battery from the ICE, while the EM is devoted to the vehicle propulsion and the energy recuperation during regenerative braking. Among the main advantages are the facts that the ICE operating point is not related to vehicle power requirements (allowing theoretical use at maximum efficiency conditions only) and that a clutch can be avoided.

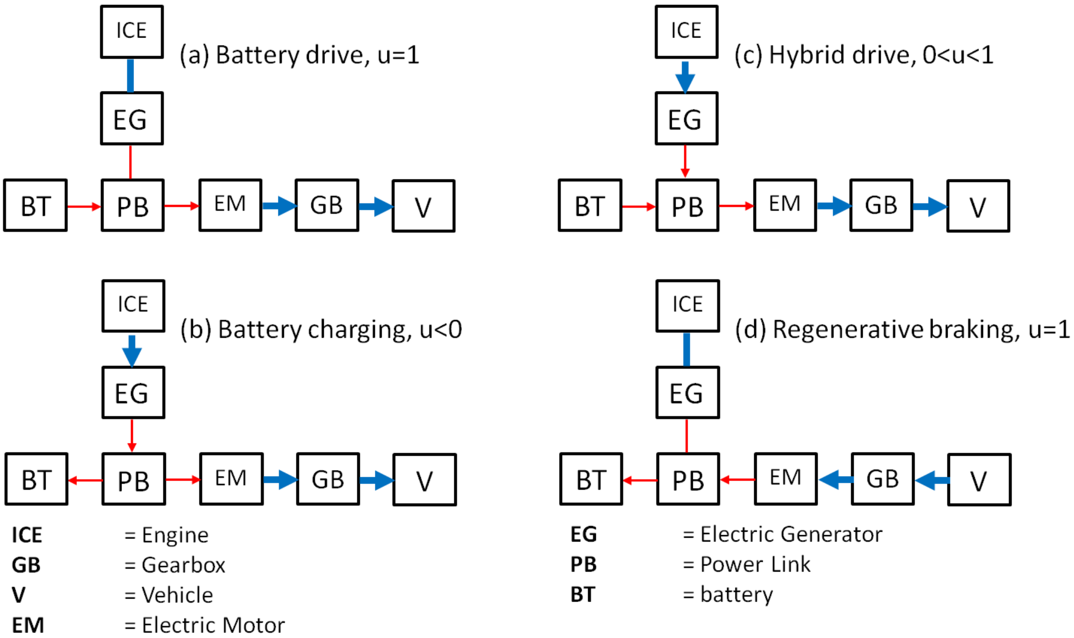

Figure 2.6: sHEV operating modes.

The main disadvantages are the increased cost and weight due to the presence of two electrical machines (or equivalent components for other hybrid types).

As depicted in Figure 2.6, four are the main operating modes for a sHEV. Once the power split ratio $u_{ps}$ is defined at the power link PB as the ratio between the power from/to the battery and the total requested power at the link, all modes can be properly defined. The ZEV mode ($u_{ps} = 1$) may be used during the urban driving and in general if regenerative braking occurs ($u_{ps} = 1$). The engine is turned on to recharge the battery every time the SOC is below a defined level. In this case a duty-cycle-operation takes place ($u_{ps} < 0$). If the maximum-efficiency engine power is below the value requested at the power link, a seldom operating mode where the missing power is provided directly by the battery ($0 < u_{ps} < 1$) is possible.

### 2.2.3 Combined Serial/Parallel and Complex Hybrid Vehicles

Combined HVs are basically parallel HVs, with some features of series HVs. Indeed, there are a mechanical and an electric link, and two electric machines are present. One is mostly used in parallel mode and it is a prime mover that propels the vehicle and recuperates kinetic energy during regenerative braking phases, while the second either acts as a generator to recharge the battery utilizing the ICE power or it operates during engine start/stop.

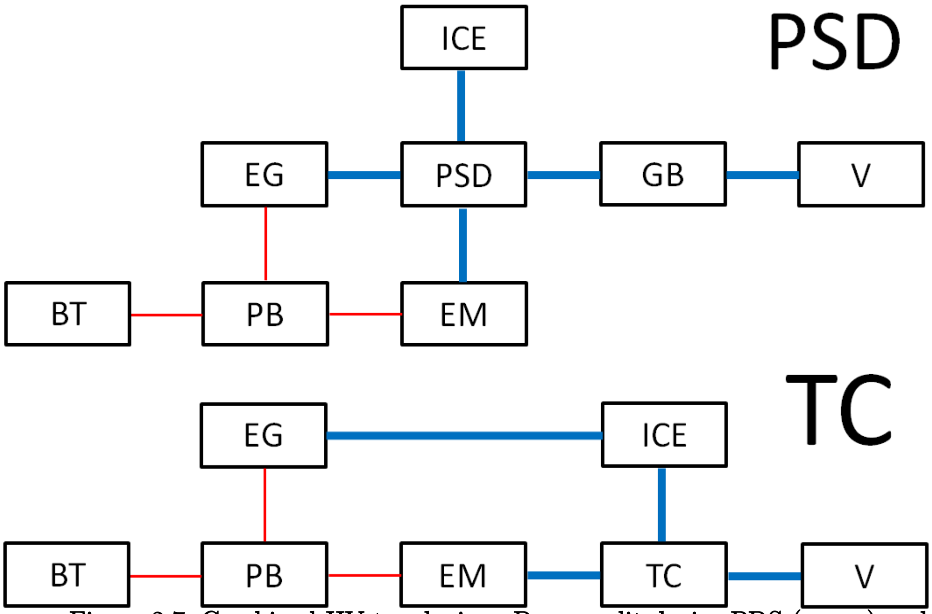

Figure 2.7: Combined HV topologies - Power-split device PDS (upper) and Torque Coupler TC (lower).

Very common configurations, as illustrated in the upper plot of Figure 2.7, include a Planetary Gear Set (PSG) or a power split device PSD.

The latter is the installation adopted in a very common passenger car HV model named Toyota THS (see [50, 84, 119, 131, 132, 199, 215]). Another option is depicted in the lower plot of the previous figure, where a Torque Coupler is installed to connect the EM and the ICE to the vehicle transmission. An overview of the possible combined hybrid operating modes is reported in Figure 2.8.

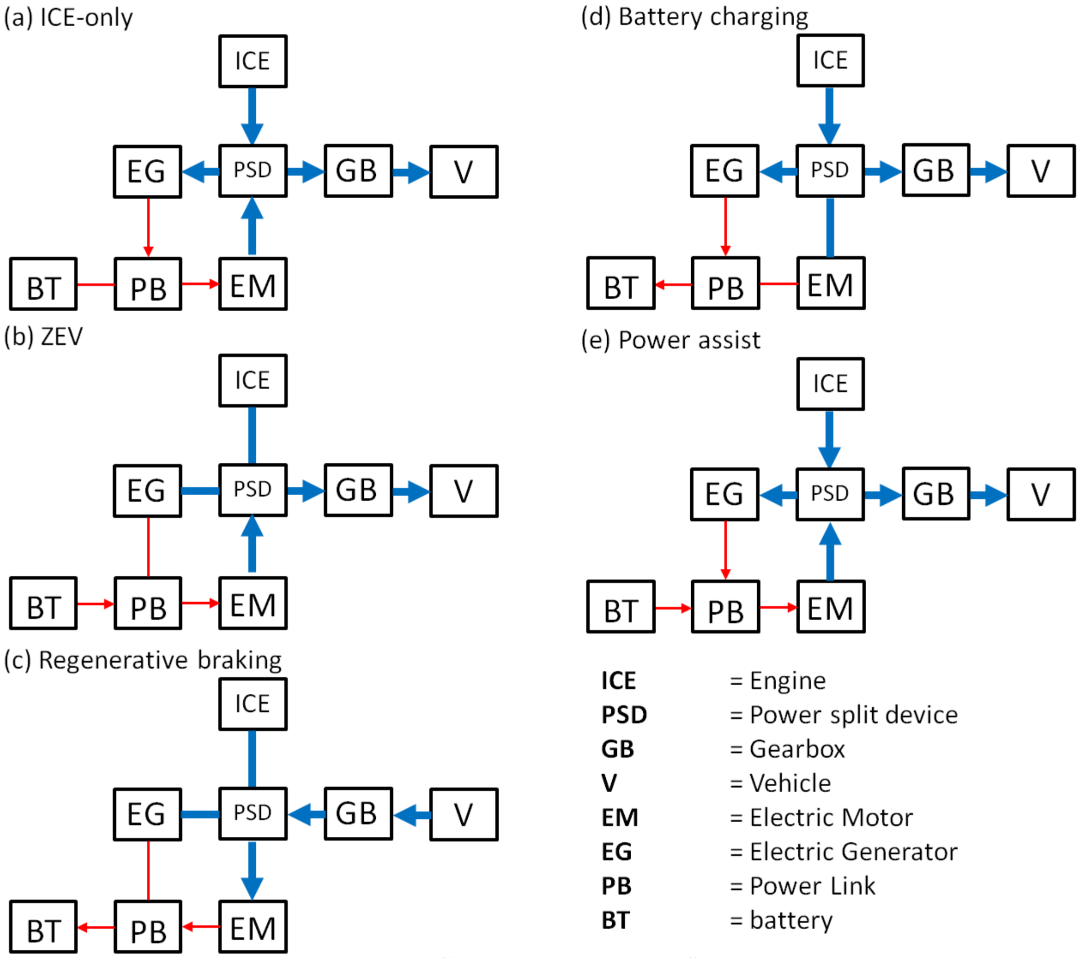

Figure 2.8: Combined HV with PSD - operating modes.

Theoretically, the series/parallel HV should benefit from all possible power flows of a pHV and of a sHV. However, the installation of a power split device (PSG) put some constraints, limiting the feasible energy paths. In particular, the ICE mode is often associated with a power flow through the EG and the EM.

### 2.2.4 Complex Hybrid Vehicles

In addition to the three previous configurations, which are also the most common in passenger car applications, a fourth category named Complex hybrid can be identified, whose structure is depicted in the schematic of Figure 2.9.

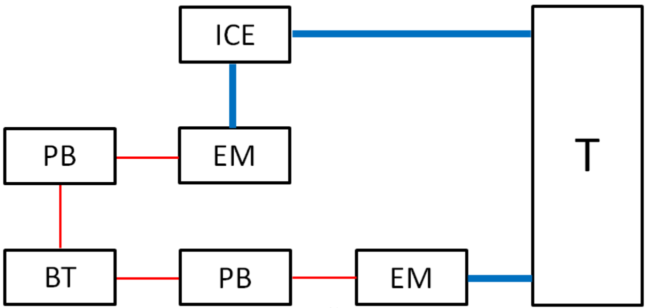

Figure 2.9: Complex HV topology.

Although it seems to be similar to the series/parallel architecture, since two electric machines are present and the ICE can propel the vehicle, the key difference is due to the bidirectional power flow allowed for both electric motors in this case. This can add versatility in the use of the prime movers, allowing a three-propulsion power mode.

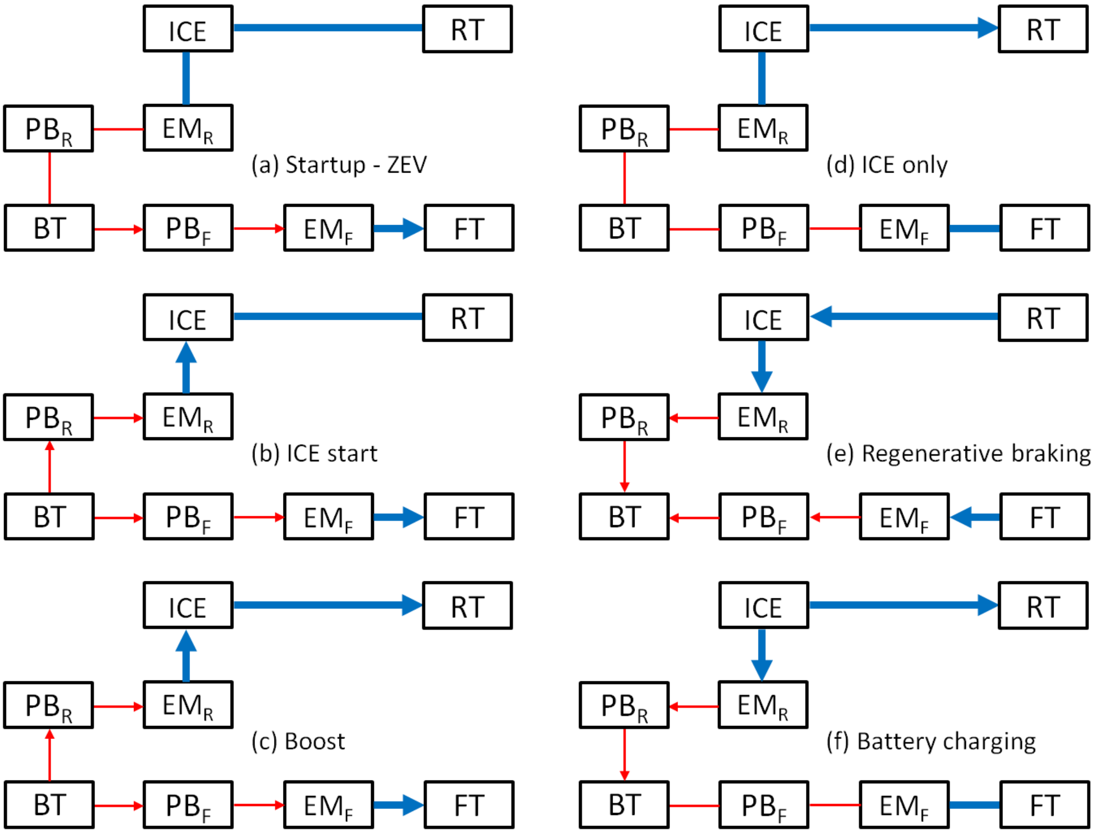

(a) Startup - ZEV

(b) ICE start

(c) Boost

(d) ICE only

(e) Regenerative braking

(f) Battery charging

**ICE** = Engine
**GB** = Gearbox
**FT** = Front axle
**RT** = Rear axle
**$EM_F$** = Front axle Electric Motor
**$EM_R$** = Rear axle Electric Motor
**PB** = Power Link
**BT** = battery

Figure 2.10: Dual-axle complex HV (electric front) - operating modes.

This system suffers from high complexity and costs. Nevertheless, as illustrated in Figure 2.10, it can be proficiently adopted for dual-axle hybrid concepts, where the rear axle is a parallel electric hybrid, and the front axle is electric. A DP-based sizing optimization analysis for such a Complex hybrid is given in Appendix A.1.

## 2.3 Secondary Energy Source

A further classification of HVs can be done in terms of nature of the secondary energy storage. Apart from electrochemical energy stored in batteries, several other technologies exist. Although they usually are characterized by lower energy density, they can provide the same typical HV operating modes, such as engine load shift towards higher efficiency points, regenerative braking and engine start/stop. A comprehensive list of all existent principles is the following:

- Electrochemical energy, EMG and battery (HEV);
- Electrostatic energy, EMG and supercapacitors;
- Electromagnetic energy, EMG and superconductor coil;
- Kinetic energy, CVT and flywheel (HSF-HV);
- Elastic potential energy, CVT and torsion spring;
- Pneumatic, PMP and AST (PHV);
- Hydraulic, HMP and accumulator (HHV).

Among the previous possibilities, the next paragraphs focus on parallel hybrid vehicle architectures, analyzing both HEV and HSF-HV in the research activity presented in Chapter 4, and HEV in Chapter 5. A Complex hybrid HEV is then considered in Appendix A.1. A common framework capable of allocating four different energy storage systems (HEV, HSF-HV, HHV and PVH) is presented in the following sections.

### 2.3.1 Hybrid Electric Vehicle (HEV)

The pHEV architecture presented in Figure 2.11 is the basic concept of an electric hybrid system, whose model is described in details in Chapter 3 and is valid for both gasoline and diesel ICEs.

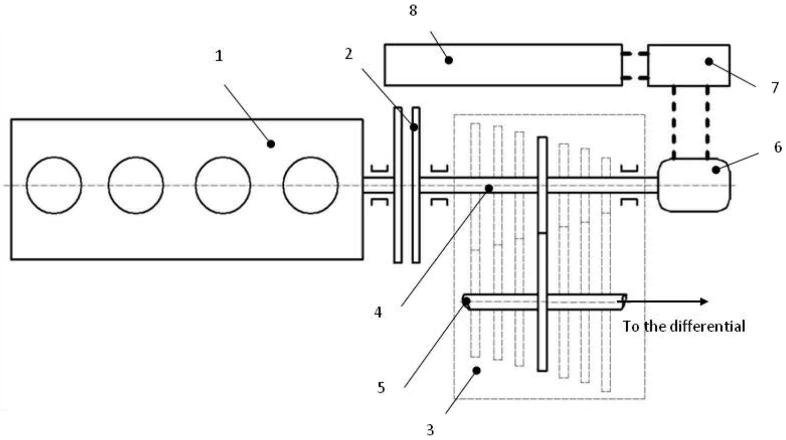

**Figure 2.11: Parallel HEV components detail; (1) ICE, (2) ICE Clutch, (3) AMT, (4) primary AMT shaft, (5) secondary AMT shaft, (6) EMG, (7) PE, (8) Battery, [188].**

In the proposed architecture the EMG is installed on the GB primary shaft, so that it can benefit from a dedicated gearshift strategy, to further improve the electric machine efficiency during ZEV operation.

### 2.3.2 Mechanical Hybrid Vehicle (HSF-HV)

The use of low-speed flywheels is a well-established automotive technology. Every ICE is nowadays equipped with a similar component, to smooth the irregularities of power flow typical of a reciprocating machine. The use in hybrid inertial powertains is also a viable technical solution, as described in [152]. Different mechanical HV topologies can be adopted, to include a kinetic energy storage device into a vehicle propulsion system. Each solution requires a different number of components such as CVT, gearbox and clutches.

Some comparative analysis of diverse architectures can be found in literature [31, 21]. Since the flywheel must rotate at high speed and its rotational speed must be allowed to vary independently from vehicle speed, a CVT system with a very wide range is needed [30, 129] between the HSF and the drive train.

In some applications, as described by the authors of [2, 74], mixed inertial/electric hybrid concepts have been designed.

The main features of HSF-HV technology are a very high power density and a relatively low energy density, the latter being one of the major disadvantages of this solution for hybrid car applications. Since very high speeds (up to 3000 rev/s) are needed to achieve a sufficient amount of stored energy, the spinning disc is constructed out of materials of the highest tensile strength. For these reasons, composite materials employing carbon fibers are preferred to metals ([190]), and vacuum operation is requested for reducing aerodynamic drag losses.

The authors of [126] propose a comparison between two different topologies for mechanical HVs equipped with CVT and HSF. In the schematic of Figure 2.12 the two variants are illustrated. A fixed-ratio gearbox and an additional friction clutch are added to the CVT to form the hybrid part of the powertrain. Since variant (B), where the hybrid system is coupled with the primary shaft of the GB of the ICE, offers an additional degree of freedom for KERS utilization (GB gearshift strategy), this configuration is selected as the reference for the later analysis of the HSF-HV.

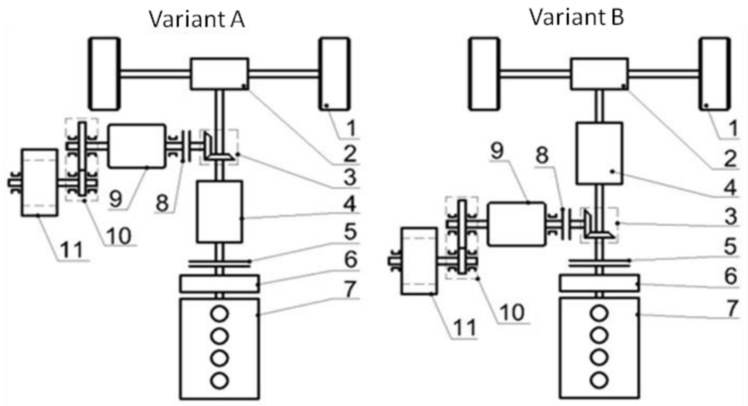

Figure 2.12: Possible HSF-HV configurations; (1) wheels, (2) Differential, (3) step-up GB, (4) AMT, (5) Clutch, (6) ICE flywheel, (7) ICE, (8) HSF clutch, (9) CVT, (10) step-up GB, (11) HSF, [126].

Further details of HSF-HV components are illustrated in Figure 2.13.

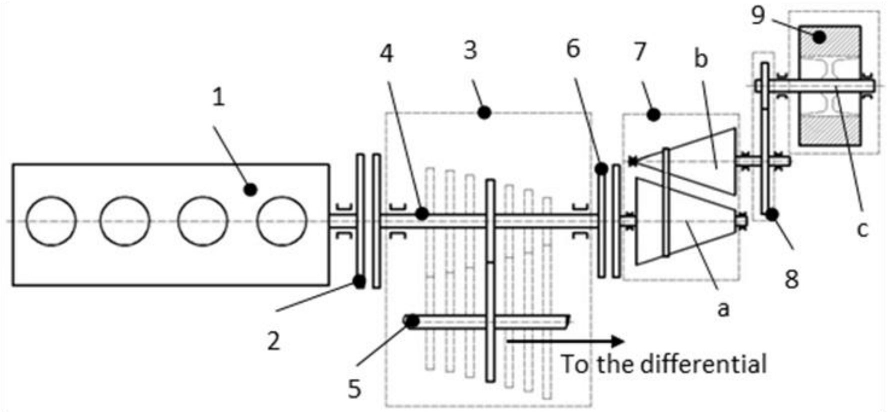

Figure 2.13: Parallel HSF-HV components detail; (1) ICE, (2) ICE Clutch, (3) AMT, (4) primary AMT shaft, (5) secondary AMT shaft, (6) HSF clutch, (7) CVT, (8) step-up GB, (9) HSF, [188].

### 2.3.3 Hydraulic Hybrid Vehicle (HHV)

Hydraulic energy is considered a viable technical solution to equip HVs, especially in case of heavy-duty applications and delivery trucks, due to its high specific power leading to a use compatible with high deceleration powers. Another advantage of hydraulic accumulators is their ability to tolerate high charging/discharging rates and high power frequencies, which is not the case of electrochemical accumulators. A drawback is the lower energy density compared to batteries. HHVs can be both series ([125]) and parallel ([205]) hybrid powertrains. A parallel HHV configuration is depicted in Figure 2.14.

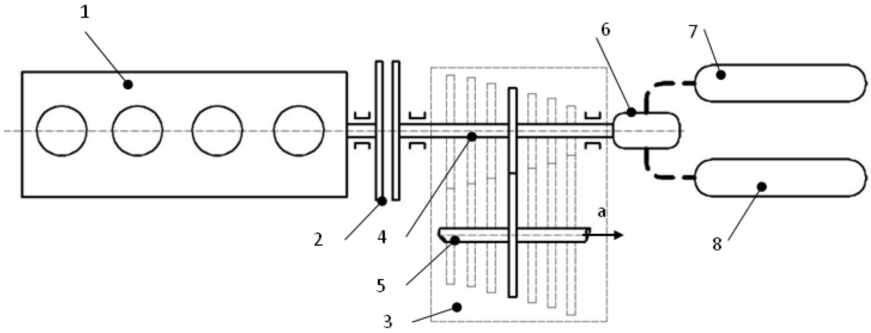

**Figure 2.14: Parallel HHV components detail; (1) ICE, (2) ICE Clutch, (3) AMT, (4) primary AMT shaft, (5) secondary AMT shaft, (6) HMP, (7) HPA, (8) LPA, [188].**

It usually includes a reversible hydraulic machine HMP and two hydraulic accumulators filled with inert gas, one for each pressure level.

### 2.3.4 Pneumatic Hybrid Vehicle (PHV)

The possibility to realize a Pneumatic Hybrid Engine system has been investigated as a way to achieve potentially consistent FE improvements, as reported by the authors in [49, 48, 187]. This is possible due to the combination of an ICE with a short-term pneumatic storage system. The ICE is used as a motor/compressor, recuperating during braking and enhancing the elimination of some low-efficiency operating points, e.g. low loads and idling. Such system could be also efficiently coupled with a downsized turbocharged concept, simultaneously improving FE and drivability. A different approach presenting a synergic use of an exhaust gas heat recovery and an air compressor is proposed in [73] and validated in [71]. Apart from the latter ICE-based solutions, there are studies concerning hybrid vehicles equipped with a reciprocating air compressor to recuperate kinetic energy during braking ([53]) or with both a pneumatic motor and compressor to constitute a real hybrid vehicle, as described in [72]. However, a more sophisticated solution is described in [47] and can be observed in the schematic of Figure 2.15.

Here, the operation of a reversible PMC is designed and assessed, while a further FE improvement is attained thanks to a heat recovery system that exploits exhaust gas heat flow by means of a heat exchanger surrounding the AST.

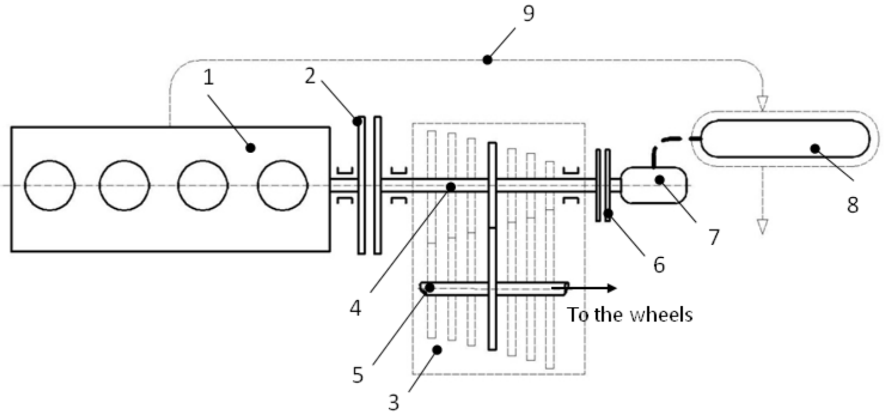

Figure 2.15: Parallel PHV components detail; (1) ICE, (2) ICE Clutch, (3) AMT, (4) primary AMT shaft, (5) secondary AMT shaft, (6) Secondary clutch, (7) PMC, (8) AST, (9) ICE exhaust gas, [188].

## 2.4 Supervisory Control of Hybrid Vehicles

The main purpose of a Supervisory Control for a hybrid vehicle is to coordinate the different power flows from the different sources, fulfilling the given power requirement of the driver.

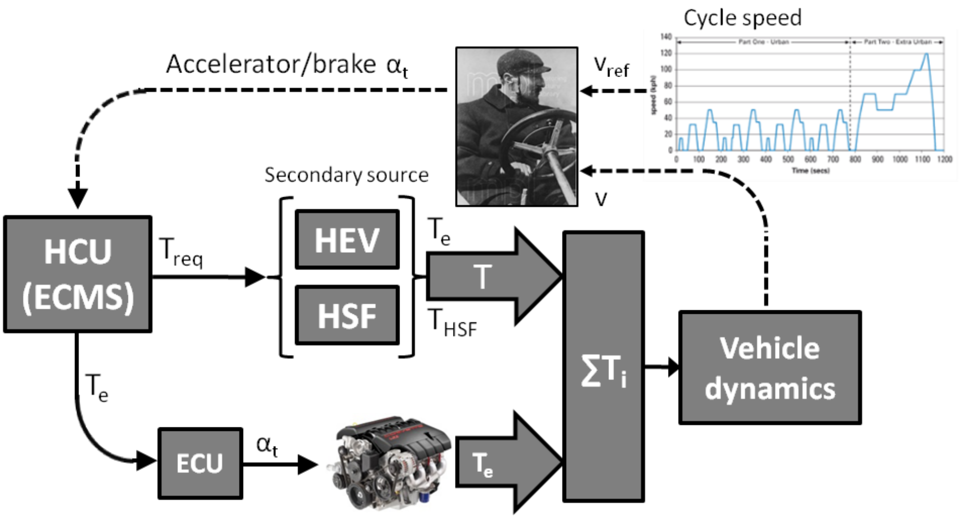

Figure 2.16: Simplified supervisory control for the EMS of HVs, see [188].

It generally manages three main control inputs, precisely the power/torque split factor between conventional and secondary prime movers (or equivalent definition for a sHV, see Section 2.2.2), the ICE start/stop command and the clutch(s) command. In other words, it determines the driving mode aiming at the most efficient utilization of the available energy storage systems. Figure 2.16 depicts a block diagram for a simplified Supervisory control for parallel hybrid architectures. Generally speaking, a supervisory control must handle with many constraints regarding the current driving conditions (e.g. engine speed, engine state, motor speed, clutch state, battery SOC) or physical limitations of the installed components and has to fulfill drivability requirements. The final task is to supply set points for all the low level controllers involved in the powertrain (e.g. engine torque, motor torque, etc.) and manage the dynamic coordination during transient maneuvers, i.e. involving driving mode changes.

### 2.4.1 Motivations and classification

A proper design of the Supervisory Control system, also called EMS, is a key factor to obtain the FE and pollutant emissions performance expected from a HV. As a consequence, it is important to select the best controller for each system, as several researchers have tried to point out in papers dealing with comparative analysis of different EMSs, such as [167, 104, 39, 203, 197, 148, 166, 103, 164, 94, 85, 186]. A primary classification criterion for an EMS is the dependency on the knowledge of future driving conditions, distinguishing between:

- *Non-causal controllers*: a detailed knowledge is required, as in case of regulatory driving cycles or repetitive public transportation routes;
- *Causal controllers*: in this case a driving profile is not predictable, therefore control actions only rely on past and present system conditions.

A second condition is related to the use of optimal control theory in the setup of the controller framework:

- *Heuristic controller*: causal;
- *Optimal controller*: inherently non-causal;
- *Sub-optimal controller*: often causal.

### 2.4.2 Heuristic Strategies

Heuristic controllers rely on intuitive rules correlating various physical variables of the vehicle system. A common rule is that the ICE must be used exclusively in its high efficiency operating region, therefore it will not be turned on if such condition cannot be fulfilled. Another typical guiding rule is the one concerning SOC limitations, prescribing the battery level of energy to always lie in a given range. Temperature levels and ICE/catalyst warm-ups are often included in similar rules. This kind of criteria can form a rule-based approach, where the EMS is implemented in a finite-state machine, as in the example of Figure 2.17.

Sometimes rule-based approach can even be derived from the results obtained by means of optimal control algorithms, as the authors of [23, 192] claim. Another way to generate rules for mode transitions in Heuristic strategies is the implementation of Fuzzy Logic rules (see [114, 38]).

A Fuzzy Logic-based technique has also been applied to mechanical HVs [55]. The main advantage of heuristic control is its intuitive approach. On the contrary, a great disadvantage is that its performance depends on the tuning of a great number of parameters (like thresholds, switches, etc.), that makes its setup a time-consuming procedure. Moreover, determining priority between many conflicting boolean operators can lead to a poor FE benefit, highlighting the need of a more quantitative criterion.

Another interesting rule-based controller is the object of the research activity carried out in [7], where an explicit control law is derived from the application of optimal control theory by means of a fully analytical simplified model of the vehicle system.

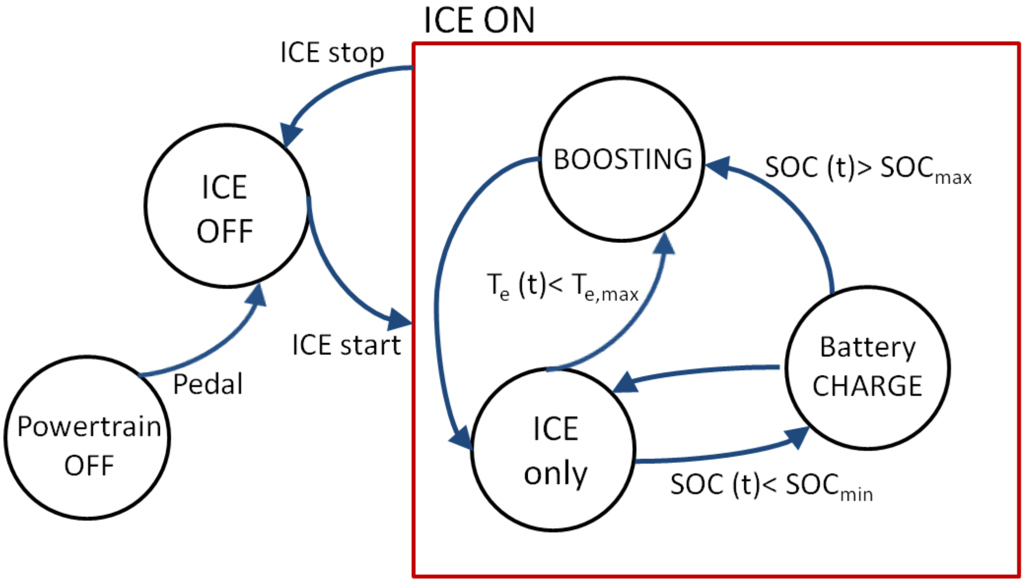

**Figure 2.17: Schematic of a Finite-state machine for HV control.**

DP results can be also used to enforce rule-based strategies obtaining the desired thresholds or the information about the logic of operating mode switching, as demonstrated in [115].

### 2.4.3 Optimal EMS

Optimal Control theory [57] can be applied to a predefined control mission for a HV. In general, this leads to a purely non-causal controller, since its solution depends on the full knowledge of the disturbances over the entire time horizon.

However, in some cases sub-optimal controllers can be extracted from the results of the optimization method, generating an EMS that is suitable for on-line implementation.

#### 2.4.3.1 *Off-line Optimization Methodologies*

The application of optimization methods to the HV control is discussed in details in Chapter 4. A generic classification of off-line causal methods is:

- *Dynamic Programming* (DP): a numerical algorithm based on Bellman's Principle of Optimality ([176, 150, 22, 121]);
- *Pontryagin's Minimum Principle* (PMP): an analytical method that often leads to the solution of a two-point boundary value problem ([96]);
- *Convex Optimization*: based on mathematical hypotheses about the convex shape of the cost function ([185, 135]).

Even though the previous methodologies cannot be directly implemented on-board, they can provide a benchmarking performance, to be compared to the results of any suboptimal causal controller. In some cases, on-line suboptimal EMSs can be generated starting from the structure of an optimal solution, as it happens with PMP and ECMS.

### 2.4.4 On-line Control Strategies

Causal controllers don't need a full knowledge of the future conditions to be applied. For this reason they can be applied online for the on-board application of an EMS. A first classification of such methodologies can be the following:

- Predictive Control;
- Time-invariant feedback controllers and SDP;
- ECMS-type controllers.

ECMS-type controllers directly arise from PMP, as demonstrated by the authors of [168], where the uncertainty about future conditions is shifted to an uncertainty on the correct optimal value of the adjoint state (co-state). Usually, this leads to a time-variable estimation of the equivalence factor, for which various methodologies are available in literature. A detailed analysis of ECMS-type controllers is provided in Section 4.2.2.2, for parallel hybrid vehicles. However, similar approaches have been developed for series HVs as well, as reported in [208].

Time-invariant feedback controllers are constituted by feedback maps, tabulated as a function of some input variables, typically SOC and torque/power demand for HEV applications. Those maps are computed from the solution of some previous optimization procedure, e.g. deterministic DP.

#### *2.4.4.1 Model Predictive Control (MPC) and Stochastic Dynamic Programming (SDP)*

The use of an optimization procedure relies on the knowledge of future driving profiles. Based on previously measured velocity profiles on the current route, a prediction of the future power demand on a finite future time horizon can be performed on-line. This estimation, combined with DP, leads to MPC control paradigm. This approach is based on the application of DP to generate the optimal control trajectories of all control inputs, on a determined future time range, where all estimated may could be provided by the combination of GPS, onboard instruments and traffic information (see [214, 213, 111, 97, 38, 16, 3, 178]).

Another interesting application in the field of predictive control is Stochastic Dynamic Programming (SDP), where the future trajectory extrapolation is based on a stochastic process generated by collected data, identifying the transitions probability of Markov chains. Several studies [117, 101, 79, 1] assess the feasibility of similar methodologies for the online control of hybrid vehicles in real driving conditions. SDP can be used to generate time-invariant feedback controllers, based on the solution of an infinite-horizon optimization. This process produces a feedback control law that is applicable in general driving conditions [117, 79]. A further evolution of SDP applied to the control of hybrid vehicles is proposed by the authors of [83], where reinforcement learning and neuro-dynamic programming techniques are implemented to approximate the cost-to-go function using a neural network.

# 3. Control-oriented Models of Parallel Hybrid Vehicles

This Chapter illustrates the modeling paradigms applied to the hybrid vehicle architectures investigated. First, different approaches are compared; then a detailed description of the governing equations is given and in the conclusive section the data of the vehicles used in simulations is provided. The treatise focuses on HEV and HSF-HV parallel vehicles, which are used for the later analyses presented in the next Chapters.

## 3.1 Quasi-static and Dynamic Models

The optimization of control strategies for HVs strongly depends on the model used to simulate and develop the different control frameworks, aiming at FE, emissions reduction or performance optimization. For these reasons, several approaches have been investigated and can be found in the literature related to this topic. The main distinction is between:

- *Quasi-static* simulation (QSS) or *backward-facing* approach;
- *Dynamic* simulation or *forward-facing* approach.

The QSS models, described in [65, 64, 17, 88, 155], assume that the vehicle always perfectly meets the required speed trace, calculating the required force to accelerate it at each time step. The vehicle speed is translated into rotational speed while the traction/braking force is converted to torque assuming some components efficiencies. The computation flows upstream, from the wheels to the prime movers, against the physical power flow. The main advantages of the latter backward-facing approach can be summarized as follows:

- Experimental efficiency tables (maps) are often computed in terms of speed and torque, so that they can be directly implemented within this approach;
- It allows very simple integration routines (i.e., Euler) to be implemented with large time steps (typically 1 s);
- Quick execution.

The major disadvantages that can be encountered due to the implementation of a QSS approach are:

- It is not suitable for ”best effort” performance simulations, since it requires the theoretical speed profile to be always perfectly matched;
- Since the energy use is estimated by means of quasi-static steady-state experimental maps, its use does not take into account dynamic effects;
- It is not based directly on relevant control signals for the vehicle, e,g. the throttle position and the brake pedal position.

If the purpose of the simulator is to develop an appropriate and realistic description of the real control signals, for control hardware and software development, dynamic forward-facing models are needed ([116, 11]). They include a driver model that provides appropriate accelerator and brake pedal signals. The calculation proceeds from the prime movers through the transmission to the wheels, finally computing the vehicle acceleration. The main paybacks are:

- Measurable and realistic control signals and torques are used;
- Dynamic models and high frequency effects (i.e. elasticity and dampers) can be included;
- WOT events can be simulated.

Conversely, some of the major drawbacks are:

- Lower simulation speed caused by the need of integration for vehicle components speed. They are executed at smaller time steps to provide stability and accuracy of the higher order integration scheme applied;
- The implementation of a PI driver model is not suitable for the integration of dynamic models into an optimization procedure based on dynamic programming (DP), since the latter proceeds backward in time.

To overcome the disadvantages of both the QSS and the dynamic modeling paradigms, mixed forward/backward approaches have been investigated. The authors of [204] developed an extended backward-facing parametric library that is enhanced by additional forward-facing features, e.g. correction loops for the consideration of physical limitations of the machines, the wheels slip etc.

In the next Chapters, both backward and forward approaches are adopted.

The key idea beyond both methodologies is that only the longitudinal vehicle dynamics is relevant to achieve the goal of optimal control strategies of interest. Figure 3.1 illustrates the main forces acting on a vehicle on a road grade.

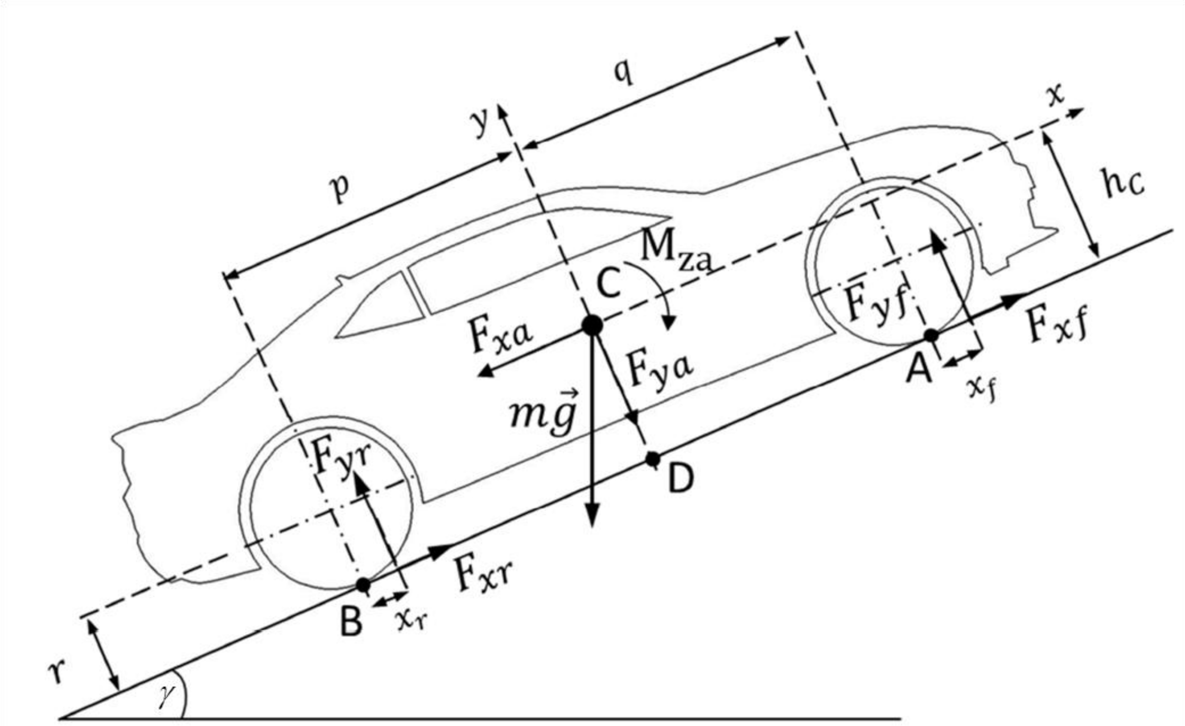

**Figure 3.1: Forces acting on a vehicle on a road grade, see [58].**

In the next sections, a detailed description of the equations used to model the vehicle behavior is provided for each component. The main difference between QSS and dynamic approaches lies in the physical causality of the signal routing.

Although the basic balance equations employed are the same, in many cases the input/output criterion is the opposite.

Figure 3.2 depicts the schematic QSS model for the parallel HEV in study, while Figure 3.3 offers a representation of the dynamic input/output causality for the same hybrid vehicle architecture.

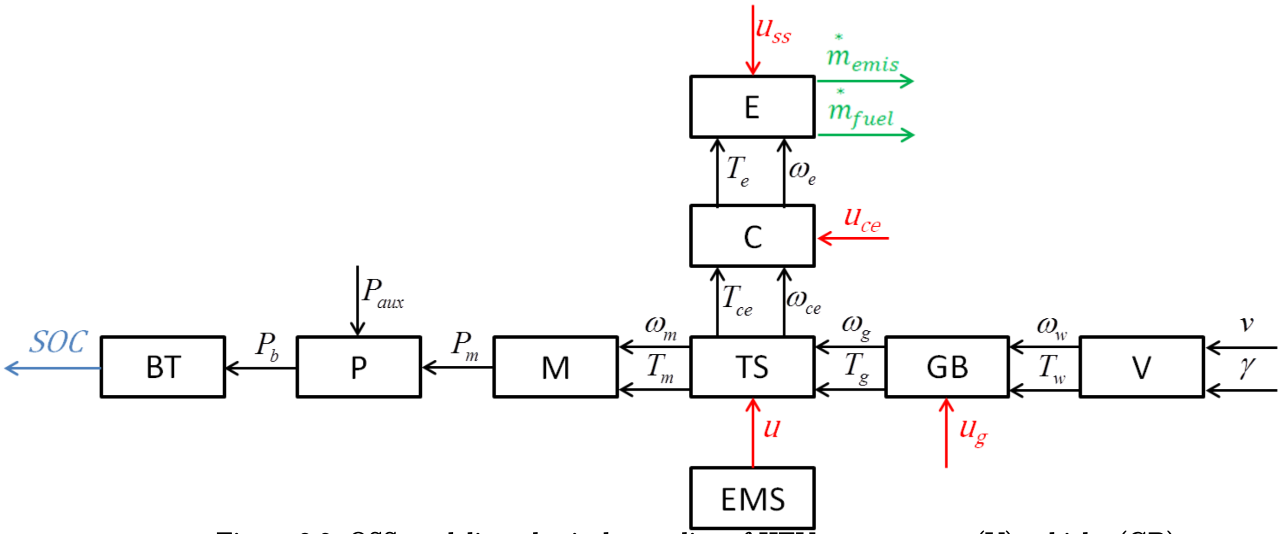

Figure 3.2: QSS modeling physical causality of HEV components; (V) vehicle, (GB) gearbox, (TS) torque-split link, (M) EMG, (P) power electronics/amplifier, (BT) battery, (C) clutch, (E) ICE.

It can be observed that a major difference between the above QSS and the dynamic model below lies in the causality of torques and speeds for the energy converters (machines and mechanical transmissions) and in the presence of a Driver, who tackles the desired speed, imposed by the driving cycle profile DC.

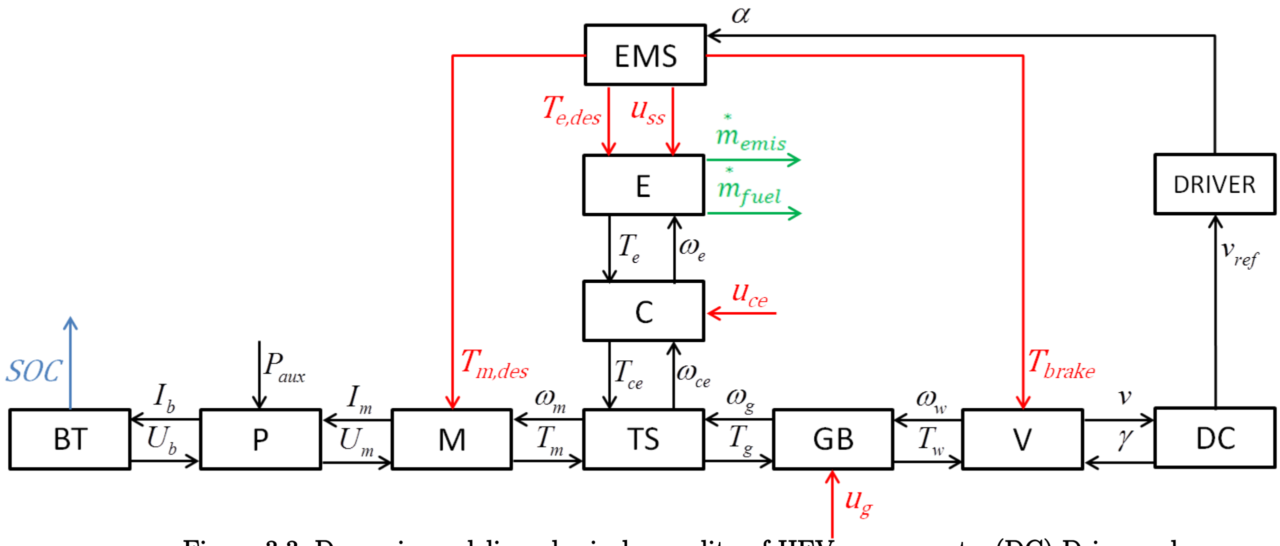

Figure 3.3: Dynamic modeling physical causality of HEV components; (DC) Drive cycle, (V) vehicle, (GB) gearbox, (TS) torque-split link, (M) EMG, (P) power electronics/amplifier, (BT) battery, (C) clutch, (E) ICE, (EMS).

Similar considerations can be applied to the schematics reported in Figure 3.4 and in Figure 3.5, representing a QSS and a dynamic model for a parallel HSF-HV powertrain.

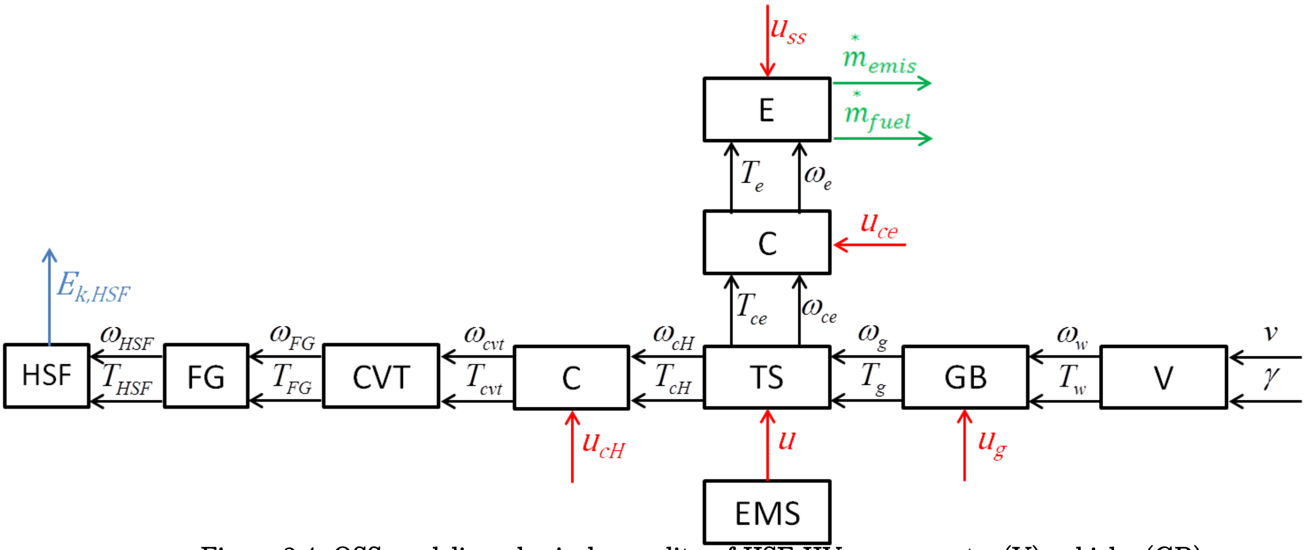

**Figure 3.4:** QSS modeling physical causality of HSF-HV components; (V) vehicle, (GB) gearbox, (TS) torque-split link, (CVT), (FG) fixed-ratio gear, (HSF), (C) clutch, (E) ICE.

In this case, the forward-facing model of the HSF-HV in Figure 3.5 includes a CVT controller, whose behavior is instead inherently included by the governing equations in case of QSS approach.

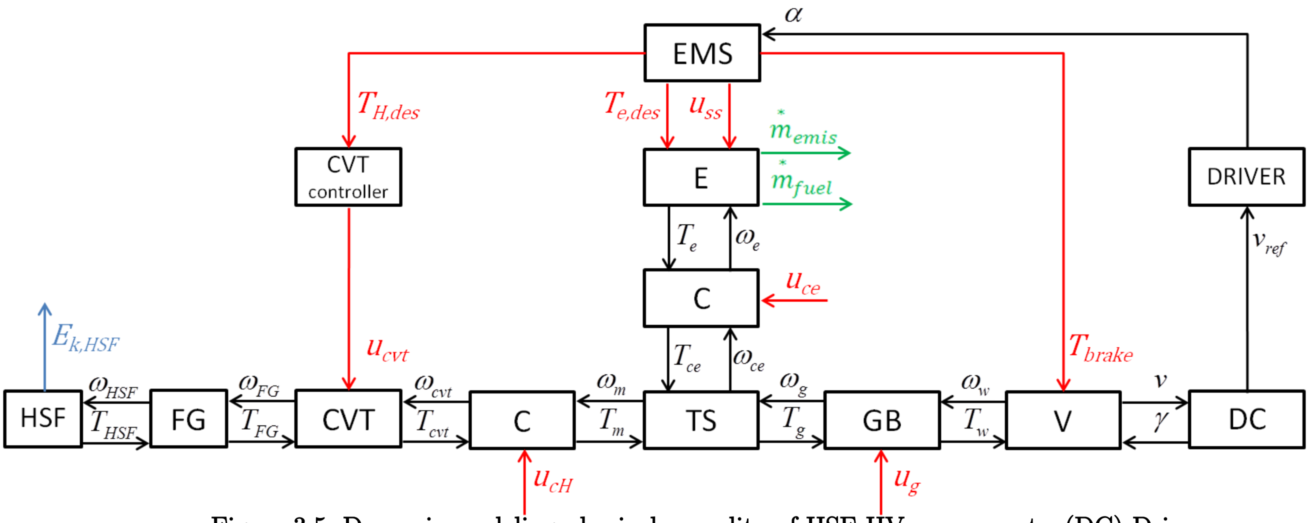

**Figure 3.5:** Dynamic modeling physical causality of HSF-HV components; (DC) Drive cycle, (V) vehicle, (GB) gearbox, (TS) torque-split link, (CVT) and controller, (FG) fixed-ratio gear, (HSF), (C) clutch, (E) ICE, (EMS).

The following treatise provides a full mathematical description of all powertrain components included in the vehicle models adopted.

## 3.2 Conventional Vehicle Components

First, the components of conventional vehicles are described. The equations reported in the next sections are valid for each ICE-based vehicle model, both for the QSS and for the dynamic approach, following the distinction in terms of physical input/output causality previously introduced.

### 3.2.1 Driver Model

The driver block consists of a PI controller that is aimed at reducing the error between the actual vehicle speed $v(t)$ and the reference value $v_{ref}(t)$, adapting the theoretical extended throttle $\tilde{\alpha}_t(t)$ as follows:

$$\tilde{\alpha}_t(t) = k_{p,D} \cdot \left(v_{ref}(t) - v(t)\right) + \frac{1}{T_{i,D}} \cdot \int_0^t \left(v_{ref}(t) - v(t)\right) d\tau \tag{3.1}$$

The theoretical throttle $\tilde{\alpha}_t(t)$ equals the physical throttle position in case of positive torque demand and corresponds to the brake pedal position when its value is negative. The theoretical value must be saturated as the following equations express:

$$\alpha_t(t) = \begin{cases} 100 & if \;\; \tilde{\alpha}_t(t) > 100 \\ \tilde{\alpha}_t & if \;\; -100 \le \tilde{\alpha}_t(t) \le 100 \\ -100 & if \;\; \tilde{\alpha}_t(t) < -100 \end{cases} \tag{3.2}$$

The driver model is only included in forward-facing modeling approaches. In case of parallel hybrid vehicles, this signal is transmitted to the EMS block, where the actual split factor is computed and the desired torques are converted into ICE/EMG commands.

### 3.2.2 Longitudinal Vehicle Model

The total traction force necessary to accelerate the vehicle can be split into four contributions as:

$$F_t(t) = F_i(t) + F_a(t) + F_r(t) + F_g(t) \tag{3.3}$$

They represent the inertial $F_i(t)$, the air drag $F_a(t)$, the rolling friction $F_r(t)$ and the slope $F_g(t)$ forces. They can be calculated by means of the equations below:

$$\begin{aligned} F_i(t) &= m_v \cdot \dot{v}(t) \\ F_a(t) &= \frac{1}{2}\rho_{air} A_f c_x v^2(t) \\ F_r(t) &= \left(\sum_{n=0}^{4} c_{r,n} v^n(t)\right) \cdot m_v g cos(\gamma(t)) \\ F_g(t) &= m_v g sin(\gamma(t)) \end{aligned} \tag{3.4}$$

Instead of the vehicle mass $m_v$ the total mass $m(t)$ including all equivalent masses related to rotating elements of relevant inertia, could be used in (3.4). For the parallel HEV, where the electric motor is always linked to the GB primary shaft, its value would be written as follows:

$$m(t) = m_v + \frac{\Theta_\mathrm{w}}{r_w^2} + \frac{\Theta_\mathrm{m} \cdot i_\mathrm{g}^2(u_g(\mathrm{t}))}{r_w^2} \tag{3.5}$$

where the major inertias always connected to the driveline are the wheels and the electric motor, whose equivalent mass depends on the gear ratio $i_g$ that is a function of the gearshift command $u_g(t)$. Angular speed and acceleration of the wheels depend on the wheel radius $r_w$:

$$\begin{aligned} \omega_w(t) &= \frac{v(t)}{r_w} \\ \dot{\omega}_w(t) &= \frac{\dot{v}(t)}{r_w} \end{aligned} \tag{3.6}$$

The wheel torque can be computed using the following rotational balance expression:

$$T_w(t) = F_t(t) \cdot r_w + \Theta_w \cdot \dot{\omega}_w(t) \tag{3.7}$$

If the forward-facing modeling approach is chosen, the causality of the considered block is inverted. For the vehicle dynamics block, the vehicle acceleration is an output and is computed by the equation (3.8).

$$\dot{v}(t) = \frac{1}{m_v} \cdot \left( \frac{T_w(t)}{r_w} - \left(F_a(t) + F_r(t) + F_g(t)\right) \right) \tag{3.8}$$

Similar considerations concerning differences between the input/output of QSS and dynamic models are valid for the blocks described in the next sections. They will be omitted since the equations are suitable for both modeling paradigms.

### 3.2.3 Gearbox

The task of the gearbox block is to provide the current selected gear (or gearshift command) $u_g(t)$ discrete input, so that torques and speeds at the primary shaft, where the propellers are installed, can be calculated by means of the corresponding overall gear ratio $i_g$. The latter comprises the final drive gear ratio. A simplified gearshift pattern is depicted in Figure 3.6, where $u_g(t) = f_g(v(t))$ as a function of vehicle speed only.

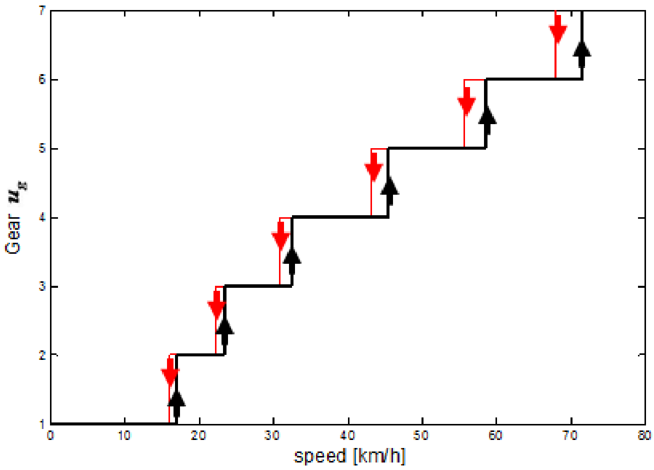

**Figure 3.6: AMT gearshift pattern based on vehicle speed.**

A hysteresis between up-shift and down-shift events is often present to enforce drivability. As explained in the next Chapter, gearshift strategy can be also included in the EMS, to enhance the optimal gear selection. However, in this case the resulting gear trajectories could lead to high frequencies of gearshift events, often related to small theoretical FE advantage, associated to the numerical discretization of the experimental maps. For this reason, heuristic gearshift patterns are more commonly used in practice. In real world driving conditions, where strong acceleration or deceleration can occur, a purely speed-based shift pattern may be not sufficient to fully exploit the potential of the vehicle components. As a consequence, more detailed maps can be utilized, where up-shift and down-shift lines also depend on throttle/brake pedal position (driver's power demand). An example is shown in Figure 3.7 for an automatic transmission (AT).

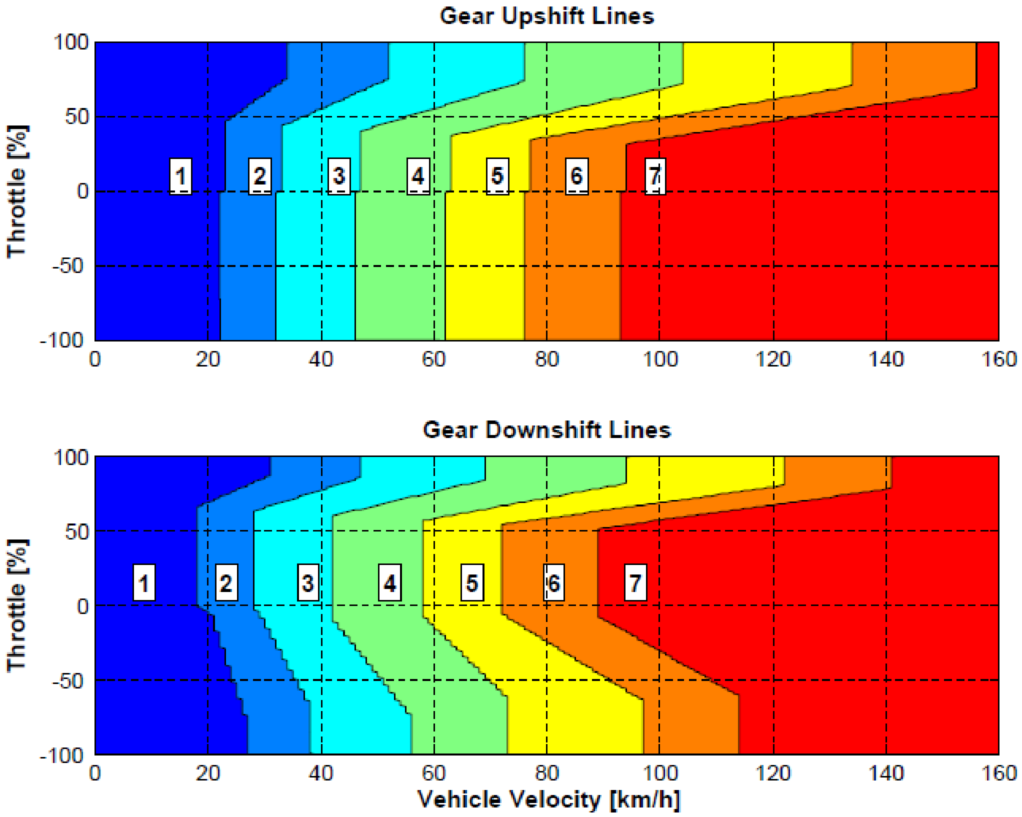

Figure 3.7: AT gearshift pattern for an HEV; positive and negative torque.

In this case, not only up-shift and down-shift lines are shifted, but a dedicated gearshift pattern is designed for the deceleration operations, to optimally exploit the regenerative braking at the highest efficiency of the electric machine. The gearshift command is then expressed by:

$$u_g(t) = f_g(v(t), \alpha_t(t)) \tag{3.9}$$

Once the resulting overall gear ratio $i_g\left(u_g(t)\right)$ is known, the angular speed and acceleration at the torque link on the primary shaft can be computed.

$$\begin{aligned} \omega_g(t) &= i_g\left(u_g(t)\right)\cdot\omega_w(t) \\ \dot{\omega}_g(t) &= i_g\left(u_g(t)\right)\cdot\dot{\omega}_w(t) \end{aligned} \tag{3.10}$$

If the hypothesis of constant mechanical GB efficiency holds, the torque can be calculated as follows:

$$T_g(t) = \frac{T_w(t)}{i_g\left(u_g(t)\right)\cdot\eta_g^{sign(T_w(t))}} \tag{3.11}$$

A more detailed model can take into account that the friction losses increase with the speed. In this case the introduction of additional parameters to be identified is necessary, leading to the expression below.

$$T_w(t) = T_g(t)\cdot i_g\left(u_g(t)\right)\cdot\left(\eta_{g,0}-\frac{\eta_{g,1}}{\omega_{g,1}}\cdot\omega_g(t)\right)^{sign(T_g(t))} \tag{3.12}$$

The latter is valid for a forward-facing approach.

### 3.2.4 Torque split

At the torque split link (or mechanical power link), the torque balance leads to the following equations, for HEV and HSF-HV respectively:

$$\begin{aligned} T_g(t) &= T_{c,e}(t) + T_m(t) \\ T_g(t) &= T_{c,e}(t) + T_{c,H}(t) \end{aligned} \tag{3.13}$$

The control input of the EMS is the torque split factor $u_{ts}(t)$ and it is expressed by the equations below, valid in case of HEV and HSF-HV.

$$u_{ts}(t) = \begin{cases} \dfrac{T_m(t)}{T_m(t) + T_{c,e}(t)} \\ \dfrac{T_{c,H}(t)}{T_{c,H}(t) + T_{c,e}(t)} \end{cases} \tag{3.14}$$

The torques coming from the clutch blocks depend on the current status of the clutches, which can be a simple discrete on/off command or an accurate signal describing the realistic command of the clutch actuator, capable of describing both stick and slip phases.

### 3.2.5 Clutches

In both QSS and forward-facing models implemented in the simulations described in the next Chapters, except for a case regarding one of the two modeling paradigms investigated for the HSF-HV, the clutch command is a discrete variable, identifying the engaged and the disengaged status as follows:

$$u_{c,i}(t) = \begin{cases} 1 \ \Rightarrow T_{c,i}(t) = T_i(t), \quad \omega_{c,i}(t) = \omega_i(t) = \omega_g(t) \\ 0 \ \Rightarrow T_{c,i}(t) = 0, \quad \omega_{c,i}(t) = \omega_g(t) \end{cases} \tag{3.15}$$

Observing Figure 3.8, a more detailed description can be provided for dry friction clutches.

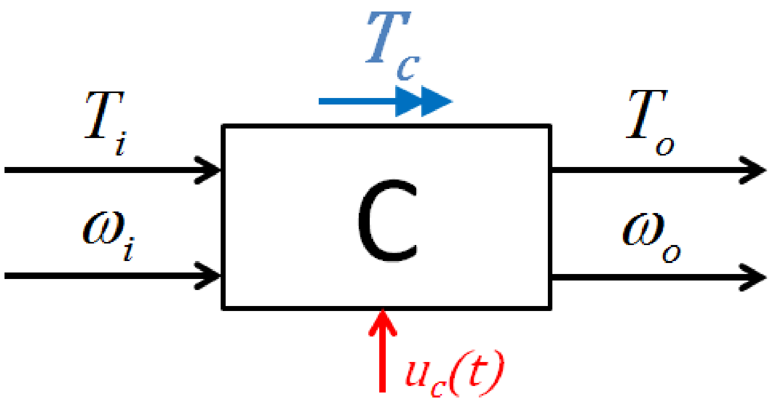

Figure 3.8: QSS schematic representation of a friction clutch element block.

When the clutch is engaged and sticking, the following equation holds, describing the identity of input/output torques and speeds:

$$\begin{aligned} T_c(t) &= T_i(t) = T_o(t) \\ \omega_i(t) &= \omega_o(t) \end{aligned} \tag{3.16}$$

Several modeling approaches are available in literature, to represent the slipping operation of clutches [159, 41, 8, 14], occurring every time the engine (or hybrid system) and the transmission speeds are different. Some of these methods rely on Karnopp's approach, while a more simplified expression of the torque transmitted by the clutch during slipping can be found as follows:

$$T_c(t) = T_{c,max}(\Delta\omega(t)) \cdot \left( T_{c,b} - \left(T_{c,b} - T_{c,a}\right) \cdot e^{\frac{-|\Delta\omega(t)|}{\Delta\omega_{0c}}} \right) \tag{3.17}$$

where $T_{c,a}, T_{c,b}, \Delta\omega_{0c}$ are experimental parameters. In the present dissertation, when a model of the clutch slipping is needed, such as in Section 4.3.2.1, the clutch efficiency is supposed to depend on the direction of the power flow:

$$\eta_c(t) = \begin{cases} 1 - \dfrac{|\Delta\omega(t)|}{\omega_i}, & if\ P_i(t) > 0 \\ 1 - \dfrac{|\Delta\omega(t)|}{\omega_o}, & if\ P_i(t) < 0 \end{cases} \tag{3.18}$$

The power at the input/output of the clutch is calculated based on the equation below:

$$P_c(t) = \frac{P_i(t) + \Theta_c \omega_o(t) \dot{\omega}_o(t)}{\eta_c(t)^{sign(P_i(t))}} \tag{3.19}$$

### 3.2.6 Internal Combustion Engine

The representation of an ICE in control-oriented models devoted to the optimization of optimal supervisory control is often a simple experimental steady-state map. An example of specific FC (SFC) for a SI engine (vehicle (b) of Section 3.6) is illustrated in Figure 3.9.

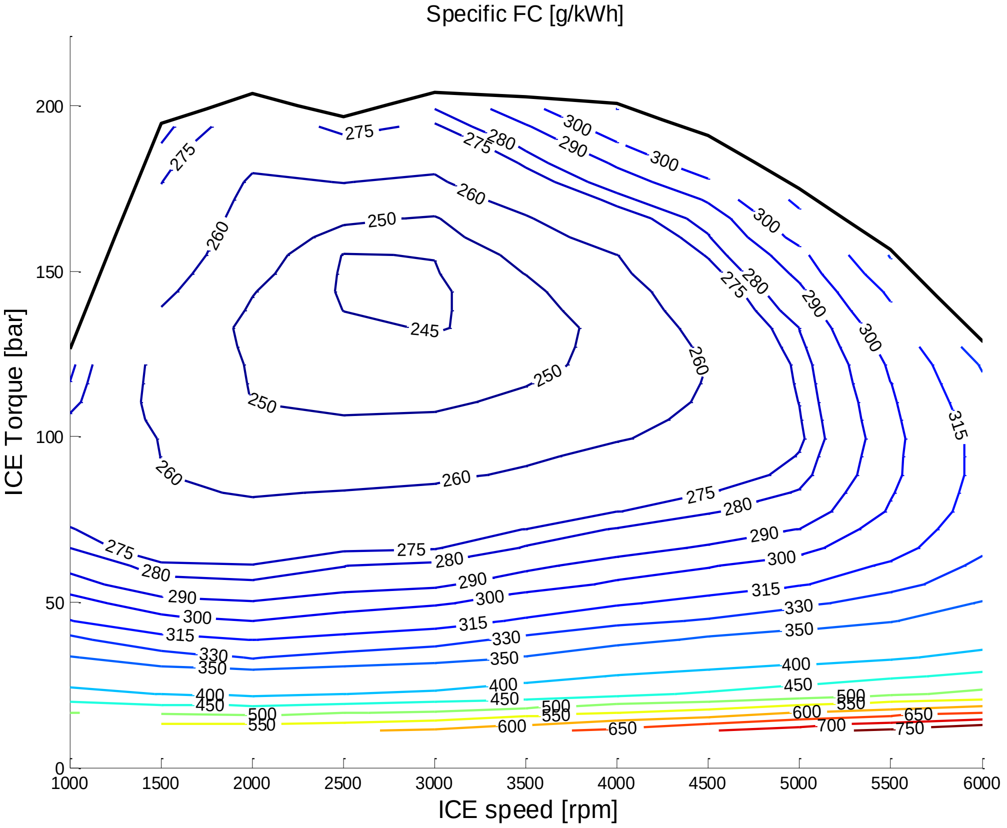

Figure 3.9: SI-ICE steady-state specific FC and max. torque experimental map.

Further examples of similar maps are shown in Figure 3.10 for a CI engine (vehicle (a) of Section 3.6).

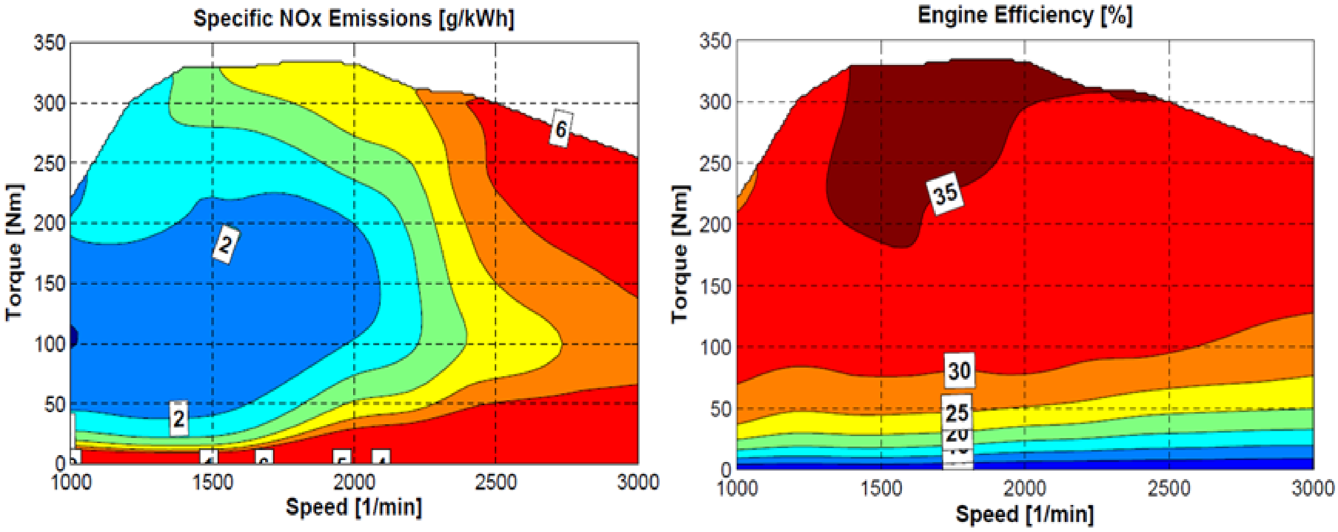

Figure 3.10: CI-ICE steady-state specific NOx (left plot), efficiency (right plot) and maximum torque experimental maps.

In this case $SNO_x$ emissions and engine efficiency are depicted. If the engine is mechanically connected to the driveline, an internal engine torque can be computed, considering its inertial term:

$$T_{i,e}(t) = T_e(t) + \Theta_e \dot{\omega}_e(t) \tag{3.20}$$

Once the net engine torque is known, the computation of emissions and fuel mass flow is done by means of the previously introduced maps, based on the current operating point:

$$\begin{aligned} \overset{*}{m}_{fuel}(t) &= f_{e,fuel}\left(\omega_e(t), T_{i,e}(t)\right) \\ \overset{*}{m}_{NO_x}(t) &= f_{e,NO_x}\left(\omega_e(t), T_{i,e}(t)\right) \end{aligned} \tag{3.21}$$

The constraints regarding the engine speed and the torque limitations must always be fulfilled.

$$\begin{aligned} &\omega_{e,min} \leq \omega_e(t) \leq \omega_{e,max} \\ &T_{e,crank} \leq T_{i,e}(t) \leq T_{e,max}\left(\omega_e(t)\right) \end{aligned} \tag{3.22}$$

The maximum torque also depends on the current rotational speed, as illustrated in Figure 3.9 and in Figure 3.10.

## 3.3 Hybrid Vehicle Components: HEV

### 3.3.1 Electric Motor/Generator

Detailed dynamic models of electric machines for HEVs are described in literature ([183, 66]). However, simple steady-state maps can be implemented even in forward-facing approaches. Figure 3.11 illustrates a motor efficiency and maximum/minimum torques map.

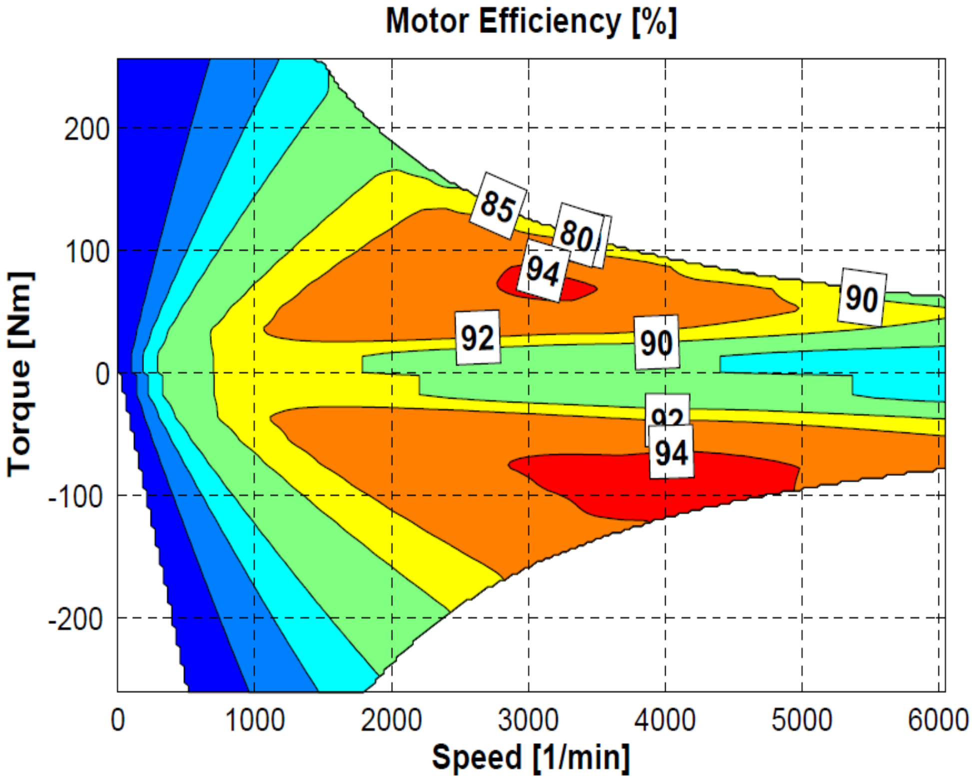

Figure 3.11: EMG steady-state efficiency and max./min. torque maps.

The inner motor torque is expressed by:

$$T_{i,m}(t) = T_m(t) + \Theta_m \dot{\omega}_m(t) \tag{3.23}$$

Speed and torque limitations must hold at every simulation step:

$$\begin{aligned} &0 \leq \omega_m(t) \leq \omega_{m,max} \\ &T_{m,min}\big(\omega_m(t)\big) \leq T_{i,m}(t) \leq T_{m,max}\big(\omega_m(t)\big) \end{aligned} \tag{3.24}$$

The electric power depends on the operating point, as follows:

$$P_m(t) = f_m\left(\omega_m(t), T_{i,m}(t)\right) \tag{3.25}$$

It can be noticed that the efficiency and the torque limits in generator/motor modes may differ considerably.

### 3.3.2 Battery

At the electric power link, the powers balance equation must hold, considering a possible auxiliary power system request $P_{aux}(t)$ and electric motor power $P_m(t)$.

$$P_b(t) = P_m(t) + P_{aux}(t) \tag{3.26}$$

Hence, a model for the battery is required to compute the $\mathrm{SOC}(t)$ variation at each time step. Several modeling techniques have been investigated, both for batteries and super-capacitors ([67, 12, 184]). Some of them focus on lead-acid batteries ([34, 76]), others on Ni-MH batteries ([13, 40]), or on Li-Ion technologies ([81, 42]). The main difference between the modeling approaches lies in the choice of the physical details represented. Advanced physical models ([25, 130]) are used to represent high transient dynamics, while simplified models are useful and reliable representations in standard operating conditions ([68, 28, 80]). Another task regarding battery modeling is related to the determination of its most relevant parameter, i.e. SOC. The authors of [149] present a review of possible methodologies for the on-line estimation of the state-of-charge, while the authors of [146] focus on Kalman's filter technique, considered the most effective one. Other important aspects that should be taken into account are the battery ageing phenomena ([77, 169]) and the battery thermal behavior ([81, 215]). Throughout the present dissertation, neither temperature dependencies nor ageing phenomena are treated, and the batteries are modeled by means of a resistive equivalent circuit, as illustrated in Figure 3.12.

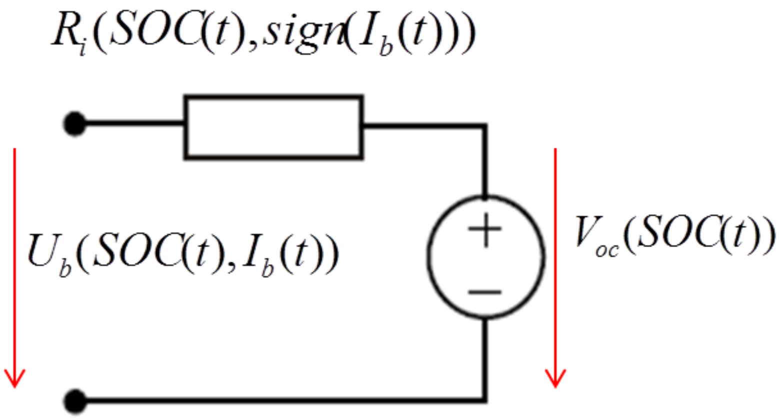

Figure 3.12: Equivalent resistive circuit of a battery.

The battery electric power is expressed by:

$$P_b(t) = U_b\big(SOC(t), I_b(t)\big) \cdot I_b(t) \tag{3.27}$$

The voltage at the battery clamps $U_b$ depends on the inner (open-circuit) voltage $V_{oc}\big(\mathrm{SOC}(t)\big)$ and on the internal resistance $R_i$, which is also a function of the current $I_b$ direction and of the SOC. The equation below describes such relationships.

$$U_b\big(SOC(t), I_b(t)\big) = V_{oc}\big(SOC(t)\big) - R_i(SOC(t), sign(I_b(t))) \cdot I_b(t) \tag{3.28}$$

The current flowing from/to the battery can be modeled through the following equation, where dependencies of the various signals are omitted:

$$I_b(t) = \frac{V_{oc}(\cdot) - \sqrt{{V_{oc}}^2(\cdot) - 4R_i(\cdot) \cdot P_b(t)}}{2R_i(\cdot)} \tag{3.29}$$

The state-of-charge can be found, once the battery maximum charge capacity $Q_0$ is known:

$$\begin{gathered} SOC(t) = \frac{Q(t)}{Q_0} \\ \frac{dSOC(t)}{dt} = -\frac{I_b(t)}{Q_0} \end{gathered} \tag{3.30}$$

Constraints can be active both on SOC range and on maximum/minimum current limitations:

$$\begin{gathered} SOC_{min} \leq SOC(t) \leq SOC_{max} \\ I_{b,min} \leq I_b(t) \leq I_{b,max} \end{gathered} \tag{3.31}$$

## 3.4 Hybrid Vehicle Components: HSF-HV

In this section, the modeling features of the considered parallel HSF-HV are described. The studied vehicle topology and its main components are depicted in Figure 3.13.

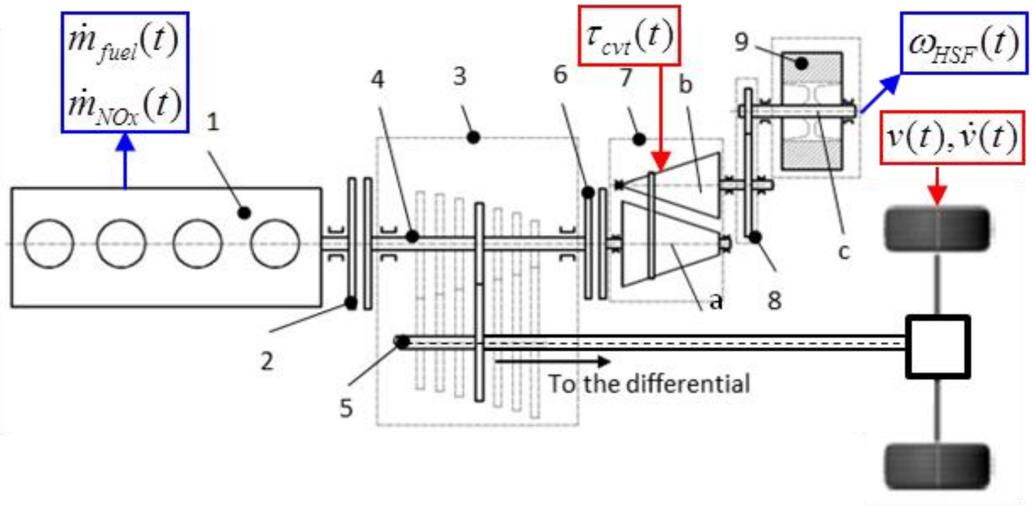

Figure 3.13: Schematic of the parallel HSF-HV, see [46].

A metal-belt CVT (7) is adopted to synchronize the HSF and the primary GB shaft speeds. A fixed gear ratio (9) is inserted between the CVT and the flywheel shaft. The nomenclature adopted for the main signals is referred to Figure 3.4 and Figure 3.5. Both simplified ([20, 27]) and detailed ([196]) models of mechanical hybrid vehicles can be found in literature, for different vehicle topologies. The sections below provide an overview of the equations needed to describe the dynamic behavior of the system illustrated in Figure 3.13.

### 3.4.1 Continuously Variable Transmission (CVT)

Although several studies ([26, 162, 161, 177]) are available in literature to cope with detailed physics-based modeling of metal-belt CVTs, more simplified and control-oriented techniques, like those proposed by the authors of [144, 145, 122] are followed in the present research. The kinematic and dynamic relationships between speeds and accelerations at the input (*FG*) and output (*cvt*) shafts of the CVT can be expressed by:

$$\begin{aligned} \omega_{FG}(t) &= \omega_{cvt}(t) \cdot \tau_{cvt}(t) \\ \dot{\omega}_{FG}(t) &= \dot{\omega}_{cvt}(t) \cdot \tau_{cvt}(t) + \omega_{cvt}(t) \cdot \dot{\tau}_{cvt}(t) \end{aligned} \tag{3.32}$$

The dynamic balance equations of the input and output CVT shafts can be written by introducing the torque transmitted through the belt to the shafts, $T_{cvt,a}$ and $T_{cvt,b}$:

$$\begin{aligned} \Theta_{cvt,a} \cdot \dot{\omega}_{cvt}(t) &= T_{cvt,a}(t) - T_{c,H}(t) \\ \Theta_{cvt,b} \cdot \dot{\omega}_{FG}(t) &= T_{FG}(t) - T_{cvt,b}(t) \end{aligned} \tag{3.33}$$

The mechanical efficiency of the CVT can be mapped as a function of three parameters: the CVT transmission ratio $\tau_{cvt}$, the angular speed $\omega_{cvt}$ and the torque $T_{FG}$. However, a simplified approach is followed here, where the efficiency depends only on the transmission ratio ([29]). An equivalent expression can be found for the torque transmitted to the output shaft:

$$\begin{aligned} &\eta_{cvt} = \eta_{cvt}\big(\tau_{cvt}(t), \omega_{cvt}(t), T_{FG}(t)\big) = \eta_{cvt}(\cdot) \\ &T_{cvt,a}(t) = T_{cvt,b}(t) \cdot \tau_{cvt}(t) \cdot \eta_{cvt}^{sign(T_{c,H}(t))} \end{aligned} \tag{3.34}$$

In the equation above, the dependencies of the mechanical efficiency of the CVT are omitted. By combining equations (3.32), (3.33) and (3.34), the torque transmitted to the fixed-gear ratio gearbox $T_{FG}(t)$ can be reformulated as follows:

$$\begin{aligned} T_{FG}(t) = \dot{\omega}_{cvt.a} &\left[ \frac{\Theta_{cvt,a}}{\tau_{cvt} \cdot \eta_{cvt}^{sign(T_{c,H})}} + \tau_{cvt} \cdot \Theta_{cvt,b} \right] + \\ &+ \frac{T_{c,H}}{\tau_{cvt} \cdot \eta_{cvt}^{sign(T_{c,H})}} + \dot{\tau}_{cvt} \cdot \omega_{cvt.a} \cdot \Theta_{cvt,b} \end{aligned} \tag{3.35}$$

where dependencies on time of all the involved variables are omitted for the sake of simplicity.

### 3.4.2 High Speed Flywheel (HSF)

The considered flywheel system comprises a vacuum system ([52]) to keep the air drag losses as low as possible, enhancing the conservation of the stored kinetic energy. The efficiency of the fixed gear FG is considered constant, such as:

$$T_{HSF}(t) = \frac{T_{FG}(t)}{\tau_{HSF} \cdot \eta_{HSF}^{sign(T_{c,H}(t))}} \tag{3.36}$$

expresses the torque at the flywheel system shaft. Its relative power is:

$$P_{HSF}(t) = T_{HSF}(t) \cdot \omega_{HSF}(t) \tag{3.37}$$

The power balance at the rotor shaft leads to:

$$\Theta_{\mathrm{HSF}} \cdot \dot{\omega}_{HSF}(t) \cdot \omega_{HSF}(t) = -P_{HSF}(t) - k_f \cdot \omega_{HSF}^2(t) \tag{3.38}$$

where the power lost due to mechanical frictions is modeled as a quadratic function of the flywheel speed (the friction torque increasing linearly with rotational speed). The kinetic energy stored in the flywheel is expressed by:

$$E_{k,HSF}(t) = \frac{1}{2} \Theta_{\mathrm{HSF}} \cdot \omega_{HSF}^2(t) \tag{3.39}$$

A reformulation of the torque transmitted to the FG can be found combining equations (3.36), (3.37) and (3.38) leading to the equation below:

$$T_{FG}(t) = -R \cdot \tau_{HSF} \cdot \eta_{HSF}^{(.)} - \Theta_{\mathrm{HSF}} \cdot \tau^2{}_{HSF} \cdot \eta_{HSF}^{(.)} \cdot (\dot{\omega}_{cvt.a} \cdot \tau_{cvt} + \omega_{cvt.a} \cdot \dot{\tau}_{cvt}) \tag{3.40}$$

In the previous expression the following substitution is adopted for the HSF angular acceleration:

$$\dot{\omega}_{HSF}(t) = \tau_{HSF} \cdot (\dot{\omega}_{cvt.a}(t) \cdot \tau_{cvt}(t) + \omega_{cvt.a}(t) \cdot \dot{\tau}_{cvt}(t)) \tag{3.41}$$

A mathematical expression of the CVT ratio dynamics derives from the combination of equations (3.35) and (3.40):

$$\begin{aligned}
\dot{\tau}_{cvt}(t) &= \frac{C_{\dot{\omega}} + T_{c,H} + C_R}{-\left[\omega_{cvt,a}\cdot\eta_{cvt}^{(\cdot)}\cdot\tau_{cvt}\cdot\left(\Theta_{cvt,b}+\Theta_{HSF}\cdot\tau^{2}{}_{HSF}\cdot\eta_{HSF}^{(\cdot)}\right)\right]}\\
C_R(t) &= R\cdot\tau_{HSF}\cdot\eta_{HSF}^{(\cdot)}\cdot\tau_{cvt}\cdot\eta_{cvt}^{(\cdot)}\\
C_{\dot{\omega}}(t) &= \dot{\omega}_{cvt,a}\cdot\left[\Theta_{cvt,a}+\tau_{cvt}^{2}\eta_{cvt}^{(\cdot)}\cdot\left(\Theta_{cvt,b}+\Theta_{HSF}\cdot\tau^{2}{}_{HSF}\cdot\eta_{HSF}^{(\cdot)}\right)\right]
\end{aligned} \tag{3.42}$$

The latter can be considered an output for the QSS modeling paradigm, where the torque value required from the hybrid power system is known. In case of a dynamic forward-facing approach, comprising a CVT controller as illustrated in Figure 3.5, the derivative of the CVT ratio is a function of the control input of the belt actuator (hydraulic or electric) and therefore shall be chosen, at all times, to reduce the error between the desired and the actual CVT torque, as requested by the EMS ([173]).

## 3.5 QSS models validation

This section presents some simulation results of QSS models for HEV. The considered vehicle data (vehicle (a)) can be found in Section 3.6.

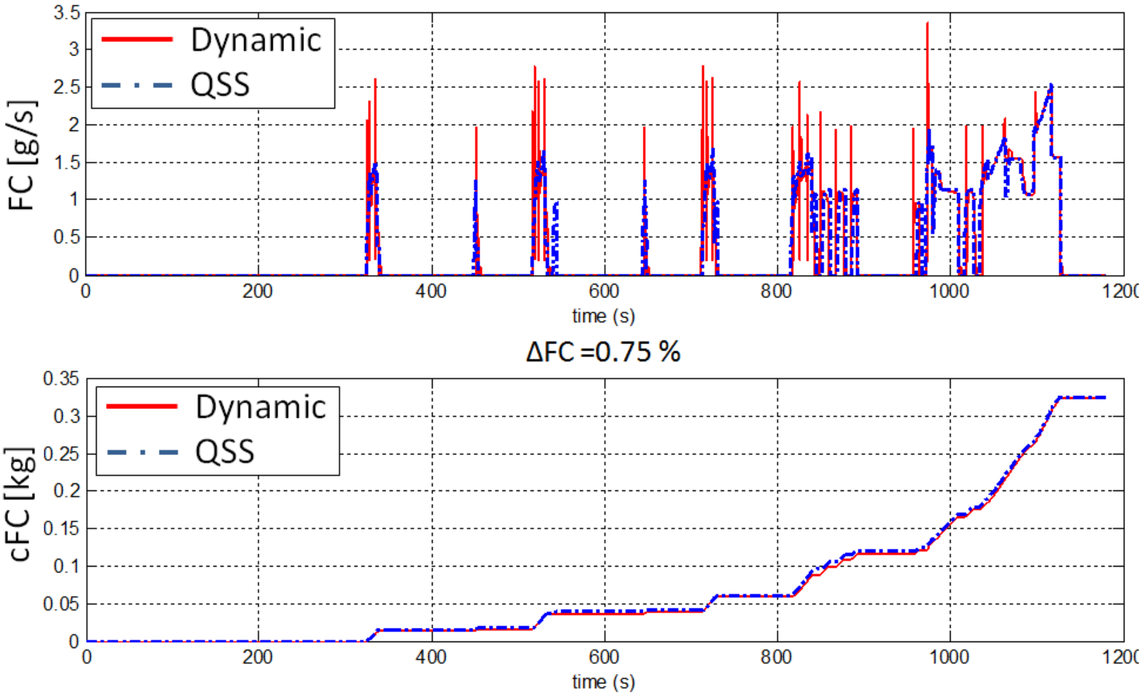

**Figure 3.14: QSS vs. Dynamic model validation; instantaneous and cumulative FC.**

The QSS results are compared to the results of a forward-facing model for the same vehicle. Figure 3.14 shows the comparison for the instantaneous and the cumulative FC. The relative difference in terms of FC is lower than 1%, which can be considered an acceptable value, sufficient for a model validation. Figure 3.15 illustrates a detail of the previous figure.

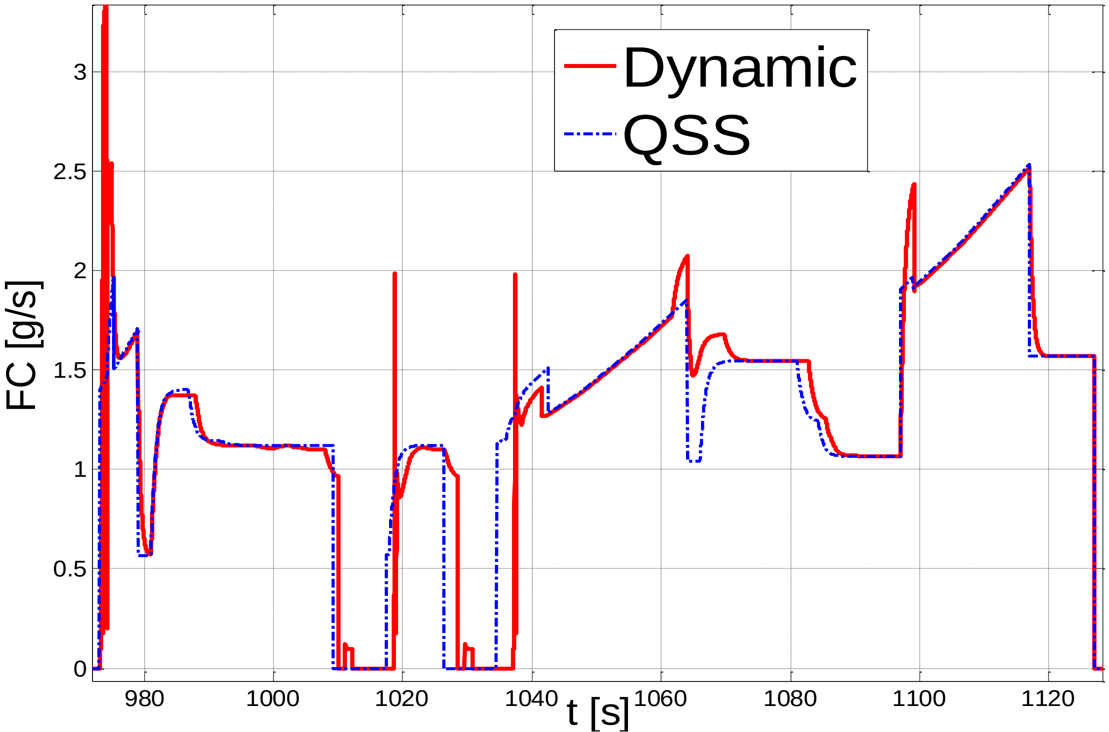

**Figure 3.15: Detail of the instantaneous FC; QSS vs. Dynamic simulation.**

As it can be noticed in the previous illustration, focusing on the final part of the EUDC homologation cycle, the QSS is capable of accurately capturing the steady-state fuel mass flow rate, while some differences due to transient operation of the engine occur.

The main deviation sources between the two analyzed modeling paradigms arise from:

- Real torque supply profile: the torque transient always implies a dynamic behavior of the prime movers, leading to a corresponding time-delay; the QSS always considers the requested torque to be supplied instantaneously;
- Real behavior of friction clutches: since the QSS approach does not model clutch slipping, the mechanical power dissipated, from the beginning of clutch engagement to the stick condition, is not accounted;
- Gear-shifting: the gear shift operation requires a finite time, during which the error with the desired speed profile grows significantly, requiring a substantial torque gradient immediately following.

Figure 3.16 provides an example of a gear-shift operation in a portion of the ECE cycle.

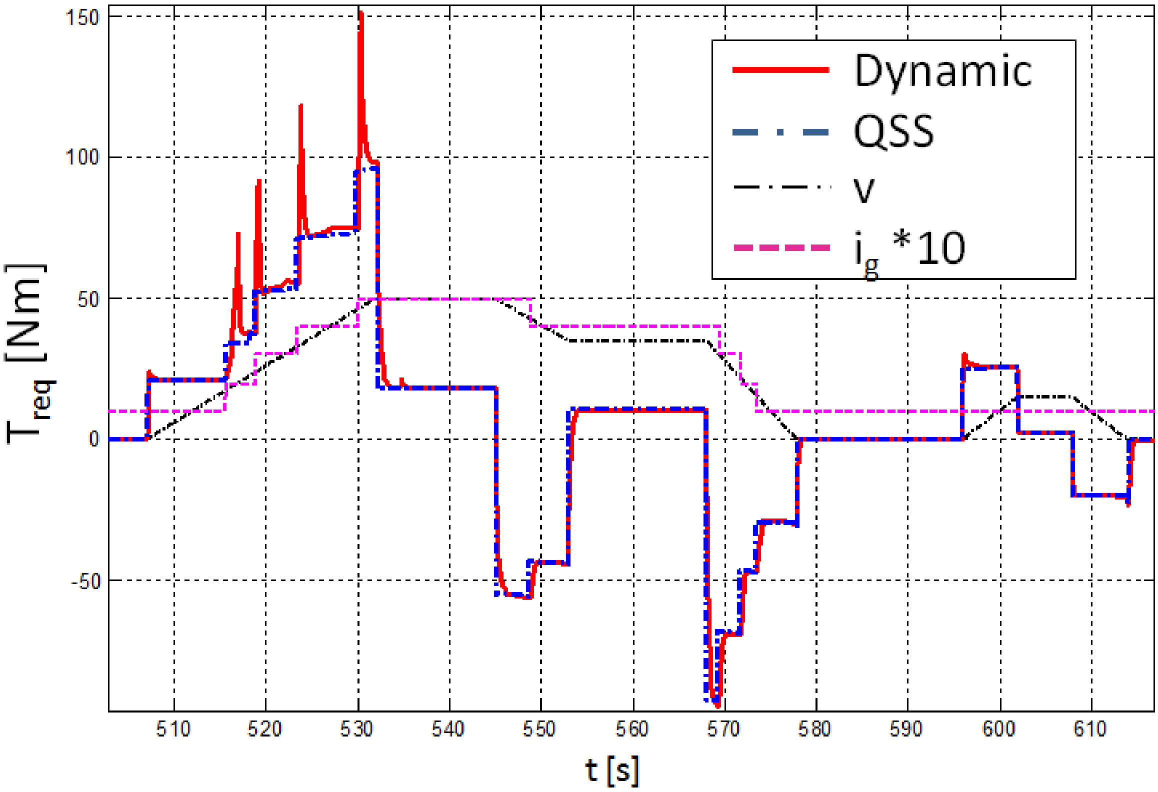

**Figure 3.16: Detail of the comparison between QSS and Dynamic model simulation; torques during gear-shifting sequence on an ECE profile.**

Torque peaks following each gear-shift event are clearly visible between 510-530 s.

Depending on the driving mission considered, especially concerning the number and the intensity of acceleration/deceleration maneuvers involved, the accuracy of a QSS simulation can vary.

However, in standard vehicle homologation cycles, very high adhesion is expected, around 1% in terms of cumulated FC. As a consequence, the SOC trajectories in case of a hybrid vehicle are also expected to be very close for the whole driving mission considered. Figure 3.17 depicts an example of such validation.

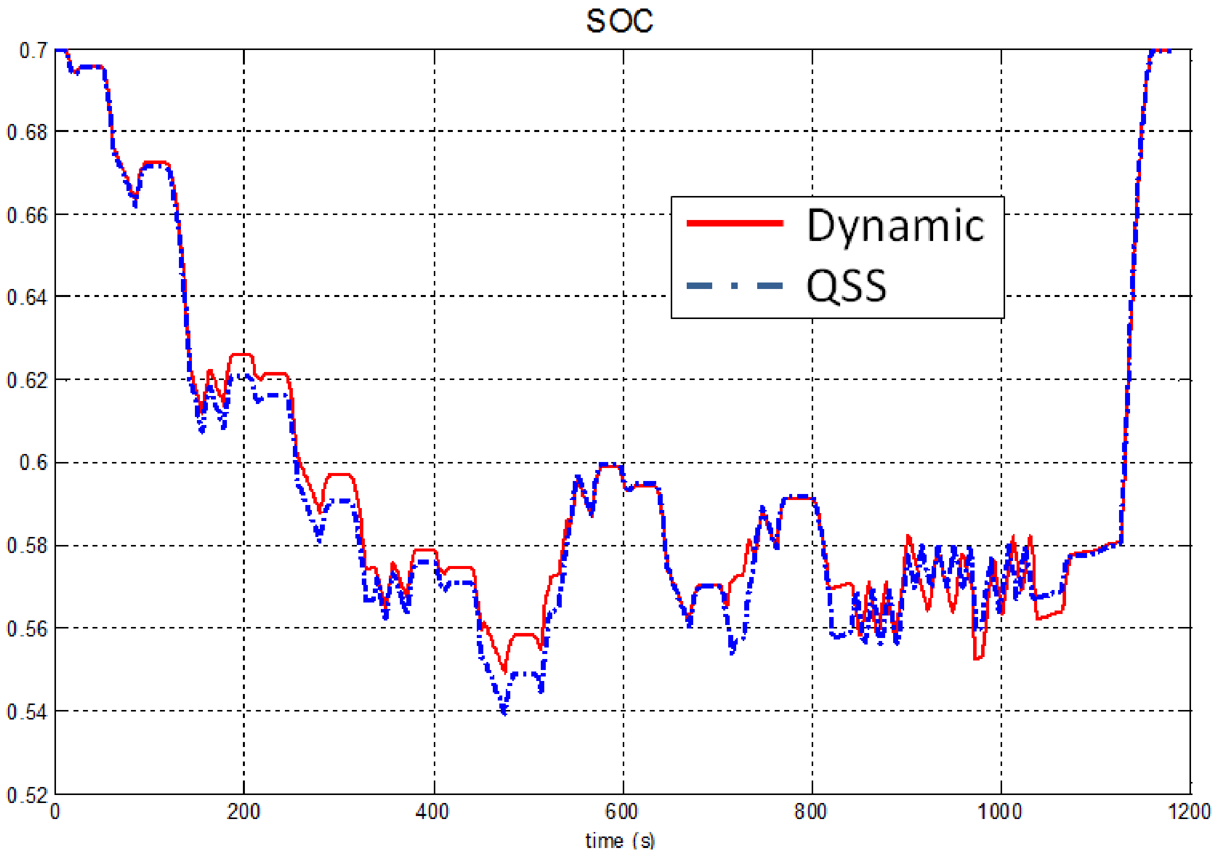

Figure 3.17: QSS vs. Dynamic model validation; SOC profiles.

## 3.6 Vehicles Data

Table 3.1: Vehicle (a) and its powertrain components; nominal data.

| Parameter | Symbol | Value | Unit |
|---|---|---|---|
| Wheel radius | $r_w$ | 0.32 | [m] |
| Air Density | $\rho_{air}$ | 1.24 | [kg/m$^3$] |
| Effective frontal area | $A_f c_x$ | 0.60 | [m$^2$] |
| Rolling friction coefficient | $c_{r,0}$ | 0.012 | [-] |
| Gravitational constant | $g$ | 9.81 | [m/s$^2$] |
| Total vehicle mass | $m_v$ | 1800 | [kg] |
| Wheels Inertia | $\Theta_w$ | 4.78 | [kgm$^2$] |
| Rotational equivalent mass (gear-dependent) | $m_r$ | [129,84, 72,55, 52,51] | [kg] |
| Gear ratios | $i_g$ | [10.8, 7.1,4.7 2.5, 2.0,1.8] | [-] |
| Gearbox efficiency parameter | $\eta_{g,0}$ | 0.95 | [-] |
| Gearbox efficiency parameter | $\eta_{g,1}$ | 0.02 | [(rad/s)$^{-1}$] |
| Gearbox efficiency parameter | $\omega_{g,1}$ | 400 | [rad/s] |
| Nominal motor power | $P_{m,max}$ | 40 | [kW] |
| Max. motor speed | $\omega_{m,max}$ | 628 | [rad/s] |
| Motor Inertia | $\Theta_m$ | 0.0435 | [kgm$^2$] |
| Nominal engine power | $P_{e,max}$ | 150 | [kW] |
| Min. engine speed | $\omega_{e,min}$ | 105 | [rad/s] |
| Max. engine speed | $\omega_{e,max}$ | 628 | [rad/s] |
| Engine Inertia | $\Theta_e$ | 0.135 | [kgm$^2$] |
| Max. battery capacity | $Q_0$ | 7.64 | [Ah] |
| Nominal open circuit voltage | $V_{oc}$ | 263 | [V] |
| Battery internal resistance | $R_i$ | 0.24 | [- ] |
| Min. battery current | $I_{b,min}$ | -200 | [A] |
| Max. battery current | $I_{b,max}$ | 200 | [A] |
| Min. SOC | $SOC_{min}$ | 0.2 | [-] |
| Max. SOC | $SOC_{max}$ | 0.8 | [-] |
| Auxiliary power demand | $P_{aux}$ | 400 | [W] |

Table 3.2: Vehicle (b) HEV/HSF-HV and its powertrain components; nominal data.

| Parameter | Symbol | Value | Unit |
|---|---|---|---|
| Wheel radius | $r_w$ | 0.308 | [m] |
| Air Density | $\rho_{air}$ | 1.24 | [kg/m$^3$] |
| Effective frontal area | $A_f c_x$ | 0.69 | [m$^2$] |
| Rolling friction coefficient | $c_{r,0}$ | 0.008 | [-] |
| Gravitational constant | $g$ | 9.81 | [m/s$^2$] |
| Total vehicle mass | $m_v$ | 1570 | [kg] |
| Wheels Inertia | $\Theta_w$ | 3.793 | [kgm$^2$] |
| Gear ratios | $i_g$ | [16.7, 10.1,6.8 4.97,3.8 3.1,2.6] | [-] |
| Gearbox efficiency parameter | $\eta_g$ | 0.9 | [-] |
| Nominal engine power | $P_{e,max}$ | 90 | [kW] |
| Min. engine speed | $\omega_{e,min}$ | 99.5 | [rad/s] |
| Max. engine speed | $\omega_{e,max}$ | 628 | [rad/s] |
| Engine Inertia | $\Theta_e$ | 0.15 | [kgm$^2$] |
| **HEV** | | | |
| Nominal motor power | $P_{m,max}$ | 50 | [kW] |
| Max. motor speed | $\omega_{\mathrm{m,max}}$ | 628 | [rad/s] |
| Motor Inertia | $\Theta_m$ | 0.03 | [kgm$^2$] |
| Max. battery capacity | $Q_0$ | 6.1 | [Ah] |
| Nominal open circuit voltage | $V_{oc}$ | 216 | [V] |
| Average battery internal resistance | $R_i$ | 0.18 | [- ] |
| Min. battery current | $I_{b,min}$ | -150 | [A] |
| Max. battery current | $I_{b,max}$ | 150 | [A] |
| Min. SOC | $SOC_{min}$ | 0.4 | [-] |
| Max. SOC | $SOC_{max}$ | 0.8 | [-] |
| Auxiliary power demand | $P_{aux}$ | 400 | [W] |
| **HSF-HV** | | | |
| HSF inertia | $\Theta_{\mathrm{HSF}}$ | 0.05 | [kgm$^2$] |
| HSF Max. speed | $\omega_{\mathrm{HSF,max}}$ | 48000 | [rpm] |
| HSF Max. energy storage capacity | $\mathrm{E_{k,HSF}}$ | 625 | [kJ] |
| HSF Speed loss coefficient | $\mathrm{k_f}$ | 3 | [%/min] |
| CVT Max. Power | $\mathrm{P_{cvt,max}}$ | 86 | [kW] |
| CVT Max. Torque | $\mathrm{T_{cvt,max}}$ | 170 | [Nm] |
| CVT mean efficiency | $\eta_{\mathrm{cvt}}$ | 0.9 | [-] |
| CVT Transmission ratios range | $\tau_{\mathrm{cvt}}$ | [0.4-2.4] | [-] |
| CVT primary/secondary shaft inertias | $\Theta_{\mathrm{cvt,a/b}}$ | 0.005 | [kgm$^2$] |

# 4. Fuel Economy Optimization of Hybrid Vehicles

The primary goal of this Chapter is to describe the two methodologies adopted here for FE optimization of HVs. This is done in Section 4.1, including a general overview of how the problem is defined from a mathematical point of view. In Section 4.2, for the two hybrid system architectures described in the previous Chapter, both ECMS-based method and a DP-based procedure are described in details. Then the focus is on the major modeling issues encountered in the HSF-HV case. Regarding the latter, two different approaches are described, adopting different levels of detail of the relevant physical phenomena. Section 4.3 illustrates the results of the benchmark simulations for the chosen ECMS structure compared to the DP optimum, obtained using the models described in Chapter 3 (vehicle (b)).

## 4.1 Control framework for Hybrid Vehicle Systems

Some researchers have tried to establish comparisons between the performances of control strategies for HVs. Mainly different approaches based on Optimal Control Theory are considered, as in [166, 148, 167, 156, 174, 102, 100, 99]. They are based on PMP (or its on-line version ECMS) and DP among the others.

ECMS is an on-line fully causal control strategy, hence not relying on the system future conditions but only on the present and past knowledge. As a consequence it is inherently sub-optimal. On the contrary, a DP control policy is fully predictive, hence based on a complete knowledge of the time evolution of the prescribed mission.

The first step is to define the optimal control framework to optimize the EMS of a HV. In the following subsections, different optimization criteria are illustrated. At the end of this section the main control variable (torque split factor) is introduced, valid both for HEV and HSF-HV.

### 4.1.1 Definition of the objective function

The goal here is to find the optimal sequence of control inputs that actuates the HV on the prescribed driving mission such that the overall cost functional is minimized. The mathematical formulation of such control problem can be expressed as follows:

$$\min_{u(t)} J\big(u(t)\big) = \min_{u(t)} \left\{ G(x(T)) + \int_0^T L\big(x(t), u(t)\big) dt \right\} \tag{4.1}$$

s.t.

$$\dot{x}(t) = f(x(t), u(t), t) \tag{4.2}$$

$$x(0) = x_0, \qquad x(T) \in \left[x_{f,min}, x_{f,max}\right] \tag{4.3}$$

$$x(t) \in [x_{min}, x_{max}], \qquad \forall t \in [0, T] \tag{4.4}$$

$$u(t) \in [u_{min}(t), u_{max}(t)], \quad \forall t \in [0, T] \tag{4.5}$$

The goal is to minimize the cost functional $J$, which is the integral of the instantaneous cost function $L\big(x(t), u(t)\big)$ over a cycle of time duration $T$, with respect to the control variables vector $u(t)$. An additional penalty associated to the final state $G(x(T))$ can be included. The problem is subjected to boundary and initial conditions that add constraints to $u(t)$ and to the state variables vector $x(t)$. In the following subsections a review of possible objective functions is given. Depending on the considered system, the number of state and control variables in the vectors $x(t)$ and $u(t)$ can vary. While the HEV can easily be reduced to a single-state and single-control variable case, the HSF-HV is a multivariable problem and will be approached with two different modeling choices.

#### *4.1.1.1 Fuel Consumption*

In case of FC-oriented optimization problems, the cost function can be simply expressed by the following equation:

$$J\big(u(t)\big) = \int_0^T \overset{*}{m}_{fuel}(u(t), t) \cdot H_l dt \tag{4.6}$$

where the cost function inside the integral represents the fuel chemical power, $\overset{*}{m}_{fuel}$ being the fuel mass flow rate and $H_l$ the fuel lower heating value.

### *4.1.1.2 Drivability*

A tradeoff is known to exist between the drivability and the FE or pollutant emissions, as pointed out in [147, 139, 206, 105]. The authors of [140] state that an extended definition of drivability includes many various different features, such as performance during acceleration, engine noise, braking, shifting activity and shifting time, etc. They provide a simplified set of fundamental drivability criteria, including only:

- frequency and timing of gear-shift events;
- frequency and timing of engine start/stop events;

The resulting cost function becomes:

$$L^{driv}(x,u,t) = \Big[H_l \cdot \overset{*}{m}_{fuel}(u,t) + P_{ss,eq}(x,u,t,t_s) + P_{gs,eq}(x,u,t,t_s)\Big] \tag{4.7}$$

$$P_{ss,eq}(x,u,t,t_s) = P_{ss,eq} \cdot [(x_e(t) = 1) \land (x_e(t - t_s) = 0)] \tag{4.8}$$

$$P_{gs,eq}(x,u,t,t_s) = P_{gs,eq} \cdot [g_s(t) \neq g_s(t - t_s)] \tag{4.9}$$

where the term $P_{ss,eq}(x,u,t,t_s)$ represents a power penalty related to an engine start event, being not zero only if there is a difference between the engine state $x_e$ at the time $t$ and the previous objective function evaluation at the time $(t - t_s)$, as formulated in (4.8). A similar formulation can be used to penalize a gear-shifting event by means of a penalty power $P_{gs,eq}(x,u,t,t_s)$, if the selected gear $g_s(t)$ has changed during the considered time step $t_s$ (4.9).

A proof of the consequent optimal control strategy is given [138] by analyzing the main drivability metrics (number of gear-shift and engine start events over time).

Another fundamental criterion used to address the problem of enhancing driver's comfort is the concept of torque/power reserve that includes a penalty that increases as the current value of ICE and/or EMG approaches to its maximum value at the current speed. This concept quantifies the acceleration capability of the vehicle during a future possible overtaking phase. A possible formulation of the overall cost function, in case of power reserve, is the following, where dependencies on time are omitted for the sake of simplicity:

$$L^{P,res}(u) = \left[H_l \cdot \overset{*}{m}_{fuel}(u) + \varphi_{P,res} \cdot \omega_e(u) \cdot \left(T_{e,max}(\omega_e(u)) - T_e(u)\right)\right] \tag{4.10}$$

In (4.10) the term $\varphi_{P,res}$ is a non-dimensional penalty factor to account for the total power reserve level.

#### 4.1.1.3 *Battery ageing*

The issue of battery aging can be also included in the EMS for a HEV. The authors of the research study [169] have reformulated the standard fuel-optimal control problem adding a cost associated with a severity factor map that is correlated with battery lifetime. The problem is solved using a PMP approach, with the following reformulation of an extended cost functional:

$$L^{ba}(\xi, u) = (1 - \alpha_{ba}) \cdot \overset{*}{m}_{fuel}(u) \cdot H_l + \alpha_{ba} \cdot c \frac{1}{\Gamma} \sigma(I_b(u), \theta, \xi) \cdot |I_b(u)| \tag{4.11}$$

where $\xi = \mathrm{SOC}$ is the only element of the state vector $x$, $c$ is a transformation coefficient for the battery wear, making its dimensions compliant with fuel chemical power, $\alpha_{ba}$ is a weighting factor to adjust the relative impact of the two contributions on the overall cost function. $\Gamma$ is the total charge-throughput when the battery is subject to its nominal load cycle, while $\sigma$ is the severity factor characterizing the aging effect of any load cycle, referred to the nominal load cycle.

### 4.1.2 Definition of state variables and control inputs: Common Path

In the present section, the description of the main control inputs $u(t)$ and state variables $x(t)$ commonly used to describe an HV systems is given.

$$x(t) = \begin{bmatrix} x_1 \\ \dots \\ x_i \\ \dots \\ x_M \end{bmatrix}; \qquad u(t) = \begin{bmatrix} u_1 \\ \dots \\ u_i \\ \dots \\ u_N \end{bmatrix} \tag{4.12}$$

Some of these solutions are adopted in the simulations and in the experimental analyses conducted in the next sections and in the next Chapter. In Section 4.1.3 the framework for the HEV problem is proposed, while in Section 4.1.4 the problem of the system description for the HSF-HV is introduced.

#### *4.1.2.1 Torque/Power split factor*

The main control input related to the Supervisory Control of a parallel hybrid vehicle is the factor that determines the distribution between torque/power delivered by the conventional power path and by the secondary power source. The authors of [203] have pointed out that the difference between the choices of torque or power split factor as input in a DP procedure doesn't affect the solution substantially, considering that the resulting FC differences always lie in a 1% range. However, power split strategies are more suitable for high average speed driving cycles, while torque split should guarantee better performances in low speed missions.

The torque split is defined in (3.14), while the power split factor $u_{ps}(t)$ can be defined as follows for a HEV:

$$u_{ps}(t) = \frac{P_m(t)}{P_m(t) + P_{c,e}(t)} \tag{4.13}$$

A similar definition can be used for the HSF-HV. However, in the following, torque split factor is always used, both for HEV and HSF-HV.

#### *4.1.2.2 Gear-shift strategy*

Gear-shifting strategy is one of the most relevant factors to reduce FC and pollutant emissions performance of conventional and hybrid vehicles. As a consequence, several studies can be found in literature to cope with optimal gear-shifting operation.

Some studies focus on the generation of gear-shift tables for conventional ICE-based vehicles ([210, 112, 154]), aiming at the optimal performance based on heuristic rules. Rule-based approaches for the optimal generation of gear-shift lines are proposed for hybrid vehicles as well [200, 120, 113]. Multi-performance gear-shift tables aiming at minimizing multiple cost criteria, including pollutant emissions, is described by the authors of [209].

Dynamic Programming can be also applied to infer optimal gear selection over a prescribed driving mission. It has been applied to a conventional vehicle [78], to an ICE-based vehicle with AT and automatic throttle control (ATC) [95] and to a hybrid vehicle [198].

An innovative approach is to run several DP optimizations on a range of representative driving cycles, extrapolating gear-shift events on a typical gear-shift table, as the one illustrated in Figure 3.7. From these results, thanks to the use of data clustering methods, gear-shifting lines that are only slightly suboptimal can be generated [134]. According to [133, 194] a similar methodology can be applied to HEVs as well, splitting the strategy into multiple maps depending on the current driving mode.

A straightforward approach to include the selected gear into an optimal control framework is the following:

$$u(t) = \begin{bmatrix} u_1 \dots u_{i-1} \\ g_s(t) \\ u_{i+1} \dots u_N \end{bmatrix} \tag{4.14}$$

where $g_s(t)$ represents the selected gear at the time $t$, in a generic position $i$ in the control input vector $u(t)$ of $N$ elements.

A second way is to use the definition of gear-shift command $u_g(t)$ as the input, while the current gear represents a state:

$$\begin{aligned} x(t) &= \begin{bmatrix} x_1 \dots x_{j-1} \\ g_s(t) \\ x_{j+1} \dots x_M \end{bmatrix} \\ u(t) &= \begin{bmatrix} u_1 \dots u_{i-1} \\ u_g(t) \\ u_{i+1} \dots u_N \end{bmatrix} \end{aligned} \tag{4.15}$$

The latter definition permits to include the gear-shifting penalty (4.9), even in a calculation of the optimal strategy that proceeds backward in time, as the DP.

The gear-shift input can be further limited to a single gear ratio up-shift or down-shift at each time step $t_s$ (with $u_g(t) = \pm 1$).

$$g_s(t + t_s) = g_s(t) + u_g(t) \tag{4.16}$$

#### 4.1.2.3 Engine Start/Stop

A predictive control strategy for the optimal engine start/stop definition is demonstrated in [6]. In this case the corresponding elements in state and input vectors produce the following formulation:

$$\begin{gathered} x(t) = \begin{bmatrix} x_1 \dots x_{j-1} \\ x_e(t) \\ x_{j+1} \dots x_M \end{bmatrix} \\ u(t) = \begin{bmatrix} u_1 \dots u_{i-1} \\ u_{ss}(t) \\ u_{i+1} \dots u_N \end{bmatrix} \end{gathered} \tag{4.17}$$

with $u_{ss}(t) = \pm 1$ and $x_e(t) = [0,1]$.

### 4.1.3 Definition of state variables and control inputs: HEV

The HEV can be easily reduced to a single-state and single-control variable case, with the SOC being represented by the state variable $\xi(t)$ in the following:

$$x(t) = [\xi(t)]; \qquad u(t) = [u_{ts}(t)] \tag{4.18}$$

Except for the constraints regarding the single components involved in the power path, i.e. EMG, ICE, and reported in Section 3.6, Table 3.2, other limitations take place in the optimization problem, which can be expressed as follows:

$$HEV \rightarrow \begin{cases} \xi_{min} \leq \xi(t) \leq \xi_{max} \\ u_{left} \leq u_{ts}(t) \leq 1 \\ \xi(0) = \xi(T) \end{cases} \tag{4.19}$$

where $u_{left}$ is the minimum value allowed for the torque split factor, depending on the size of the ICE and of the EMG.

### 4.1.4 Definition of state variables and control inputs: HSF-HV

On the contrary, the HSF-HV is a multivariable system and it is addressed in Section 4.2.1.5 for the discrete-time modeling approach used in the DP solution. Here, two distinct continuous-time formulations are proposed. A first approach, called $DP_1$ in the following sections, describes the system by means of the following states and inputs definition:

$$DP_1 \rightarrow \begin{cases} x(t) = \begin{bmatrix} \omega_{HSF}(t) \\ \tau_{cvt}(t) \end{bmatrix} \\ u(t) = [u_{ts}(t)] \end{cases} \tag{4.20}$$

A second formulation, named $DP_2$, is based on the definition below:

$$DP_2 \rightarrow \begin{cases} x(t) = \begin{bmatrix} \omega_{HSF}(t) \\ DM(t) \end{bmatrix} \\ u(t) = \begin{bmatrix} u_{ts}(t) \\ DM(t+t_s) \end{bmatrix} \end{cases} \tag{4.21}$$

A detailed description of the meaning of the discrete variable DM is given in Section 4.2.1.5. The constraints can be summarized by the following expression:

$$HSF-HV \rightarrow \begin{cases} 0 \leq \omega_{HSF}(t) \leq \omega_{HSF,max} \\ u_{left} \leq u_{ts}(t) \leq 1 \\ 0 \leq |T_{c,H}| \leq |T_{c,H,max}| \end{cases} \tag{4.22}$$

## 4.2 Optimal Fuel Economy for Hybrid Vehicles

Discrete Dynamic Programming has found increasing interest in HV control optimization problems ([151, 181, 193]). The authors of [180] have developed a generic MATLAB function to implement the DP algorithm in any kind of optimization problem. This algorithm has been applied in the present research activity to solve the optimization problem and to find a benchmark of the FE for online controllers.

### 4.2.1 Deterministic Dynamic Programming

The DP procedure is a numerical algorithm, which requires a discretization of the continuous-time problem (4.1)-(4.5).

#### *4.2.1.1 Problem discretization*

The discrete-time system dynamics (4.2) at the generic discrete stage $k$ may be described as:

$$x_{k+1} = f_k(x_k, u_k) \qquad k = 0,1, \dots N-1 \tag{4.23}$$

At each time stage $k$ the disturbance vector $w_k$ is completely known for the control mission, which is the homologation cycle. It comprises the vehicle speed, the acceleration and the selected gear $g_{s,k}$, the latter being possibly considered as an additional control variable:

$$w_k = \begin{bmatrix} v_k \\ \dot{v}_k \\ g_{s,k} \end{bmatrix} \tag{4.24}$$

The outcome of the DP procedure is an optimal control policy $\pi = \{\mu_0, \mu_1, \dots \mu_{N-1}\}$, such that when implementing this policy starting from the initial state $x(0) = x_0$, the discrete form of the cost function (4.1) results in:

$$J_\pi(x_0) = g_N(x_N) + \varphi_N(x_N) + \sum_{k=0}^{N-1} l_k(x_k, \mu_k(x_k)) + \varphi_k(x_k) \tag{4.25}$$

The term $g_N(x_N)$ corresponds to the final cost associated to the particular values of the final state vector, while $\varphi_k(x_k)$ describes the penalty function of the constraints applied to the state variables at each time stage $k$. The function

$l_k(x_k, \mu_k(x_k))$ is the cost of applying the control actions vector $\mu_k(x_k)$ to $x_k$ at the given stage $k$. The optimal control policy, which is the target of this method, is obviously the one that minimizes the discrete cost functional (4.25):

$$J^o(x_0) = \min_{\pi \in \Pi}\{J_\pi(x_0)\} \tag{4.26}$$

### 4.2.1.2 *DP Algorithm*

The basic DP algorithm relies on Bellmann's principle of optimality [22, 150, 176] and it evaluates, at each time stage $k$ and for each generic state variable $x_p \in x_k$, the optimal-cost-to-go function $C_k\left(x_p^i\right)$, associated with its *i*-th breakpoint discrete value. The computation proceeds backwards in time, starting from the final stage *N* relative to the end of the mission:

$$C_N\left(x_p^i\right) = g_N\left(x_p^i\right) + \varphi_N\left(x_p^i\right) \qquad \forall(p, i) \tag{4.27}$$

The optimal policy can be found, for each node of the discretized states-time domain, by calculating backwards, for every intermediate stage, until the beginning of the mission is reached:

$$C_k\left(x_p^i\right) = \min_{\mu_k}\left\{l_k\left(x_p^i, \mu_k\right) + \varphi_k\left(x_p^i\right) + C_{k+1}\left(f_k\left(x_p^i, \mu_k\right)\right)\right\} \tag{4.28}$$

The optimal policy $\pi^o$ can be found by minimizing the right side of (4.28), starting from the end state *N*, where no control actions are applied and penalties due to possible constraints are introduced, and proceeding for each step $k$ until the beginning of the cycle is reached. The output of the algorithm is a control signal map, evaluated for each node of the discrete state-time grid. Linear interpolation is chosen to interpolate between the discrete values that are compared with the value resulting from the expression $C_{k+1}\left(f_k\left(x_p^i, \mu_k\right)\right)$, in (4.28).

### 4.2.1.3 *Final state constraints: Boundary-line Method*

One common issue of the DP algorithm is how the infeasible states and inputs are treated in the recursive computation. They are usually associated with infinitely large cost:

$$\varphi_k\left(x_p^i \notin \chi_k\right) \coloneqq \infty, \qquad k = 0,1, \dots N \tag{4.29}$$

since the defined objectives cannot be achieved due to model limitations or constraints on the final state vector. The implementation of an infinite cost however, can lead to substantial numerical errors when the interpolation in the discretized time-state grid occurs between a feasible and an infeasible state, in a region that is called boundary line [123]. If the boundary line can be calculated in advance, before the standard DP algorithm and the cost-to-go associated to the points lying on the upper and lower boundaries of the feasible range are stored, the numerical issues can be strongly reduced. Such procedure has been described by the authors of [182] and is implemented here in the HEV optimization only, since it is designed for single-state systems.

#### 4.2.1.4 *Definition of state variables and control inputs: HEV*

In the HEV model, (4.23) is replaced by a discrete form of (3.30). The discrete state variables vector $x_k$ and control variables vector $u_k$ can be simply modeled as follows:

$$x_x = \left[\xi_k\right]; \qquad u_k = \left[u_{ts,k}\right] \tag{4.30}$$

where $\xi_k$ is the battery state-of-charge and $u_k$ is the torque split factor on the GB primary shaft introduced in (3.14). The hard constraint on the state variable, defined as $\xi(0) = \xi(T)$, can be easily handled in this case. This possibility is given by the implementation of the previously described modified DP algorithm, called *boundary line* DP [182]. It allows forcing similar charge-sustaining constraints, while avoiding typical numerical issues associated with the interpolation near the boundary lines of the state-of-charge feasible trajectories. This occurs because out-of-range conditions for $x_p^i$ are usually modeled using $\varphi_N\left(x_p^i\right) = \infty$.

#### 4.2.1.5 *Definition of state variables and control inputs: HSF-HV*

Unlike the HEV system, the DP modeling approach to the HSF-HV does not appear univocal. In fact, there isn't any general set of rules to determine the proper choice of the state and the control variables, when facing a DP-oriented modeling problem. Often, a careful study aided by engineering and numerical considerations is necessary. In this paper, two different approaches are presented, named *$DP_1$* and *$DP_2$*. By analogy with the DP approach to HEV, the common structure of both solutions is the choice of the first state, in this case the flywheel angular speed $\omega_{HSF}$, and the choice of the first control input, the torque split factor $u_{ts}$. Simulations proved that the choice of flywheel speed instead of its kinetic energy does not affect the results of the DP algorithm. Since this problem clearly requires to be addressed as a multivariable system, for reasons that are strictly connected to its topology and components, the boundary line methodology cannot be applied [181].

### HSF-HV Model (1) - DP$_1$

Due to the DP basic algorithm procedure, calculating backwards in time, at every time stage $k$ there cannot be any information about the past conditions of the system. The first straightforward model for the DP problem applied to the HSF-HV system should be designed to take into account that, at any given time, the hybrid powertrain could be in any of the possible conditions, which are with HSF clutch engaged, disengaged or slipping. As a consequence, the simple knowledge of the flywheel speed and split factor, determining whether the hybrid requested torque is different from zero or not, is not sufficient to provide a full knowledge of the system dynamics, capable of solving (4.23). A possible solution is the one to select the CVT ratio as additional state variable, so that:

$$x_k = \begin{bmatrix} \omega_{HSF,k} \\ \tau_{cvt,k} \end{bmatrix}; \qquad u_k = \left[u_{ts,k}\right]; \tag{4.31}$$

The state of the HSF clutch $u_{c,H}$, at the time stage $k$, is then defined by the given value of $\omega_{cvt,1,k}^{mn}$, resulting from the combination of all the allowed possible values of the flywheel speed and of the CVT ratio $\left[\omega_{HSF,k}^{m}, \tau_{cvt,k}^{n}\right]$:

$$u_{c,H} = \begin{cases} 0, & if\ (u = 0) \\ 1, & if\ (u \neq 0) \wedge \left(\left|\omega_{cvt,1,k}^{mn} - \omega_{gb,k}\right| \leq \varepsilon_{\Delta\omega}\right) \\ 2, & if\ (u \neq 0) \wedge \left(\left|\omega_{cvt,1,k}^{mn} - \omega_{gb,k}\right| > \varepsilon_{\Delta\omega}\right) \end{cases} \tag{4.32}$$

where $\varepsilon_{\Delta\omega}$ is a tolerance introduced to define a threshold for the angular speeds difference, below which the clutch can be considered engaged, thus the slipping efficiency of (3.18) is equal to one. It should be highlighted that, although this approach allows taking into consideration all the possible system behaviors, the engaged condition ($u_{c,H} = 1$), which is of primary importance, is affected by the likelihood of falling below the speeds difference threshold. Obviously, this strongly depends on the state variables discretization, namely the number of $\omega_{HSF}$ breakpoints $M$ and $\tau_{cvt}$ nodes $N$. Ideally, the latter two parameters should be chosen as large as possible. Unfortunately, this is in contrast with the biggest issue regarding the DP methodology, which is its huge computational cost, often referred to as the *curse of dimensionality*.

### HSF-HV Model (2) - $DP_2$

The second modeling technique, presented in this section, aims at reducing the dimensional characteristics of the selected variables. A similar approach is followed in [18, 19] for a different mechanical hybrid concept, comprising a CVT as the only transmission device between the propulsion systems and the wheels. The key idea is to simplify the HSF system description, adopting a state-control variable that allows describing the switching management between different driving modes. This can be obtained thanks to the discrete variable $DM_K$ with three possible values:

$$DM_K \to \begin{cases} 1, & \text{ICEonly-mech. brakes} \\ 2, & \text{HSF hybrid mode} \\ 3, & \text{Boost-Charging} \end{cases} \tag{4.33}$$

The HSF clutch operation is treated as an on/off variable, with $u_{c,H} = [0, 1]$, whose value immediately descends from $DM_K$. Its actuation is supposed to be feasible within the DP simulation time step $t_s$. Under this hypothesis, the instantaneous value of the CVT ratio is:

$$\tau_{cvt,k} = \begin{cases} \frac{\omega_{HSF,k}}{\omega_{g,k} \cdot \tau_{HSF}}, & if(DM_K = 2) \vee (DM_K = 3) \\ \min\left(\tau_{cvt,k,max}, max\left(\tau_{cvt,k,min}, \frac{\omega_{HSF,k}}{\omega_{g,k} \cdot \tau_{HSF}}\right)\right), else \end{cases} \tag{4.34}$$

The lower condition, relative to disengaged HSF clutch, simply describes the best possible primary shaft tracking operation, considering the CVT ratio range limits. The state and control variables vectors can be summarized as:

$$x_k = \begin{bmatrix} \omega_{HSF,k} \\ DM_K \end{bmatrix}; \qquad u_k = \begin{bmatrix} u_{ts,k} \\ DM_{K+1} \end{bmatrix}; \tag{4.35}$$

Although the overall number of variables, with respect to the $DP_1$ method, is increased by one, this simplified approach is favored by the fact that the $DM_K$

state and $DM_{K+1}$ control are discrete variables with only three allowed numerical values. The consequence of this choice is a largely reduced computational cost, as it will be demonstrated in Section 4.3.2.

### 4.2.2 Equivalent Consumption Minimization Strategy (ECMS)

The ECMS has been introduced for HEVs, as a derivation of PMP. In previous studies ([46, 47]) its applicability to other systems, such as HSF-HV and HHV has been demonstrated. Here, the fundamental theoretical hypotheses of the ECMS and its derivation are briefly recalled for a HEV.

#### *4.2.2.1 PMP: Optimal Control Theory applied to HVs*

The generic optimization problem (4.1)-(4.5) is addressed here, with $\xi(t)$ denoting the battery SOC and being the only relevant state of the HEV system. In this case, (4.2) can be rearranged as:

$$\dot{\xi}(t) = -\frac{I_b(\xi(t), u(t), t)}{Q_0} \tag{4.36}$$

and the final state constraint can be reformulated to include strictly charge-sustaining conditions. The general expression (4.3) becomes:

$$\xi(T) = \xi(0) = \xi_0 \tag{4.37}$$

The necessary conditions for optimality are related to the definition of the Hamiltonian function of the system. From (4.6) and (4.36) it results:

$$H(\xi(t), u(t), \lambda(t), t) = H_l \overset{*}{m}_{fuel}(u(t), t) - \lambda(t) \frac{I_b(\xi(t), u(t), t)}{Q_0} \tag{4.38}$$

where $\lambda(t)$ denotes the only co-state, sometimes referred to as Lagrange multiplier or adjoint state. According to PMP [57] the optimal control policy, indicated with the superscript ”*o*”, must satisfy the necessary conditions for optimality listed in the following:

1. State and co-state dynamics and boundary conditions:

$$\dot{\xi}^o(t) = \nabla_\lambda H_{|o} = -\frac{I_b(\xi(t), u(t), t)}{Q_0} \tag{4.39}$$

$$\xi^o(0) = \xi_0 \tag{4.40}$$

$$\xi^o(T) = \xi_f = \xi_0 \tag{4.41}$$

$$\dot{\lambda}^o(t) = \nabla_\xi H_{|o} = \lambda(t) \frac{1}{Q_0} \frac{\partial}{\partial \xi} I_b(\xi^o(t), u^o(t), t) \tag{4.42}$$

2. For all times $t \in [0, T]$ the Hamiltonian associated with the optimal sequence $H(\xi^o(t), u^o(t), \lambda^o(t), t)$ is the global optimal with respect to $u(t)$:

$$H(\xi^o(t), u^o(t), \lambda^o(t), t) \leq H(\xi^o(t), u(t), \lambda^o(t), t) \tag{4.43}$$

#### *4.2.2.2 Sub-optimal on-line control EMS for a HV: ECMS*

The so called ECMS can be regarded as a direct derivation of the PMP applied to the control of HVs, with the application of some restrictive conditions introduced in the previous subsection. Some researchers [168, 142, 45, 43, 96] have demonstrated the mathematical assumptions of this hypothesis in a strict manner.

If the following substitution is introduced:

$$s(\xi(t), t) := -\frac{\lambda(t)}{V_{oc}(\xi(t)) Q_0} \tag{4.44}$$

the Hamiltonian (4.38) can be reformulated as follows:

$$H(\xi(t), u(t), \lambda(t), t) = H_l \cdot \overset{*}{m}_{fuel}(\cdot) + s(\cdot) V_{oc}(\cdot) Q_0 \frac{I_b(\cdot)}{Q_0} \tag{4.45}$$

where dependencies on time, state and input variables are omitted for simplicity. The final expression for the Hamiltonian yields to:

$$H(\xi(t),u(t),\lambda(t),t) = P_{fuel}(u(t),t)) + s(\xi(t),t) \cdot P_{b,i}(\xi(t),u(t),t)) \tag{4.46}$$

The fuel chemical power $P_{fuel}$ and battery inner electrochemical power $P_{b,i}$ are defined:

$$P_{fuel}(u(t),t)) = H_l \cdot \overset{*}{m}_{fuel}(u(t),t)) \tag{4.47}$$

$$P_{b,i}(\xi(t),u(t),t)) = V_{oc}\big(\xi(t)\big) \cdot I_b(\xi(t),u(t),t) \tag{4.48}$$

Now, the PMP method shows how the global optimization problem can be translated into a local optimization of the function (4.46). The latter is a weighted sum of fuel power and of an equivalent fuel power, defined by an equivalence factor $s$ that converts the inner battery power into fuel units.

To solve the problem, the values of $\lambda(t)$ should be found solving (4.42). This is not a straightforward task, and represents a two-point boundary value problem, which is often solved using shooting method, to identify the initial condition $\lambda(0)$ that minimizes the Hamiltonian while satisfying the conditions (4.40)-(4.41).

If the assumption of reduced sensitivity of the battery current with respect to the state-of-charge holds, (4.42) leads to:

$$\dot{\lambda}^o(t) = \lambda(t)\frac{1}{Q_0}\frac{\partial}{\partial\xi}I_b(\xi^o(t),u^o(t),t) \approx 0 \tag{4.49}$$

Hence, the value of the co-state remains constant:

$$\lambda(t) = \lambda(0) = \lambda_0 \tag{4.50}$$

As a consequence, a constant value of the equivalence factor $s_0$ exists that allows solving the optimization problem as the minimization of the instantaneous function (4.46). Such value depends both on the system and on the driving mission. For these reasons, its value will be time-variant in real online controllers, leading to a general framework for suboptimal controllers. Several adaptation rules are proposed in the following subsections. The formulation (4.46) can be adapted to the HSF-HV, replacing $P_{b,i}$ with $P_{HSF}$ and $\xi$ with $E_{k,HSF}/E_{k,HSF.max}$.

Since a causal version of ECMS is needed to be applied in an online controller, several methodologies have been proposed to achieve this goal. They are analyzed in details in the following subsections.

#### *4.2.2.3 Equivalence factor control*

A review of various adaptation methods is presented in [137], while the impact of the choice of the adaptation rule for the equivalence factor is analyzed in [36]. Some authors claim that an efficient way to find out robust adaptation rules for the Lagrangian multiplier of the standard ECMS can be derived from the results of the DP applied on the same control mission ([63, 174]). A major classification of the different adaptation methods is the following:

- Adaptation based on SOC-feedback;
- Adaptation based on driving cycle prediction;
- Adaptation based on driving pattern recognition.

The first category doesn't require any information about future driving condition and therefore it is fully causal and can be directly implemented online. A first formulation includes a pure proportional term:

$$s(\xi(t),t) = s_0 + k_{P,\xi}\left(\xi_{ref} - \xi(t)\right) \tag{4.51}$$

However, an integral term is necessary, as formally demonstrated in [6], to obtain better results and properly compensate the lack of knowledge about future driving conditions and consequent future operating points, which are necessary to consider the first term in the previous expression as a constant. Its derivation is made starting from the optimal solution with PMP, then converting it into a causal controller by adding some penalty function as a function of the SOC deviation. The resulting expression is:

$$s(\xi(t),t) = s_0 + k_{P,\xi}\left(\xi_{ref} - \xi(t)\right)^{2q-1} + \int_0^t \frac{\xi_{ref} - \xi(\tau)}{T_{i,\xi}}\,d\tau \tag{4.52}$$

An approach similar to a PI-controller, although its mathematical formulation is different, is the following, where a law is built to penalize deviation from a reference value of the state-of-charge $\xi_{ref}$, so that the nominal value $s_{nom}$ is corrected thanks to the effect of the function $f_{SOC}$:

$$
\begin{aligned}
s(\xi(t),t) &= f_{SOC}\big(\xi(t)\big)\cdot\, s_{nom}(t)\\
f_{SOC}\big(\xi(t)\big) &= \left[1+\left(\frac{\xi_{ref}-\xi(t)}{\xi_{ref}-\xi_{min}}\right)^{2q+1}\right]\cdot\left[1+tanh\left(\frac{f_{SOC,I}\big(\xi(t)\big)}{\xi_{th}}\right)^{2q+1}\right]\\
f_{SOC,I}\big(\xi(t)\big) &= 0.99 f_{SOC,I}(t-t_s)+0.01(\xi_{ref}-\xi(t))
\end{aligned}
\tag{4.53}
$$

This is proposed in [167, 105], where the use of the hybrid power when the SOC approaches its range limits is penalized. The main parameters, which are the reference value $\xi_{ref}$, the minimum value $\xi_{min}$, the additional parameters $\xi_{th}$ and $q$, must be carefully selected. The ECMS sampling time is $t_s$ (usually 0.01 s is adopted). To improve the capability of the strategy to handle different driving conditions, the SOC behavior is monitored, leading to the definition of the additional function $\psi_\xi(\xi(t))$, that allows the implementation of an adaptive term, designed to modify the standard and constant value $s_0$. The following definition of $s_{nom}(t)$ is adopted:

$$
s_{nom}(t) = s_0 + \psi_\xi\big(\xi(t)\big) \tag{4.54}
$$

A proof of the closed-loop stability of a PI controller for the co-state adaptation based on SOC error is found by the author of [186] for a series HV application. A third adaptation rule can be formulated by means of the equation below.

$$
s(\xi(t),t) = \frac{s_{k-1}+s_{k-2}}{2} + k_P^d\left(\xi_{ref}-\xi(T_{ma})\right) \tag{4.55}
$$

Here, an autoregressive moving average is performed, including two autoregressive terms and one moving average term. The fact that the adaptation rule only applies every period $T_{ma}$, allows greater SOC excursions.

Several attempts have been made to include driving cycle prediction into the adaptation rule for the co-state of ECMS strategy. An adaptive version called A-ECMS has been proposed in [127], consisting of a periodical refreshing technique to adapt the control parameter to the current driving conditions. It is causal, since it only relies on the current road load to predict data on a future optimization segment. A second way to attempt to include future driving behavior without any additional information about the future driving profile is proposed by the authors of [165], where the adaptation rules is:

$$s(t) = p(t) \cdot s_{dis} + (1 - p(t)) \cdot s_{chg} \tag{4.56}$$

where the factor $p(t)$ represents the estimated probability of the electrical energy use of the battery being positive at the end of the driving mission. The two constant terms $s_{dis}$ and $s_{chg}$can be defined as follows:

$$\begin{aligned} s_{dis} &= \frac{1}{\bar{\eta}_e \bar{\eta}_f} \\ s_{chg} &= \frac{\bar{\eta}_e}{\bar{\eta}_f} \end{aligned} \tag{4.57}$$

where $\bar{\eta}_e$ and $\bar{\eta}_f$ represent the average efficiencies of the electrical and thermal energy paths respectively. This version is a causal controller as well. In [5] the adaptation scheme, called predictive reference signal generator (pRSG) is combined with a SOC-based controller, computing the desired state-of-charge trajectory as a function of the future vehicle position. The topographic profile and the average speeds on the future segments must be known. Other approaches that are based on prediction of future driving condition aided by Intelligent Transportation System (ITS) have been proposed [214, 3, 59, 54]. In [163] instead, a heuristic logic is applied to obtain an online adaptation of the co-state.

In driving pattern recognition methodology (see [62]) a time window of past driving conditions is analyzed periodically while the vehicle is running, aiming at its recognition as one of the predetermined patterns. Once the representative pattern is recognized, a corresponding pre-computed optimal value of the equivalence factor is assigned for the following time segment. The method is causal and has high memory requirements.

Driving cycle prediction or pattern recognition methodologies could be added even to the first category of SOC-based feedback controllers, by tuning the parameters $s_o$ and $\xi_{ref}$. For instance, the knowledge of the actual vehicle speed and relative altitude can be used to adapt the SOC reference value, considering that its corresponding kinetic and potential energy will be recuperated in the future and stored into electrical energy, with efficiencies $\eta_{c,K}$ and $\eta_{c,P}$:

$$\xi_{ref}(t) = \xi_0 - \left( \eta_{c,K} \cdot \frac{\frac{1}{2} m(t) \cdot v^2(t)}{Q_0 V_{oc}(\xi_0)} + \eta_{c,P} \cdot \frac{m(t) \cdot g \cdot h(t)}{Q_0 V_{oc}(\xi_0)} \right) \tag{4.58}$$

where $h(t)$ is the slope variation relative to the altitude at the initial time of the driving mission.

The advantage of adding an adaptive term dependent on the kinetic and the potential energy of the vehicle is proved in simulation and experimental tests [92, 93] in terms of FE. The same concept can be applied to a PHEV, where the reference state-of-charge signal is linear with time and terminates as close as possible to the minimum charge at the end of the driving mission [189].

#### *4.2.2.4 ECMS drivability issues: straightforward approaches*

The online implementation of the ECMS requires some stabilization algorithms to cope with its practicality in real systems. In effect, the theoretical optimal $u^o(t)$ could be practically infeasible, leading to chattering phenomena, causing too frequent and non realistic [143, 44] ICE start/stop events. This phenomenon must be prevented in real driving operations. Different methods can be adopted to address this issue. An approach based on the combined use of three timers with three different delays to regulate engine on/off command is proposed in [109]. A more straightforward approach consists of introducing a penalty to every ICE on/off event, to form the overall compound instantaneous cost function as formulated in (4.8).

#### *4.2.2.5 Other ECMS versions*

The development of rule-based strategies whose structure is partially similar to that of the ECMS has been proposed in the studies [69, 70, 90, 89]. In these research activities, the target is a heuristic strategy, purely based on physical characteristics of the vehicle and on engineering considerations. However, the structure of some operating modes, and more precisely of those involving the combined used of both prime movers, implies the minimization of a Hamiltonian function, just as the basic ECMS application requires. The authors claim that very good results can be achieved, requiring the tuning of a limited set of parameters. Other ECMS variations can be in the field of map-based algorithms. A map-based ECMS is proposed by the authors of [175], where an optimal torque distribution map is computed by means of DP and stored in maps, and the consequent sub-optimal real-time strategy is efficiently solved online. A similar approach is followed in [87] where an off-line optimization procedure is solved and a fast map formulation allows its application in real-time control. The considered scenario is a hybrid vehicle on a prescribed route, where the actual input values are updated to compensate the deviation between theoretical and actual vehicle route.

## 4.3 Simulation results

The chosen ECMS version implements the co-state adaptation rule (4.53)-(4.54) and includes a comfort function to prevent frequent engine start/stop events. This is simply obtained due to the combined effect of a delay, inserted to prevent too frequent switching between driving modes that imply different ICE states, and of a low-pass filtering of the optimal theoretical instantaneous torque split factor. The two latter features, together with a heuristic gear-shifting based on the map of Figure 3.6, clearly have the consequence to add further sub-optimality to the resulting strategy. Figure 4.1 depicts the flow chart of the ECMS-based HCU framework.

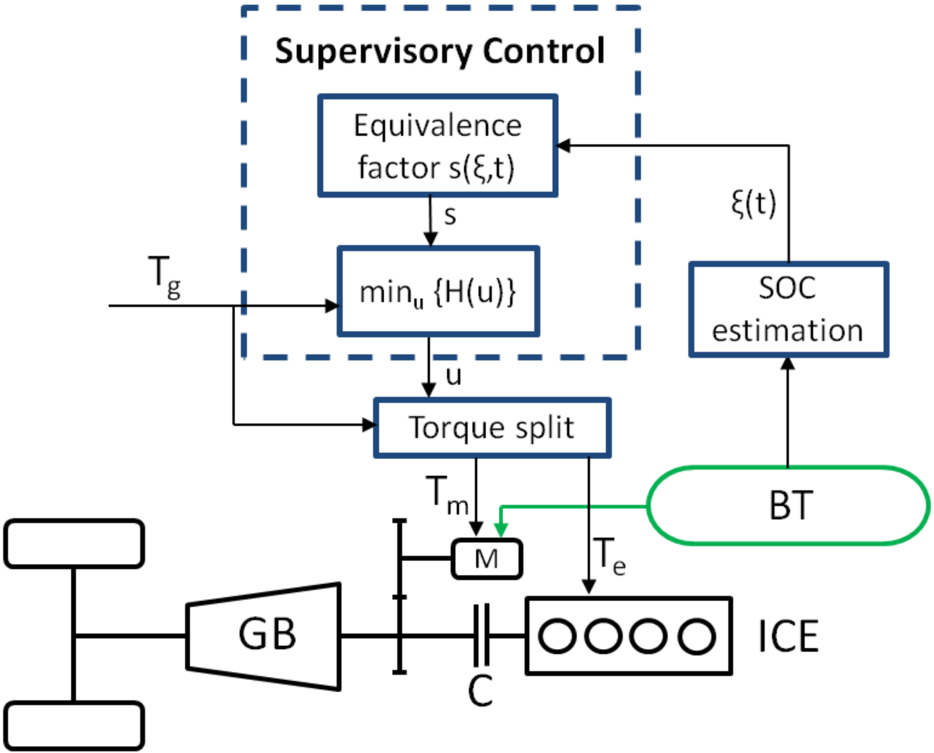

Figure 4.1: Flow chart of the ECMS strategy for the HEV system.

However, the advantage in terms of ICE start/stop and gear-shifting events, which are good metrics to describe the driver's comfort, is clear and it is illustrated in Subsection 4.3.3, with a comparison to the optimal unconstrained DP results.

In this section, the results of the DP procedures are compared to those of ECMS applied to different homologation cycles, namely NEDC, FTP-75 and JN-1015. The only indicator adopted to estimate the performances of the two strategies is the FE.

In case of the HEV system, charge-sustaining condition (4.19) is guaranteed, adopting the boundary line method for the DP and varying the $s_0$ parameter in (4.54) for the ECMS. In general, if hard constraints on the final state are not feasible, an indicator capable of taking into account the differences related to a different final state-of charge between the two strategies must be introduced.

Focusing on the HSF-HV model, if $FC_{DP}$ is the DP gross fuel consumption and $FC_{ECMS}$ its equivalent for the ECMS, the corrected DP fuel consumption $FC_{DP}^{corr}$ can be expressed as:

$$FC_{DP}^{corr} = FC_{DP} + \frac{\frac{1}{2}\Theta_{HSF}\left(\omega_{HSF,ECMS}^{2}(T) - \omega_{HSF,DP}^{2}(T)\right)}{H_l \cdot \bar{\eta}_{e,DP} \cdot \bar{\eta}_{cvt,DP} \cdot \eta_{HSF}} \tag{4.59}$$

where the difference in terms of final kinetic energies of the flywheel is converted into fuel mass equivalent units due to the calculation of the effective round trip efficiencies. Then the corrected relative fuel economy $crFE$ can be calculated as:

$$crFE = \frac{FC_{ECMS} - FC_{DP}^{corr}}{FC_{ECMS}} \cdot 100 \tag{4.60}$$

The same expression of (4.59) can be formulated for the HEV system, substituting the kinetic energy content with battery state-of-energy or state-of-charge.

## 4.3.1 HEV

The numerical results of DP/ECMS FE comparisons are reported in Table 4.1. Figure 4.2, Figure 4.3 and Figure 4.4 depict the different SOC trajectories that result from the application of the two control policies on the same homologation cycle.

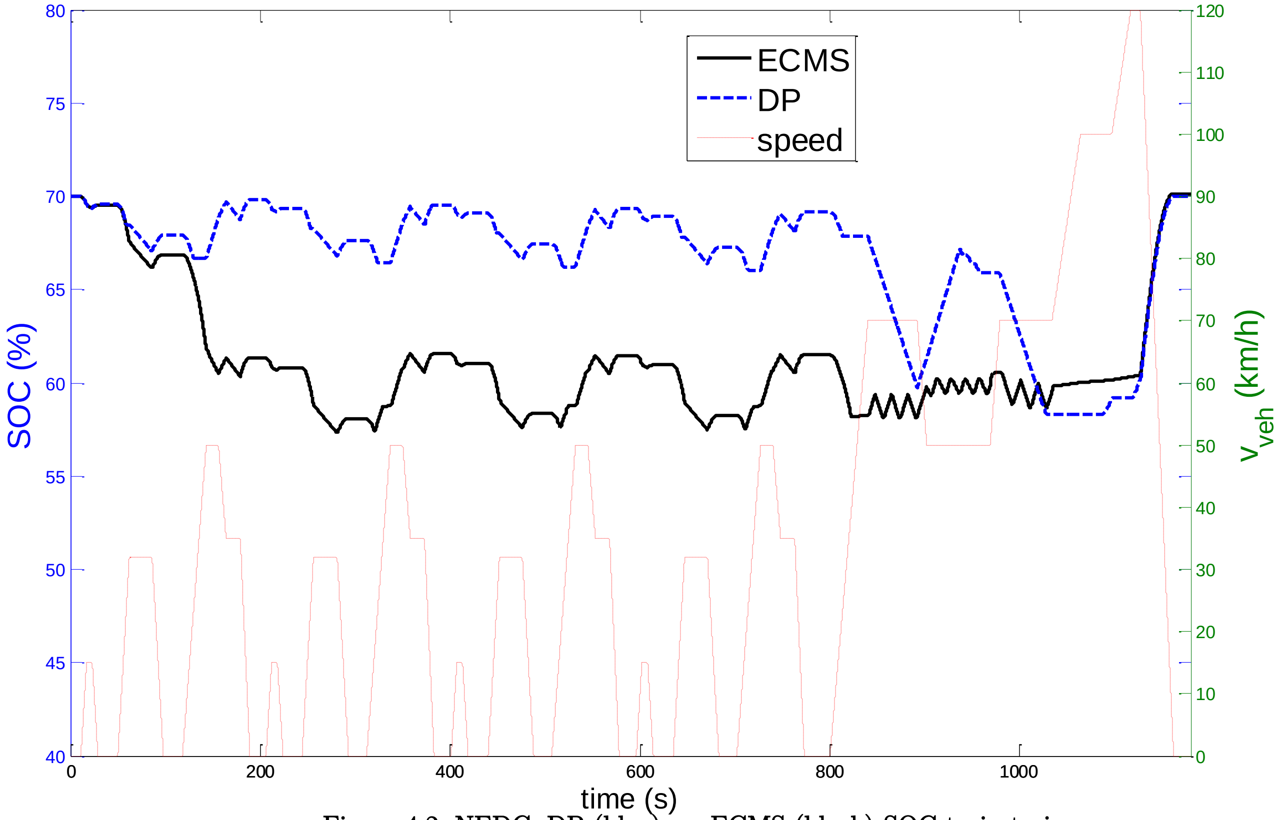

Figure 4.2: NEDC: DP (blue) vs. ECMS (black) SOC trajectories.

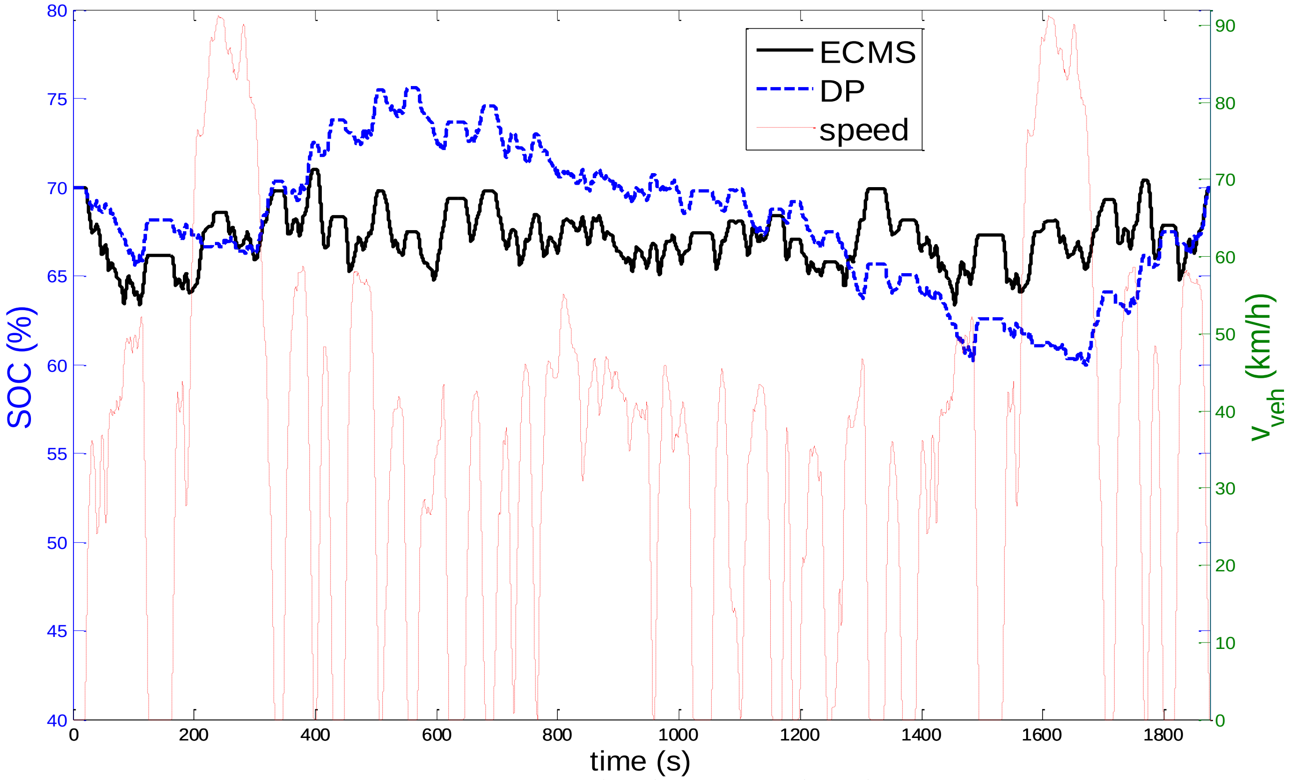

Figure 4.3: FTP-75 DP (blue) vs. ECMS (black) SOC trajectories.

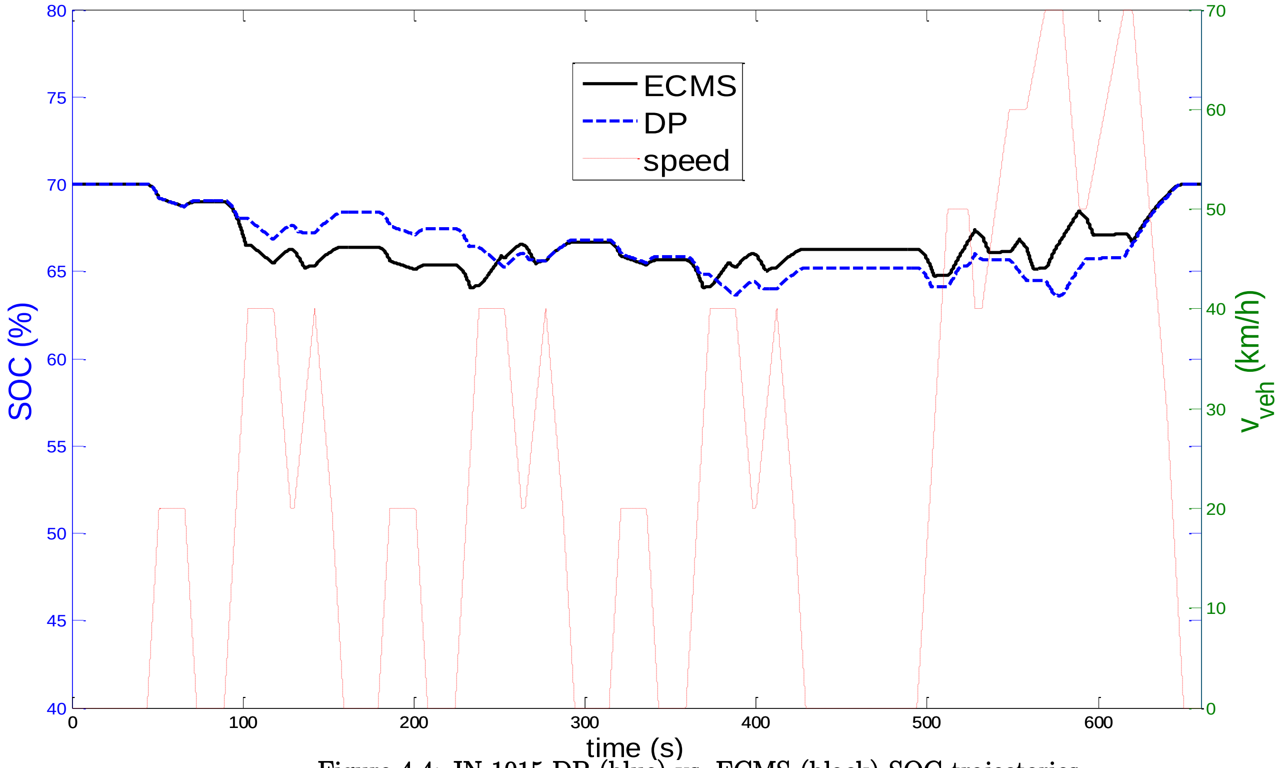

**Figure 4.4: JN-1015 DP (blue) vs. ECMS (black) SOC trajectories.**

It can be noticed that, except for the JN-1015, the state variable trajectories are substantially different, indicating that the ECMS sub-optimal strategy deviates from the global optimal one that is calculated by the DP algorithm.

**Table 4.1: HEV results for the ECMS/DP comparison simulations.**

| **Cycle** | **FC ECMS [l/100 km]** | **FC DP [l/100km]** | **crFE [%]** |
|---|---|---|---|
| NEDC | 4.37 | 4.22 | 2.99 |
| JN-1015 | 3.92 | 3.81 | 4.67 |
| FTP-75 | 4.35 | 3.97 | 8.83 |

Literature analyses concerning flat homologation cycles ([137, 127, 6, 66]) over DP/ECMS comparisons indicate that an optimally tuned and cycle-based ECMS should not lead to FE results worse than 1% of the global optimum. The higher values in Table 4.1 can be explained considering that the proposed ECMS algorithm, as explained in the dedicated section of this paper, includes modifications and filtering of the raw theoretical minimizing $u_{ts}^{o}(t)$ signal, oriented to driver comfort and real drivability constraints, with unknown vehicle mission. These effects are quantified in Section 4.3.3.

### 4.3.2 HSF-HV

For the HSF-HV system, the definition of charge-sustaining hard constraints on the first state variable, such as $\omega_{HSF}(0) = \omega_{HSF}(T)$, would compromise the numerical reliability of the DP result, due to well-known issues related to the interpolation near the boundaries of the feasible state-space region. Nonetheless, the short discharging time typical of mechanical energy storage, due to friction and air drag, suggests that the simulation of homologation cycles with initial flywheel energy different from zero could not be considered representative of real vehicle operation. Consequently, imposing that the flywheel is still at the end of any homologation cycle would result in a strong penalization of this hybrid concept, since it would inhibit kinetic energy recuperation during the final braking stage. The problem, both for $DP_1$ and $DP_2$, is addressed with the introduction of a final state cost:

$$g_N(x_N) = g_N(\omega_{HSF,N}) = \frac{\frac{1}{2}\Theta_{HSF}\left(\omega_{HSF,N}^2 - \omega_{HSF}^2(0)\right) \cdot \bar{\eta}_{cvt} \cdot \eta_{HSF}}{H_l \cdot \bar{\eta}_e} \tag{4.61}$$

where the average efficiencies of the CVT and the ICE should be estimated in advance, introducing an error with respect to the actual values. The term in (4.61) represents the fuel mass equivalent of charging the flywheel to a final value different from the initial one. Before the analysis of DP/ECMS comparison for the HSF-HV, a study on the impact of the different choices for the modeling approach, that is $DP_1$ and $DP_2$, is carried out in the next subsections.

#### *4.3.2.1 Model (1) - $DP_1$*

The two DP-oriented modeling techniques can be evaluated in terms of fuel consumption, introducing the following corrected fuel mass $cFM$ indicator:

$$cFM = FM - \frac{\frac{1}{2}\Theta_{HSF}\left(\omega_{HSF}^2(T) - \omega_{ref}^2\right)}{H_l \cdot \bar{\eta}_{e,DP} \cdot \bar{\eta}_{cvt,DP} \cdot \eta_{HSF}} \tag{4.62}$$

where the difference in terms of end-of-cycle kinetic energy is evaluated with respect to a common reference value $\frac{1}{2}\Theta_{HSF}\omega_{ref}^2$. Then a parametric analysis has been conducted, firstly regarding the factor to which the sensitivity of the $DP_1$ results is considered prominent. This is the state variables grid density or, in other words, the selection of the two previously introduced parameters *M* and *N*. In Table 4.2, *cFM* comparative values are reported for the JN-1015 cycle.

Table 4.2: Parametric analysis for $DP_1$ grid density selection. $DP_1$ vs. $DP_2$ simulations.

| DP | Time-step $t_s$ [s] | $\omega_{HSF}$ values M [-] | $\tau_{cvt}$ values N [-] | u values U [-] | cFM [g] |
|---|---|---|---|---|---|
| $DP_2$ | 0.1 | 701 | - | 51 | 106.5 |
| $DP_1$ | 0.1 | 701 | 91 | 51 | 115.3 |
| | 0.1 | 501 | 71 | 51 | 120.4 |
| | 0.1 | 301 | 51 | 51 | 140.4 |
| | 0.1 | 401 | 61 | 51 | 128.8 |
| | 0.1 | 201 | 36 | 51 | 145.5 |
| | 0.1 | 151 | 31 | 51 | 149.4 |

The listed values are also compared to the *cFM* obtained with $DP_2$, with same choice of $\omega_{HSF}$ and $u$ breakpoints. Figure 4.5 graphically represents the results of Table 4.2.

The influence of the grid density parameterization is quite evident. The benefits of reducing the states matrix resolution obviously comes along with a substantially increased computational cost of the DP procedure. The difference between the value obtained from $DP_2$ (106.5 g), and the one from $DP_1$ at the highest grid density (115.3 g), strictly equals the fuel-equivalent value of the energy dissipated by friction losses in the HSF clutch during slipping, which are neglected in $DP_2$.

The second investigated parameter is the simulation time step $t_S$, kept constant for the previous analysis.

As shown in Table 4.3, the sensitivity of $DP_1$ to the time-step selection can be considered of secondary importance compared to the number of breakpoints

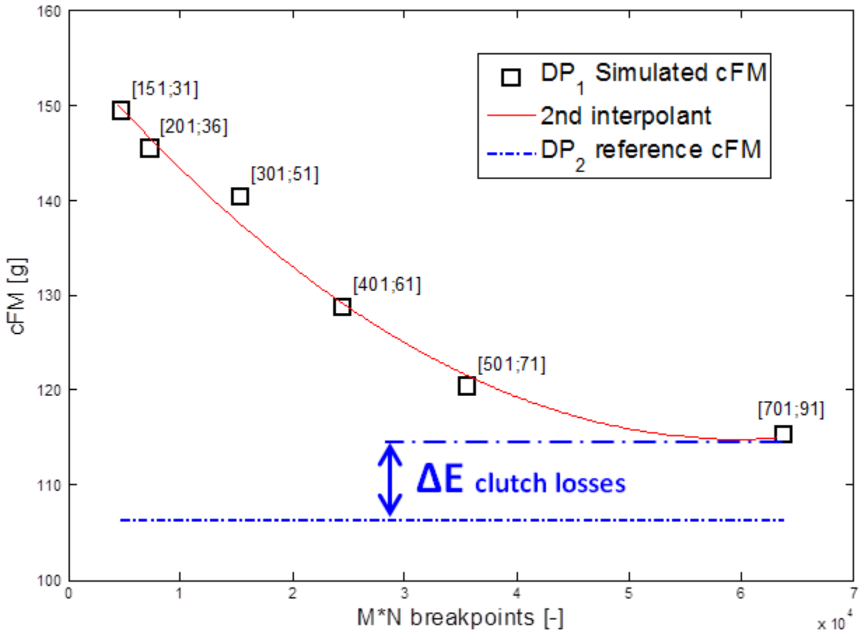

Figure 4.5: $DP_1$; effect of the number of state variables total breakpoints on cFM, JN-1015 cycle.

Table 4.3: HSF-HV; parametric analysis for the $DP_1$ simulation time-step.

| DP | Time-step $t_s$ [s] | $\omega_{HSF}$ values M [-] | $\tau_{cvt}$ values N [-] | u values U [-] | cFM [g] |
|---|---|---|---|---|---|
| $DP_1$ | 0.1 | 701 | 91 | 51 | 117.8 |
| | 0.25 | 701 | 91 | 51 | 118.7 |
| | 0.5 | 701 | 91 | 51 | 121.2 |
| | 0.75 | 701 | 91 | 51 | 119.3 |

### *4.3.2.2 Model (2) - $DP_2$*

As highlighted in the analysis of the previous section, the $DP_2$ methodology should be preferred, since the overall computational time required is strongly reduced compared to the $DP_1$. The fact that the slipping losses are neglected can be considered of secondary importance, if the goal of the simulations is to carry out relative comparisons between ECMS and DP. In this case the latter simplification is adopted equally for both strategies. The resulting $\omega_{HSF}$ trajectories, over the same set of homologation cycles analyzed in case of the HEV vehicle, are depicted in Figure 4.6, Figure 4.7 and Figure 4.8. The numerical results are listed in Table 4.4.

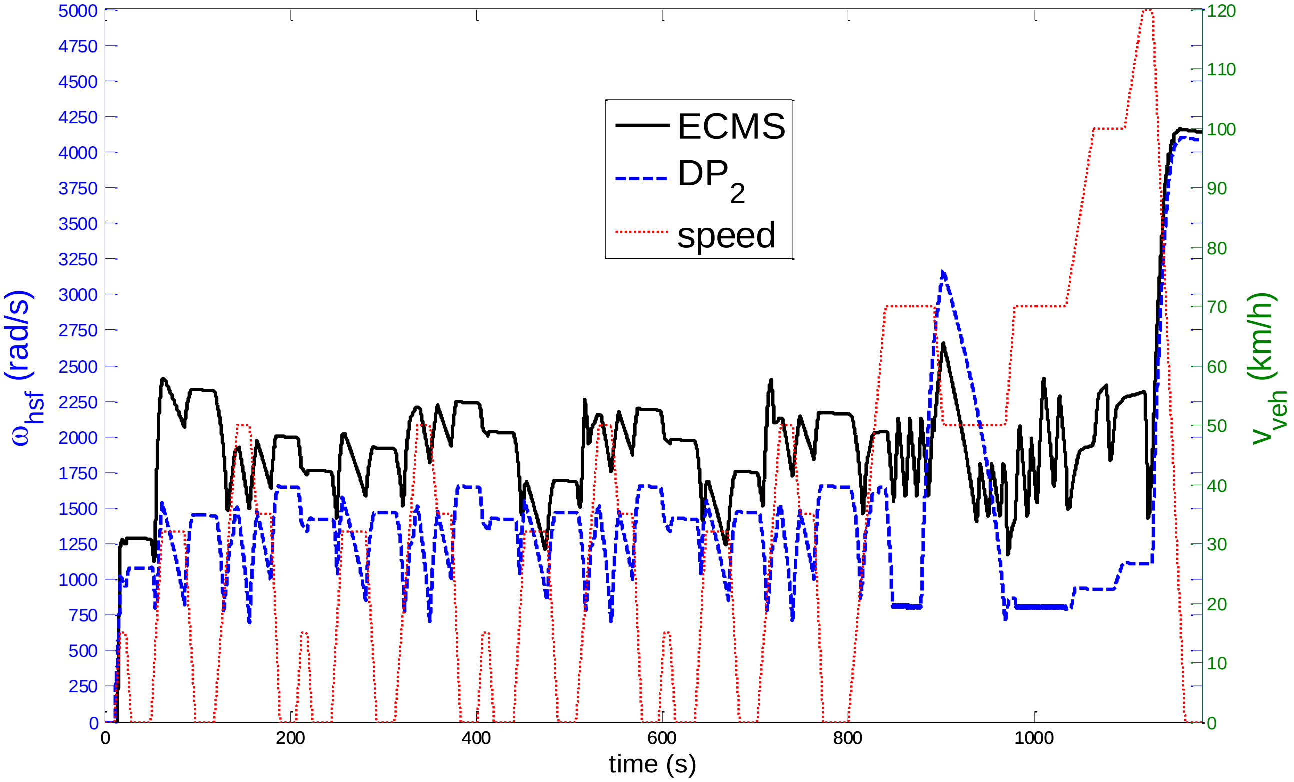

Figure 4.6: NEDC DP$_2$ (blue) vs. ECMS (black) $\omega_{HSF}$ trajectories.

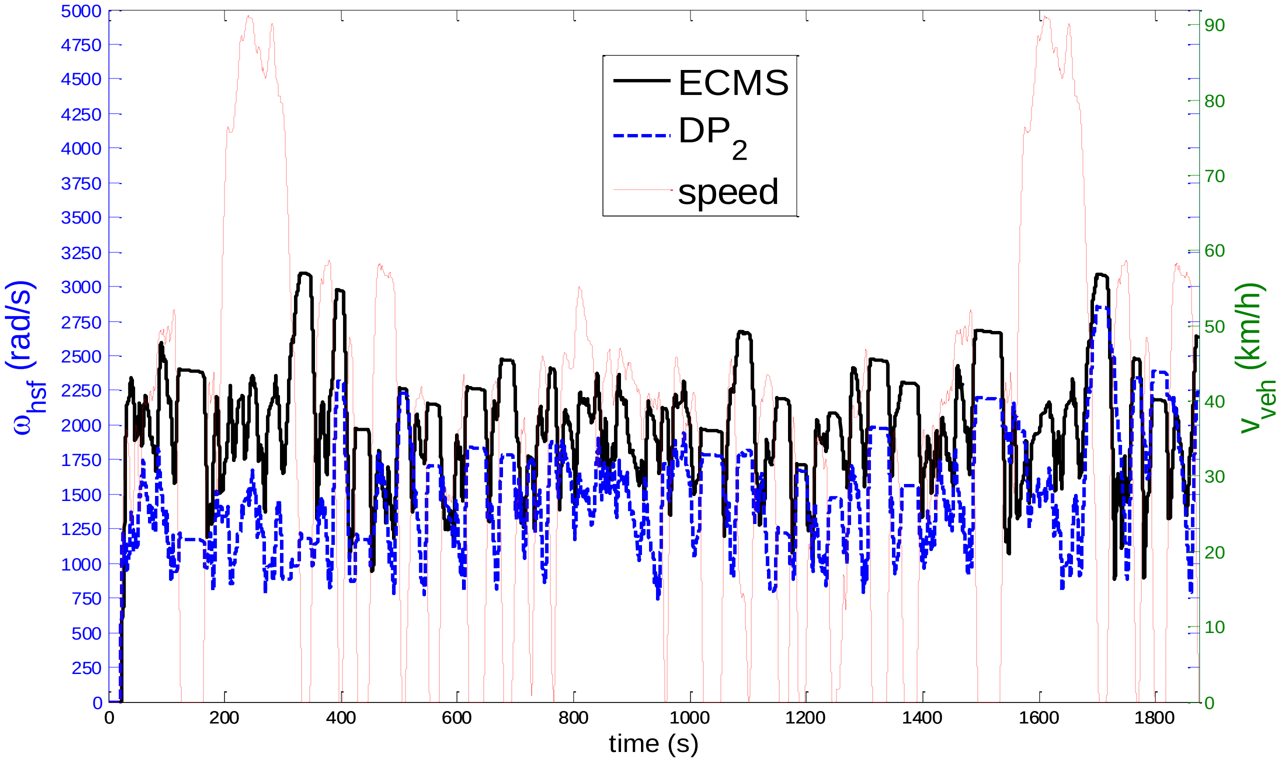

Figure 4.7: FTP-75 DP$_2$ (blue) vs. ECMS (black) $\omega_{HSF}$ trajectories.

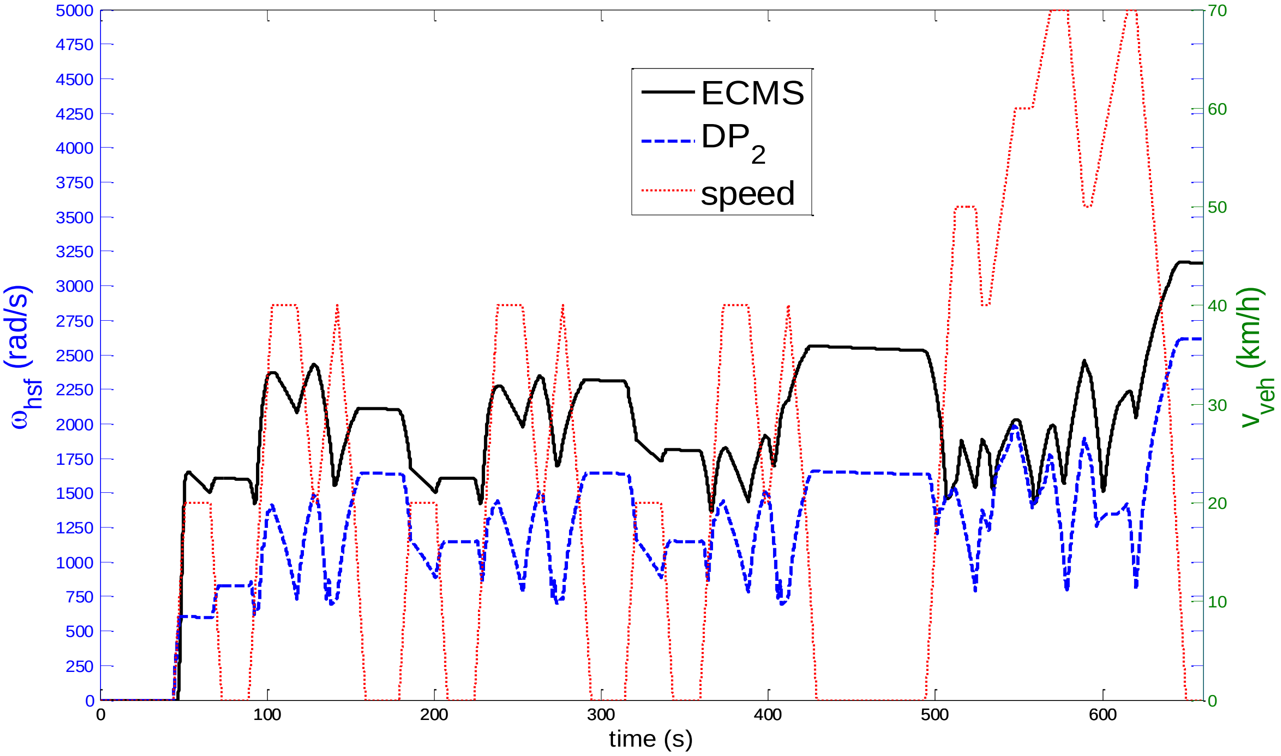

**Figure 4.8: JN-1015 DP$_2$ (blue) vs. ECMS (black) $\boldsymbol{\omega}_{\mathrm{HSF}}$ trajectories.**

### *4.3.2.3 Optimal gear-shifting*

An additional and interesting investigation is related to the study on the impact of gear selection on FE. This can be easily provided by means of a DP algorithm, simply introducing an additional control input to the control variables vector $u_k$, so that the DP problem becomes:

$$x_k = \begin{bmatrix} \omega_{HSF,k} \\ DM_K \end{bmatrix}; \qquad u_k = \begin{bmatrix} u_{ts,k} \\ DM_{k+1} \\ g_{s,k} \end{bmatrix}; \tag{4.63}$$

The model must take into account all the additional constraints that this further degree-of-freedom introduces, especially regarding ICE speed limits. A comparison of the SOC trajectories for NEDC cycle, with and without DP optimal gear selection, is shown in Figure 4.9.

Table 4.4: HSF Hybrid Vehicle; results for the ECMS/DP comparison simulations. ** DP-based gear selection.

| Cycle | FC ECMS [l/100 km] | FC DP [l/100km] | crFE [%] |
|---|---|---|---|
| NEDC | 4.49 | 4.31<br>4.18** | 3.97<br>6.71** |
| JN-1015 | 4.28 | 4.06 | 5.02 |
| FTP-75 | 4.27 | 3.98 | 6.92 |

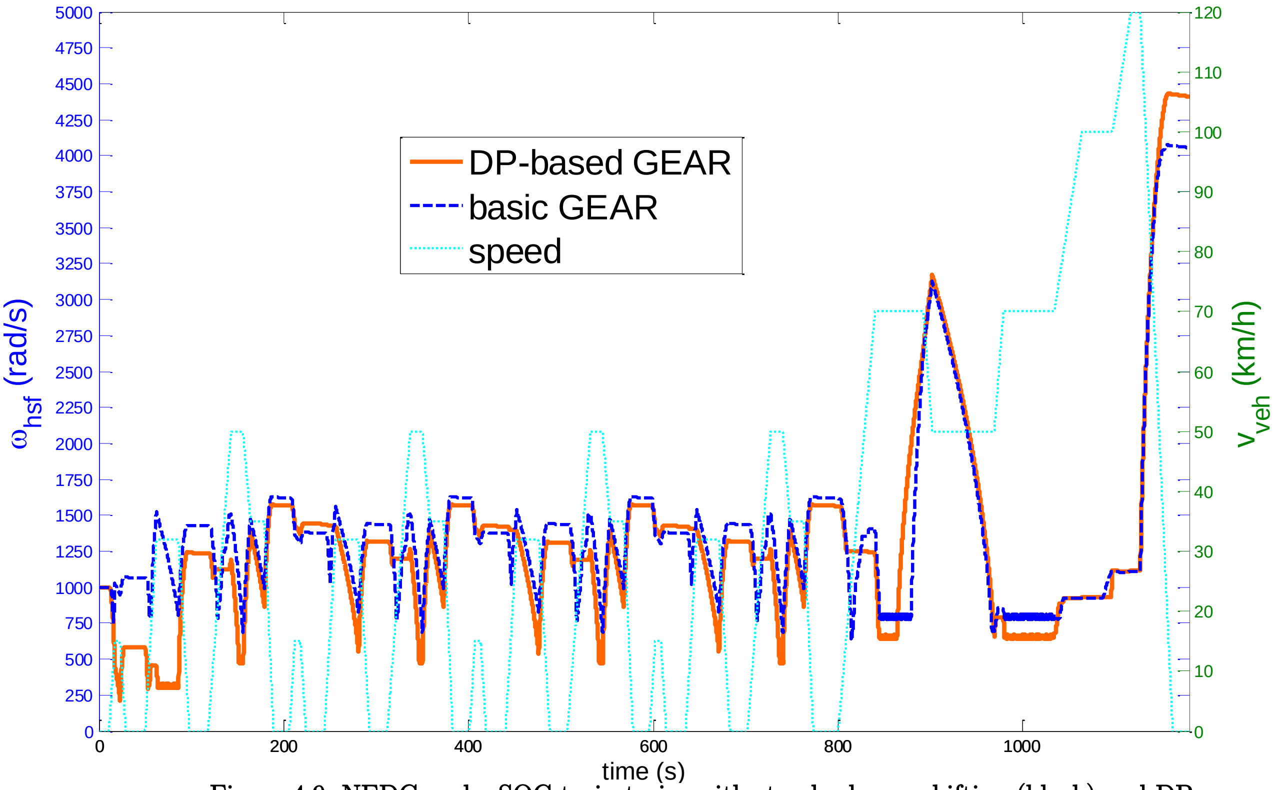

Figure 4.9: NEDC cycle: SOC trajectories with standard gear-shifting (black) and DP gear selection (red).

The numerical values of *cr*FE are quite close to those obtained for the HSF-HV system, except for the simulation where the DP-optimized gear selection is adopted, which underlines the potential advantage of adding this control input in terms of FE.

### 4.3.3 Summary of Results

The main task of the simulation results presented in this Chapter was to benchmark the performance of on-line Energy Management Strategies for hybrid vehicles. Among the various hybrid concepts, two were selected to carry out this analysis, namely HEV and HSF-HV. Discrete Dynamic Programming was selected as a tool to perform such benchmarking activity. It provides an optimal solution of any control problem with a known prescribed mission, such as the homologation cycles under analysis. Throughout this Chapter, a particular focus is given to the development of a DP-oriented modeling approach for hybrid vehicle systems. This can be summarized as the best choice of state and control variables, whose purpose is to correctly describe the system dynamics, without increasing the computational time over acceptable limits. While this can be a very simple task when dealing with a parallel HEV, it reveals to be more complex when applied to the HSF-HV. More in detail, two different approaches, named $DP_1$ and $DP_2$, are described. These two methods differ for the number and the meaning of the adopted state and control variables, the first one being more straightforward but leading to an overall higher dimension of the state-control matrix.

A parametric analysis has been conducted by comparing the sensitivity of FE results to the selection of the DP grid density. Once the $DP_2$ was identified as the best solution to address the problem, a quantitative study has been carried out to compare the DP off-line optimal solution to the ECMS on-line strategy, for three flat standard homologations cycles.

The results are summarized in Figure 4.10, both for the electric and the mechanical hybrid vehicle.

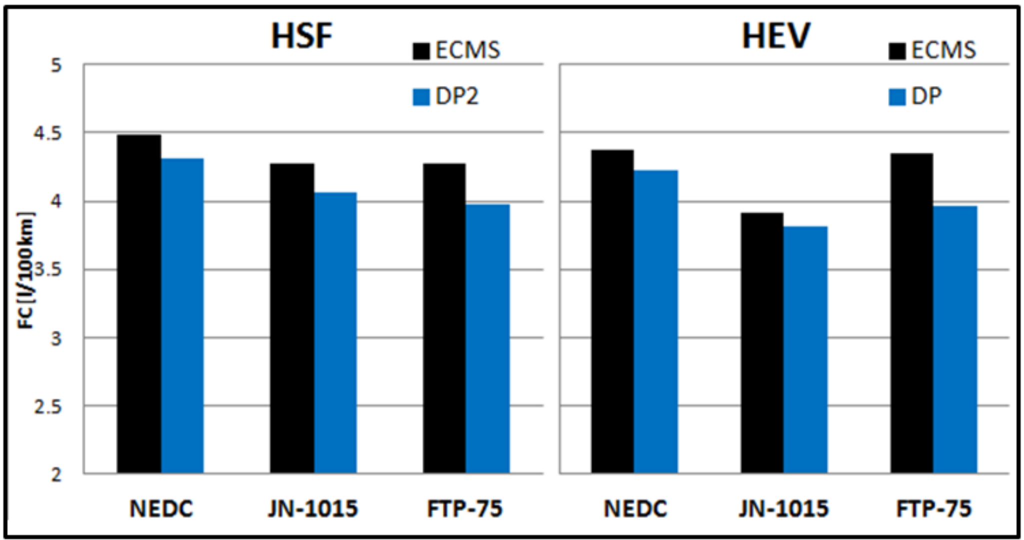

**Figure 4.10: Summary of DP/ECMS FE comparisons for HEV and HSF-HV systems.**

The use of comfort functions modifies the theoretical behavior of the EMS. The equivalence factor (4.53)-(4.54) would lead to a theoretical optimal $u_{ts}^{o}(t)$ which is later modified by additional functions, as previously sketched. This is obtained through the actions listed below:

- $u_{ts}^{o}(t)$ signal is subjected to a low-pass filter, to prevent high-frequency oscillations of the torque split between the electric motor and the thermal engine;
- A time delay is applied to regulate the switching between driving modes characterized by different engine states $x_e$;
- Heuristic gear-shift pattern is adopted.

The results of the latter software devices can be summarized using the following drivability metrics:

- Number of ICE start events;
- Time span between consecutive engine start events.

The first metric is illustrated in Figure 4.11, where the comparison between the ECMS and the DP solutions for a JN-1015 cycle is shown.

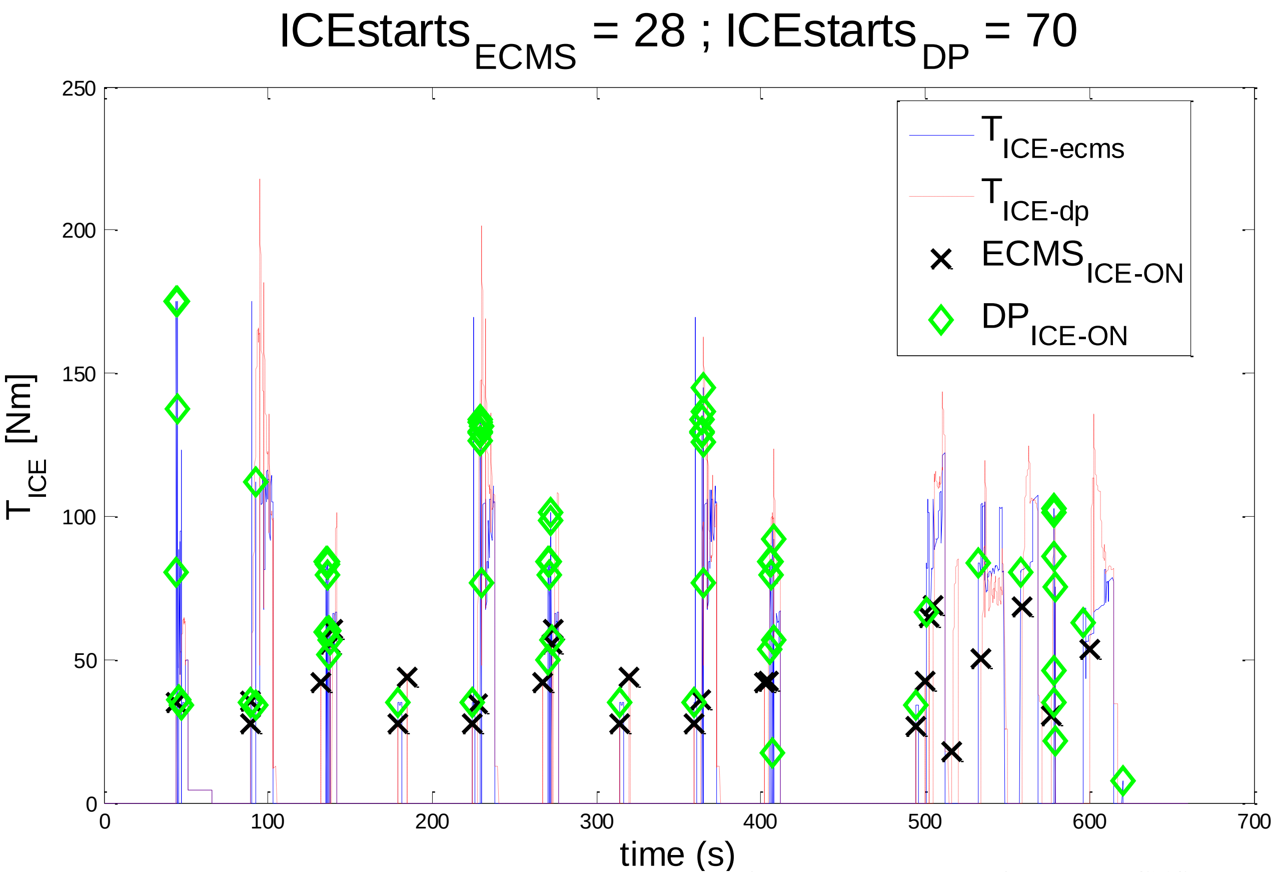

**Figure 4.11: HEV on JN-1015 cycle; number of engine start events of DP and ECMS strategy.**

Figure 4.12 illustrates the average time elapsed between two consecutive ICE starts. In both the examples, the difference is clearly evident. It can be concluded that the FE benchmark provided by a simple deterministic DP algorithm, not taking into account drivability constraints, should always be carefully evaluated to really achieve meaningful and unbiased comparisons with other strategies.

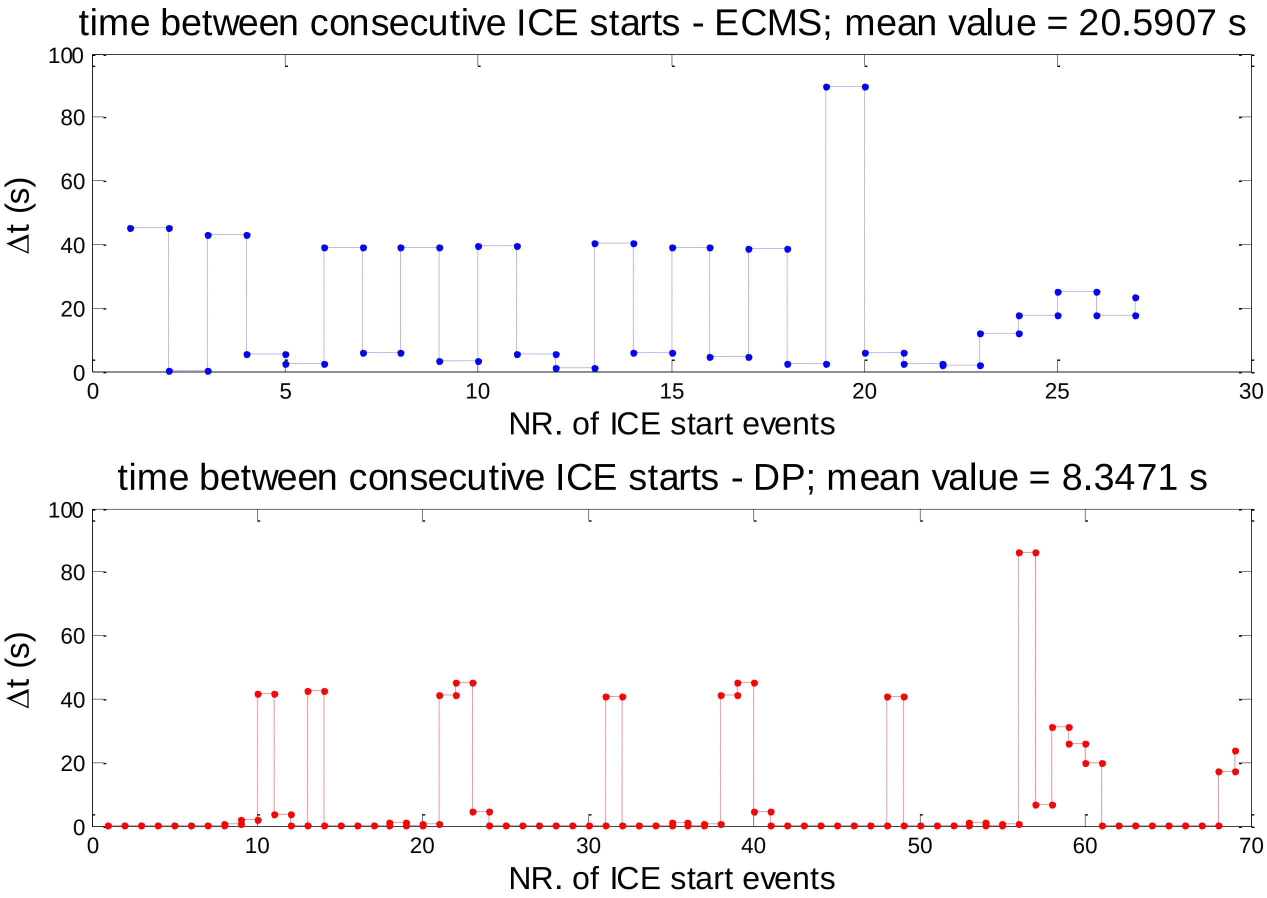

Figure 4.12: HEV on JN-1015 cycle; time spacing between consecutive engine start events of DP and ECMS strategy.

# 5. On-line $NO_x$ Emissions Control of Hybrid Vehicles

This Chapter is devoted to the development of a strategy named real-driving-emissions ECMS (RDE-ECMS). Its purpose is to minimize the FC of a HEV based on a Diesel ICE, while guaranteeing a limitation imposed on $\mathtt{NO}_x$ emissions. Section 5.1 presents an overview of the general problems related to the emissions control of hybrid vehicles. Section 5.2 focuses on HEVs comprising a CI engine, recalling the main techniques developed by previous researches about this topic. The proposed methodology, based on Optimal Control and aiming at the definition of a causal controller, is demonstrated in Section 5.3. The validation of the latter RDE-ECMS controller is given in Section 5.4, by means of experiments conducted on a HiL engine test-bench, where HiL describes a test bench where the ICE is the hardware part, while the EMS and the vehicle are simulated.

## 5.1 Introduction

Light-duty Diesel vehicles are known for their low fuel consumption compared to gasoline vehicles. However, due to legislative restrictions, vehicle manufacturers continuously have to make considerable efforts to reduce the pollutant emissions of Diesel vehicles. Although the legislative limits have been continuously reduced over the last decade, the real driving emissions, which are the emissions during every-day driving, can exceed the legislative limits by far, even for Euro 6 certified light-duty vehicles, as shown in several studies [158, 157, 195, 202, 201]. One reason is that the homologation of the vehicles is performed under well-defined conditions such that the manufacturers optimize the design and operation of the vehicles specifically to meet these legislative requirements. To reduce the discrepancy between the certified and the real-world pollutant emissions, the

European commission is currently discussing measures to limit real driving emissions [202]. One option to cope with such a radical change would be to continuously monitor and control the pollutant emissions by means of an appropriate exhaust after-treatment system.

### 5.1.1 Diesel and Gasoline Hybrid Vehicles

Another option is provided by the electric hybridization of the vehicles, which not only offers a reduction of pollutant emissions, but also a simultaneous reduction of the $\mathtt{CO}_2$ emissions. Since HEVs have an additional degree of freedom for the control of the energy flows in the powertrain, the trade-off between fuel consumption and pollutant emissions can be better controlled.

Otto and Diesel engines strongly differ in terms of emissions. Observing Figure 5.1, which depicts the fuel and emissions minima on a CI speed-load operating range, and Figure 5.2, containing the same information for a fictitious SI engine, these differences emerge.

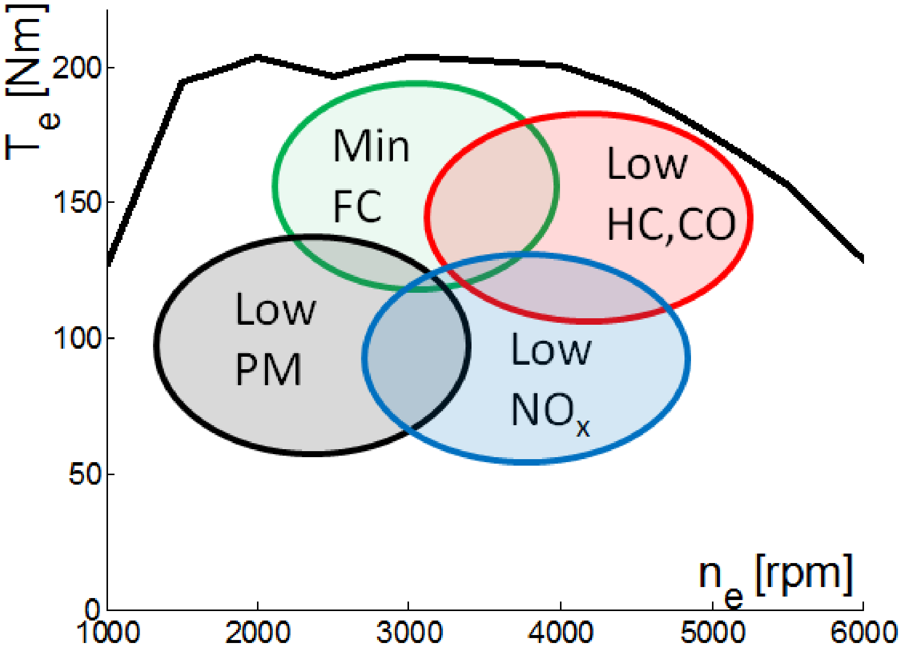

**Figure 5.1: Example of FE and Emissions tradeoff for a CI engine.**

Since Diesel engines are more fuel efficient, the combination of a CI engine with an electric motor obviously leads to the lowest FC. However, higher $\mathtt{NO}_x$ and PM emissions compared to Otto HEVs arise in this case. Furthermore, the Diesel engine concept is basically more expensive than an Otto engine of the same size. As a consequence, if the emissions need to be further reduced by means of expensive after-treatment systems, the overall costs of the hybrid vehicle may increase too much to attract automotive industries to invest on the Diesel HEV solution.

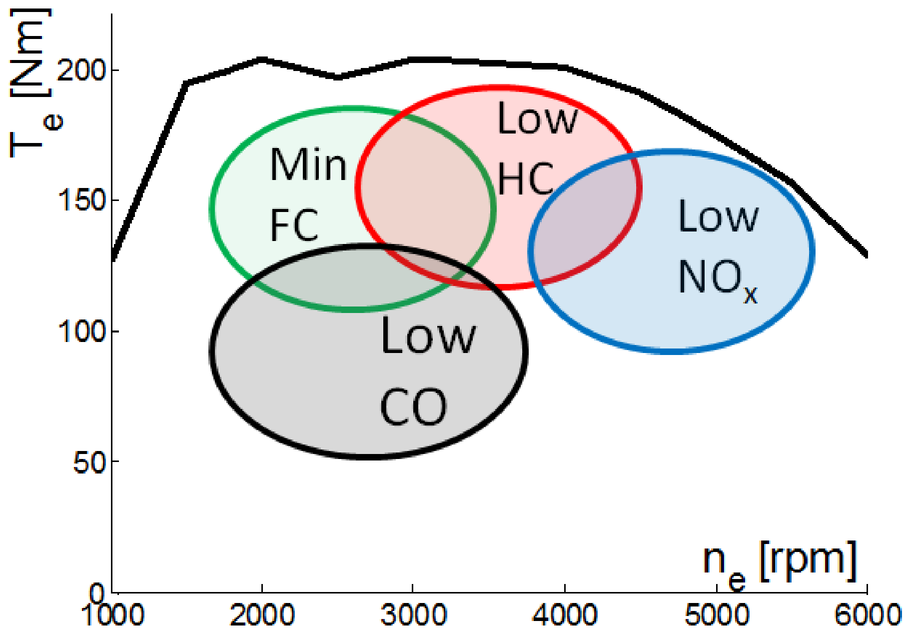

Figure 5.2: Example of FE and emissions tradeoff for a SI engine.

Apart from traditional control levers used in Diesel engines to reduce pollutant emissions, i.e. fuel injection patterns, charging process and EGR, a parallel HEV vehicle with a Diesel engine can further benefit from the additional degree of freedom offered by the presence of the electric motor: the torque split factor. Indeed, this can be used to shift the engine operating point during the driving mission, moving towards more fuel efficient or lower emissions areas of the ICE map. Moreover, it can be used to limit the dynamic operations of the engine, reducing the amount of torque provided by the ICE during transients, which are the events responsible for the highest impact on pollutant emissions.

## 5.2 Diesel-Hybrid Vehicle Emissions Control

Some studies can be found in literature about the control of pollutant emissions for a HEV. The authors of [82] propose a real-time rule-based strategy to optimize both fuel economy and pollutant emissions, taking into account cold-start emissions by minimizing an overall normalized impact function.

Similar approaches have been presented in [128, 160, 124, 4] where an instantaneous optimization algorithm, whose structure is similar to the ECMS, is built with the target of minimizing a weighted sum of multiple factors, e.g. fuel consumption, $NO_x$ emissions, $CO/CO_2$ emissions, while guaranteeing charge-sustaining conditions for various driving cycles. The weighting factors between the various components of the target cost function are constant and considered as tuning parameters.

For a Diesel-HEV equipped with an SCR system, an extended ECMS is proposed in [91], including the minimization of tailpipe emissions, while considering cold start behavior. A control framework formed by three state variables arises from the energy management extended with an emissions management: energy stored in the battery, SCR catalyst temperature and total $NO_x$ tailpipe mass. This results in a controller with an unstable co-state, which can only be used for a fixed time window.

DP has also been applied to address the problem of building a supervisory control system for fuel and emissions reduction, as described in [107, 108] for a pHEV, where the gearshift strategy and the engine start/stop decisions are optimized along with the torque split factor, and in [10] considering the power split as only control input; in both studies constant weighting factors for the multiple emission sources are implemented.

A general approach based on Optimal Control theory is proposed in [170], with a description of several possible extensions of the ECMS basic framework, to include different pollutant components for a HEV, and possibly taking into consideration thermal effects and after-treatment systems. The authors claim that the solution of such general problem is not yet available.

An experimental validation of a method based on a constant weighting factor for $NO_x$ emissions, has been provided in [61] by means of a HiL test-bench.

#### *5.2.1.1 Torque Phlegmatisation*

Some studies focus on the control of transient emissions, especially regarding hybrid powertrains relying on a Diesel ICE. An optimal strategy is provided by the authors of [136] with a DP approach for constant weighting factors related to $NO_x$ and PM emissions. A key idea, when dealing with Diesel-HEV, is to use the Electric Motor for Torque Phlegmatisation during transients, as proposed in [32, 118] adopting heuristic methods, or as reported in [60] using model-based frameworks.

#### *5.2.1.2 Extension of ECMS: map-based methods*

Emissions can be also included in map-based ECMS approaches, as suggested in [171].

#### *5.2.1.3 Decoupling Powertrain and ICE control variables*

The problem of reducing the overall $\mathtt{NO}_x$ emissions for a HEV, while minimizing fuel consumption, can be addressed separating the torque-split control and the engine management control, thus deriving a near-optimal strategy for simultaneously optimally manage the engine calibration and the power split. In the following, the focus is given on the torque split factor, while the effect of the other engine control inputs having an effect on the emissions is not directly taken into account, i.e. the standard, production ECU calibration is considered. Thus, it's understood that the optimal engine management can be decoupled from the optimal supervisory control. The importance of the gearshift strategy to reduce pollutant emissions over a driving cycle is underlined in [9].

#### *5.2.1.4 Adaptation of the $NO_x$ emissions weighting factor*

A control strategy that includes the online adaptation of the weighting factors for the pollutant emission, to take into account real-world driving conditions and possible modification of the emissions level target, has not yet been demonstrated. A possible approach is provided by the authors of [212], for a conventional diesel engine.

Therefore, in the present Chapter, an energy management strategy is presented that allows for the tracking of a specific emission level to respect real driving emission constraints. Under these hypotheses, the strategy is designed to minimize the fuel consumption, while sustaining the battery state of charge.

## 5.3 On-line Control of Real Driving Emissions for Diesel Hybrid Electric Vehicles

In this Section a detailed description of the controller developed to optimize FE of a diesel hybrid vehicle under upper constraints for the cumulative $\mathtt{NO}_x$ emissions is presented. The description of the system is given in the previous Sections 3.2-3.3, while the solution of the control problem by means of Optimal Control theory is found in Section 5.3.1. Then, Section 5.3.2 proposes a derivation of a causal online controller for the desired variables. To implement such controller, the dependency between the co-states must be identified, which is illustrated in Sec. 5.3.2.2. The final structure of the controller is reported in Sec. 5.3.3, and the assignment of corresponding reference signal trajectories is described in Sec. 5.3.3.1.

### 5.3.1 Optimal Control Theory

The hybrid vehicle system can be described by a system of ordinary differential equations of the first order:

$$\dot{x}(t) = f(x(t), u(t)) \tag{5.1}$$

where $x$ is the vector of state variables and $u$ is the control inputs vector. The system dynamics model is based on the description presented in Sections 2.3.1, using a forward modeling technique. The input vector can include the engaged gear command $u_g$, the clutch state $u_c$, the engine state $u_e$, and the torque split factor $u_{ts}$, as previously introduced Chapter 3. The state vector is expressed as:

$$x(t) = \begin{bmatrix} x_b \\ x_{NO_x} \end{bmatrix} = \begin{bmatrix} \xi \\ m_{NO_x} \end{bmatrix} \tag{5.2}$$

where $\xi$ is the battery SOC and $m_{NO_x}$ the cumulated $\mathrm{NO}_x$ emissions. The choice of cumulative emissions value has an advantage compared to the specific emission level, defined in legislations as:

$$\overline{m}_{NO_x} = \frac{m_{NO_x}}{d} \tag{5.3}$$

with $d$ being the total vehicle distance. The derivative of the latter expression would be:

$$\dot{\overline{m}}_{NO_x} = \frac{\dot{m}_{NO_x} \cdot d - m_{NO_x} \cdot v}{d^2} = \frac{1}{d} \cdot (\dot{m}_{NO_x} - \overline{m}_{NO_x} \cdot v) \tag{5.4}$$

with $v$ being the vehicle speed and $\dot{m}_{NO_x}$ being the derivative of the absolute cumulated emissions $m_{NO_x}$. The following equation holds:

$$\dot{m}_{NO_x} = \overset{*}{m}_{NO_x} \tag{5.5}$$

where $\overset{*}{m}_{NO_x}$ is the $\mathrm{NO}_x$ mass flow rate. The following property, that plays a role in the treatise of the next sections, holds:

$$\begin{gathered} \frac{\partial \overline{m}_{NO_x}}{\partial \overline{m}_{NO_x}} = -\frac{v}{d} \neq 0 \\ \frac{\partial \dot{m}_{NO_x}}{\partial m_{NO_x}} = 0 \end{gathered} \tag{5.6}$$

The extended state dynamics equations become:

$$\dot{x}(t) = f(x(t), u(t)) = \begin{bmatrix} f_b(x(t), u(t)) \\ f_{NO_x}(x(t), u(t)) \end{bmatrix} = \begin{bmatrix} \dot{\xi}_b(x, u) \\ \overset{*}{m}_{NO_x}(x, u) \end{bmatrix} \tag{5.7}$$

Accordingly to the general methodology introduced in [57] the problem can be defined as an optimal control problem with partially constrained final states.

$$\min_u \{J(u) = \int_0^T L(x(t), u(t))dt = \int_0^T \overset{*}{m}_{fuel}(x(t), u(t))dt\} \tag{5.8}$$

s.t.

$$x(0) = x_0 \tag{5.9}$$

$$\dot{x}(t) = f\big(x(t), u(t)\big) \quad \text{for all} \quad t \in [0, T] \tag{5.10}$$

$$x(T) \in S \tag{5.11}$$

The closed final-time set $S$ describes the constraints for the final state vectors: $x_{NO_x}$ has an upper constraint, since it has to lie below a certain emission level, while $x_b$ has to satisfy charge-sustaining conditions for the battery.

The optimal solution is found using Pontryagin's minimum principle, defining an Hamiltonian function as follows:

$$H(u) = \overset{*}{m}_{fuel}(x(t), u(t)) + \lambda^T(t) \cdot f(x(t), u(t)) \tag{5.12}$$

The optimal solution must satisfy the following conditions:

$$x(0) = x_0 \tag{5.13}$$

$$\dot{x}^o(t) = \nabla_\lambda H_{|0} = f(x^o(t), u^o(t)) \tag{5.14}$$

and for the co-states the following equation must be valid at any time:

$$\begin{aligned} \dot{\lambda}^o(t) &= -\nabla_x H_{|0} \\ &= -\nabla_x \overset{*}{m}_{fuel}(x^o(t), u^o(\mathrm{t})) - [\frac{\partial f}{\partial x}(x^o(t), u^o(t))]^T \cdot \lambda^o(t) \end{aligned} \tag{5.15}$$

The co-states vector must stay within the normal cone $T^*$ of the target set $S$ at the final time for $x^o(T)$.

$$\lambda^o(T) \in T^*(S, x^o(T)) \tag{5.16}$$

The Hamiltonian of the system must be minimized at all times with respect to all the admissible inputs $u$:

$$H(x^o(t), u^o(t), \lambda^o(t)) \leq H(x(t), u(t), \lambda(t)) \tag{5.17}$$

The dynamics of co-states can be rewritten by separating the battery SOC and the cumulated $\mathrm{NO}_x$ co-states as follows (where dependencies on input and states are omitted for the sake of simplicity):

$$\begin{bmatrix} \dot{\lambda}_\xi^o(t) \\ \dot{\lambda}_{NO_x}^o(t) \end{bmatrix} = \begin{bmatrix} -\nabla_x \overset{*}{m}_{fuel} - \left[\frac{\partial f}{\partial \xi}\right]^T \cdot \lambda^o(t) \\ -\frac{\partial \overset{*}{m}_{fuel}}{\partial m_{NO_x}} - \left[\frac{\partial f}{\partial x_{NO_x}}\right]^T \cdot \lambda^o(t) \end{bmatrix} \tag{5.18}$$

Since neither the system dynamics nor the fuel mass flow directly depend on the cumulated $\mathrm{NO}_x$ emissions, the following expressions hold:

$$\frac{\partial \overset{*}{m}_{fuel}}{\partial x_{NO_x}}(x(t), u(t)) = 0 \tag{5.19}$$

$$\frac{\partial f}{\partial x_{NO_x}}(x(t), u(t)) = 0 \tag{5.20}$$

The latter, combined with (5.18), leads to the following rewritten expression for the co-states dynamics:

$$\begin{bmatrix} \dot{\lambda}_\xi^o(t) \\ \dot{\lambda}_{NO_x}^o(t) \end{bmatrix} = \begin{bmatrix} -\nabla_x \overset{*}{m}_{fuel} - \left[\frac{\partial f}{\partial \xi}\right]^T \cdot \lambda^o(t) \\ 0 \end{bmatrix} \tag{5.21}$$

The importance of the choice of cumulated emissions is here demonstrated, since the term $\frac{\partial f}{\partial x_{NO_x}}$ would not have vanished, with the choice of specific $\mathrm{NO}_x$ emissions (5.3) as a state variable.

Considering (5.21) and that $\lambda_{NO_x}^o(T) \geq 0$, we have that:

$$\lambda_{NO_x}^o = const. = \lambda_{NO_x} \geq 0 \tag{5.22}$$

The Hamiltonian (5.17) can be now rewritten, having defined $\lambda_{NO_x}$:

$$\begin{aligned} H(\cdot) &= \overset{*}{m}_{fuel}(u) + \lambda^T(t) \cdot f(\xi, u) \\ &= \overset{*}{m}_{fuel}(u) + \lambda_{NO_x} \cdot f(\xi, u) + \lambda_\xi \cdot f(\xi, u) \\ &= \overset{*}{m}_{fuel}(u) + \lambda_{NO_x} \cdot \overset{*}{m}_{NO_x}(u) + \lambda_\xi \cdot f(\xi, u) := \widetilde{H}(\cdot) \end{aligned} \tag{5.23}$$

The latter new expression for the Hamiltonian (5.23) leads to a new Hamiltonian $\widetilde{H}$ for the system aimed at the minimization of a weighted sum of fuel and emissions. This allows for a new problem definition:

$$\begin{aligned}\min_{u}\{\tilde{J}(u) &= \int_0^T L(\xi,u)dt \\ &= \int_0^T (\overset{*}{m}_{fuel}(\xi,u) + \lambda_{NO_x} \cdot \overset{*}{m}_{NO_x}(\xi,u))dt\}\end{aligned} \tag{5.24}$$

s.t

$$\xi(0) = \xi_0 \tag{5.25}$$

$$\dot{\xi}(t) = f_{\xi}\big(\xi(t), u(t)\big) \quad \text{for all} \quad t \in [0,T] \tag{5.26}$$

$$\xi(T) = \xi_f (= \xi_0) \tag{5.27}$$

For the reformulated optimization problem $\lambda_{NO_x}$ is not a co-state but a weighting factor, and therefore a given parameter. It quantifies the fuel equivalent of a given amount of $\mathrm{NO}_x$ emissions in a new Lagrangian reformulation. For this reason, the authors of [212] have introduced a definition for the equivalent problem (5.24)-(5.27): Equivalent Emissions Minimization Strategy (EEMS). The equivalence of the minimization problem (5.24)-(5.27) to the previous formulation (5.8)-(5.11) is guaranteed, since the eliminated state does not appear in any of the other equations and it was introduced only to enforce the limit on cumulated emissions, by means of a final-state constraint. As a consequence, if the constant equivalence factor is known, the same optimal results will be achieved for the redefined problem. As a matter of fact, such value is not known a priori. For this reason, a causal controller based on the online calculation of the equivalence factor is proposed in the following section.

### 5.3.2 Derivation of the RDE-ECMS strategy: a causal controller

The objective of this section is to develop a feedback controller for the online control of cumulative $\mathrm{NO}_x$ emissions. Before the derivation of the proposed causal control framework, the cost function (5.24) can be conveniently rearranged by introducing the normalized $\mathrm{NO}_x$ mass flow rate $\widetilde{\overset{*}{m}}_{NO_x}$:

$$\tilde{\overset{*}{m}}_{NO_x} = \overset{*}{m}_{NO_x} \cdot \frac{\overset{*}{m}_{NO_{x,MAX}}}{\overset{*}{m}_{fuel_{MAX}}} \tag{5.28}$$

$$\bar{J}(u) = \int_0^T \bar{L}(\xi,u)dt = \int_0^T (\overset{*}{m}_{fuel}(\xi,u) + \lambda_{NO_x} \cdot \tilde{\overset{*}{m}}_{NO_x}(\xi,u))dt \tag{5.29}$$

where the normalization takes place using the maximum flow rates of fuel and $NO_x$ for the given ICE. By means of the rewritten cost functional (5.29), the argument of the objective function and of the corresponding Hamiltonian, are now expressed by homogenous measuring units.

#### 5.3.2.1 Equivalent cost function definition

To achieve the goal of generating a charge and emissions sustaining strategy, two terms can be added to the expression (5.29), penalizing deviations from the reference values for state-of-charge $\xi_{ref}$, and from the normalized cumulated emission $\tilde{m}_{NO_x}$. Thus a new formulation for the cost functional can be obtained:

$$\begin{gathered}\hat{J}(u) = \int_0^T \hat{L}(x,u)dt \\ = \int_0^T \left(\overset{*}{m}_{fuel}(u) + \mu \cdot \left(\frac{\tilde{m}_{NO_x,ref}(t) - \tilde{m}_{NO_x}(t)}{\Delta\tilde{m}_{NO_x,norm}}\right)^{2q} + \beta \cdot \left(\frac{\xi_{ref}(t) - \xi(t)}{\Delta\xi_{norm}}\right)^{2p}\right) dt\end{gathered} \tag{5.30}$$

leading to the extended Hamiltonian:

$$\begin{gathered}\hat{H}(u) = \overset{*}{m}_{fuel}(u) + \mu \cdot \left(\frac{\tilde{m}_{NO_x,ref}(t) - \tilde{m}_{NO_x}(t)}{\Delta\tilde{m}_{NO_x,norm}}\right)^{2q} + \\ +\beta \cdot \left(\frac{\xi_{ref}(t) - \xi(t)}{\Delta\xi_{norm}}\right)^{2p} + \lambda^T \cdot f(x,u)\end{gathered} \tag{5.31}$$

which must be minimized by the optimal input sequence:

$$u^o = argmin(\hat{H}(u)) \tag{5.32}$$

Since the additional terms of the extended Hamiltonian do not depend explicitly on the control input, they will be minimized by the same optimal policy $u^o$. The Hamilton-Jacobi-Bellman equations provide the following expression [22] for the optimal co-states vector $\lambda^o$:

$$\lambda^o(x,t) = \frac{\partial \hat{C}^o(x,t)}{\partial x} \tag{5.33}$$

with $\hat{C}^o(x,t)$ being the optimal cost-to-go function, associated with the optimal cost function $\hat{L}(x,u)$, at the time instant $t$ of the total horizon of duration $T$:

$$\hat{C}^o(x,t) = \min_u \left\{ \int_t^T \hat{L}(x(\tau),u(\tau))d\tau \quad |x(t) = x \right\} \tag{5.34}$$

The latter optimal cost-to-go function can be substituted with a sub-optimal function formed by the sum of different independent cost indexes, as follows:

$$\begin{gathered} \hat{C}(x) = \hat{C}\left(\xi, \widetilde{m}_{NO_x}\right) = \\ = \hat{C}_{f_1,\xi}(\xi, \widetilde{m}_{NO_x}) + \hat{C}_{f_1,NO_x}(\widetilde{m}_{NO_x}) + \widetilde{\mathrm{C}}_{f_2} + \tilde{C}_\xi(\xi) + \tilde{C}_{\widetilde{m}_{NO_x}}(\widetilde{m}_{NO_x}) \end{gathered} \tag{5.35}$$

where the five terms correspond to:

- $\hat{C}_{f_1,\xi}(\xi, \widetilde{m}_{NO_x})$: the additional fuel consumption caused by compensating the current state-of-charge deviation;
- $\hat{C}_{f_1,NO_x}(\widetilde{m}_{NO_x})$: the additional fuel consumption caused by bringing the cumulated $\mathrm{NO}_x$ close to the reference level;
- $\tilde{C}_{f_2}$: a fuel consumption that is supposed to be independent from both the state-of-charge and the emissions level, needed to cover the rest of the driving mission with the correct reference values;
- $\tilde{C}_\xi(\xi)$: a term denoting the penalty of SOC deviations from the reference value;
- $\tilde{C}_{\widetilde{m}_{NO_x}}(\widetilde{m}_{NO_x})$: a term that denotes the penalty of $\widetilde{m}_{NO_x}$ deviations from the reference value.

Cost of saving NOx emissions

An expression for the additional fuel cost of saving $\mathrm{NO}_x$ emissions can be found under the hypothesis that the other state $\xi$ has a much smaller time constant than the time horizon considered to bring the cumulated emissions close to the reference value (e.g. minutes).

If this holds, and the parameter $K_{FCN}$ identifies the relationship between fuel consumption and $\mathrm{NO}_x$ emissions for the given ICE, the associated cost-to-go can be expressed as follows:

$$\begin{aligned}\hat{C}_{f_1,NO_x}\left(\widetilde{m}_{NO_x}\right) &= \Delta m_{fuel} = \\ &= K_{FCN}\cdot\Delta\widetilde{m}_{NO_x} = K_{FCN}\cdot\left(\widetilde{m}_{NO_x}-\widetilde{m}_{NO_x,ref}\right)\end{aligned} \tag{5.36}$$

Cost of emissions deviation penalty

Under the hypothesis that the $\mathrm{NO}_x$ controller is able to diminish the error between the actual and the reference target value linearly with time, the cost of the emissions penalty in the future can be estimated. Firstly, the evolution of the error decreasing after the time $T_h$ is introduced:

$$\begin{aligned}&\widetilde{m}_{NO_x,ref-fut}(\tau)-\widetilde{m}_{NO_x-fut}(\tau) = \\ &= \left(\widetilde{m}_{NO_x,ref}(t)-\widetilde{m}_{NO_x}(t)\right)\cdot\left(1-\frac{\tau}{T_h}\right)\end{aligned} \tag{5.37}$$

Now, the total penalty is obtained by integrating on the future trajectory of the controlled variable, as follows:

$$\begin{aligned}\tilde{C}_{\widetilde{m}_{NO_x}}\left(\widetilde{m}_{NO_x}\right) &= \int_0^{T_h}\mu\cdot\left(\frac{\widetilde{m}_{NO_x,ref-fut}(\tau)-\widetilde{m}_{NO_x-fut}(\tau)}{\Delta\widetilde{m}_{NO_x,norm}}\right)^{2q}d\tau \\ &= \frac{\mu\cdot T_h}{2q+1}\cdot\left(\frac{\widetilde{m}_{NO_x,ref}(t)-\widetilde{m}_{NO_x}(t)}{\Delta\widetilde{m}_{NO_x,norm}}\right)^{2q}\end{aligned} \tag{5.38}$$

**Cost of sustaining the battery SOC**

Following the methodology described in [6], the fuel energy used to compensate the state-of-charge deviations from the target value can be approximated, by first estimating the energy stored in the battery at a certain $\xi(t)$, with respect to the reference $\xi_{ref}(t)$, as:

$$E_{BT,\Delta\xi} = Q_0 \int_{\xi(t)}^{\xi_{ref}(t)} V_{oc}(\tilde{\xi}) d\tilde{\xi} \tag{5.39}$$

Since, in the future, this energy must be compensated using the thermal path, a certain amount of fuel will be saved/consumed to discharge/charge the battery. Such quantity will clearly depend on the engine efficiency and on the electric path efficiency used in the future, which in turn depends on the ICE operating points. Moreover, the used ICE operating points will also depend on the cumulated $\mathtt{NO}_x$ emissions, since a second controller acts in parallel, modifying the choice of the control inputs to tackle the desired emissions level. As a consequence, the average future charging/discharging overall efficiency $\eta_c$, is a function of $\widetilde{m}_{NO_x}$:

$$\begin{aligned} \hat{C}_{f_1,\xi}\left(\xi, \widetilde{m}_{NO_x}\right) &\approx \frac{E_{BT,\Delta\xi}}{\eta_c\left(\widetilde{m}_{NO_x}\right) \cdot H_l} \\ &= \frac{Q_0}{\eta_c\left(\widetilde{m}_{NO_x}\right) \cdot H_l} \cdot \int_{\xi(t)}^{\xi_{ref}(t)} V_{oc}(\tilde{\xi}) d\tilde{\xi} \end{aligned} \tag{5.40}$$

where $H_l$ denotes the fuel lower heating value.

**Cost of the SOC deviation penalty**

Similarly to the previous treatise regarding the emissions deviation, the SOC deviation penalty can be expressed by an equation equivalent to (5.37), where the time constant $T_k$ is introduced. This leads to the following integral for the calculation of the total penalty:

$$\begin{aligned}\tilde{C}_{\xi}(\xi) = \int_{0}^{T_k} \beta \cdot \left(\frac{\xi_{ref-fut}(\tau) - \xi_{fut}(\tau)}{\Delta\xi_{norm}}\right)^{2p} \\ = \frac{\beta \cdot T_k}{2p+1} \cdot \left(\frac{\xi_{ref}(t) - \xi(t)}{\Delta\xi_{norm}}\right)^{2p}\end{aligned} \tag{5.41}$$

**Total cost and equivalence factors**

The total suboptimal cost-to-go (5.35) can now be expressed, using (5.36)-(5.41):

$$\begin{aligned}&\hat{C}(x) = \hat{C}\left(\xi, \widetilde{m}_{NO_x}\right) = \\ &= \frac{Q_0}{\eta_c\left(\widetilde{m}_{NO_x}\right) \cdot H_l} \cdot \int_{\xi(t)}^{\xi_{ref}(t)} V_{oc}\left(\tilde{\xi}\right) d\tilde{\xi} + \\ &+ K_{FCN} \cdot \left(\widetilde{m}_{NO_x}(t) - \widetilde{m}_{NO_x,ref}(t)\right) + \\ &+ \tilde{C}_{f_2} + \frac{\beta \cdot T_k}{2p+1} \cdot \left(\frac{\xi_{ref}(t) - \xi(t)}{\Delta\xi_{norm}}\right)^{2p} + \\ &+ \frac{\mu \cdot T_h}{2q+1} \cdot \left(\frac{\widetilde{m}_{NO_x,ref}(t) - \widetilde{m}_{NO_x}(t)}{\Delta\widetilde{m}_{NO_x,norm}}\right)^{2q}\end{aligned} \tag{5.42}$$

and the suboptimal co-states can be now calculated:

$$\lambda(x) = \begin{bmatrix} \lambda_{\xi}(x) \\ \lambda_{NO_x}(x) \end{bmatrix} = \frac{\partial \hat{C}(x)}{\partial x} = \begin{bmatrix} \dfrac{\partial}{\partial \xi} \hat{C}(x) \\ \dfrac{\partial}{\partial \widetilde{m}_{NO_x}} \hat{C}(x) \end{bmatrix} \tag{5.43}$$

The partial derivatives of (5.42) generate the following expressions for the two co-states (5.43):

$$\lambda_{\xi}(x) = \frac{\partial \hat{C}(x)}{\partial \xi} = -\frac{Q_0 \cdot V_{oc}(\xi)}{\eta_c(\widetilde{m}_{NO_x}) \cdot H_l} - \tilde{\beta} \cdot (\xi_{ref}(t) - \xi(t))^{2p-1} \tag{5.44}$$

$$\lambda_{NO_x}(x) = \frac{\partial \hat{C}(x)}{\partial \widetilde{m}_{NO_x}} = K_{FCN} + \tag{5.45}$$

$$+\frac{Q_0}{H_l} \cdot \int_{\xi(t)}^{\xi_{ref}(t)} V_{oc}(\tilde{\xi}) d\tilde{\xi} \cdot \frac{\partial}{\partial \widetilde{m}_{NO_x}} \left( \frac{1}{\eta_c(\widetilde{m}_{NO_x})} \right) +$$
$$+\tilde{\mu} \cdot (\widetilde{m}_{NO_x,ref}(t) - \widetilde{m}_{NO_x}(t))^{2q-1}$$

where the following substitutions are adopted:

$$\tilde{\mu} = \frac{-2q\mu T_k}{(2q+1) \cdot \Delta\widetilde{m}_{NO_x,norm}^{2q}} \tag{5.46}$$

$$\tilde{\beta} = \frac{2p\beta T_h}{(2p+1) \cdot \Delta\xi_{norm}^{2p}} \tag{5.47}$$

By analyzing (5.44)-(5.45), the mutual relationship between the co-states is evident.

More in details, the first two terms of (5.45) are formed by a theoretically constant term $K_{FCN}$, which instead depends on the operating points occurring in the period considered, and by another term, that we suppose to be negligible, under the hypothesis that the dynamics of the average charging/discharging efficiency does not directly depend on the cumulated emissions. The simplified approach followed in this section is to replace the constant equivalent term with the sum of $\lambda_{NO_x,0}$ and of an integrator used to adapt it online, during the operation, to track the average emissions.

$$\begin{aligned} \lambda_{NO_x}(\widetilde{m}_{NO_x}) = \lambda_{NO_x,0} + \tilde{\mu} \cdot (\widetilde{m}_{NO_x,ref}(t) - \widetilde{m}_{NO_x}(t))^{2q-1} \\ + \int_0^t \frac{\widetilde{m}_{NO_x,ref}(\tau) - \widetilde{m}_{NO_x}(\tau)}{T_{i,NO_x}} d\tau \end{aligned} \tag{5.48}$$

The previous equation represents a PI controller for the cumulative emissions level, which in the online applications will be measured by means of a dedicated sensor. The term $\lambda_{NO_x}$ can be directly implemented in the cost functional (5.29), which solves the equivalent problem (5.24)-(5.27), and its corresponding Hamiltonian is expressed by:

$$\overline{H}(x,u,\lambda) = \left[\overset{*}{m}_{fuel}(u) + \lambda_{NO_x}(\widetilde{m}_{NO_x}) \cdot \overset{\widetilde{*}}{m}_{NO_x}(u) + \lambda_\xi(\xi, \widetilde{m}_{NO_x}) \cdot \dot{\xi}(\xi, u)\right] \tag{5.49}$$

The latter can be rearranged to be expressed in terms of powers, by multiplying the whole Hamiltonian with the fuel lower heating value $H_l$:

$$\begin{aligned}\underline{H}(x,u,\lambda) &= \left[P_{fuel}(u) + \lambda_{NO_x}(\widetilde{m}_{NO_x}) \cdot \tilde{P}_{NO_x}(u) - H_l \cdot \lambda_\xi(\xi,\widetilde{m}_{NO_x}) \cdot \tfrac{I_b(\xi,u)}{Q_0}\right] \\ &= \left[P_{fuel}(u) + \lambda_{NO_x}(\widetilde{m}_{NO_x}) \cdot \tilde{P}_{NO_x}(u) + s^*(\xi,\widetilde{m}_{NO_x}) \cdot P_b(\xi,u)\right]\end{aligned} \tag{5.50}$$

where $P_b$ represents the inner electrochemical battery power and:

$$s^*(\xi,\widetilde{m}_{NO_x}) = -\frac{\lambda_\xi(\xi,\widetilde{m}_{NO_x}) \cdot H_l}{V_{oc}(\xi) \cdot Q_0} \tag{5.51}$$

The combination of (5.51) and (5.44) leads to a reformulated expression for the electrical energy equivalence factor $s^*$:

$$\begin{aligned}s^*(\xi,\widetilde{m}_{NO_x}) &= \frac{1}{\eta_c(\widetilde{m}_{NO_x})} + \frac{H_l}{V_{oc}(\xi) \cdot Q_0} \cdot \tilde{\beta}_* \cdot (\xi_{ref}(t) - \xi(t))^{2p-1} \\ &= s_0^*(\widetilde{m}_{NO_x},\xi) + \tilde{\beta}^* \cdot (\xi_{ref}(t) - \xi(t))^{2p-1}\end{aligned} \tag{5.52}$$

Since the average conversion efficiency $\eta_c$ will vary depending on the operating points of the components involved (ICE, electric motor, battery), and the operating points will vary as a function of the driving cycle and of the $\mathrm{NO}_x$ feedback controller already introduced, $s_0^*$ is adjusted during operation. A first adjustment depends directly on the actual normalized cumulative emission mass $\widetilde{m}_{NO_x}$, due to the action of the dedicated controller that online adapts $\lambda_{NO_x}$, and will be clarified in the next section. The second adaptation is achieved using an integrator, with integration time period $T_{i,\xi}$, as follows:

$$\begin{aligned}s^*(\xi,\widetilde{m}_{NO_x}) &= s_0^*\left(\lambda_{NO_x}(\widetilde{m}_{NO_x})\right) + \tilde{\beta}^* \cdot (\xi_{ref}(t) - \xi(t))^{2p-1} \\ &\quad + \int_0^t \frac{\xi_{ref}(\tau) - \xi(\tau)}{T_{i,\xi}} d\tau\end{aligned} \tag{5.53}$$

Equations (5.48) and (5.53) represent the structure of the desired online causal emission and charge-sustaining controller. It is formed by two feedback PI controllers, linked together by a relationship between the constant values of the co-states $s_0^*(\lambda_{NO_x}(\widetilde{m}_{NO_x}))$. The final structure of the controller is depicted in Section 5.3.3.

#### 5.3.2.2 *Identification of the relationship between co-states*

The goal of this section is to describe the methodology applied to identify the desired dependency $s_0^*\left(\lambda_{NO_x}(\tilde{m}_{NO_x})\right)$.

The key idea is to apply an optimal control method to the optimization problem described by the Hamiltonian function (5.50), i.e. DP or Pontryagin's minimum principle, with constant values of the weighting factors $\lambda_{NO_x}$ and $s_0^*$. In this case PMP is adopted, since it is more suitable for the present application of forward-facing vehicle model including more input variables.

This procedure is applied for several different values of $\lambda_{NO_x}$, in order to identify, for each value, the corresponding unique constant equivalence factor $s_0^*$ that ensures charge sustaining conditions.

The methodology is repeated for various driving scenarios, in this case four standard homologation cycles (NEDC, FTP-75, WLTP, LA92).

The Hamiltonian can be also reformulated by dividing it by $(\lambda_{NO_x} + 1)$:

$$\begin{aligned}\bar{\bar{H}}(x,u,\lambda) &= \frac{1}{(\lambda_{NO_x}+1)} \cdot \left[P_{fuel}(u) + \lambda_{NO_x} \cdot \tilde{P}_{NO_x}(u) + s_0^*(\lambda_{NO_x}) \cdot P_b(\xi,u)\right] \\ &= \left[\frac{1}{\lambda_{NO_x}+1} \cdot P_{fuel}(u) + \frac{\lambda_{NO_x}}{\lambda_{NO_x}+1} \cdot \tilde{P}_{NO_x}(u) + \frac{s_0^*(\lambda_{NO_x})}{\lambda_{NO_x}+1} \cdot P_b(\xi,u)\right] \\ &= \left[\alpha_{NO_x} \cdot P_{fuel}(u) + (1-\alpha_{NO_x}) \cdot \tilde{P}_{NO_x}(u) + s_0(\alpha_{NO_x}) \cdot P_b(\xi,u)\right]\end{aligned} \tag{5.54}$$

The introduction of the reformulated weighting factor $\alpha_{NO_x}$ for the $\mathrm{NO}_x$ emissions leads to the following possible cases:

$$\alpha_{NO_x}(t) = \begin{cases} 0 & \mathrm{NO_x optimal} \\ 0 < \alpha_{NO_x}(t) < 1 & \mathrm{NO_x - fueltradeoff} \\ 1 & \mathrm{fueloptimal.} \end{cases} \tag{5.55}$$

The results of the identification procedure are depicted in Figure 5.3.

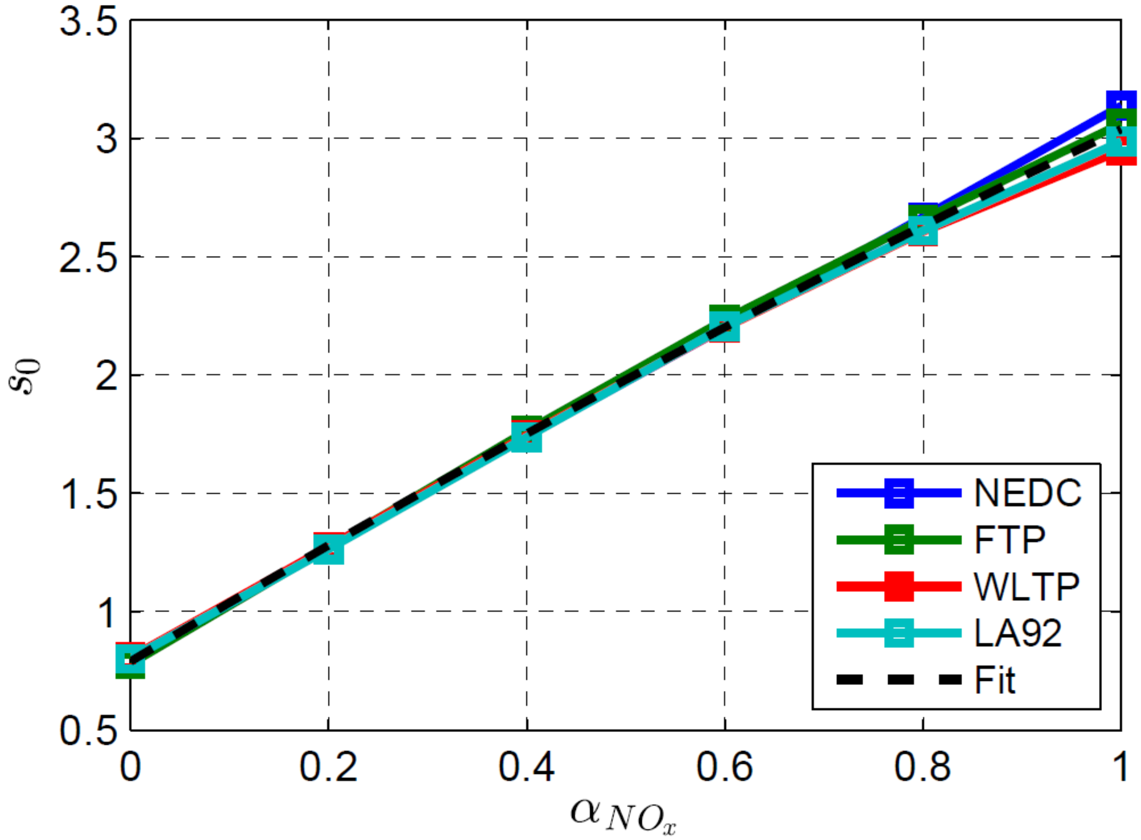

Figure 5.3: Relationship between the equivalence factors.

A quadratic interpolating function is chosen to generate a unique relationship between the emissions weighting factor and the equivalence factor, to be used for all driving scenarios.

### 5.3.3 SOC and SNOx controller structure

Based on the mathematical derivation of the controller presented in the previous sections, the desired controller, to be tested in the simulations and in the experimental tests in the following sections, is illustrated in Figure 5.4.

Since the controller is able to control the real driving $NO_x$ emissions, and since it is based on the equivalent consumption minimization strategy, the controller is referred to as the RDE-ECMS.

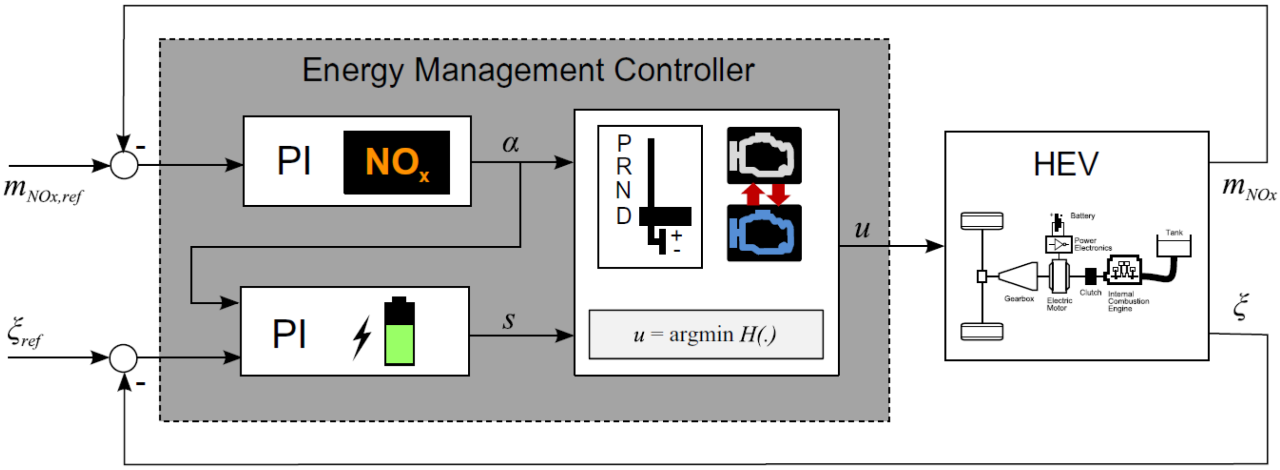

**Figure 5.4: Structure of the charge and emissions sustaining causal controller.**

The proportional gains of the PI controllers then become:

$$
\begin{aligned}
k_{P,\xi} &= \frac{\tilde{\beta}^*}{\lambda_{NO_x} + 1} \\
k_{P,NO_x} &= \frac{\tilde{\mu}}{\lambda_{NO_x} + 1}
\end{aligned}
\tag{5.56}
$$

Since both the PI controller outputs can be saturated, the controllers are extended with an anti-windup scheme [106, 7].

To prevent excessively frequent engine starts and stops that can arise due to the application of optimal control based methods, a penalty $P_{ss,eq}$ for the change of the engine on/off state, similarly to the previous formulation (4.7)-(4.8), is here introduced as follows:

$$
\begin{aligned}
\overset{ss}{\tilde{H}}(x,u,\lambda) \coloneqq \alpha_{NO_x} \cdot P_{fuel}(u) + \left(1 - \alpha_{NO_x}\right) \cdot \tilde{P}_{NO_x}(u) + \\
+ s_0\left(\alpha_{NO_x}\right) \cdot P_b(\xi,u) + P_{ss,eq}(x,u)
\end{aligned}
\tag{5.57}
$$

Therefore, an additional heuristic engine on/off comfort function is implemented, similarly to the one presented in [109]. In this comfort function, the desired engine on/off change request signal from the extended ECMS is *not* realized instantaneously. Instead, it has to remain in the same state, either on or off, for at least 1 s until it is transferred to the next level of a series of checks. At the next level, an engine on/off change request is only realized if the previously requested engine on/off state has remained for at least 5 s in its state. As a consequence, the engine is either on or off for at least 5 s. This hysteresis can only be overruled if the throttle is fully depressed.

Due to these measures, the average number of engine start/stops, in the four considered driving cycles, is reduced to a reasonable amount of 2.1 starts per minute compared to 4.6 starts per minute, obtained without any measure to prevent frequent starts/stops. The relative loss in FE due to the comfort function is in average 3.8%, compared to the theoretical value for the FC obtained without any comfort function. The minimum engine on/off dwell time amounts to 5 s, in almost any case for the four driving scenarios considered.

#### *5.3.3.1 Calculation of SOC and cumulative $NO_x$ reference signals*

The two PI controllers of Figure 5.4 require a proper definition of the reference trajectories for the respective controlled variables. The $\xi_{ref}(t)$ could simply be a constant value representing the desired final state-of-charge, which also coincides with the initial value $\xi_0$, to enforce a charge-sustaining constraint. Alternatively, the reference value can take into account that the current amount of vehicle kinetic and potential energies can be recuperated in the future and stored into electrical energy. The latter definition, as previously defined (4.58), is adopted here.

The reference cumulative emissions can be computed in a simple fashion, if one knows the desired specific emission level $\overline{m}_{NO_x}$ (5.3), i.e. expressed in [mg/km], imposed by the legislation or by a custom control strategy.

$$m_{NO_x,ref}(t) = \int_0^t \overline{m}_{NO_x} \cdot v(\tau) d\tau \tag{5.58}$$

### 5.3.4 On-line control vs. constant-weight control

Here, a case study is presented in which the benefit of using the RDE-ECMS is compared to an ECMS with a constant emission-related equivalence factor $\alpha_{NO_x}$. To show that the RDE-ECMS yields a lower FC than a non-adaptive ECMS, these two strategies are compared on four different sequences of repeated driving cycles, namely the NEDC, the FTP-79, the WLTP, and the LA92.

#### 5.3.4.1 *$NO_x$-FC Trade-off*

Figure 5.5 shows the trade-off between the fuel consumption and the $\mathrm{NO}_x$ emissions, obtained using charge sustaining $s_0$ values, for each $\alpha_{NO_x} \in \{0, 0.25, 0.5, 0.75, 1\}$ value. For each driving cycle, the corresponding curve represents the *optimal trade-off* for the approach presented using (5.57). Any causal method based on (5.57) cannot yield results which are to the left or below the corresponding trade-off for the given driving cycle.

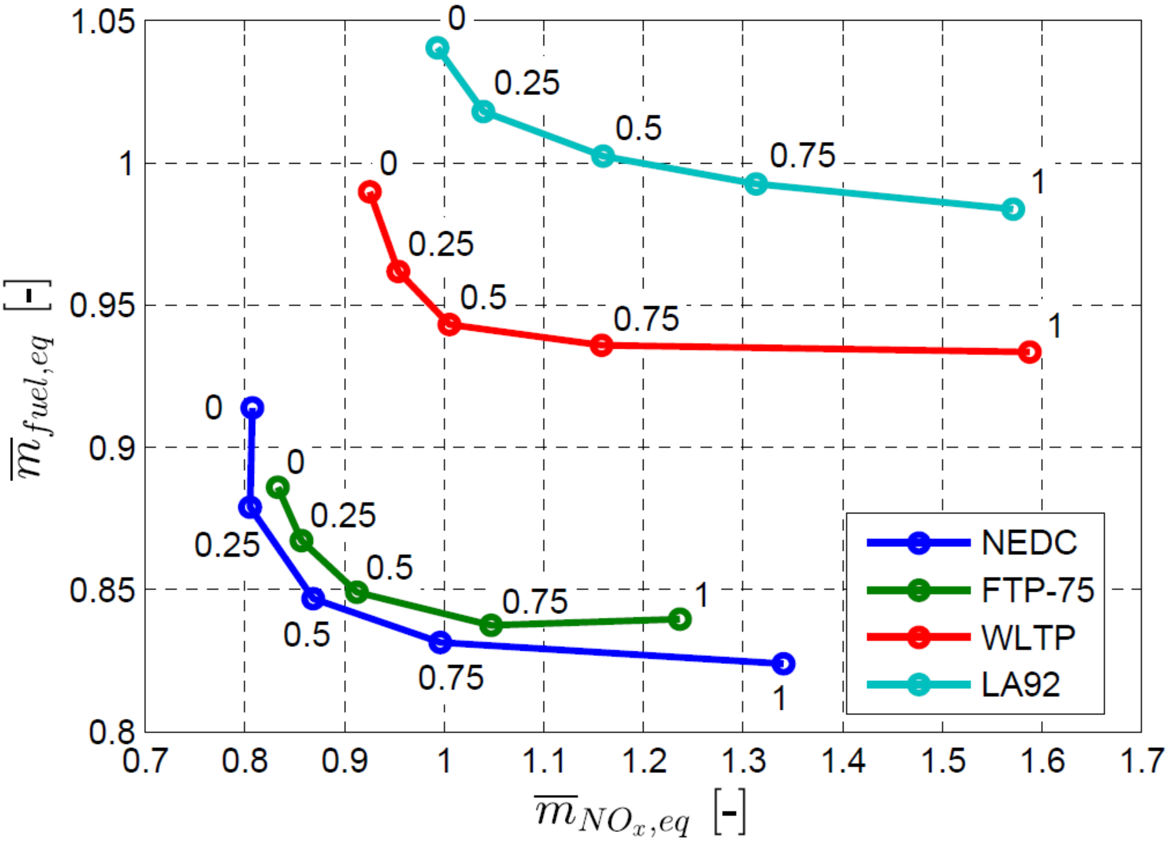

**Figure 5.5: Tradeoff between normalized fuel consumption and $NO_x$ emissions as a function of the $NO_x$ weighting factor for the four driving cycles.**

It can be noted that the LA92 cycle is the most demanding, both for FC and $\mathrm{NO}_x$ emissions. As a consequence, it is taken as the reference driving cycle to compare the performances of RDE-ECMS in the following treatise.

#### 5.3.4.2 *Simulation Results*

Assuming that the real driving $\mathrm{NO}_x$ emissions have to be lower than a specific value, say 1.0 or 100% in this case. Two causal strategies are considered, which respect this $\mathrm{NO}_x$ limit:

1. A non-adaptive PI-controlled ECMS, which is the RDE-ECMS but with a *fixed* value for $\alpha_{NO_x}$;
2. The RDE-ECMS presented in Section 5.3.2.

The non-adaptive ECMS is previously tuned, to respect the $\mathrm{NO}_x$ emission limit on the worst-case driving cycle, which here is the LA92, while giving the lowest possible fuel consumption on all driving cycles.

The optimized parameters of the non-adaptive PI-controlled ECMS are: $k_p^{SOC} = 2$, $T_i^{SOC} = 480$ and $\alpha_{NO_x} = 0$.

For the comparison case study, the parameters of the RDE-ECMS are: $k_p^{SOC} = 2$, $T_i^{SOC} = 480$, $k_p = 0.1$, $T_i = 75000$, and $\alpha_{NO_x}(0) = 0$.

Note that, for simplicity, the values of the parameters $k_p^{SOC}$ and $T_i^{SOC}$, for the RDE-ECMS, were taken from the non-adaptive ECMS.

The two other parameters, $k_p$ and $T_i$, are optimized on the NEDC and on the WLTP driving cycles, to yield an acceptable reference tracking, namely neither a too fast nor a too slow tracking.

To ensure an unbiased comparison, the initial value for the variable $\alpha_{NO_x}(t)$ is chosen to be equal to the one of the non-adaptive ECMS.

The two strategies are applied, each on a sequence of five repetitions of the four different driving cycles NEDC, FTP-75, WLTP and LA92.

Figure 5.6 shows the normalized specific equivalent fuel consumption, the relative fuel consumption difference of the RDE-ECMS, compared to the non-adaptive ECMS, and the normalized specific equivalent $\mathrm{NO}_x$ emissions, for both the non-adaptive ECMS ("$\alpha_{NO_x} = 0$") and the adaptive RDE-ECMS ("$\alpha_{NO_x}$ var.").

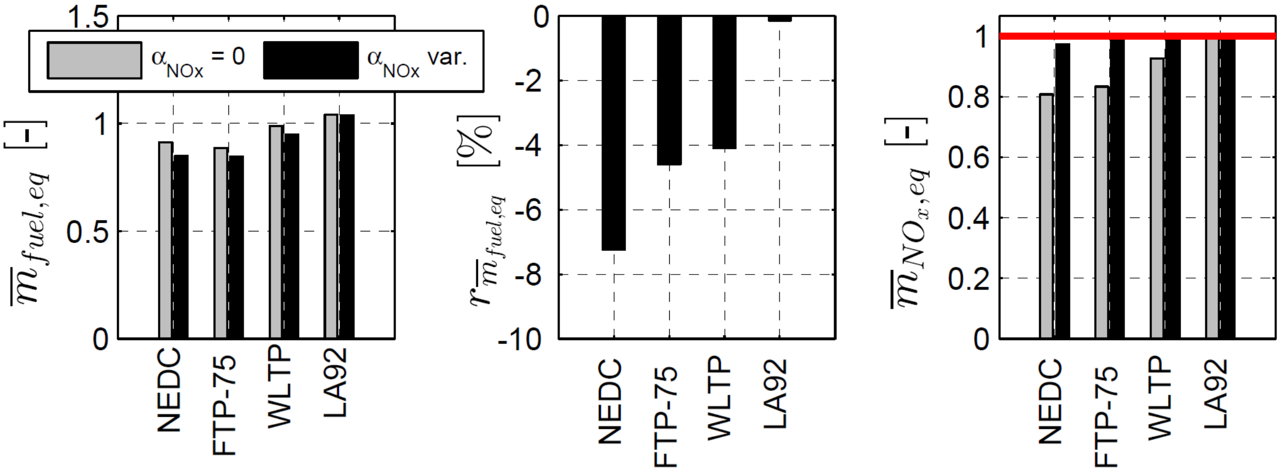

**Figure 5.6: Comparative results of a non adaptive ECMS (gray) and the RDE-ECMS (black) on four driving cycles with five repetitions each.**

As depicted in the middle plot of Figure 5.6, the fuel savings of the RDE-ECMS amount to 0-7%, compared to the non-adaptive ECMS. On all driving cycles, both strategies respect the prescribed $\mathrm{NO}_x$ emissions limit, indicated as a red line in the subplot on the right-hand side. In the case of the LA92 driving cycle, the RDE-ECMS performs very similarly to the non-adaptive ECMS, which is the reason why in practice no fuel saving occurs. On all the other driving cycles, the RDE-ECMS provides a lower fuel consumption than the non-adaptive ECMS, since the RDE-ECMS increases the emission-related equivalence factor $\alpha_{NO_x}$ to move along the fuel-optimal trade-off.

Figure 5.7 shows the performance of the RDE-ECMS and of the non-adaptive ECMS, compared to the optimal trade-off between the fuel consumption and the emissions.

The non-adaptive ECMS (”diamond marker”) achieves practically the identical performance as the optimal non-causal solution for $\alpha_{NO_x} = 0$, in terms of fuel consumption and emissions.

The RDE-ECMS (”star marker”) achieves a performance that is close to the optimal trade-off curve, for the driving cycles FTP-75, WLTP and LA92. For the NEDC, there is still a potential to reduce the fuel consumption by about 1.6%, for the same amount of $\mathrm{NO}_x$ emissions, as calculated with the non-causal ECMS.

In general, the RDE-ECMS proves to minimize the fuel consumption, while tracking a reference $\mathrm{NO}_x$ emission level and sustaining the battery state-of-charge.

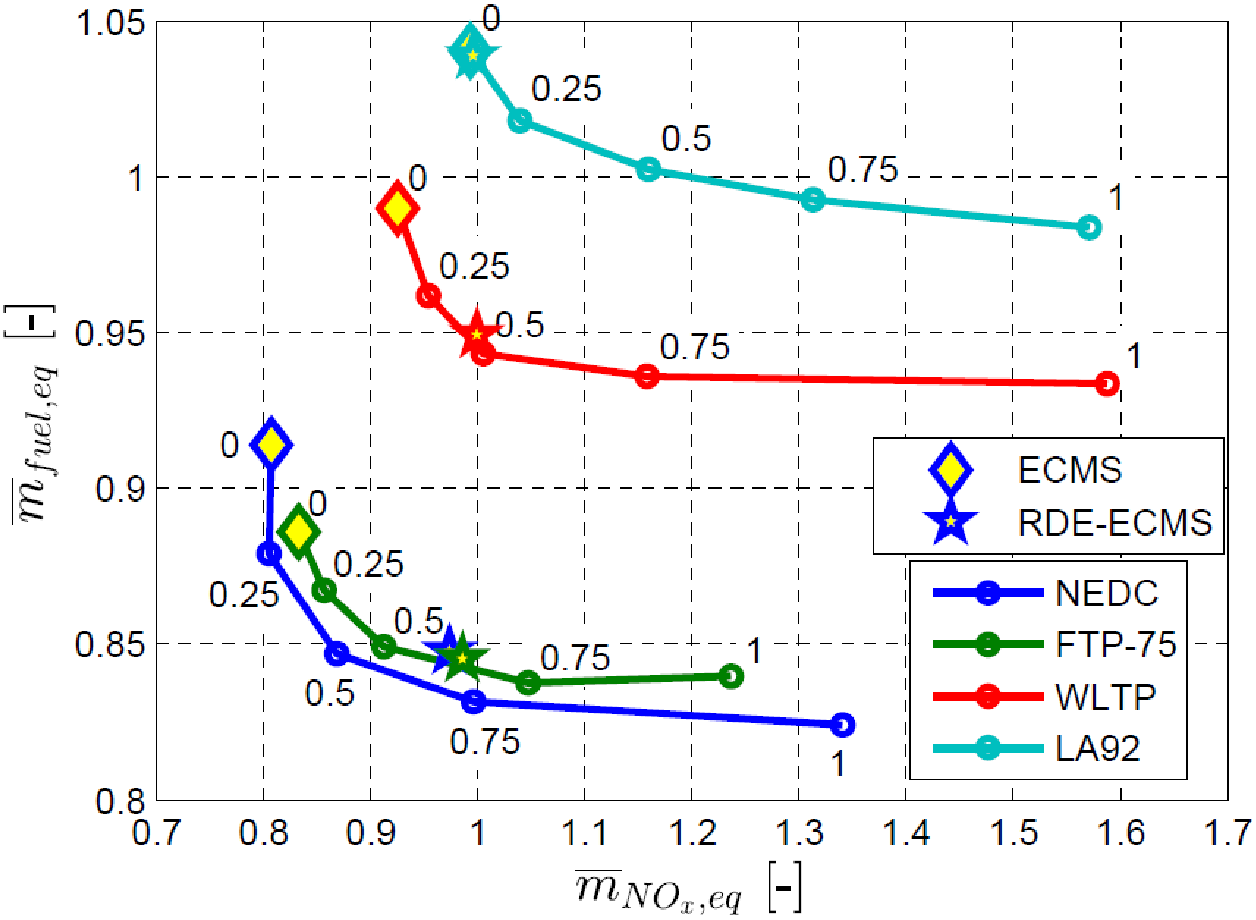

Figure 5.7: Comparative results of the $NO_x$-optimal ECMS (diamond) and the RDE-ECMS (star); normalized FC-$SNO_x$ tradeoff.

## 5.4 Experimental Results

An experimental validation of the models and of the method presented in Sections 3.2-3.3 and 5.3, simulated with the vehicle (b) data listed in Section 3.6, and of the results of the simulation case study reported in Section 5.3.4.2, is shown here.

The goal of this subsection is firstly to show that the RDE-ECMS presented in Section 5.3 works also in practice, and secondly, that the quasi-static modeling for the fuel consumption and the $NO_x$ emissions is sufficient.

### 5.4.1 Description of the HiL test-bench

For the experimental validation of the RDE-ECMS, the method presented in Section 5.3, is applied both in simulation and in hardware-in-the-loop (HiL) experiments. In the HiL experiments, only the engine is used as the real hardware. The longitudinal dynamics, as well as the hybrid vehicle components, are simulated on a computer. This setup allowed for the measurement of the real fuel consumption and of the real $\mathtt{NO}_x$ emissions, without requiring the physical presence of the entire vehicle. For more details on HiL experiments, interested readers are referred to the literature [141, 172, 35].

A schematic of the layout for the HiL implemented is given in Figure 5.8.

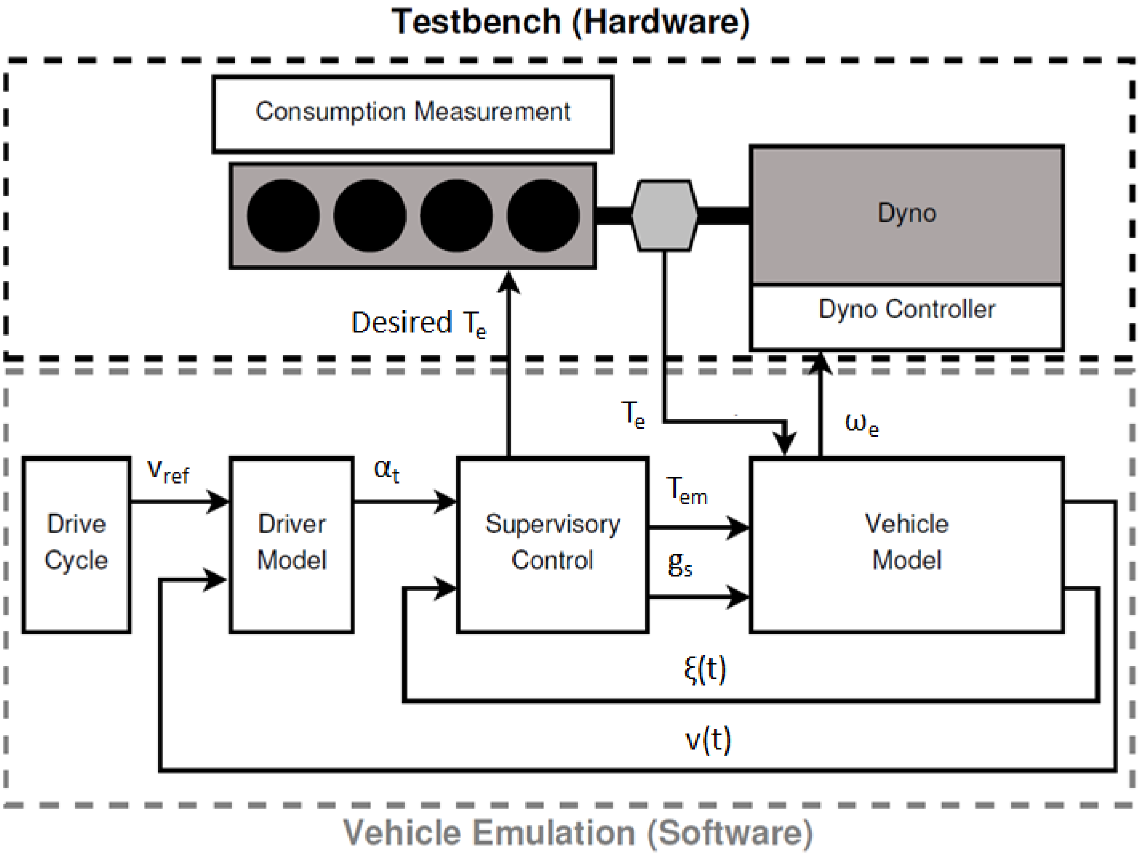

Figure 5.8: HiL test-bench for the HV emulation, see [141] for details.

In the HiL experiments here, the desired torque command, which is calculated by the energy management controller, is sent to the electronic control unit (ECU) of the engine, while the desired engine speed command is sent to the dynamometer of the engine test bench. The emissions are measured using a *VDO/NGK UniNOx* sensor. This sensor is likely to be employed also in real vehicles, due its low price and due to its ability to additionally measure the air-to-fuel ratio. The fuel consumption is measured by the ECU-internal indication.

## 5.4.2 Results

The experimental validation is divided into four cases, with three repetitions of the same standard homologation cycle each.

The following setup is used to compare the simulation results to the results obtained with the HiL experiments:

- Driving cycles:
    - NEDC:
        - variable $\alpha_{NO_x}$;
        - constant $\alpha_{NO_x}$;
    - WLTP (Worldwide Harmonized Light Vehicles Test Procedure, Class 3 Cycle):
        - variable $\alpha_{NO_x}$;
        - constant $\alpha_{NO_x}$;
- reference signal: 100%;
- SOC reference signal: 60% with speed-dependent correction;
- Initial condition for the emission-specific equivalence factor: $\alpha_{NO_x}(0) = 0$ (emissions-optimal). In case of constant weight $\alpha_{NO_x} = \text{const.} = 0$.

## 5.4.3 NEDC cycle

The results for the NEDC are shown in Figure 5.9, for the ECMS with constant $\alpha_{NO_x}$, and in Figure 5.10 for the RDE-ECMS. It shows the vehicle speed, the battery SOC, the normalized specific emissions (normalized [mg/km]), the normalized specific fuel consumption (normalized [L/100km]), and the equivalence factors of both the $\mathrm{NO}_x$ emission and the battery power.

As visible, the vehicle speed trajectories of the simulation results and of the HiL results are identical.

The SOC trajectories of the simulation and of the HiL results show very good matching; both are charge-sustaining at the same SOC reference level. The two trajectories are very similar; after an initial transient phase, the trajectories become more stable.

A similar behavior is observed for the specific fuel consumption, which in addition exhibits a visible offset. This offset is a consequence of some of the neglected dynamics of the engine, e.g. the thermal dynamics. In fact, these effects have an influence on the entire behavior of the SOC and of the $\mathrm{NO}_x$ control, so that the trajectories of the SOC, the $\mathrm{NO}_x$ emissions etc., become different for the results obtained with the simulation and with the experiment. However, an offset between the trajectories is *not* a measure to quantify the modeling errors, because the trajectories show the actual, uncorrected emissions and the actual, uncorrected fuel consumption. For example, an offset of 5% in the trajectories for the fuel consumption does not mean that the true fuel consumption is 5% different, since there is also a certain offset in the SOC trajectories.

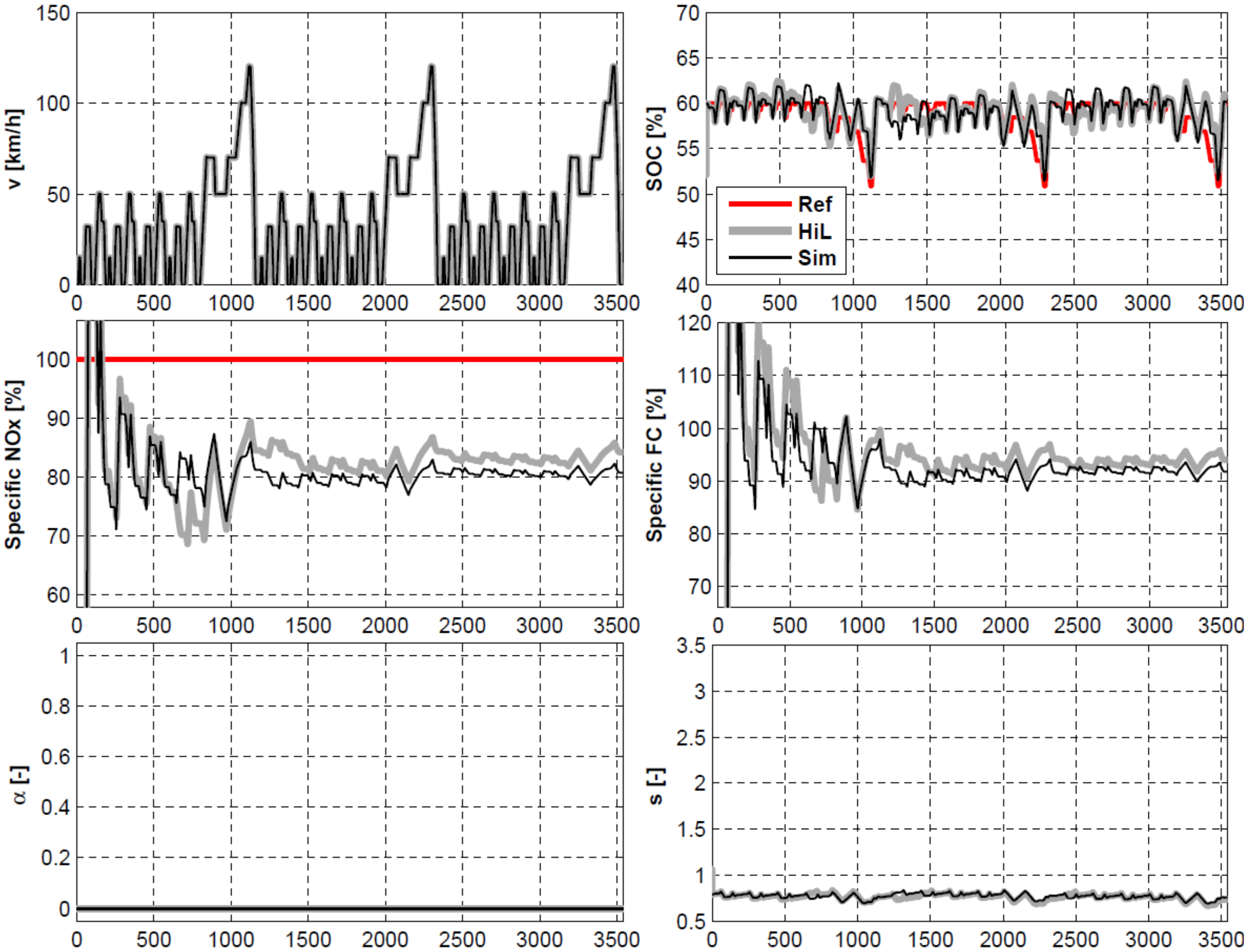

**Figure 5.9: Comparative results of the ECMS (without $\mathrm{NO}_x$ control) simulation vs. HiL test bench experimental test on three repetitions of the NEDC cycle.**

A higher final SOC means also higher fuel consumption, and typically higher $\mathrm{NO}_x$ emissions. For an unbiased comparison, the equivalent $\mathrm{NO}_x$ emissions and the equivalent fuel consumption have to be calculated. Such a comparison is made below in Section 5.4.5.

Considering Figure 5.10, where RDE-ECMS is depicted, the trajectories of the weighting factor $\alpha_{NO_x}(t)$ are also similar, for both the simulation and the HiL experiment. They both start from an initial value of zero and converge towards to a value of one, until the specific $\mathrm{NO}_x$ emissions approach the reference level. Due to the highway part, which requires a longer use of the engine, the equivalence factor $\alpha_{NO_x}$ is reduced to save some $\mathrm{NO}_x$ emissions. In the subsequent city driving part, $\alpha_{NO_x}$ approaches again a value of one (fuel-optimal), until in the next highway part the value of $\alpha_{NO_x}(t)$ is reduced again. Also, the trajectories for the equivalence factor $s(t)$ are very close to each other. This is mainly due to the fact that the value of $s(t)$ adapts to the instantaneous value of $\alpha_{NO_x}(t)$ during the cycle.

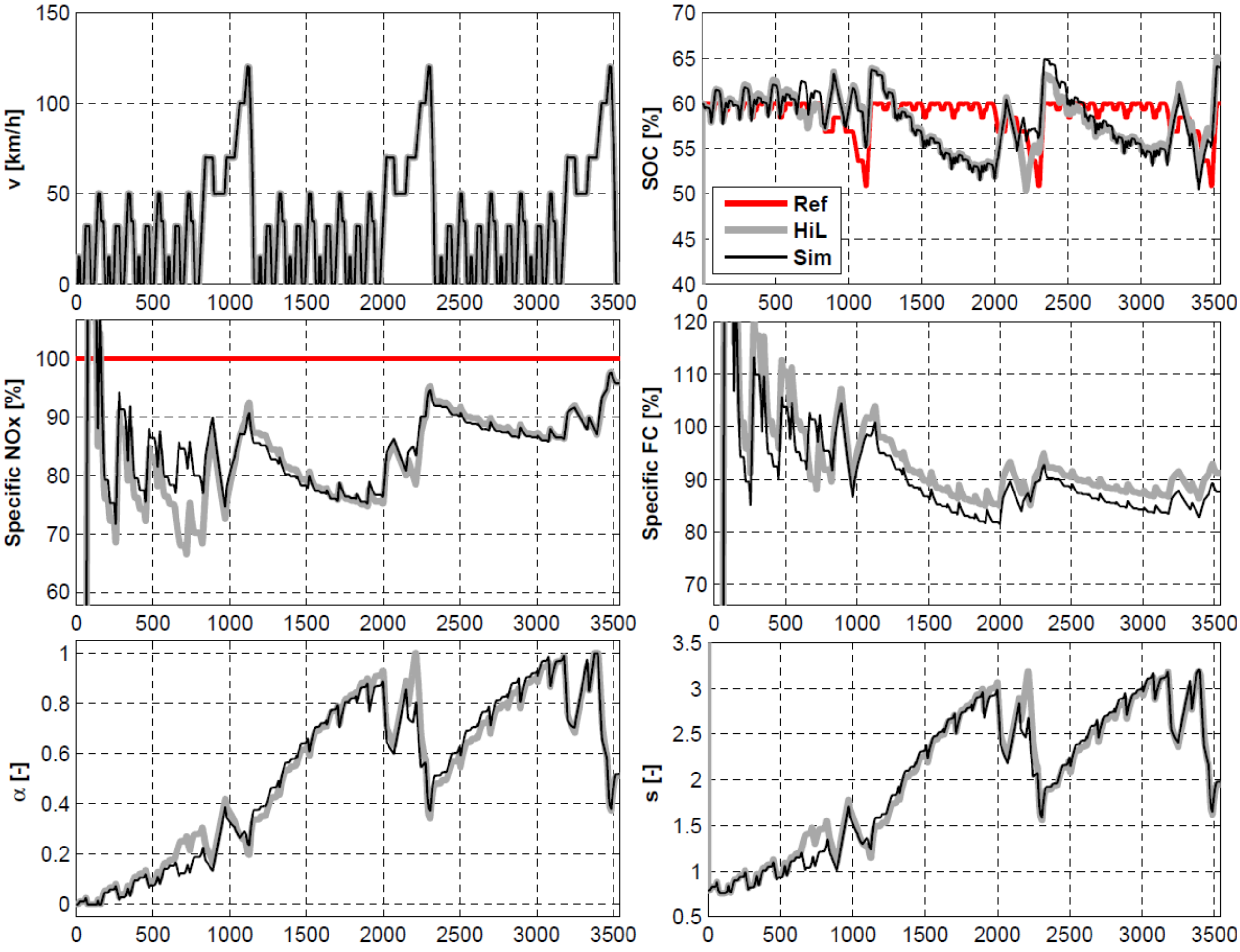

**Figure 5.10: Comparative results of RDE-ECMS simulation vs. HiL test bench experimental test on three repetitions of the NEDC cycle.**

### 5.4.4 WLTP cycle

The NEDC consists of a factitious speed trajectory, which does not represent real driving conditions. Therefore, the vehicle accelerations and speeds involved are moderate. As a consequence, the simulation and the HiL experiment are repeated on the WLTP driving cycle, which represents a more realistic driving scenario, with higher mean speeds and higher vehicle accelerations.

Figure 5.11 and Figure 5.12 show the vehicle speed, the battery SOC, the normalized specific $\mathrm{NO}_x$ emissions (normalized [mg/km]), the normalized specific fuel consumption (normalized [L/100km]), and the equivalence factors $\alpha_{NO_x} = \mathbf{const.}$, and $s(t)$, for both the $\mathrm{NO}_x$ emission and the battery power, respectively.

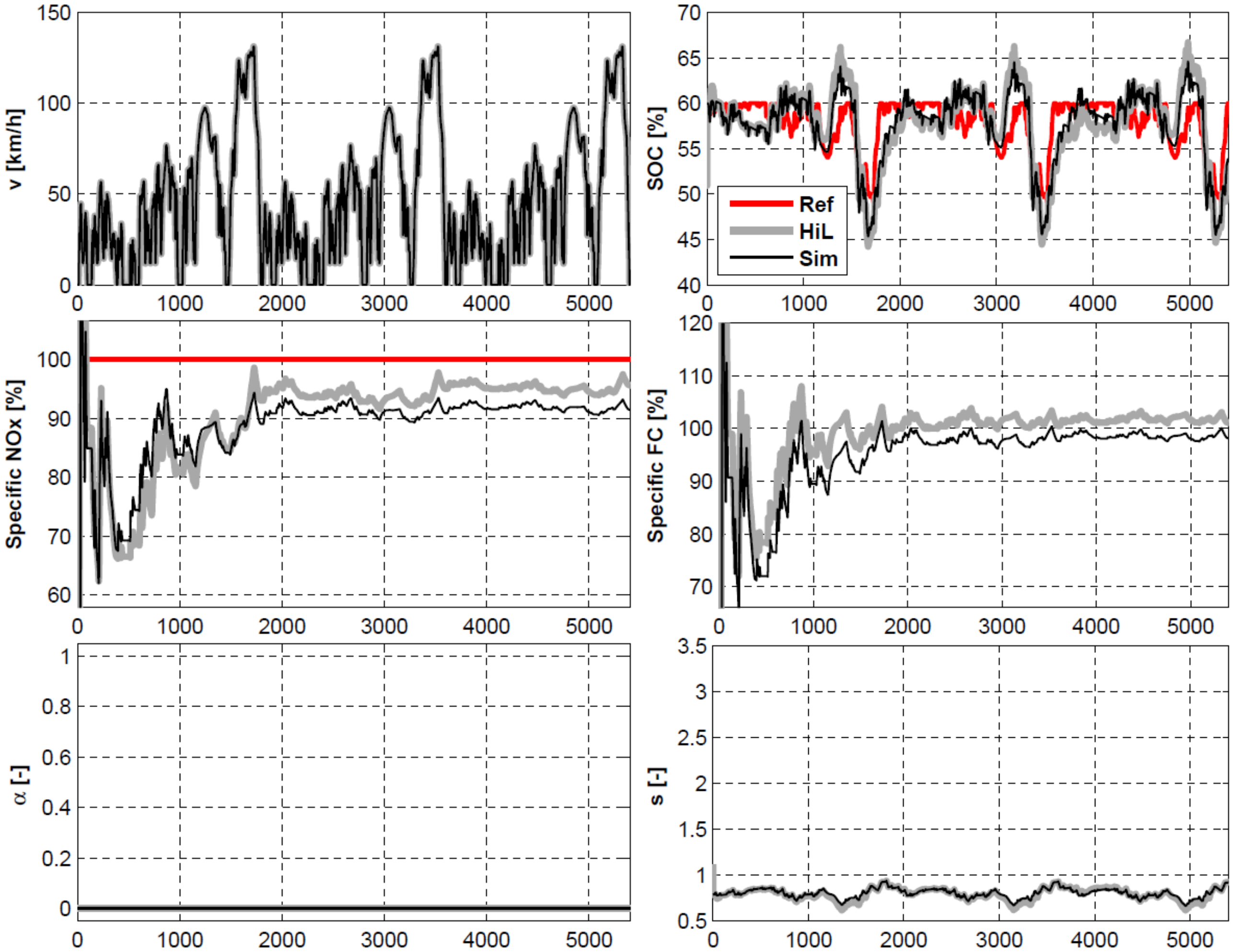

**Figure 5.11: Comparative results of the ECMS (without NOx control) simulation vs. HiL test bench experimental test on three repetitions of the WLTP cycle.**

Figure 5.12 shows the time evolution of the equivalence factors $\alpha_{NO_x}(t)$ and $s(t)$ as well, since in Figure 5.11 the value of $\alpha_{NO_x}$ is constant, because the online emisison control is inactive. As illustrated in the figure, the vehicle speed trajectories of the simulation results and of the HiL results coincide. The SOC trajectories of the simulation and of the HiL results are similar, both being charge-sustaining at around the same final SOC reference level. The two trajectories are very similar; after an initial transient phase, the trajectories become stable, approaching the desired reference level. A similar behavior is observed for the specific fuel consumption, which in addition exhibits a visible offset that is explained below. Furthermore, the trajectories of the equivalence factor $\alpha_{NO_x}(t)$ are also similar for both the simulation and the HiL experiment.

They both start from a value of zero and converge towards a value of one (fuel-optimal), until the specific $\mathrm{NO}_x$ emissions approach the desired reference level. Due to the highway part, which requires the engine to be used for longer phases, the equivalence factor $\alpha_{NO_x}(t)$ is reduced to save some emissions. In the subsequent city driving part, $\alpha_{NO_x}(t)$ again approaches a value of one, until in the next highway part the value of $\alpha_{NO_x}$ is reduced again. Also, the trajectories for the equivalence factor $s(t)$ are very close to each other. This is mainly due to the fact that the value of $s(t)$ adapts to the instantaneous value of $\alpha_{NO_x}(t)$ during the cycle. The preliminary conclusion from the comparison of the simulation results to the experimental results, is that the RDE-ECMS also works in practice.

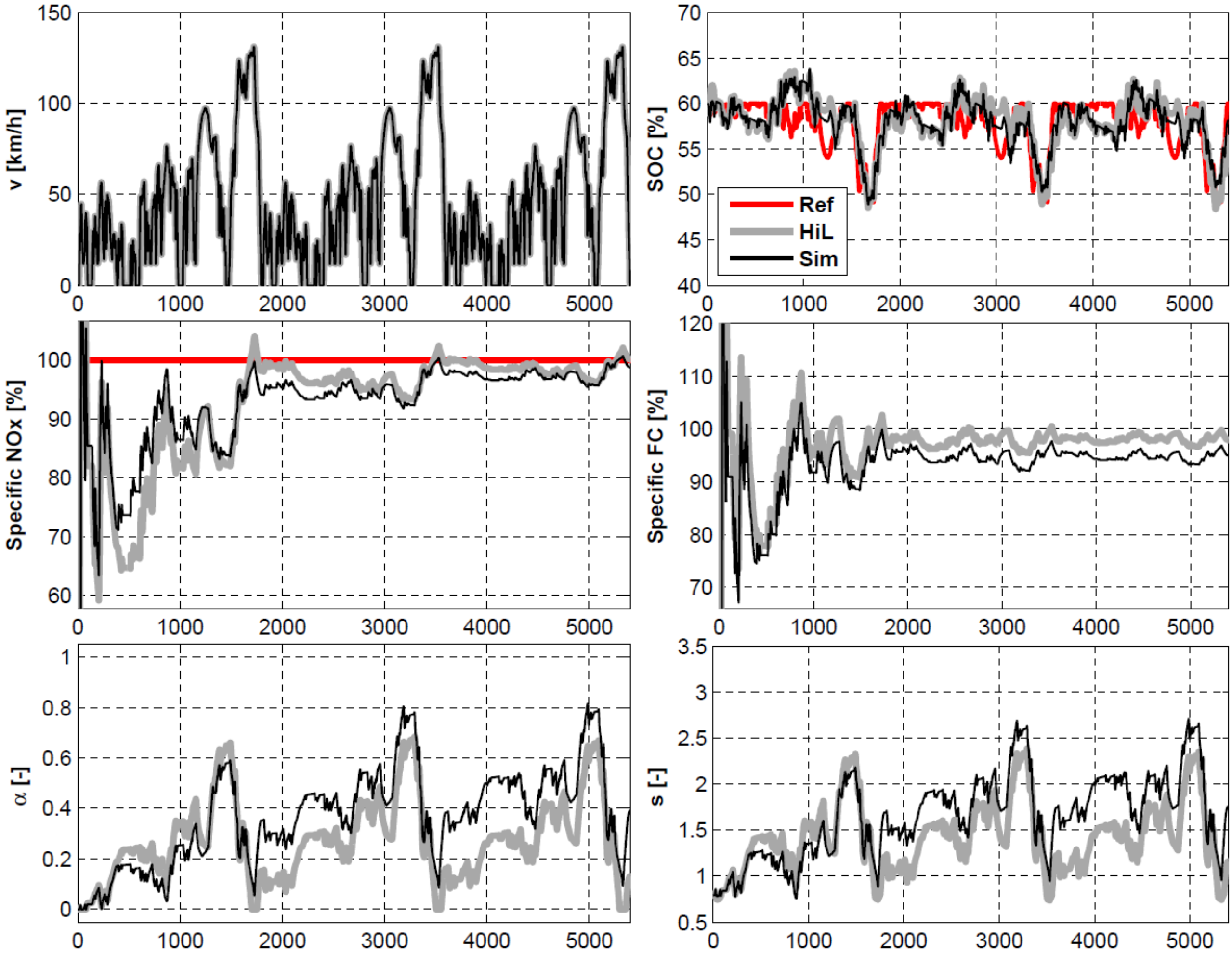

**Figure 5.12: Comparative results of RDE-ECMS simulation vs. HiL test bench experimental test on three repetitions of the WLTP cycle.**

The offset of the trajectories of the simulation and of the HiL results, is a consequence of some of the neglected dynamics in the engine model of the simulation. As previously introduced, the thermal dynamics are not considered in the simulation, although in practice they can substantially influence the formation of pollutant emissions. As a matter of fact, such effects have an influence on the SOC time evolution and on the $\mathrm{NO}_x$ control policy, so that the trajectories of the SOC, of the $\mathrm{NO}_x$ emissions etc. become different, for the results obtained with the simulation and with the experimental setup. Following an approach similar to that used in the previous section about NEDC results, for a fair comparison *equivalent* $\mathrm{NO}_x$ emissions and *equivalent* fuel consumption have to be calculated. Such a comparison is made below in Section 5.4.5.

### 5.4.5 Summary of the experimental tests

To obtain a fair comparison between the simulation and the experimental results, the $\mathrm{NO}_x$ emissions and the fuel consumption have to be corrected to account for the different levels of the final SOC. Here, the correction is made based on the following formulae:

- $\bar{m}_{fuel,eq}$ denotes the distance-specific, battery-charge-equivalent fuel consumption and $\bar{m}_{fuel,norm}$ is the normalization value for total FC;

$$\bar{m}_{fuel,eq} = \frac{1}{\bar{m}_{fuel,norm}} \cdot \frac{\left(\int_0^T \overset{*}{m}_{fuel}(t)\,dt + \Delta m_{fuel,eq}\right)}{\int_0^T v(t)\,dt} \tag{5.59}$$

- $\bar{m}_{NO_x,eq}$ is the distance-specific, battery-charge-equivalent emissions and $\bar{m}_{NO_x,norm}$ is the normalization value used for the total $\mathrm{NO}_x$ emissions;

$$\bar{m}_{NO_x,eq} = \frac{1}{\bar{m}_{NO_x,norm}} \cdot \frac{\left(\int_0^T \overset{*}{m}_{NO_x}(t)dt + \Delta m_{NO_x,eq}\right)}{\int_0^T v(t)dt} \tag{5.60}$$

- $\Delta m_{fuel,eq}$ and $\Delta m_{NO_x,eq}$ are the equivalent fuel mass and the equivalent $\mathrm{NO}_x$ mass, as a function of the final battery charge, respectively;

$$\begin{gathered}\Delta m_{fuel,eq} = \begin{cases} \dfrac{\Delta E_b}{H_l} \cdot \dfrac{1}{\bar{\eta}_b^{(d)} \cdot \bar{\eta}_m^{(d)} \cdot \bar{\eta}_e} & \text{if } \Delta \mathrm{E_b} \geq 0, \\ \dfrac{\Delta E_b}{H_l} \cdot \dfrac{\bar{\eta}_b^{(c)} \cdot \bar{\eta}_m^{(c)}}{\bar{\eta}_e} & \text{if } \Delta \mathrm{E_b} < 0, \end{cases} \\ \Delta m_{NO_x,eq} = \frac{\int_0^T \overset{*}{m}_{NO_x}(t)dt(t)}{\int_0^T \overset{*}{m}_{fuel}(t)\,dt} \cdot \Delta m_{fuel,eq}\end{gathered} \tag{5.61}$$

- $\Delta E_b$ denotes the amount of net energy stored in the battery at the end of the driving cycle.

$$\Delta E_b = \int_0^T V_{oc}\big(\xi(t)\big) \cdot I_b(t)\, dt \tag{5.62}$$

Figure 5.13 shows a comparison of the SOC-corrected equivalent $\mathrm{NO}_x$ emissions and the corrected specific fuel consumptions on the two driving cycles, NEDC and WLTP, for each with the cases of a constant $\alpha_{NO_x}$ and variable $\alpha_{NO_x}(t)$, whose trajectories are depicted from Figure 5.9 to Figure 5.12.

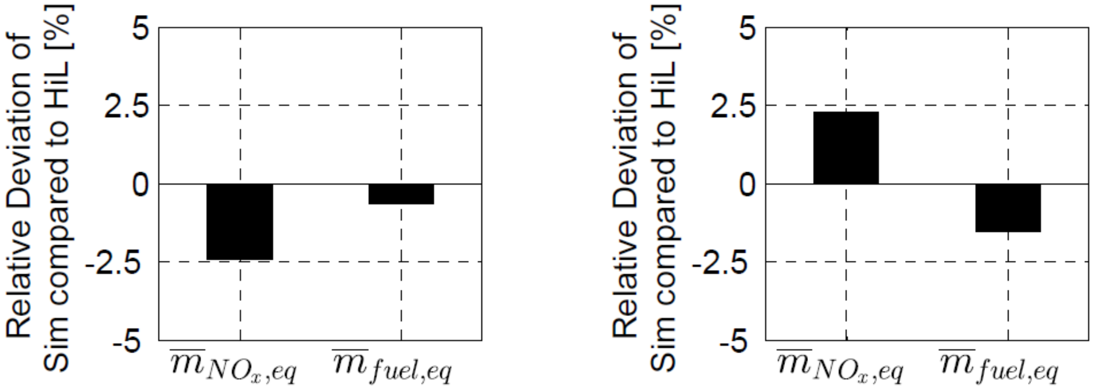

**(a)** NEDC, $\alpha_{NO_x} = 0$ **(b)** NEDC, $\alpha_{NO_x} = \text{var.}$

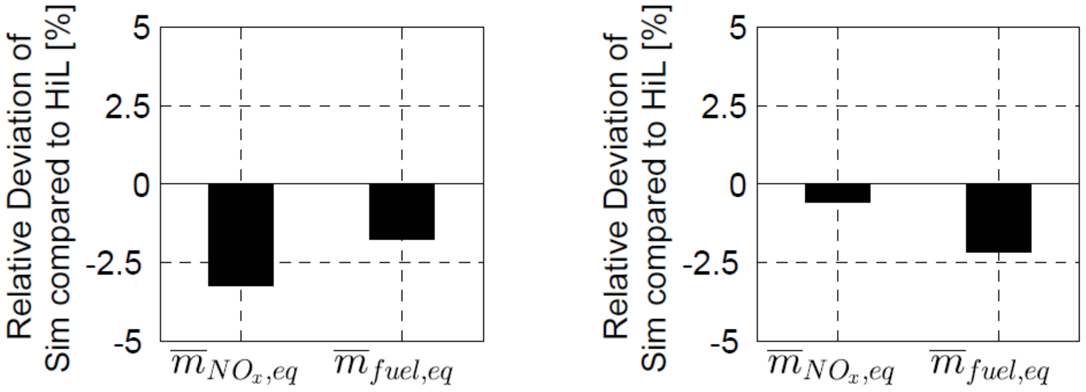

**(c)** WLTP, $\alpha_{NO_x} = 0$ **(d)** WLTP, $\alpha_{NO_x} = \text{var.}$

**Figure 5.13: Summary of comparisons between simulation and HiL results. Equivalent $\mathrm{NO}_x$ emissions and equivalent FC, accounting for SOC deviation.**

Accordingly, the results obtained with the simulations underestimate the results obtained with the HiL experiments. The error, in all the simulations compared to the experimental data, is well below 5%. Therefore, quasi-static models for the fuel consumption and for the $\mathtt{NO}_x$ emissions, are accurate enough for the simulation on the NEDC and on the WLTP driving cycles.

## 5.5 Summary of Results

This Chapter demonstrates an energy management strategy to account for real driving $\mathtt{NO}_x$ emissions of a Diesel hybrid electric vehicle. The method is based on the equivalent consumption minimization strategy, which is extended with a state accounting for the $\mathtt{NO}_x$ emissions. As demonstrated in simulation, as well as in hardware-in-the-loop experiments, the strategy is able to minimize the fuel consumption, while following given reference trajectories for the $\mathtt{NO}_x$ emissions and for the battery state of charge. On simulations, the strategy proves to optimally adjust the trade-off between the fuel consumption and the $\mathtt{NO}_x$ emissions during operation.

Compared to a conservative non-adaptive strategy, the advantages of the proposed methodology, in terms of FC, amount to more than 7% in favor of the presented technique.

The strategy can be employed also in plug-in hybrid electric vehicles, without the need to adjust the controller structure, by only modifying the reference trajectory for the battery state of charge.

So far, the presented RDE-ECMS has been applied to warm engine conditions. A future evolution of this strategy will be to investigate the control of tailpipe $\mathtt{NO}_x$ emissions for a Diesel HEV, equipped with a selective catalytic reaction (SCR) system. This will require a model of the efficiency of the after-treatment system, as a function of an additional state represented by the temperature of the SCR system. Moreover, a further potential is seen in the optimal design of the reference trajectories for the SOC and the $\mathtt{NO}_x$ emissions.

# A.1

# Parametric Optimization of a Complex Hybrid Vehicle

In this first Appendix, a DP procedure applied to a complex HV, capable of being operated at numerous modes, is shown. The goal is to assess multiple design criteria, such as the choice of electric components, the sizing of the ICE and of the HR, the number of gears and the choice of gear ratios adopted. Since the DP provides the optimal use of all components for a given scenario, it represents an optimal methodology to evaluate the choice of different components, because each comparison is done ensuring the best possible utilization of each element.

In Section A1.1, an overview of the investigations conducted in the following is given. The hybrid vehicle system is described in Section A1.2, providing an analysis of all possible operating modes of the vehicle. The description of the DP model, with the equations involved in the QSS simulation framework, is given in Section A1.3, while Section A1.4 illustrates the results of a subset of selected case studies.

## A1.1 Introduction

The goal of this Appendix is to demonstrate the application of a multivariable DP approach to the optimization of a Complex HV. The system, described in the following Section, is a Complex or Series/Parallel hybrid vehicle that allows multiple operating modes. From the complete topology several subsystems, such as parallel HV, series HV, can be derived, each characterized by the installation of different mechanical, thermal and electric components. The overall optimization includes the following topologic possibilities:

- Series/parallel HV;
- Series HV;
- Parallel HV;

with the following possible gearbox variations:

- variable number of gears for each gearbox;
- variable gear ratios;

two different technologies for the electric motors:

- Asynchronous motor (AM);
- Permanent Magnets synchronous Motor (PM);

and two ICEs investigated:

- Two cylinders SI ICE;
- Three cylinders SI ICE;

Within the set of all possible combinations for the above cited configurations, only a small subset is taken, as the set of case studies analyzed and presented in Section A1.4.

## A1.2 System Description

The system analyzed in this section is classified as a plug-in Complex HV, following the general rules introduced in Section 2.2. It comprises two electric motor/generators, mounted on two different shafts, and a small Otto ICE.

### Layout

The two electric motors are installed on different shafts, and each one is equipped with a dedicated GB, as illustrated in Figure A1.1.

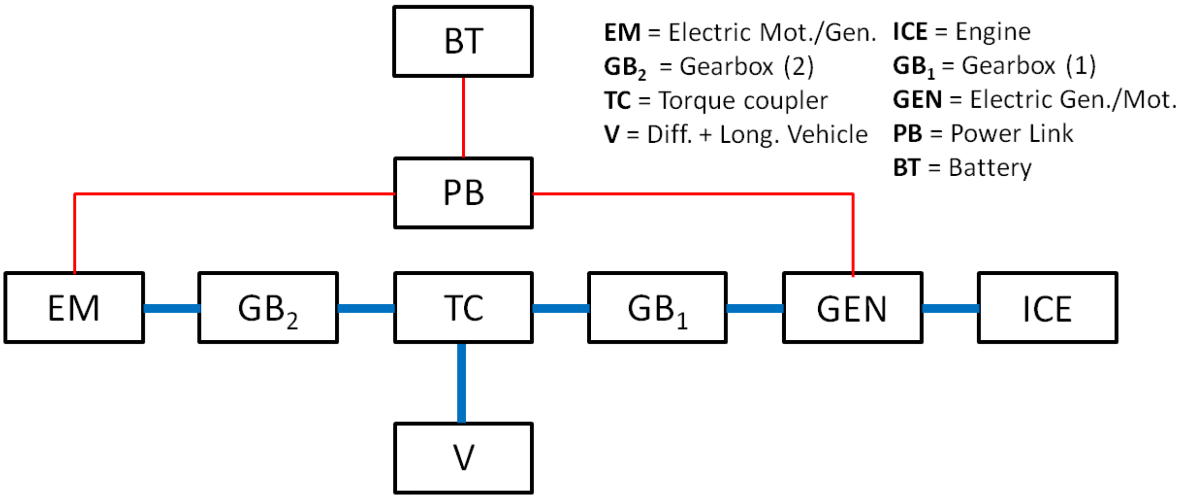

Figure A1.1: Layout of the Complex Hybrid Vehicle system.

The secondary shaft of the GBs is common. For this reason, the two GBs are represented as they were linked together through a torque coupler (TC) element in Figure A1.1. GEN is mechanically connected to the ICE, and two clutches are installed, between GEN and $GB_1$ and between EM and $GB_2$, to decouple one or the other power paths from the drive train.

## Operating Modes

The Complex HV analyzed here offers several driving modes (DM).

It can be operated as a pure series hybrid, a pure parallel hybrid with two different electric motors, and a mixed series/parallel hybrid, where one electric machine acts as a generator while the other provides positive traction torque.

The possible traction modes, when the vehicle is at constant speed or it is accelerating, are the seven classified in Figure A1.2.

Note that, during mode (6), the ICE absorbs negative power due to its cranking losses, since any additional clutch is installed between the engine and the motor GEN, to decouple the two elements.

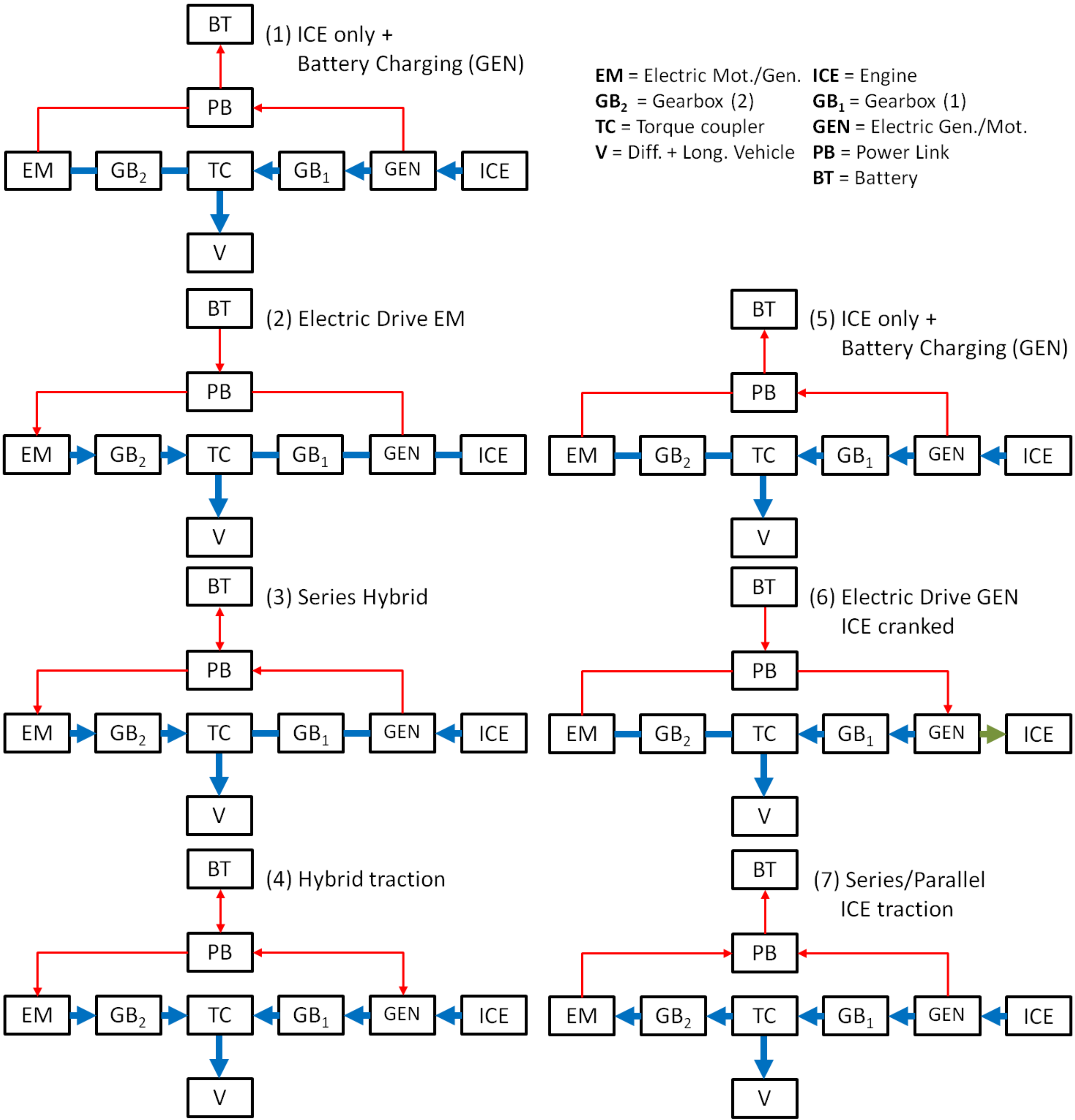

Figure A1.2: Summary of the main operating modes of the Complex HV during Traction.

The Complex HV offers several possibilities during braking operations as well. The four braking DMs are illustrated in Figure A1.3.

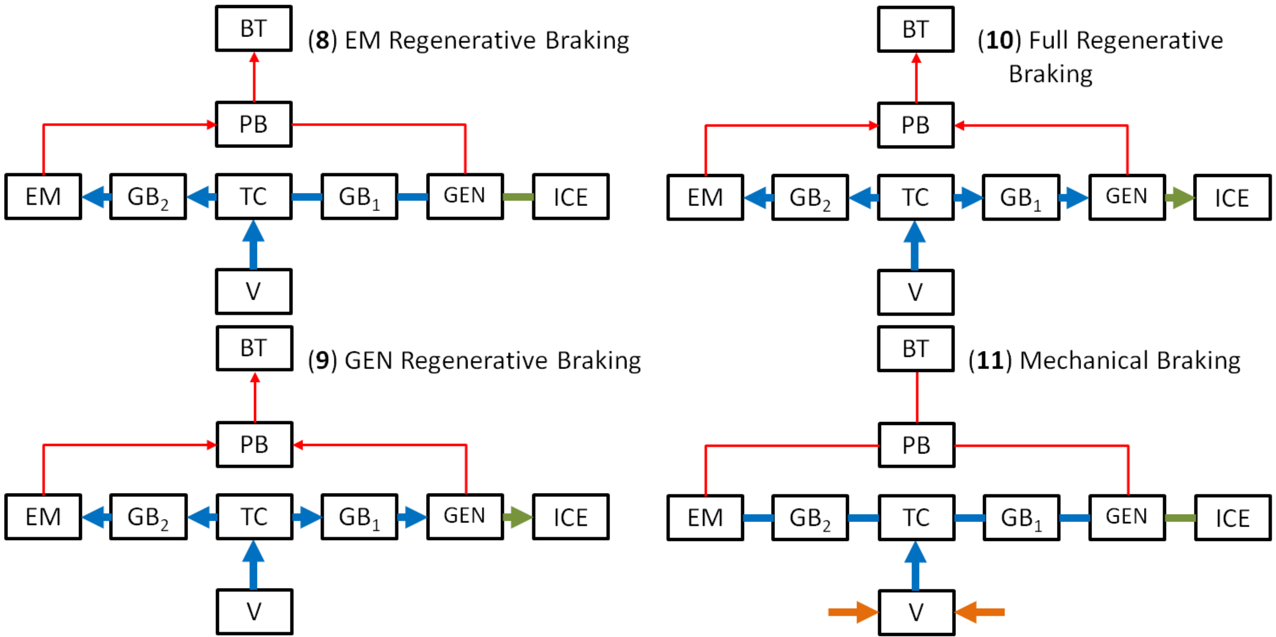

Figure A1.3: Summary of the main operating modes of the Complex HV during Braking.

Note that the vehicle is also equipped with traditional mechanical brakes, and mode (11) is used to represent every condition when the friction brakes provide at least a part of the total power needed to decelerate the vehicle.

## A1.3 DP Model

The vehicle is optimized by means of a DP algorithm, introduced in Section 4.2.1. The objective is to minimize the overall fuel mass consumed during a driving cycle (4.6). Two DP procedures must be run for each case, since the FC calculation for plug-in HVs requires the calculation of a pure electric distance, and of a FC on a driving cycle starting from minimum SOC conditions, as described in Section A1.4.

### Definition of the system variables

The DP framework requires the definition of state variables and control inputs vectors. The choice made here is the following:

$$x_k = [\xi_k]; \qquad u_k = \begin{bmatrix} u_{ts,k} \\ P_{gen,mech,k} \\ u_{g,1,k} \\ u_{g,2,k} \end{bmatrix} \tag{A1.1}$$

Here, $\xi_k$ is the state-of-charge, $u_{ts,k}$ is the torque split factor, $P_{gen,mech,k}$ is the mechanical power requested by the GEN at each time, $u_{g,1,k}$ and $u_{g,2,k}$ the gears selected. No general rule exists to guide the optimal choice of the proper variables. They should be the minimum number needed to describe the system dynamics, taking into account the well-known *curse of dimensionality* affecting DP.

In Table A1.1, the driving modes illustrated in Figure A1.2 and Figure A1.3 are associated with the corresponding ranges of the control inputs involved. An additional mode (0) is added to cover the *car stop* phases.

**Table A1.1: Summary of the Drive Modes (DM) for the Complex HV.**

| **DM nr.** | **DM** | $\mathbf{u_{ts}}$ | $\mathbf{P_{gen}}$ | $\mathbf{P_e}$ | $\mathbf{P_m}$ |
|---|---|---|---|---|---|
| 0 | Car Stop | $NaN$ | 0 | 0 | 0 |
| 1 | ICE only | $u_{ts} = 0$ | $P_{gen} = 0$ | $> 0$ | 0 |
| 2 | Electric Drive EM | $u_{ts} = 1$ | $P_{gen} = 0$ | 0 | $> 0$ |
| 3 | Series Hybrid | $u_{ts} = 1$ | $P_{gen,min} \leq P_{gen} < 0$ | $> 0$ | $> 0$ |
| 4 | Hybrid Traction | $u_{ts,min} < u_{ts} < 1$ | $P_{gen,min} \leq P_{gen} \leq P_{gen,max}$ | $> 0$ | $\geq 0$ |
| 5 | ICE only + Battery Charging | $u_{ts} = 0$ | $P_{gen,min} \leq P_{gen} < 0$ | $> 0$ | 0 |
| 6 | Electric Drive GEN | $u_{ts} = 0$ | $0 < P_{gen} \leq P_{gen,max}$ | $< 0$ | 0 |
| 7 | ICE + Series/Parallel Battery Charging | $u_{ts} < 0$ | $P_{gen,min} \leq P_{gen} < 0$ | $> 0$ | $< 0$ |
| 8 | EM Regenerative Braking | $u_{ts} = 1$ | $P_{gen} = 0$ | 0 | $< 0$ |

| **DM nr.** | **DM** | $\mathbf{u_{ts}}$ | $\mathbf{P_{gen}}$ | $\mathbf{P_e}$ | $\mathbf{P_m}$ |
|---|---|---|---|---|---|
| 9 | GEN Regenerative Braking | $u_{ts} = 0$ | $P_{gen,min} \leq P_{gen} < 0$ | $< 0$ | 0 |
| 10 | Full Regenerative Braking | $0 < u_{ts} < 1$ | $P_{gen,min} \leq P_{gen} < 0$ | $< 0$ | $< 0$ |
| 11 | Mechanical Braking | $0 \leq u_{ts} < 1$ | $P_{gen} \leq 0$ | $\leq 0$ | $\leq 0$ |

## QSS Vehicle model

In this subsection, a brief overview of the main governing equations for the system modeling is given. Figure A1.4 illustrates the QSS model for the Complex HV considered here.

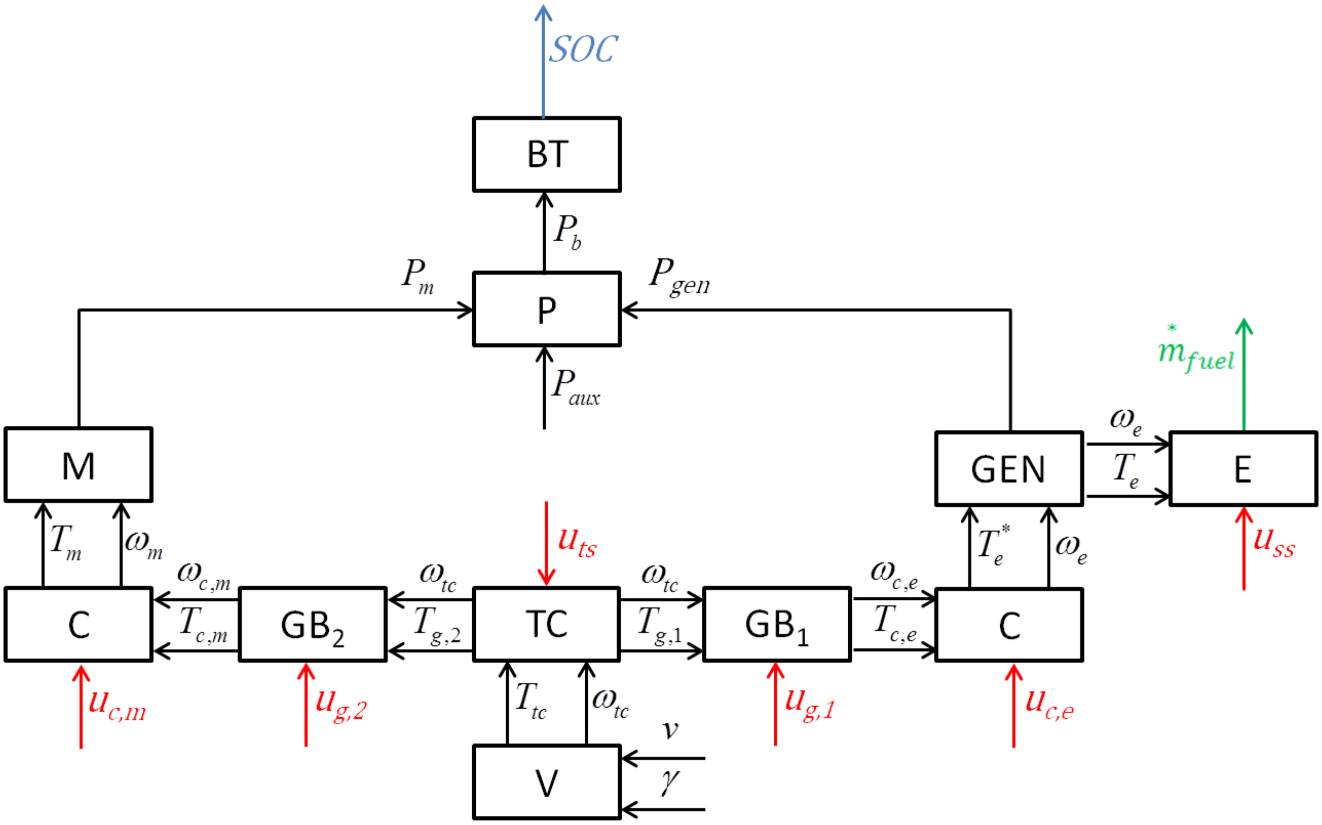

Figure A1.4: QSS Model of the Complex HV.

Based on the physical causality represented in the schematic of the previous figure, a mathematical formulation of the equations needed to properly describe the system is given in the following.

The traction force and the wheel torques and angular speed and acceleration are given by the expressions (3.3)-(3.7). Based on those, and considering a fixed gear ratio for the differential, the torque demanded and the current speed and acceleration at the TC node can be calculated as follows:

$$\begin{aligned} T_{tc}^{*}(t) &= \frac{T_w(t)}{i_{diff} \cdot \eta_{diff}^{sign(T_{tc}(t))}} \\ \omega_{tc}(t) &= \omega_w(t) \cdot i_{diff} \\ \dot{\omega}_{tc}(t) &= \dot{\omega}_w(t) \cdot i_{diff} \end{aligned} \tag{A1.2}$$

Hence, considering the contribution of the inertias of each GB, the total requested torque becomes:

$$T_{tc}(t) = T_{tc}^{*}(t) + \left( \frac{\Theta_{g,1} \dot{\omega}_{c,e}(t)}{i_{g,1}^2\big(u_{g,1}(t)\big)} + \frac{\Theta_{g,2} \dot{\omega}_{c,m}(t)}{i_{g,2}^2\big(u_{g,2}(t)\big)} \right) \tag{A1.3}$$

Having introduced the definition of the torque split factor $u_{ts}$, as part of the control vector $u(t)$, the torques demanded to each power path can be computed as follows:

$$\begin{aligned} T_{g,1}(t) &= u_{ts}(t) \cdot T_{tc}(t) \\ T_{g,2}(t) &= \big(1 - u_{ts}(t)\big) \cdot T_{tc}(t) \end{aligned} \tag{A1.4}$$

Then speeds, accelerations and torques at the EM side can be computed using the gear-shift command $u_{g,2}$:

$$\begin{aligned} T_{c,m}(t) &= \frac{T_{g,2}(t)}{i_{g,2}\left(u_{g,2}(t)\right) \cdot \eta_{g,2}^{sign(T_{tc}(t))}} \\ \omega_{c,m}(t) &= \omega_{tc}(t) \cdot i_{g,2}\left(u_{g,2}(t)\right) \\ \dot{\omega}_{c,m}(t) &= \dot{\omega}_{tc}(t) \cdot i_{g,2}\left(u_{g,2}(t)\right) \end{aligned} \tag{A1.5}$$

The friction clutch between the EM and the $GB_1$ is supposed to be actuated instantaneously. As a consequence, it can switch between the engaged and the opened status within a simulation time step.

$$u_{c,m}(t) = \begin{cases} 1 & \text{if } u_{ts}(t) \neq 0 \\ 0 & \text{if } u_{ts}(t) = 0 \end{cases} \tag{A1.6}$$

Hence, the torque requested to the EM, including the inertia of the corresponding clutch and considering that its value depends on the state of the clutch, is the following:

$$\begin{aligned} T_m(t) &= \left[T_{c,m}(t) + \Theta_{\mathrm{c,m}}\dot{\omega}_{c,m}(t)\right] \cdot \left(u_{c,m}(t) = 1\right) \\ \omega_m(t) &= \omega_{c,m}(t) \cdot \left(u_{c,m}(t) = 1\right) \\ \dot{\omega}_m(t) &= \dot{\omega}_{c,m}(t) \cdot \left(u_{c,m}(t) = 1\right) \end{aligned} \tag{A1.7}$$

The inner motor torque can now be expressed by the following equation:

$$T_{m,i}(t) = T_m(t) + \Theta_{\mathrm{m}}\dot{\omega}_m(t) \tag{A1.8}$$

The electric power delivered/absorbed by the motor $P_m(t)$ is calculated by means of an experimental map (see (3.25)). The power requested from the battery can be calculated, once the electric power balance at the power link P is written, considering the auxiliary power absorbed $P_{aux}(t)$, and the power from/to the GEN component $P_{gen}(t)$, as follows:

$$P_b(t) = -P_m(t) - P_{gen}(t) - P_{aux}(t) \tag{A1.9}$$

The calculation of the SOC evolution is now straightforward and follows the same approach previously described in (3.27)-(3.30).

The ICE path is modeled similarly, with the following equation holding for the ICE clutch:

$$\begin{aligned} T_{c,e}(t) &= \frac{T_{g,1}(t)}{i_{g,1}\left(u_{g,1}(t)\right) \cdot \eta_{g,1}^{sign(T_{tc}(t))}} \\ \omega_{c,e}(t) &= \omega_{tc}(t) \cdot i_{g,1}\left(u_{g,1}(t)\right) \\ \dot{\omega}_{c,e}(t) &= \dot{\omega}_{tc}(t) \cdot i_{g,1}\left(u_{g,1}(t)\right) \end{aligned} \tag{A1.10}$$

The ICE clutch is modeled similarly to the model adopted for the EM clutch (A1.6):

$$u_{c,e}(t) = \begin{cases} 1 & \text{if } u_{ts}(t) \neq 1 \\ 0 & \text{if } u_{ts}(t) = 1 \end{cases} \tag{A1.11}$$

The total torque, at the ICE and GEN side, can now be computed:

$$\begin{aligned} T_e^*(t) &= \left[T_{c,e}(t) + \left(\Theta_{\mathrm{c,e}} + \Theta_{\mathrm{gen}} + \Theta_{\mathrm{e}}\right)\dot{\omega}_{c,e}(t)\right] \cdot \left(u_{c,e}(t) = 1\right) \\ \omega_e(t) &= \begin{cases} \omega_{c,e}(t) & \text{if } u_{c,e}(t) = 1 \\ \omega_e^{opt}\left(P_{gen,mech}(t)\right) & \text{if } u_{c,e}(t) = 0 \end{cases} \\ \dot{\omega}_e(t) &= \dot{\omega}_{c,e}(t) \cdot \left(u_{c,e}(t) = 1\right) \end{aligned} \tag{A1.12}$$

where $\omega_e^{opt}$ represents the optimal engine speed selected in pure series hybrid operating mode, which of course depends on the mechanical power requested by the corresponding generator power $P_{gen,mech}$ control input, and on the given engine FC map. The total mechanical power requested at the engine shaft is now:

$$P_e^*(t) = T_e^*(t) \cdot \omega_e(t) \tag{A1.13}$$

The theoretical GEN torque requested on the engine crankshaft can now be formulated.

$$T_{gen}^0(t) = \frac{P_{gen,mech}(t)}{\omega_e(t)} \tag{A1.14}$$

The electrical power demanded/delivered by the GEN component depends on the component map (3.25), as a function of the generator speed and torque.

$$P_{gen,mech}(t) = \frac{P_{gen}(t)}{\left(\eta_{gen}\left(T_{gen}^{0}(t), \omega_e(t)\right)\right)^{sign\left(P_{gen,mech}(t)\right)}} \tag{A1.15}$$

The inner mechanical power requested to the ICE is given by the following equation:

$$P_{e,i}(t) = -P_e^{*}(t) - P_{gen,mech}(t) \tag{A1.16}$$

It follows the definition of the theoretical torque of the ICE:

$$T_{e,i}^{0}(t) = \frac{P_{e,i}(t)}{\omega_e(t)} \tag{A1.17}$$

The definition of control variables in (A1.1) is chosen since it represents the minimum set of variables to describe the system. However, they are physically correlated. As a consequence, the system model (A1.2)-(A1.17) requires the introduction of some additional constraints, to prevent the evaluation of infeasible operating conditions during the DP optimization procedure.

The most relevant condition is related to the fact that the torque provided by the ICE is calculated as a consequence of the torque split factor $u_{ts}(t)$, and of the mechanical power of the generator GEN. When $u_{ts}(t) \neq 1$, and the vehicle is not operated in series hybrid mode, the model can assign arbitrary negative torques to the ICE. However, the maximum negative ICE torque cannot exceed the speed-dependent cranking torque, due to mechanical frictions and pumping losses, $T_{e,loss}$.

The effective ICE torque is subjected to the following constraints:

$$T_{e,i}(t) = \begin{cases} T_{e,i}^{0}(t) & \text{if } T_e(t) > 0 \\ T_{e,loss}\left(\omega_e(t)\right) & \text{if } T_e(t) < 0 \end{cases} \tag{A1.18}$$

The engine on/off state, theoretically defined by the engine start/stop control input $u_{ss}$, is here simplified as an instantaneous actuation, defined by the demanded engine torque.

$$x_e(u_{ss}(t)) = \begin{cases} 1 & \text{if } T_{e,i}(t) > 0 \\ 0 & \text{if } T_{e,i}(t) \leq 0 \end{cases} \tag{A1.19}$$

The torque of the generator on the engine crankshaft is also redefined, taking into account the previous relationships:

$$T_{gen}(t) = \begin{cases} min\left\{T_{gen}^{0}(t), \dfrac{P_e^*(t)}{\omega_e(t)} - T_{e,loss}\big(\omega_e(t)\big)\right\}, & \text{if } P_e^*{>}0 \\ T_{gen}^{0}(t), \ \text{if } (P_e^*{<}0) \wedge \left[\left(\dfrac{P_e^*}{\omega_e} - T_{e,loss} \leq T_{gen}^{0} \leq 0\right) \vee \left(T_{gen}^{0} < \dfrac{P_e^*}{\omega_e}\right)\right] & \\ \dfrac{P_e^*(t)}{\omega_e(t)} - T_{e,loss}\big(\omega_e(t)\big), & \text{if } (P_e^*{<}0) \wedge \left(T_{gen}^{0} > 0\right) \end{cases} \tag{A1.20}$$

The power provided by the mechanical brakes, directly mounted on the wheels, follows inherently, if $P_e^*(t){<}0$:

$$P_{mech,br}^{*}(t) = P_e^*(t) - \Big(T_{gen}(t) + T_{e,loss}\big(\omega_e(t)\big)\Big) \cdot \omega_e(t) \tag{A1.21}$$

It is calculated as it was applied directly on the crankshaft.

## A1.4 Case Studies

In the present subsection, the case studies selected to test the DP optimization approach to a Complex HV topology and choice of components, are presented. The formulae used in calculation are illustrated, which rely on the regulations for plug-in HVs. At the end of this Appendix, some numerical results for the simulation study are presented as well.

## Definition of the case studies

Among the set of all possible combinations introduced in Section A1.1, only a reduced subset is presented here, comprising the most interesting cases.

The same battery, with a total capacity of 25 Ah, is used for all the investigated systems. The analyzed configurations, listed in Table A1.2, are the following ten:

- Series HV (S);
- Parallel HV:
    - 2 cylinders ICE:
        - AS mounted on EM shaft (P-1);
        - AS mounted on GEN shaft (P-2);
    - 3 cylinders ICE: AS mounted on GEN shaft (P-3);
- Series/Parallel HV:
    - 2 cylinders ICE: AS on EM shaft and PM on GEN shaft:
        - 3 gears on $GB_1$ and 2 gears on $GB_2$ (SP-1,SP-3:5);
        - 3 gears on $GB_1$ and no gears on $GB_2$ (SP-2);
    - 2 cylinders ICE: AS on EM shaft and PM on GEN shaft (SP-6):

## FC calculation for a PHEV

The calculation of fuel consumption for a plug-in hybrid vehicle is regulated by the legislation, and follows specific regulations [191]. The formula is given here.

$$FC_{PHEV} = \frac{D_e \cdot FC_{SOC_{max}} + D_{avg} \cdot FC_{SOC_{min}}}{D_e + D_{avg}} \tag{A1.22}$$

Where the terms introduced in the equation above represent:

- $FC_{SOC_{max}}$ the FC in the test procedure starting at maximum battery state-of-charge ([l/100 km]);
- $FC_{SOC_{min}}$ the FC in the test procedure starting at minimum battery state-of-charge, for the prescribed driving cycle ([l/100 km]);
- $D_e$ the pure electric distance that the vehicle can cover ([km]), with a SOC excursion from the maximum, fully charged value, to the minimum SOC;
- $D_{avg}$ the average supposed distance between two consecutive battery recharges (25 [km]).

Hence, the DP optimization for the different HV concepts analyzed here requires two distinct runs:

1. The optimal use of the HV, to maximize the pure electric distance $D_e$, starting with $\mathrm{SOC}(0) = \mathrm{SOC}_{max}$; in case the vehicle is able to travel purely electric longer than a threshold distance, the associated $FC_{SOC_{max}} = 0$.
2. The optimal use of the HV to minimize FC starting with $\mathrm{SOC}(0) = \mathrm{SOC}_{min}$ for a given driving cycle.

For each calculation, the total number of breakpoints used in the DP algorithm must be carefully selected, since the problem is multivariable, and the well-known dimensional problems associated with the application of this numerical algorithm can easily occur.

The $FC_{SOC_{min}}$is performed with the following discretization of (A1.1):

$$x_M = [M_\xi] = [100]; \qquad u_N = \begin{bmatrix} N_{u_{ts}} \\ N_{P_{gen,mech}} \\ N_{g,1} \\ N_{g,2} \end{bmatrix} = \begin{bmatrix} 20 \\ 100 \\ 3 \\ 2 \end{bmatrix} \tag{A1.23}$$

The calculation of $D_e$ requires a different discretization, since only the EM is used to propel the vehicle and to recuperate kinetic energy during braking, optimizing the gear selection to operate the vehicle at the highest efficiencies of the electric components. The SOC will vary over the entire feasible range in this case, from completely charged to totally discharged conditions. As a consequence, an increased number of SOC breakpoints is required to attain an acceptable resolution.

$$x_M = [M_\xi] = [400]; \qquad u_N = \begin{bmatrix} N_{u_{ts}} \\ N_{P_{gen,mech}} \\ N_{g,1} \\ N_{g,2} \end{bmatrix} = \begin{bmatrix} 1 \\ 1 \\ 3 \\ 2 \end{bmatrix} \tag{A1.24}$$

## Results

The numerical results are listed in Table A1.2.

**Table A1.2: Summary of relative numerical results for the case studies analyzed. (E)=number of ICE cylinders, (m) = vehicle mass ([kg]), ($GB_i$) = gear ratios of i-th GB. (*) SP-2 with no dedicated GB: final drive ratio is indicated.**

| Case | E | EM | GEN | $GB_1$ | $GB_2$ | $m$ [%] | $FC_{SOCmin}$ [%] | $D_e$ [%] | $FC_{PHEV}$ [%] |
|---|---|---|---|---|---|---|---|---|---|
| S | 2 | AS | PM | - | [6.5, 3] | 103 | 125 | 103 | 125 |
| P-1 | 2 | AS | - | [18.5, 7.2, 3.7] | [6.5, 3] | 104 | 116 | 102 | 116 |
| P-2 | 2 | - | AS | [18.5, 6.9, 3.4] | - | **100** | **100** | 103 | **100** |
| P-3 | 3 | - | AS | [15.4, 6.9, 3.4] | - | 101 | 108 | 103 | 108 |
| SP-1 | 2 | AS | PM | [18.5, 7.2, 3.7] | [6.5, 3] | 107 | 114 | 101 | 116 |
| SP-2 | 2 | AS | PM | [18.5, 7.2, 3.7] | [5]* | 103 | 105 | **108** | 102 |
| SP-3 | 2 | AS | PM | [18.5, 9.1, 4.5] | [6.5, 3] | 107 | 116 | 101 | 118 |
| SP-4 | 2 | AS | PM | [18.5, 8.3, 3.7] | [6.5, 3] | 107 | 115 | 101 | 116 |
| SP-5 | 2 | AS | PM | [18.5, 8.7, 4.1] | [6.5, 3] | 107 | 115 | 101 | 117 |
| SP-6 | 3 | AS | PM | [15.4, 6.9, 3.4] | [6.9, 3.4] | 108 | 121 | 100 | 124 |

In the Table above, all the results are normalized with respect to the minimum value of each column, set 100%.

The best overall results can be reached by means of the P-2 configuration, which is also the lightest one.

Considering the SP cases, the best solution is represented by SP-2, where the GB on the EM shaft is removed. The latter is also the configuration that covers the longest electric distance.

The following figures depict some of the more relevant signals resulting from the calculation of the optimal control sequence performed by means of DP, for the SP-5 case.

Firstly, the time evolutions of SOC (state variable), torque split factor and GEN mechanical power demand (control variables), are shown in Figure A1.5.

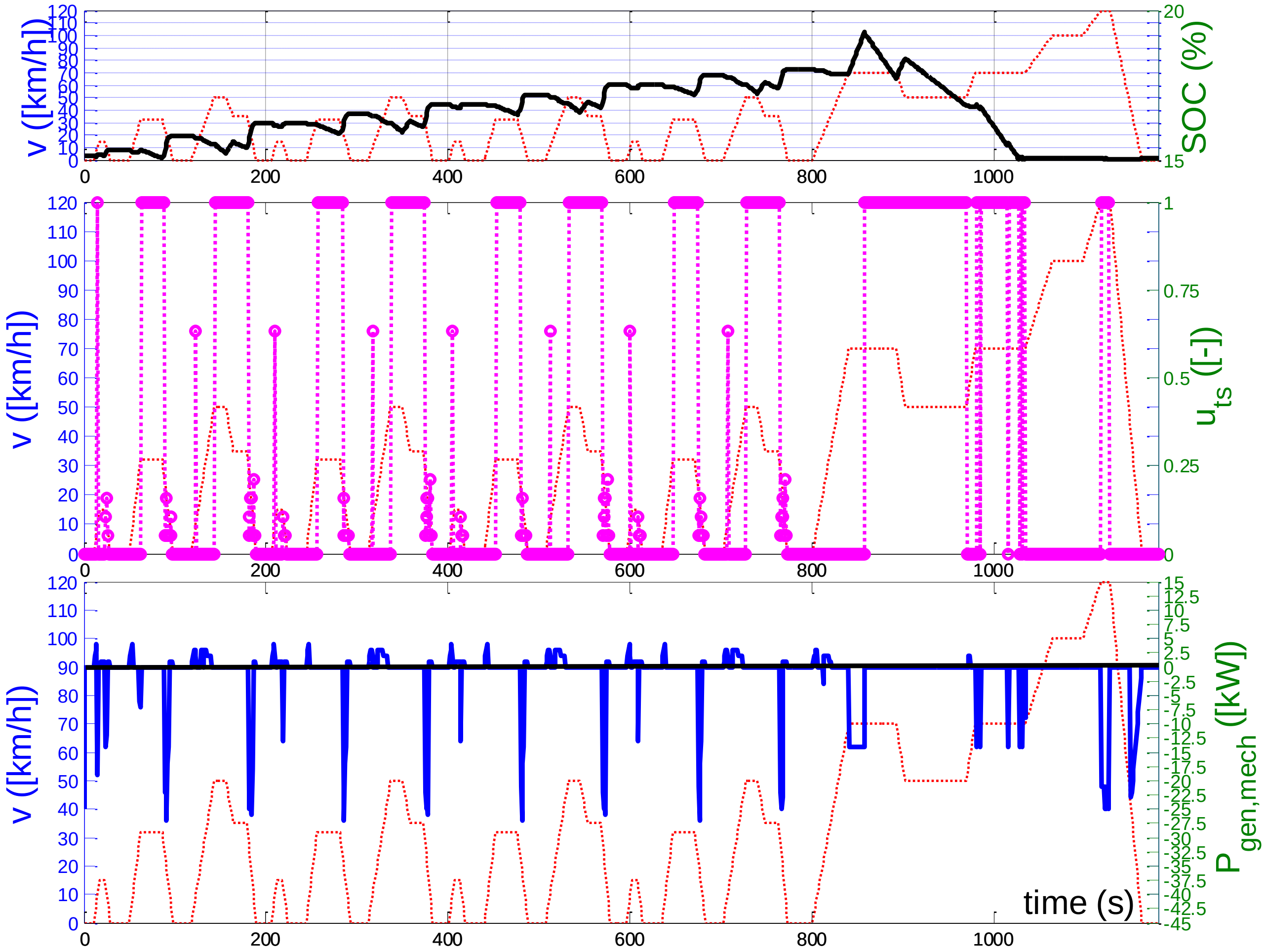

Figure A1.5: Time evolution of state and control variables; SOC, torque split factor and GEN mechanical power on a NEDC cycle, SP-5.

The remaining two control inputs, selected gears of $GB_1$ and $GB_2$, are shown in Figure A1.6.

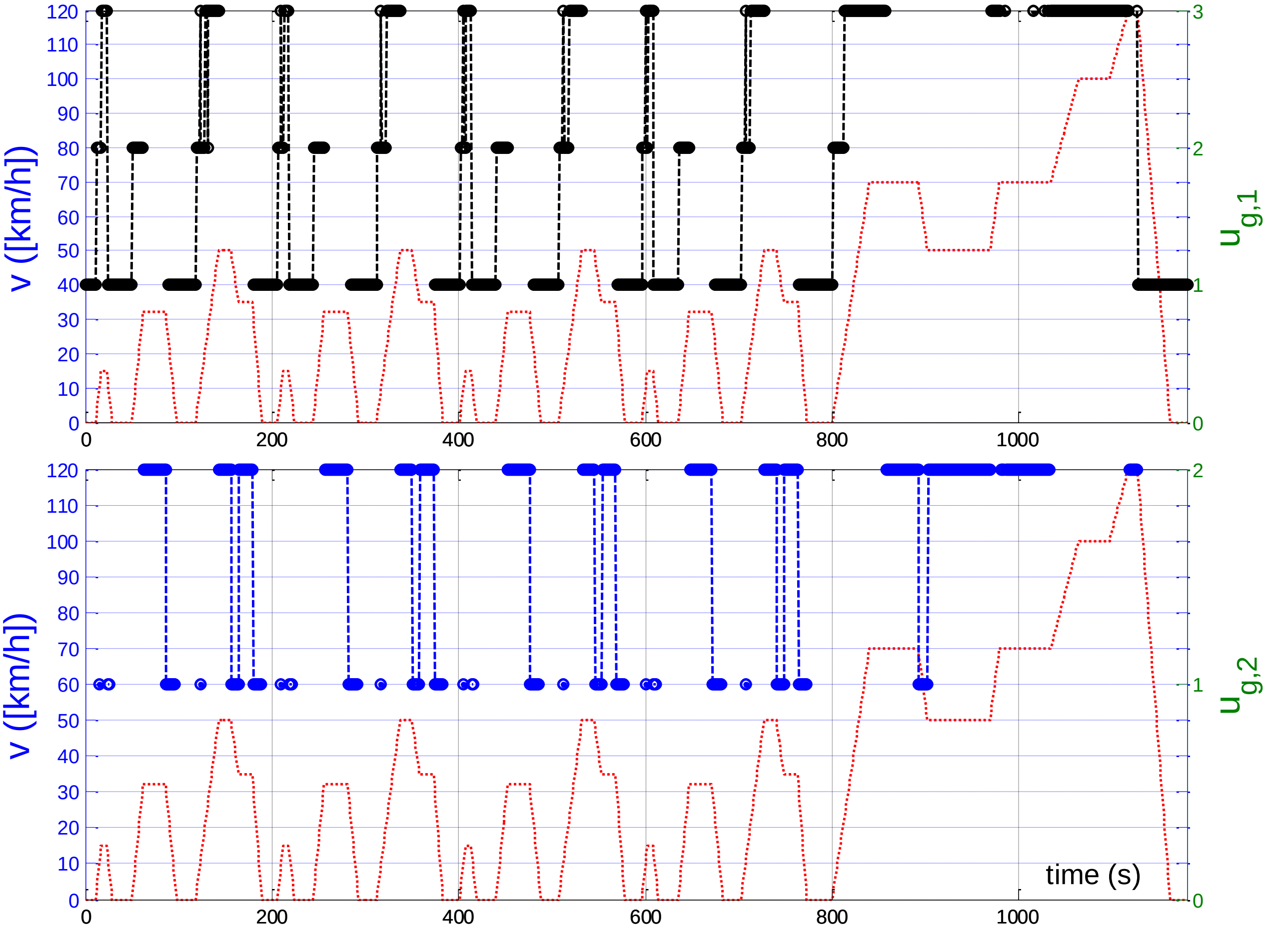

Figure A1.6: Time evolution of gear selection for both gearboxes on a NEDC cycle, SP-5.

Figure A1.7 depicts the time evolution of the torques provided/absorbed by the three prime movers forming the power unit, the ICE and the two electric motors.

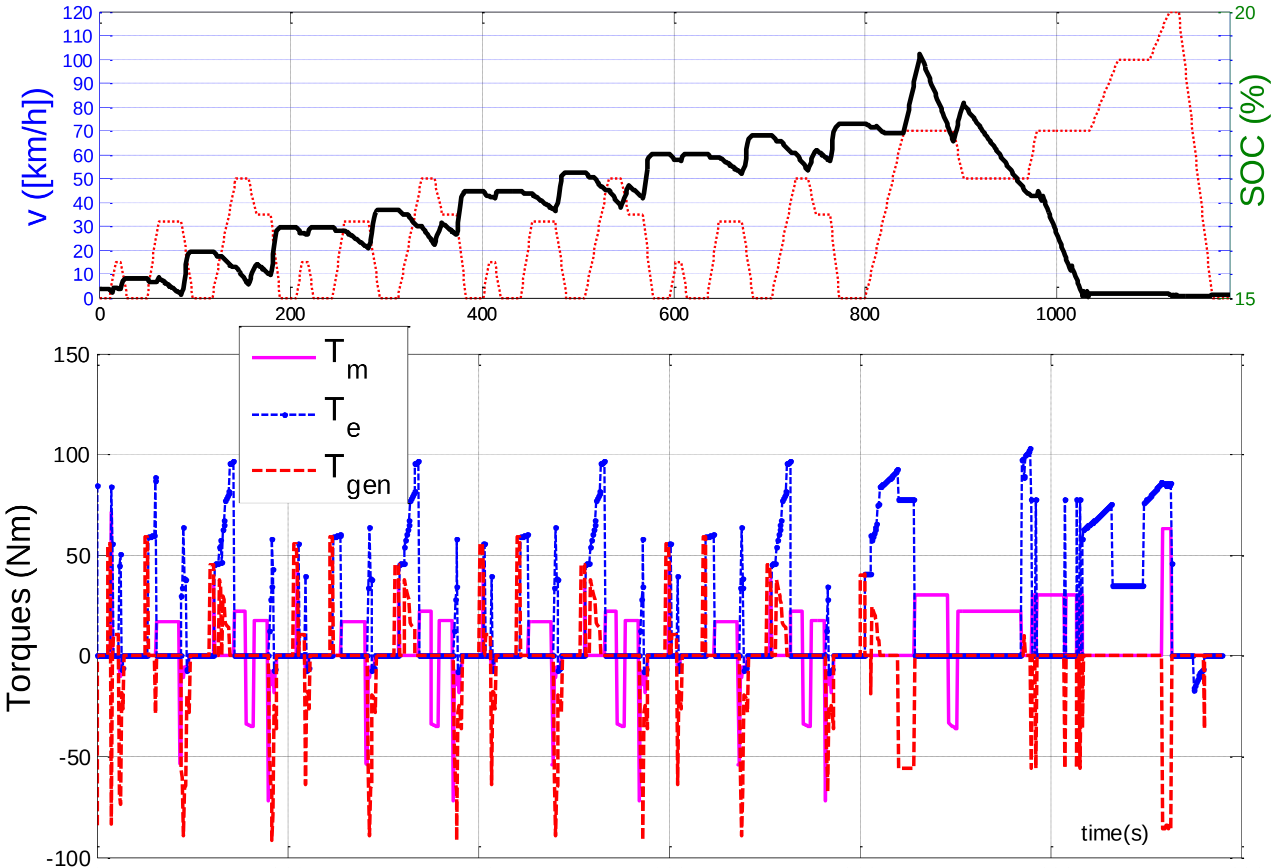

Figure A1.7: SOC evolution (upper plot) and Torques of the electric motors and ICE (lower plot) on a NEDC cycle, SP-5.

The driving modes described in Table A1.1 are depicted in Figure A1.8 for the case study analyzed here, SP-5.

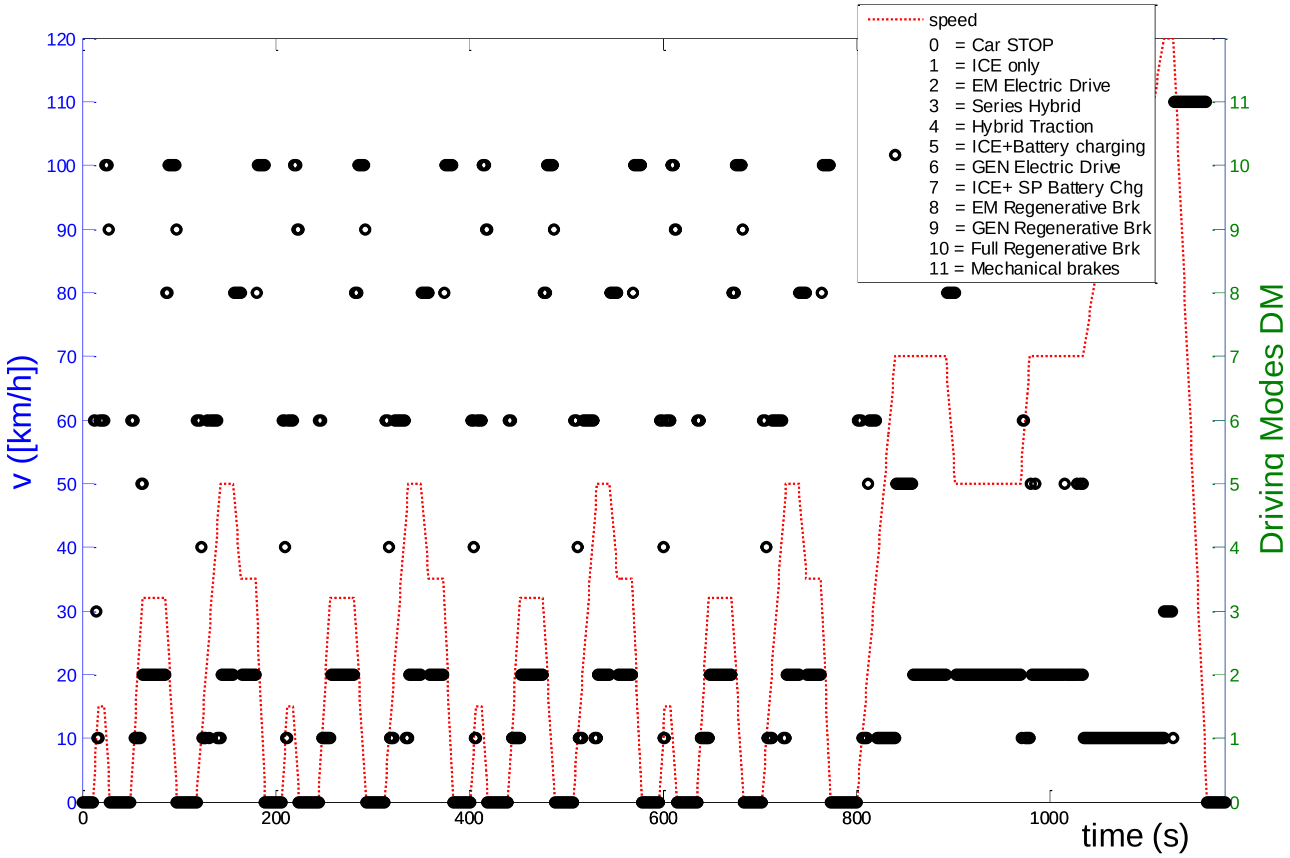

Figure A1.8: DM on NEDC cycle, SP-5.

The use of Series mode is very limited here, while mode (7) (ICE and series/parallel battery charging) never occurs.

An interesting analysis concerns the use of gears for each gearbox, affecting the ICE and the GEN in case of $GB_1$ and the EM in case of $GB_2$.

Figure A1.9 shows the frequency distribution plot of the ICE operating points, for each gear engaged.

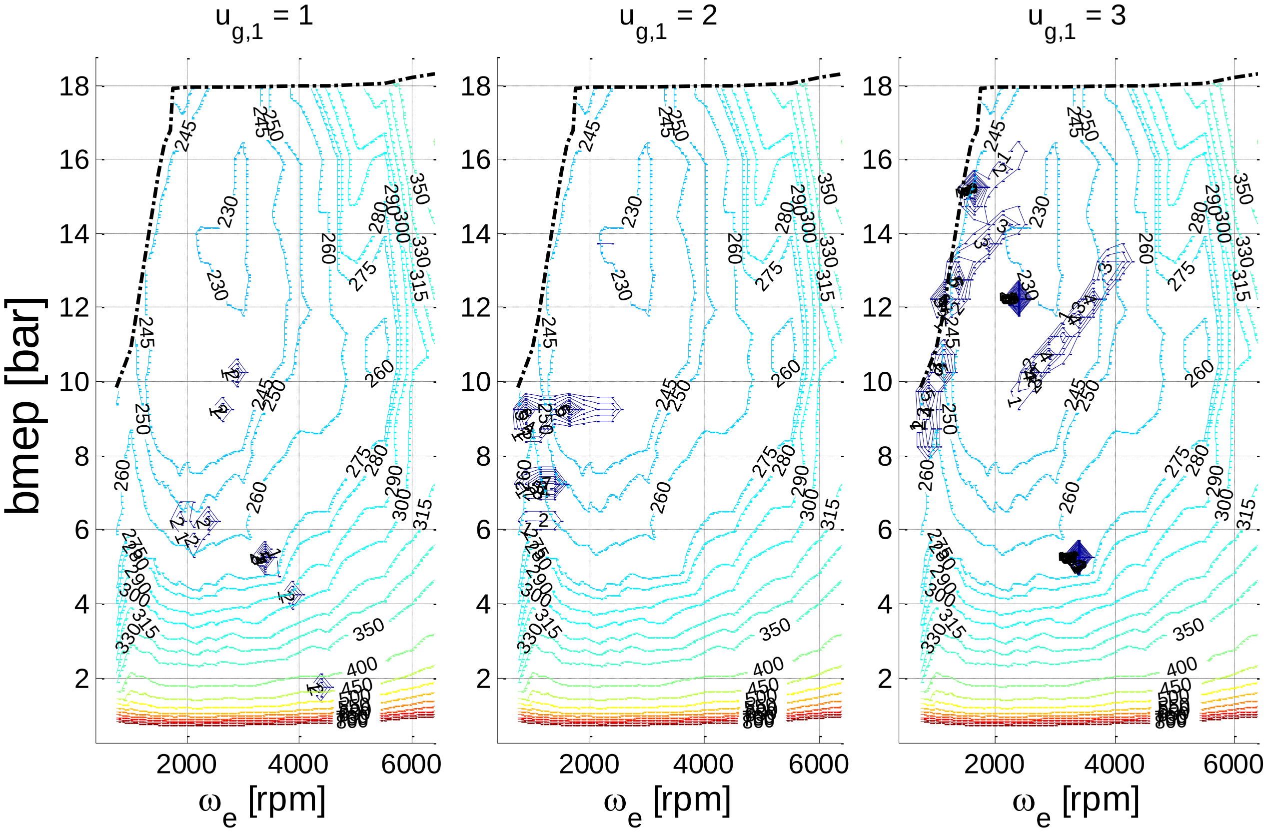

Figure A1.9: Frequency distribution of ICE operating points per gear selected, NEDC cycle, SP-5. SFC expressed in [g/kWh].

This plot enhances the designers to assess the goodness of the gear ratios implemented, since the DP algorithm always provides their optimal use for each driving mission simulated.

Similar considerations hold for Figure A1.10 and Figure A1.11, where the frequency distributions of the two electric machines are shown.

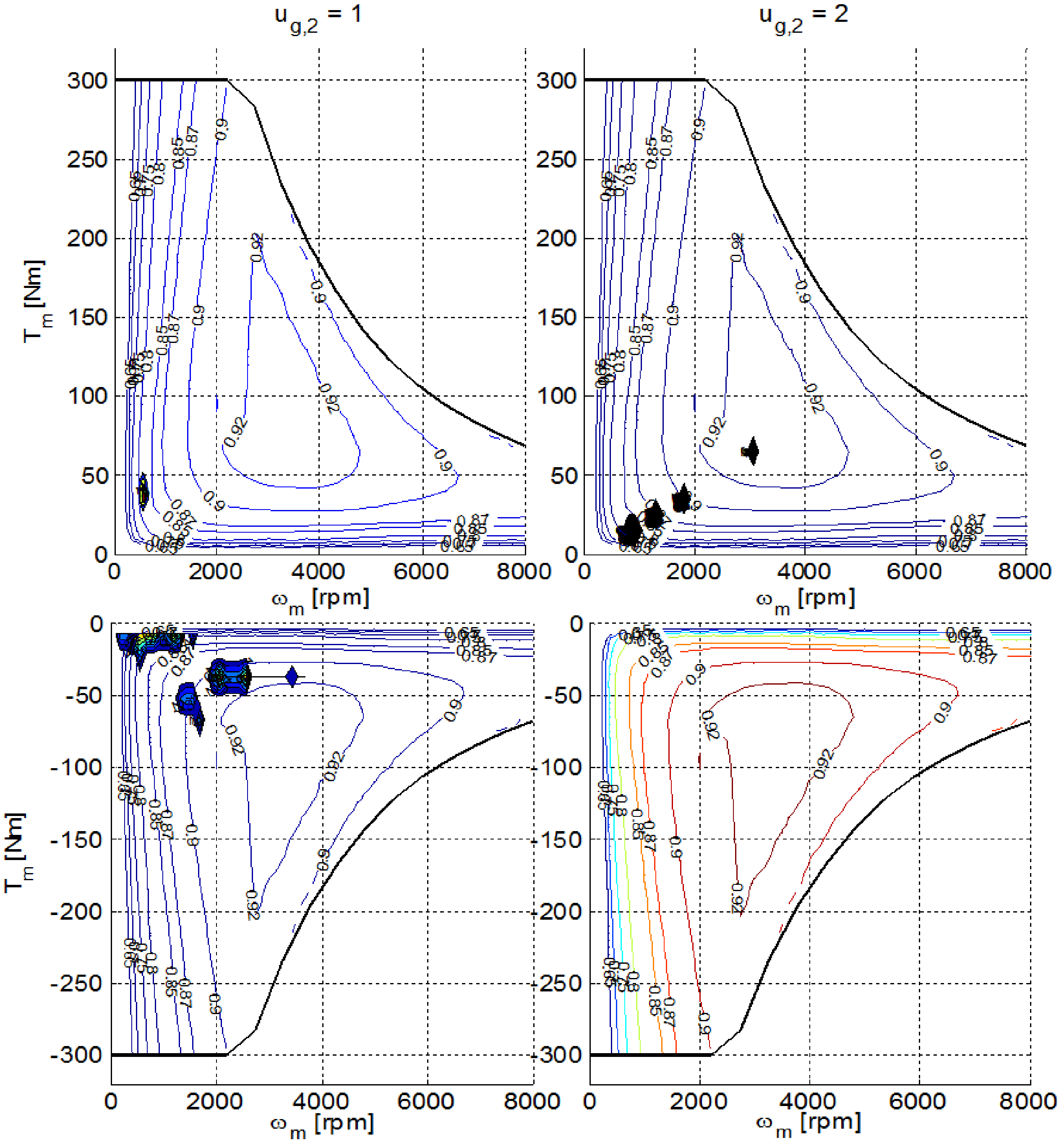

Figure A1.10: Frequency distribution of EM operating points per gear selected, NEDC cycle, SP-5.

In the figure above, it is evident how the second gear of $GB_2$ is never used to operate the EM as a generator.

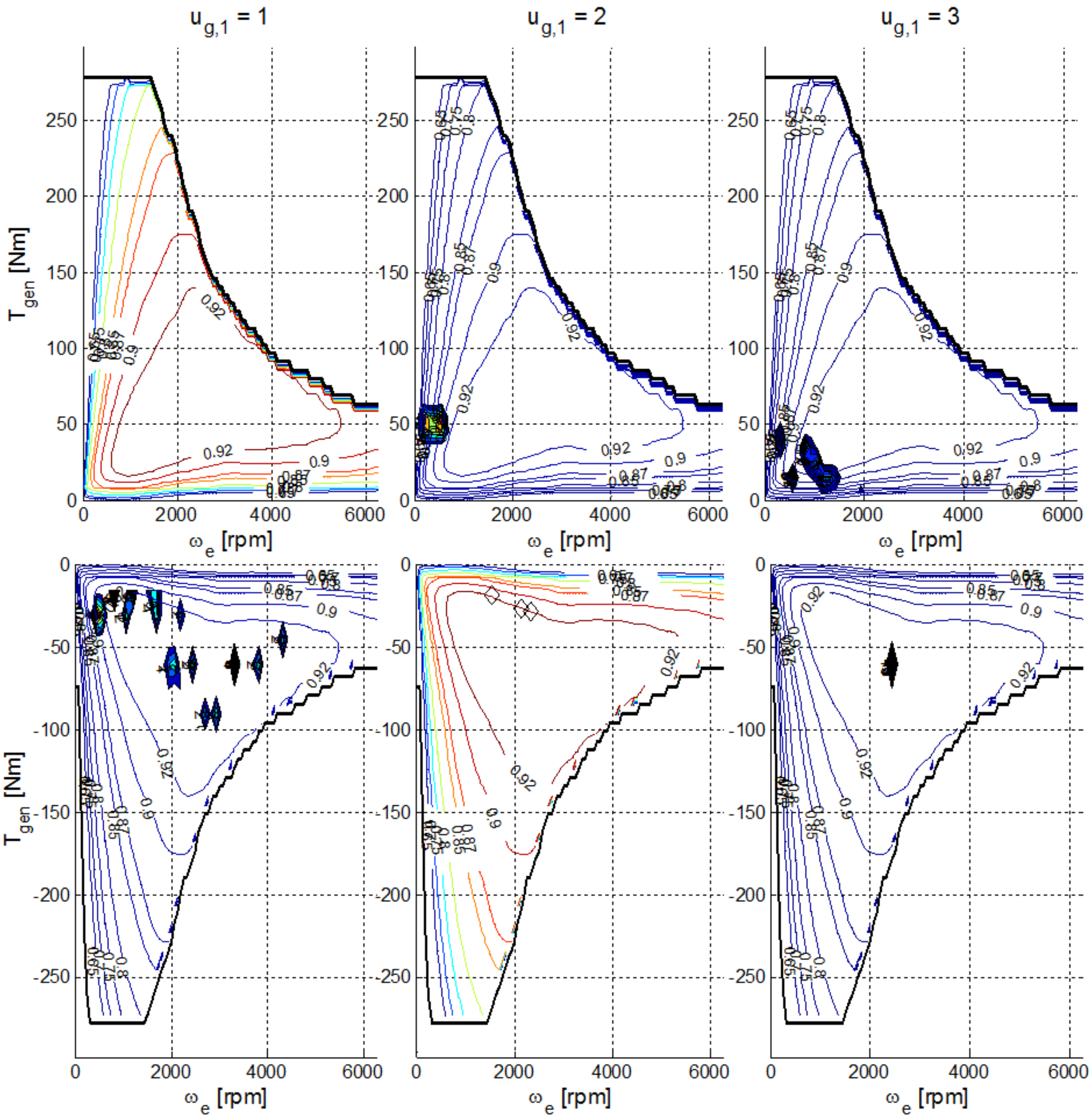

**Figure A1.11: Frequency distribution of GEN operating points per gear selected, NEDC cycle, SP-5.**

Similarly, Figure A1.11 clarifies that the first gear ratio of $GB_1$ is never engaged when GEN operates as a motor, while the second gear is seldom adopted in generator mode.

# A.2

# DP-based Benchmarking of a Hybrid Power System

This second Appendix presents a theoretical study of how wind power can be complemented by hydropower and conventional fossil fuel fired energy systems. The problem is addressed with DP. A conceptual framework is provided for a hybrid power system, which generates constant power output without the intermittent fluctuations that inherently occur when using wind power. The hybrid wind-hydro-thermal system guarantees continuous availability of firm power to the grid, combining a wind farm and complementary PSH and GTs, see Figure A2.1.

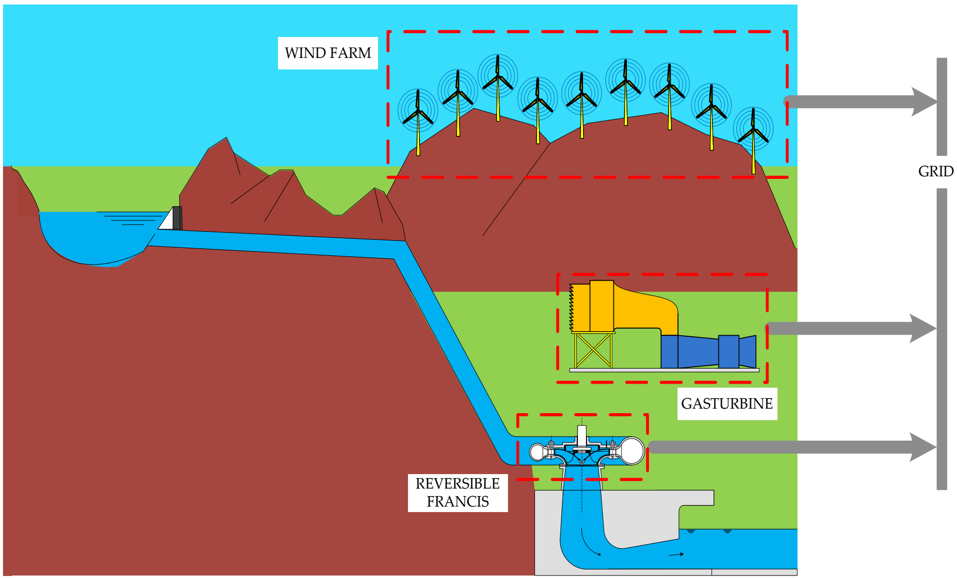

Figure A2.1: Schematic of the integrated power system.

Two different commitment strategies are analyzed and compared: (i) an in-house "custom" control strategy and (ii) an "optimal" control strategy based on Dynamic Programming (DP).

# A2.1 Hybrid System Description

Wind farm and load profiles

To analyze the behavior of the integrated system in different wind conditions, different days, representative of a high, medium and low wind power output, are considered in the following. Moreover, to investigate the effect of PSH system on GTs generation, two different sequences of wind generation are analyzed (Case (A) and Case (B)), reported in Figure A2.2 and Figure A2.3 respectively.

In both considered cases, the overall investigated time period is equal to 4 days. These two scenarios are essentially characterized by different positions, inside the total considered time span, of the maximum (located within day #1) and minimum (within day #3) of wind production.

Therefore, the expected behavior of the compensating energy sources (GTs and Hydro), affected by the residual storage capacity, could be different between Case (A) and Case (B), even if the nameplate installed capacity is the same.

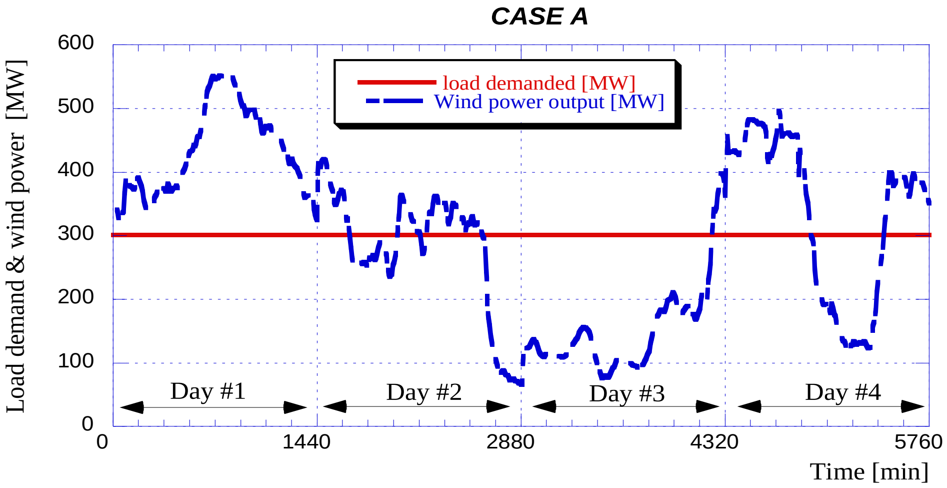

Figure A2.2: Wind farm power output and load demanded by the grid, Case (A).

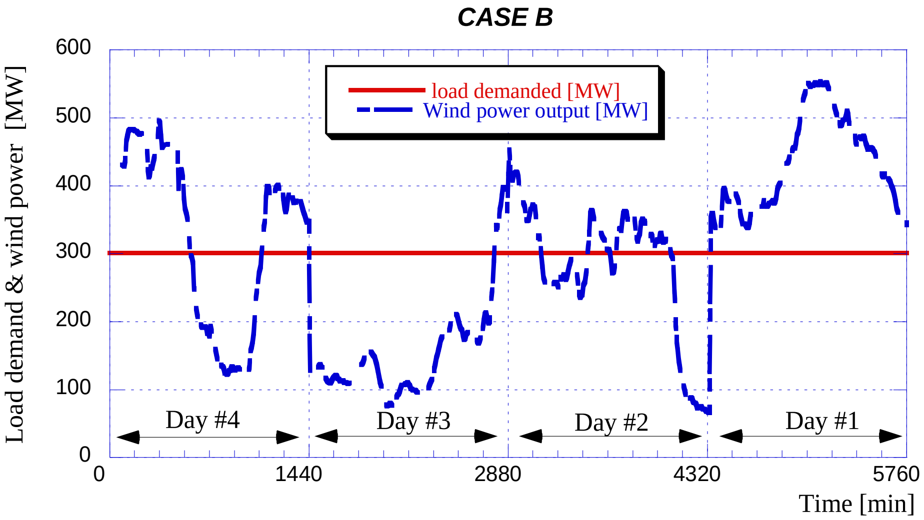

**Figure A2.3: Wind farm power output and load demanded by the grid, Case (B).**

As shown in the previous figures, the constant power output provided to the grid is fixed at 300 MW. This value is assumed according to the average Capacity Factor (CF) for the selected days. In particular, CF is defined as:

$$CF = \frac{\int P_w(t)dt}{\int P_{w,max}(t)dt} \tag{A2.1}$$

It expresses the ratio between the actual energy produced with the wind in a given time period ($P_w$) and the maximum possible energy ($P_{w,max}$), obtained when the wind turbines work all the time at the rated power output. For the selected days, the average value of CF is 0.32. Thus, the firm power guaranteed to the grid is about 32% of the nominal wind power capacity.

Storage System

Among all storage technologies for large-scale applications, pump hydro storage (PSH) is a mature and diffused technology.

It provides a technical solution for the grid manager to ensure real time balance between production and consumption, allowing the optimal use of the wind resources and avoiding unbalanced power in case of overproduction. Moreover, PSH makes easier to integrate wind power into the grid, increasing the wind energy penetration rate by means of a better control for frequency and voltage.

The specifications of the assumed PSH system are listed in Table A2.1; a reversible variable speed Francis machine is assumed. Pumped storage can operate either in pumping or in generating mode, not both.

The main advantages of the variable speed configuration are the higher efficiencies in turbine mode and the capability to adjust the pump load to the network needs. It results in a wider range of regulating capacities: typically between 60% and 100% in pumping mode, while between 15% and 100% in generation mode.

Pumped storage is represented here by a water storage reservoir. Penstock losses are accounted in the PSH model. The pump and the turbine efficiencies, for the sake of simplicity, are assumed to be constant, even at partial load. A maximum variation of the reservoir height (i.e. a limitation of the dispatchable volume of water between reservoirs) is imposed according to the PSH real operation. The limited water height variation imposed is 2 meters. Both pumping and generating are subject to ramping and minimum/maximum capacity constraints. A time resolution of 8 minutes is taken as the time step for the simulations, guaranteeing that the storage is able to switch from full pumping capacity to full generating capacity within the so defined fixed time interval.

The dispatchable volume of water can be transferred in generation mode from the upper to the lower reservoir in 11 hours, and vice versa in 10 hours in pumping mode at full capacity.

**Table A2.1: Values of the main parameters of the reversible variable-speed Francis pump-turbine**

| Data | Pump | Turbine |
|---|---|---|
| Maximum Power [MW] | 149 | 163 |
| Minimum Power [MW] | 96.9 | 24.5 |
| Volumetric flow rate [$m^3/s$] | 69. 7 | 64.4 |
| Efficiency [%] | 82.9 | 89.7 |
| Max. volume inside reservoir [$10^6$ $m^3$] | 5.00 | |
| Min. volume inside reservoir [$10^6$ $m^3$] | 2.50 | |
| Dispatchable volume [$10^6$ $m^3$] | 2.50 | |
| Surface of reservoirs [$km^2$] | 1.25 | |
| Max. water height inside reservoir [m] | 281 | |
| Allowed water height variation [m] | 2.00 | |

## Gas Turbine models

To investigate the influence of GTs performance on their capability to compensate wind power output fluctuation and variability, both an aero-derivative (AERO) and a heavy-duty (HD) GT are considered in the present study. Both GTs are characterized by their quick ramping regulation and their high efficiencies, even at partial load and in case of a fast start.

Table A2.2 lists the values of the main parameters of the selected gas turbines at ISO conditions:

- LMS 100: a three shafts machine, with 42 bar of PR, a TIT higher than 1300 ℃ and intercooled cycle, is a state-of-art high efficiency machine;
- SGT6-5000F: a single shaft, with 17 bar of PR, is a modern heavy-duty gas turbine, designed for both simple cycle and combined cycle (CC) power generation in utility and industrial service.

The total power provided by the GT units is sufficient to cover the total firm power (300 MW) power output, even if no power from the wind is available.

The LHV efficiencies of the aero-derivative and the heavy duty GTs are plotted in Figure A2.6 as function of the GTs load. As shown in figure, the efficiency of AERO GT is higher compared to the HD-GT one, both at full and at partial load, so that the regulation of the aero-derivative GT should be preferable to the heavy duty one, although if the compensating power is extremely high only the HD machine can provide it.

Figure A2.4 and Figure A2.5 show the start-up times and the fuel consumptions of the aero and the heavy-duty GTs, respectively.

While in case of LMS100, fuel consumption data are collected according to real field tests, in case of SGT6-5000F, the natural gas consumption during the start-up procedure is obtained via a linearization between the minimum and the maximum values.

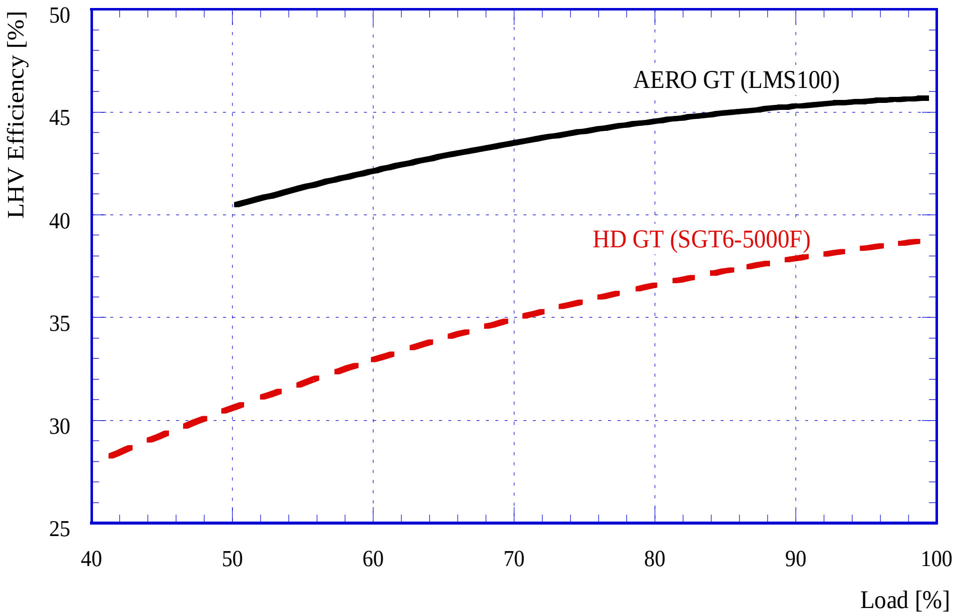

Figure A2.4: LMS100 and SGT-5000F LHV part-load performance.

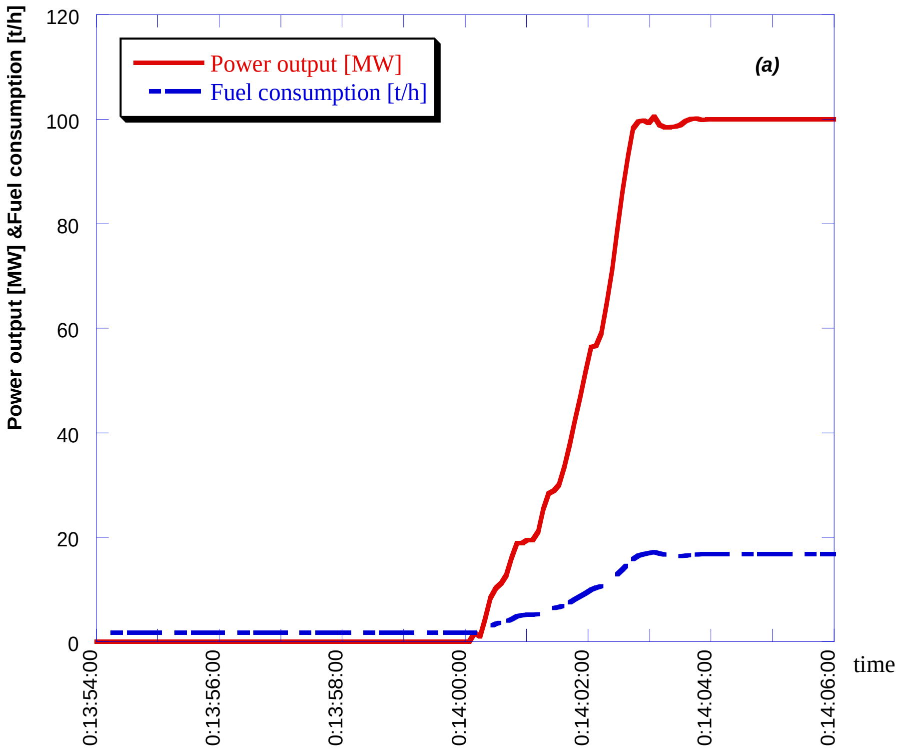

Figure A2.5: LMS100 Power output and fuel consumption during start-up.

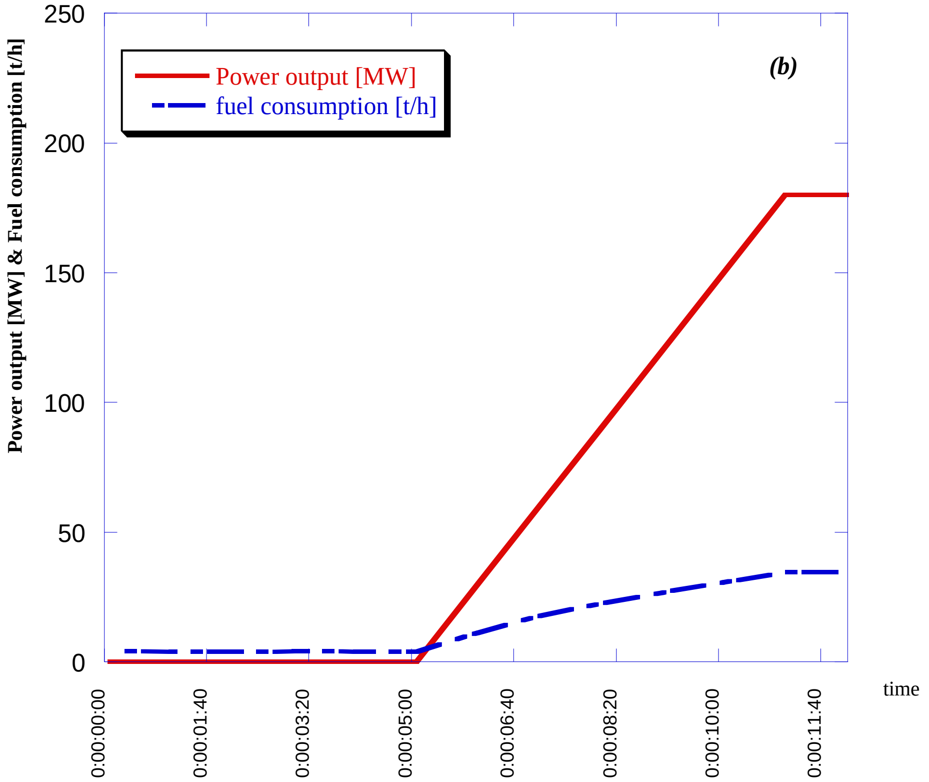

Figure A2.6: SGT6-5000F assumed Power output and FC during start-up.

Table A2.2: Data of the Gas Turbines at ISO conditions.

| Data | General Electric<br>LMS 100 | Siemens<br>SGT6-5000F |
|---|---|---|
| Max. power output [MW] | 100 | 208 |
| Min. power output [MW] | 50 | 83.2 |
| Ramp Rate [MW/min] | ∼ 50 | ∼ 30 |
| GT peak efficiency [%] | 45.0 | 38.6 |

## A2.2 Hybrid system modeling

Two control strategies are used for the power management and unit commitment: (i) a custom control strategy and (ii) Dynamic Programming (DP). Both algorithms aim at coordinating the thermal and the hydro systems to guarantee firm power to the grid during the overall time period of 4 days.

Both operating strategies used for the dispatching controller are based on these key requirements: (1) the hybrid system must be capable of delivering 300 MW of firm power to the grid for all the investigated time period; (2) the goal of both strategies is to minimize the natural gas fuel consumption, trying to avoid or to minimize overproduction. Specific features of the strategies are reported in the following sections.

Heuristic causal Custom Strategy

The custom strategy algorithm developed and assumed for the calculation of GTs and PHS operation is schematically presented in Figure A2.7.

The calculation code receives, at each time step $k$, data load and wind power profiles as an input and it provides, as output data, GTs and PSH power profiles during the day.

More in details, according to the flowchart illustrated in Figure A2.7, for each time step the custom strategy firstly evaluates the difference between the wind power output and the load demanded:

- If the wind power is lower than the grid request, the water level inside the upper reservoir needs to be higher than the minimum value to use the hydro turbine;
- If the hydro turbine cannot be used, because the actual storage level is below the minimum value, the gas turbines are turned on to meet the requested load;
- Otherwise, in case of wind overproduction, the surplus of power output can be used to pump water from the lower to the upper reservoir; in this case the overproduction power output needs to be higher than the minimum pump power requested. This is feasible only if the water volume in the upper reservoir is lower than the maximum water volume allowed.

In case of GTs operation, a specific control strategy is adopted to take into account GTs limitations in minimum turn down ratio, and different GTs efficiencies at part load operation (see Figure A2.4).

GTs control strategy is implemented by choosing as many units as possible in full load, to meet the requested power output. The difference is provided by the units that could meet partial load, determined by wind variations.

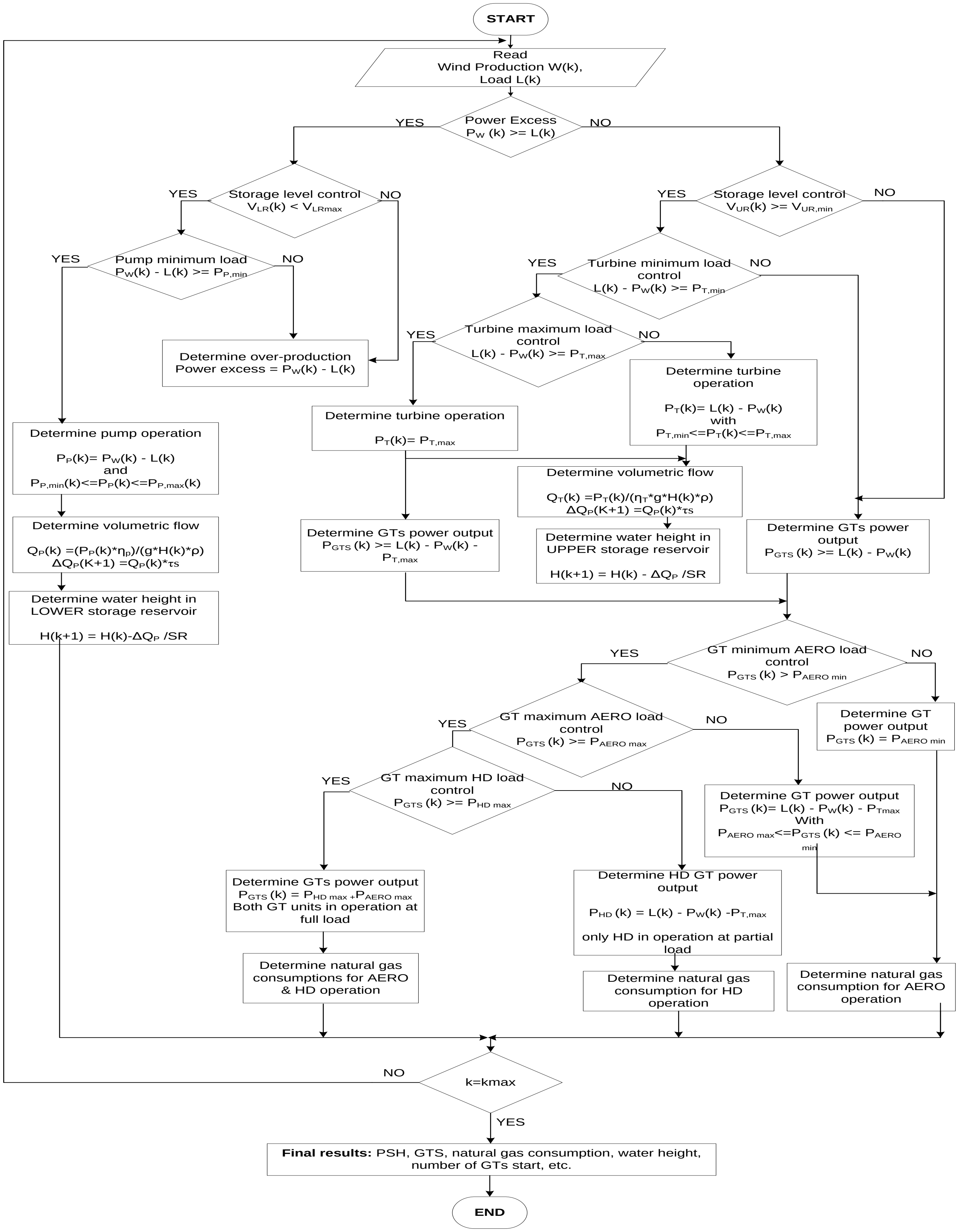

Figure A2.7: "Wind-PSH-GT" Custom Strategy algorithm - block diagram.

Dynamic Programming

To asses and compare the performance of the previously described custom management strategy, an optimal control procedure has been developed, based on the DP algorithm, see Section 4.2.1.2.

Throughout this section, the framework of the DP application to the integrated energy system is described in details.

The dynamic system model is completely defined by the choice of the state variables vector $x_k$, the control inputs vector $u_k$, the cost function expression, the constraints and the infeasibilities. The state variables and control input vectors, at any generic time step $k$, can be expressed as follows:

$$x_k = \begin{bmatrix} S_{HD,k} \\ S_{AERO,k} \\ H_k \end{bmatrix};$$

$$u_k = \begin{bmatrix} S_{HD,k+1} \\ S_{AERO,k+1} \\ P_{HD,k} \\ P_{AERO,k} \\ S_{PSH,k} \end{bmatrix}; \tag{A2.2}$$

where $S_{i,k}$ is a discrete variable (0 meaning *off* and 1 meaning *on*) that refers to the current state of the single energy converter unit (HD, AERO, PSH), whereas $S_{i,k+1}$ indicates its state at the next time stage. This idea, combined with the choice of a computational time step $t_s$ (8 min) that ensures that each of the two types of GTs can complete its start-up procedure, allows accounting for the fuel consumption amount of the considered power unit. If the turbine is on, the input variable $P_{i,k}$ determines the value of the constant power delivered for the entire time step duration. This modeling approach, with the use of discrete variables to define the power unit states and a relatively large time-step, helps keeping the computational time acceptable, while still allowing the model to capture some important physical aspects of the problem, such as the light-off consumption and the maximum power reached in a single time step when starting from off conditions. The alternative choice of utilizing $P_{i,k}$ and $P_{i,k+1}$ would lead, on one hand, to the chance of freely reducing the computational time step, while on the other hand it would require a strongly increased number of breakpoints to describe such continuous inputs, while ensuring numerical accuracy. In DP, the numerical effort increases exponentially with the number of variables and their resolution. A similar state identifier is adopted for the PSH, using $S_{PSH,k}$. When the pump-hydro-storage system is on, whether it operates in pumping mode or in turbine mode, its power is calculated as:

$$P_{PSH,k} = L_k - (P_{W,k} + P_{HD,k} + P_{AERO,k}) \tag{A2.3}$$

where $L_k$ is the requested load, $P_{HD,k}$ and $P_{AERO,k}$ the HD-GT and AERO-GT power outputs respectively and $P_{PSH,k}$ the calculated pump/hydro power output.

The water height $h_k$ dynamics can be calculated, once the volumetric flow $\dot{V}_{PSH,k}$ is determined, thus implying a given volume variation of the stored water mass:

$$\dot{V}_{PHS,k} = \begin{cases} \dfrac{P_{PSH,k}}{\eta_t \cdot g \cdot h_k \cdot \rho_w}, & if \quad P_{PSH,k} > 0 \\ \dfrac{P_{PSH,k} \cdot \eta_p}{g \cdot h_k \cdot \rho_w}, & if \quad P_{PSH,k} < 0 \end{cases} \tag{A2.4}$$

$$\Delta V_{PSH,k \to k+1} = \dot{V}_{PSH,k} \cdot t_s \tag{A2.5}$$

$$h_{k+1} = h_k + \frac{\Delta V_{PSH,k \to k+1}}{SR} \tag{A2.6}$$

At each stage during the backward DP calculation, an instantaneous cost function is evaluated, as the sum of the fuel consumption of each GT, at the power rate determined by the corresponding control input, increased by the amount of fuel requested by the turbine start-up to reach the current power level, if a turbine switch occurs, from 0 to 1:

$$C_k = \begin{cases} \displaystyle\sum_{j=HD}^{AERO} \left\{ \dot{m}_{fuel-j,k}\left(P_{j,k}\right) \cdot t_s + m_{fuel-j,k}\left(0 \to P_{j,k}\right) \right\} \\ \qquad if\left(S_{j,k+1} = 1\right) \cap \left(S_{j,k} = 0\right) \\ \displaystyle\sum_{j=HD}^{AERO} \left\{ \dot{m}_{fuel-j,k}\left(P_{j,k}\right) \cdot t_s \right\}, else \end{cases} \tag{A2.7}$$

To prevent the optimal policy from completely discharging the water reservoir, a cost must be associated with the value assumed by the energy level of the water mass stored at the end of the mission. Indeed, the cost function defined by (A2.7) would be likely to be minimized over the prescribed mission, by a strategy that tends to discharge the energy buffer as much as possible, while fulfilling the constraints on powers for every power unit. Several techniques have been developed to deal with the issues related to problems with hard constraints on the final states. In the considered problem, a straightforward approach is implemented. The state of energy $E_0$ associated with the initial water height $h_0$, and to its relative stored water mass $m_{a0}$, is known and can be calculated as:

$$E_0(h_0) = m_{a0} \cdot g \cdot h_0 = \rho_a \cdot SR \cdot (h_0 - h_{min}) \cdot g \cdot h_0 \tag{A2.8}$$

Similarly, a hydraulic energy amount $E_{if}(h_{if}) = \rho_a \cdot SR \cdot (h_{if} - h_{min}) \cdot g \cdot h_{if}$ can be associated to every possible value of the final water height state $h_{if}$ (with $i = 1 \ldots N$ discrete values of $h_k$) in the DP procedure, which is also the first computational step of the overall time backward calculation. Under these hypotheses, a fuel-equivalent cost $g_{Ni}$ can be attributed to any given water height value $h_{if}$ at the end of the time horizon, due to the introduction of an equivalence factor $s^*$, which defines an approximate correspondence between the fuel chemical energy and the hydraulic energy:

$$g_{Ni}(h_{if}) = s^* \cdot \frac{E_0(h_0) - E_{if}(h_{if})}{LHV} \tag{A2.9}$$

The equivalence factor should take into account the efficiencies of the system, involved respectively during the charging and the discharging operations. If the final energy stored in the hydraulic buffer is lower than the initial one, a certain amount of fuel must be taken into account, needed to recharge the storage system in future operations, up to the initial value. The opposite condition of overcharging at the end-of-mission, is treated by means of similar considerations. The outcome of the latter modeling approach is the use of two distinct values for $s^*$, one concerning the positive and the other one the negative energy imbalance throughout the control mission:

$$s^* = \begin{cases} s_{dis} = \dfrac{1}{\eta_{gt,chg} \cdot \eta_p}, & if \quad E_0(h_0) < E_{if}(h_{if}) \\ s_{chg} = \dfrac{\eta_t}{\eta_{gt,dis}}, & if \quad E_0(h_0) > E_{if}(h_{if}) \end{cases} \tag{A2.10}$$

where the two $\overline{\eta_{gt}}$ terms represent the weighted average efficiencies of the two gas turbines. These can be calculated by weighting the instantaneous efficiencies with the number of times that the single turbine is actually used. Of course, since these values are not known a priori, an iterative procedure must be established, to modify the final cost values for each DP run, updating the supposed equivalence factors with the actual ones, until a desired threshold is achieved.

## A2.3 DP vs. Custom Strategy: results

The output of the DP can be summarized as a map, supplying the desired optimal control inputs vector ${u_k}^{opt}$ at each time stage $k$, and for each value of the states vector $x_k(k)$.

The in-house developed Custom strategy is fully causal, meaning that the decisions applied at each time only rely on the current system conditions, based on heuristic criteria. As a consequence, it is perfectly suitable for real-time implementation, since it doesn't require any knowledge of the future evolution of the system disturbances, meaning, in the present study, a precise available wind power forecast.

The obtained results are shown for the two considered scenarios, Case (A) and Case (B), highlighting the differences between the two applied control strategies (DP and Custom).

The results provided in the following paragraphs are:

i. The AERO and the HD turbines power output duration curves and instantaneous profiles;
ii. The PSH pump and the PSH turbine power profiles;
iii. The State Of Charge (SOC) profiles of the PSH;
iv. The AERO and the HD GTs total fuel consumption including the residual PSH imbalance;
v. The number of AERO and HD GT start-up/shut-down events.

The obtained duration curves for the GTs power outputs during Case (A) scenario are plotted in Figure A2.8 for both strategies, while the Case (B) scenario is illustrated in Figure A2.9.

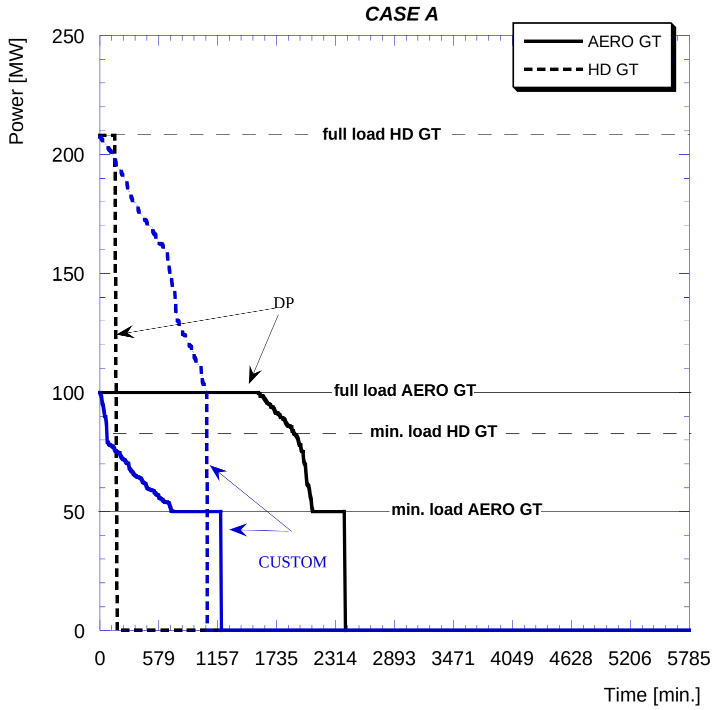

Figure A2.8: Duration curves for GTs power output during CASE (A) operation - DP vs. Custom Strategy.

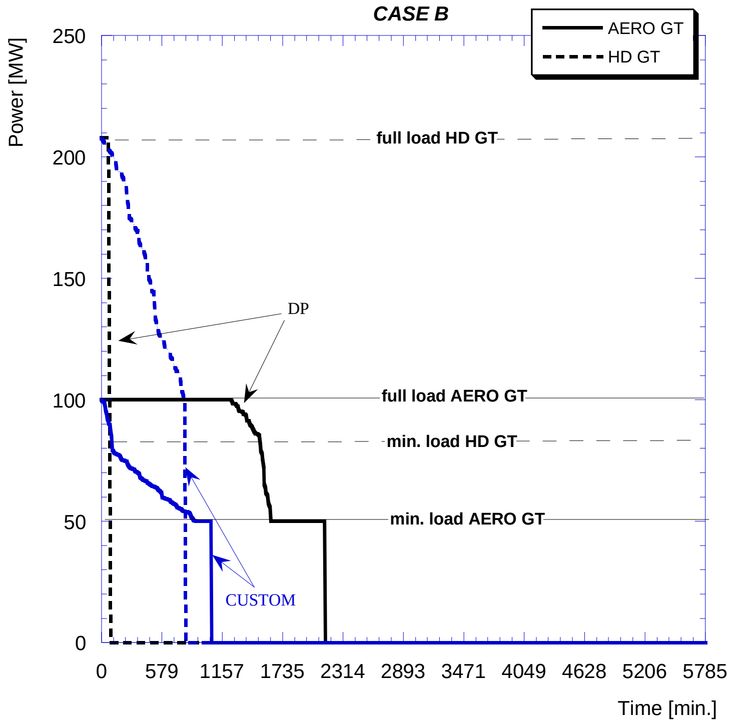

Figure A2.9: Duration curves for GTs power output during CASE (B) operation - DP vs. Custom Strategy.

More in details, the traces of instantaneous realized GTs powers for the simulation of selected days are shown, for Case (A), in Figure A2.10, for the Custom and the DP strategies respectively.

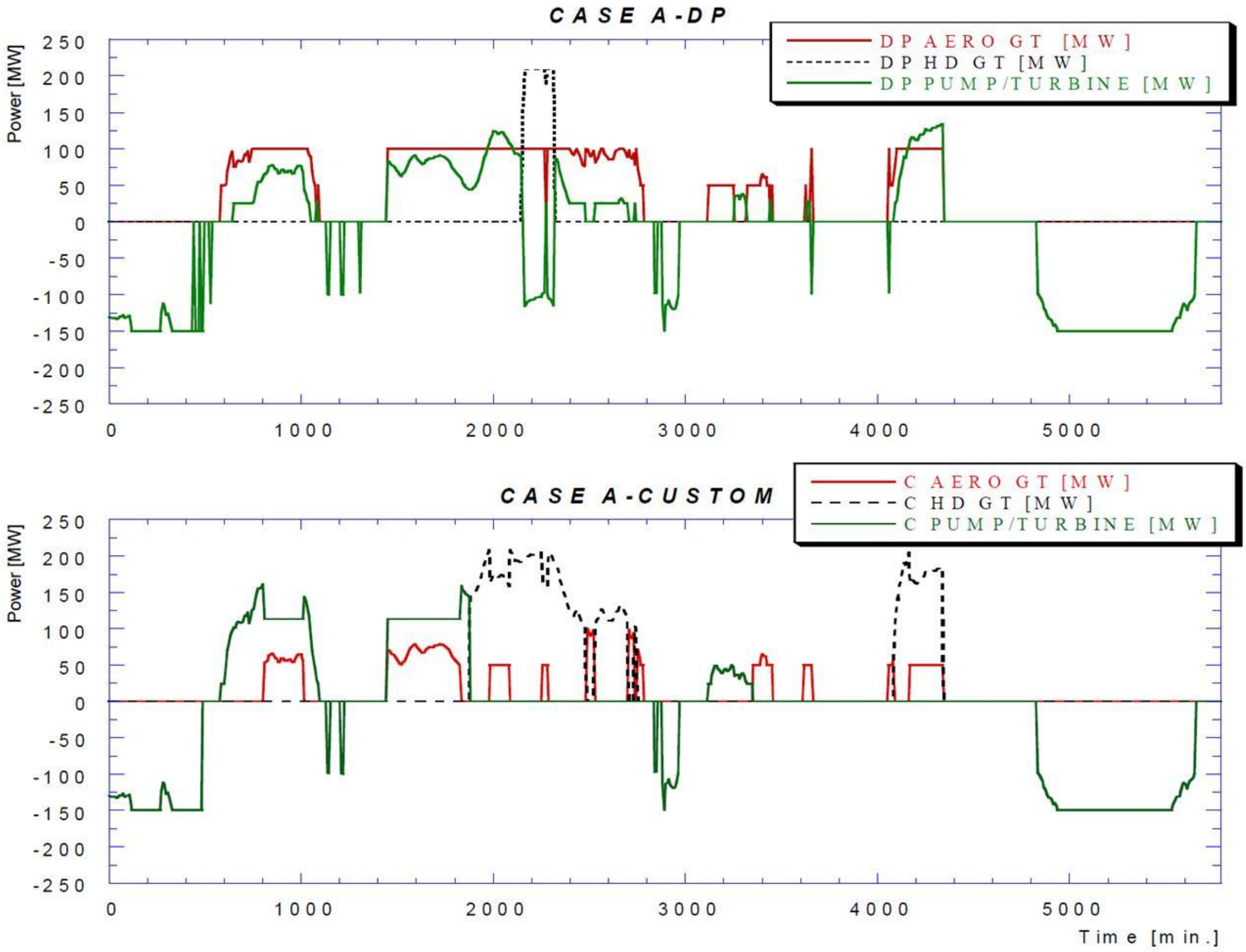

Figure A2.10: GT and PSH powers for Case (A) - DP vs. Custom strategy.

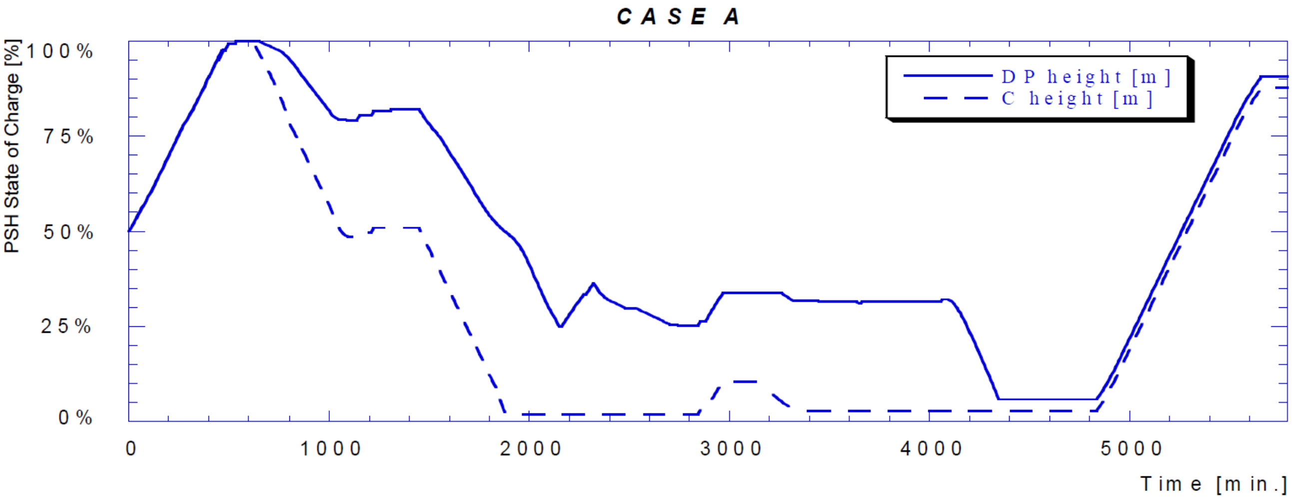

Figure A2.11: SOC trajectories for Case (A) - DP vs. Custom strategy.

Figure A2.12 depicts the different SOC trajectories for the two strategies. The following figures illustrate the same contents of the two figures above, for Case (B).

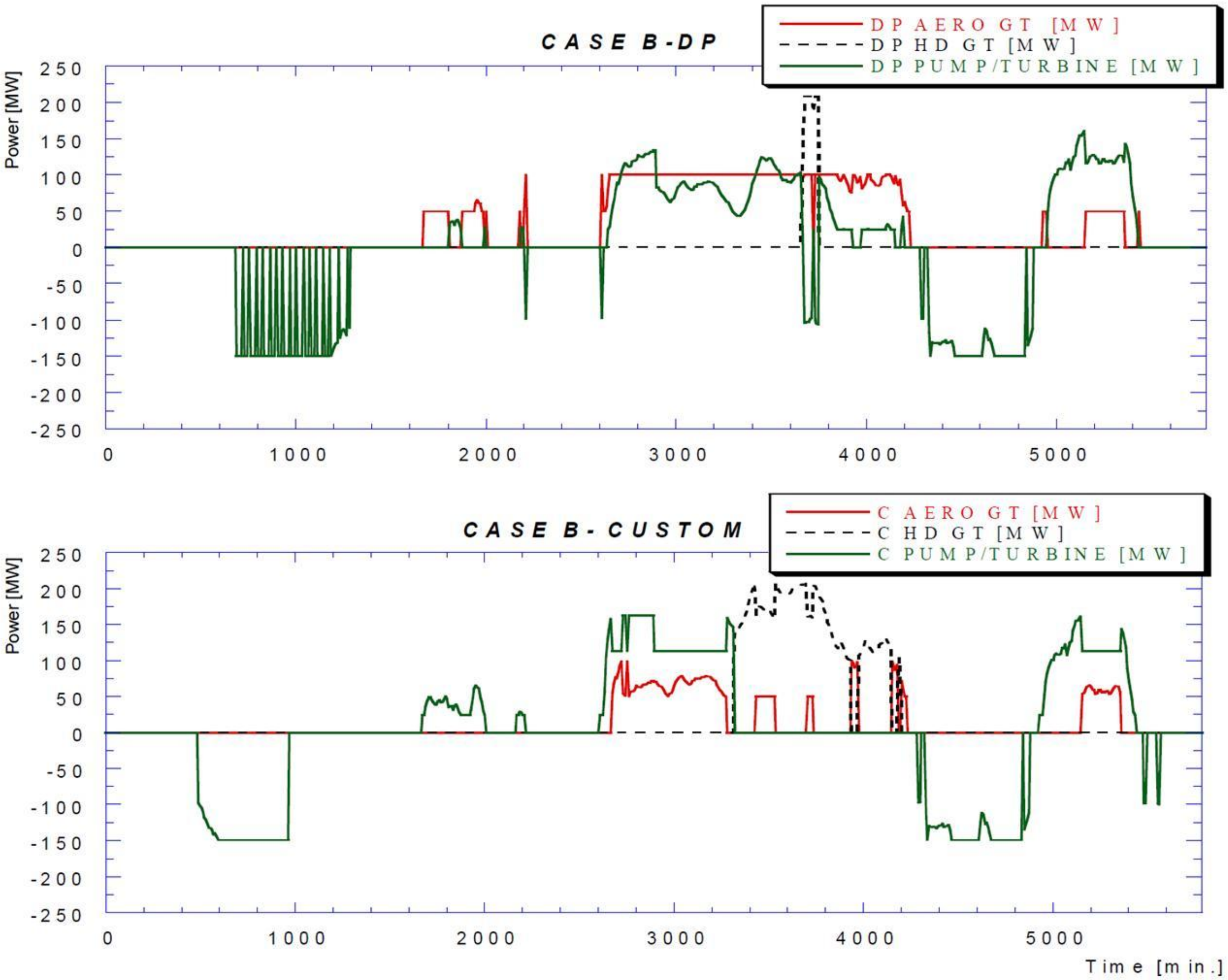

Figure A2.12: GT and PSH powers for Case (B) - DP vs. Custom strategy.

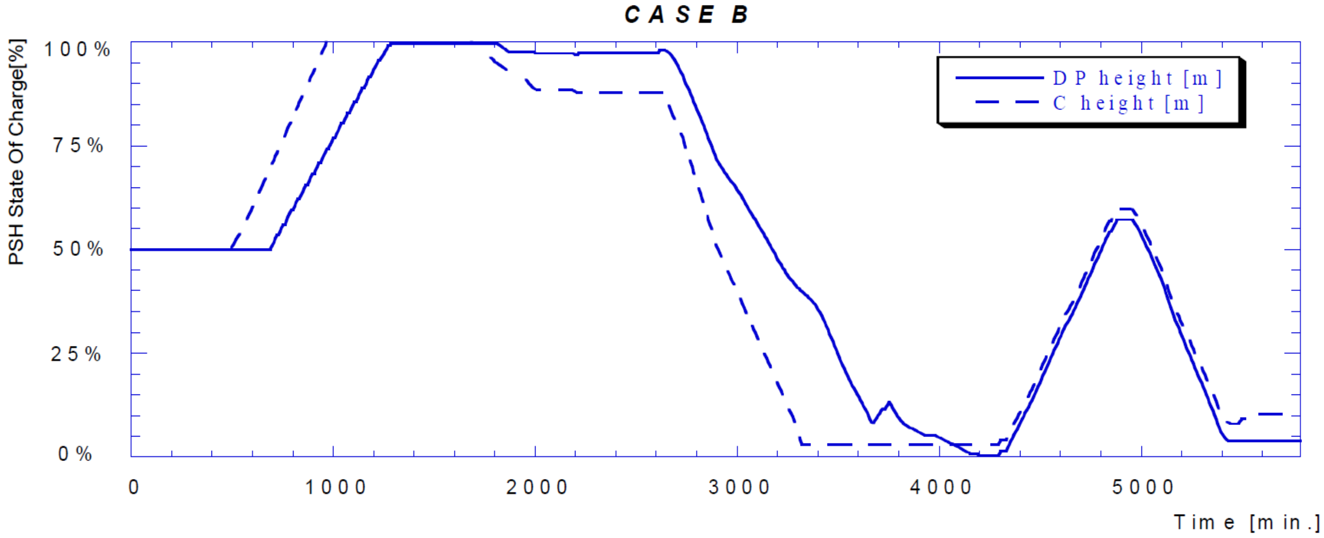

Figure A2.13: SOC trajectories for Case (B) - DP vs. Custom strategy.

If the Custom strategy is applied, both the AERO and the HD basically operate in part-load conditions.

Compared to the DP strategy, the HD machine is operated for a longer period of time, while the AERO unit operated for a shorter period.

DP allows minimizing the natural gas consumption with a significant saving compared to Custom. No daily limitation in the GTs start-up number has been imposed for both control strategies.

Table A2.3 compares the number of GTs start ups and natural gas consumption for both strategies.

Table A2.4 provides the calculated value of the hydraulic energy equivalence factors for charging ($s_{chg}$) and discharging mode ($s_{dis}$), used to calculate the final fuel consumption. The total fuel consumption during the overall time horizon, including the fuel equivalent of the hydraulic energy amount stored in upper reservoir (see (A2.10)), equals about 534 tons and 618 tons, for the DP and the Custom strategy respectively, for Case (A), and about 675 tons and 747 tons for Case (B). In both cases, during the overall time horizon, with the DP strategy the HD unit is started once, while the AERO is started ten times; in case of the Custom strategy, a higher numbers of start-ups is registered in case of the HD unit and a similar (Case (A)) or even lower (Case (B)) number of starts, compared to the DP, occurs in case of the AERO turbine.

**Table A2.3: Evaluation of GT start events for Case (A) and Case (B) - DP vs. Custom Strategy.**

| **Case (A)** | | **CUSTOM** | **DP** |
|---|---|---|---|
| GTs Start-ups number [-] | HD | 4 | 1 |
| | Aero | 11 | 10 |
| Total fuel consumed [ton] | | 778 | 685 |
| Fuel consumed including hydraulic energy equivalent [ton] | | 618 | 534 |
| **Case (B)** | | **CUSTOM** | **DP** |
| GTs Start-ups number [-] | HD | 3 | 1 |
| | Aero | 7 | 10 |
| Total fuel consumed [ton] | | 625 | 548 |
| Fuel consumed including hydraulic energy equivalent [ton] | | 747 | 675 |

**Table A2.4: Final values for s* used to compute the final energy imbalance.**

| CASE (A) | CUSTOM | DP |
|---|---|---|
| charging equivalence factor $s_{chg}$ [-] | 2.28 | 2.00 |
| discharging equivalence factor $s_{dis}$ [-] | 3.06 | 2.69 |
| **CASE (B)** | **CUSTOM** | **DP** |
| charging equivalence factor $s_{chg}$ [-] | 2.25 | 2.01 |
| discharging equivalence factor $s_{dis}$ [-] | 3.03 | 2.70 |

# List of Publications

- Cavina N., Cerofolini A., Mancini G. (University of Bologna), Guzzella L., Onder C., Nueesch T. (IDSC, ETH Zurich), Steiner R. (Daimler AG), "**Equivalent Consumption Minimization Strategy for the Control of Real Driving $NO_x$ Emissions of a Diesel Hybrid Electric Vehicle**", submitted to *Energies*.

- Bianchi M., Cavina N., Cerofolini A., De Pascale A., Melino F., "**Wind-Hydro-Gas Turbine Unit Commitment to guarantee Firm Dispatchable Power**", Accepted conference paper at *Proceedings of GT2014, June 16-20 Dusseldorf, Germany.*

- Cavina N., Cerofolini A., Corti E., Ponti F. (University of Bologna), De Cesare, M., Stola F. (Magneti Marelli S.p.A.), "**Innovative Techniques for On-Board Exhaust Gas Dynamic Properties Measurement**", SAE Paper 2013-01-0305. (SAE World Congress 2013, Detroit, USA 2013). Published on *SAE International Journal of Engines* 6(1), 2013.

- Dingel O., Pini N., Ross J., Trivic I. (IAV GmbH), Cavina N., Cerofolini A. (University of Bologna), Rioli M. (IEV S.r.l.), "**Benchmarking Hybrid Concepts: On-line vs. Off-line Fuel Economy Optimization for Different Hybrid Architectures**". SAE Paper 2013-24-0084, Published on *SAE International Journal of Alternative Powertrains* 2.3 (2013): 456-470.

- Corti E., Cerofolini A., Cavina N., Forte C., Mancini G., Moro D., Ponti F., Ravaglioli V. (University of Bologna), "**Automatic calibration of control parameters based on merit function spectral analysis**", *Energy Procedia* 45 (2014): 918-928.

- Corti E., Cerofolini A., Cavina N., Forte C., Mancini G., Moro D., Ponti F., Ravaglioli V. (University of Bologna), **"Transient Spark Advance Calibration Approach"**, *Energy Procedia* 45 (2014): 967-976.

- Branchini L., Bianchi M., Cavina N., Cerofolini A., Corti E., De Pascale A., Orlandini V., Melino F., Moro D., Peretto A., Ponti F. (University of Bologna), **"Managing Wind Variability With Pumped Hydro Storage And Gas Turbines"**, *Energy Procedia* 45 (2014): 22-31.

- Cavina N., Cerofolini A. (University of Bologna), De Cesare, M., Stola F. (Magneti Marelli S.p.A.), "**UEGO-based Exhaust Gas Mass Flow Rate Measurement**", SAE Paper 2012-01-1627. (SAE Powertrain Fuels and Lubricants, Malmo, Sweden 2012).

# References

[1] M. Åsbogård, L. Johannesson, D. Angervall, and P. Johansson. Improving System Design of a Hybrid Powertrain Using Stochastic Drive Cycles and. *SAE TECHNICAL PAPER SERIES*, (2007-01-0304), 2007.

[2] P. P. Acarnley, B. C. Mecrow, J. S. Burdess, J. N. Fawcett, J. G. Kelly, and P. G. Dickinson. Design Principles for a Flywheel Energy Store for Road Vehicles. *IEEE TRANSACTIONS ON INDUSTRY APPLICATION*, 32(6):1402–1408, 1996.

[3] S. Adhikari. *Real-time Power Management of Parallel Full Hybrid Electric Vehicles*. PhD thesis, University of Melbourne, 2010.

[4] H. Alipour and B. Asaei. An Online Fuel Consumption and Emission Reduction Power Management Strategy for Plug-in Hybrid Electric Vehicles. *Vehicle Engineering*, 1(2):41–55, 2013.

[5] L. Ambühl, D. Guzzella. Predictive reference signal generator for hybrid electric vehicle. In *IEEE Transactions on Vehicular Technology*, volume 58, pages 4730–4740, 2009.

[6] D. Ambühl. *ENERGY MANAGEMENT STRATEGIES FOR HYBRID ELECTRIC VEHICLES*. PhD thesis, ETH Zurich, 2009.

[7] D. Ambühl, O. Sundström, A. Sciarretta, and L. Guzzella. Explicit optimal control policy and its practical application for hybrid electric powertrains. *Control Engineering Practice*, 18(12):1429–1439, Dec. 2010.

[8] F. Amisano and G. Serra. Engine Control Strategy to Optimize a Shift Transient During Clutch Engagement. *SAE TECHNICAL PAPER SERIES*, (2001-01-0877), 2011.

[9] J.-m. André and M. Hugot. IMPACT OF THE GEARSHIFT STRATEGY ON EMISSION MEASUREMENTS. *Artemis 3142 report*, (March), 2003.

[10] G.-Q. Ao, J.-X. Qiang, H. Zhong, X.-J. Mao, L. Yang, and B. Zhuo. Fuel economy and NOx emission potential investigation and trade-off of a hybrid electric vehicle based on dynamic programming. *Proc. I. Mech. Eng. D - J. Aut.*, 222(10):1851–1864, Oct. 2008.

[11] D. Assanis, Z. Filipi, S. Gravante, D. Grohnke, X. Gui, L. Louca, G. Rideout, J. Stein, and Y. Wang. Validation and Use of SIMULINK Integrated , High Fidelity , Engine-In-Vehicle Simulation of the International Class VI Truck. *SAE TECHNICAL PAPER SERIES*, (2000-01-0288), 2012.

[12] A. Baisden and A. Emadi. ADVISOR-based model of a battery and an ultra-capacitor energy source for hybrid electric vehicles. *Vehicular Technology, IEEE* , 53(1):199–205, 2004.

[13] J. M. Banerjee, T.-S. Dao, and J. McPhee. Mathematical Modeling and Symbolic Sensitivity Analysis of Ni-MH Batteries. *SAE International*, (2011-01-1371), Apr. 2011.

[14] M. Bataus and A. Maciac. Automotive Clutch Models for Real Time Simulation. *Proceedings of the Romanian Academy*, (x).

[15] B. M. Baumann, G. Washington, B. C. Glenn, and G. Rizzoni. Mechatronic Design and Control of Hybrid Electric Vehicles. *IEEE/ASME TRANSACTIONS ON MECHATRONICS*, 5(1):58–72, 2000.

[16] R. Beck, S. Saenger, F. Richert, A. Bollig, K. Neiß, T. Scholt, K. Noreikat, and D. Abel. Model Predictive Control of a Parallel Hybrid Vehicle Drivetrain. In *Proceedings of the 44th IEEE Conference on Decision and Control, and the European Control Conference 2005*, pages 2670–2675, 2005.

[17] J. Beckers. Matlab Simulink modelling of a hybrid vehicle. 2005.

[18] K. V. Berkel and T. Hofman. Optimal energy management for a flywheel-based hybrid vehicle. *American Control* , pages 5255–5260, 2011.

[19] K. V. Berkel and T. Hofman. Optimal control of a mechanical hybrid powertrain. *IEEE TRANSACTIONS ON VEHICULAR TECHNOLOGY*, 61(2):485–497, 2012.

[20] K. V. Berkel, T. Hofman, B. Vroemen, and M. Steinbuch. Control Optimization for a Low-cost Flywheel Module. *mate.tue.nl*.

[21] K. V. Berkel, T. Hofman, B. Vroemen, and S. Steinbuch, Maarten Rullens. Analysis of optimal mechanical-hybrid powertrain topologies. *2012 IFAC Workshop on Engine and Powertrain Control (ECOSIM 2012)*, pages 61–68, 2012.

[22] D. Bertsekas. *Dynamic Programming and Optimal Control Vol I*. Athena Scientific, Belmont, Massachussets, 3 edition, 2005.

[23] D. Bianchi and L. Rolando. A rule-based strategy for a series/parallel hybrid electric vehicle: an approach based on dynamic programming. *2010 Dynamic* , 2010.

[24] T. J. Boehme, B. Becker, M. Ruben-Weck, M. Rothschuh, A. Boldt, C. Rollinger, R. Butz, H. Rabba, and W. Drewelow. Optimal Design Strategies for Different Hybrid Powertrain Configurations Assessed with European Drive Cycles. *SAE International*, (2013-01-1751), Apr. 2013.

[25] A. Böhm and J. Melbert. Modeling of Automotive Batteries for High Transient and Amplitude Dynamics Reprinted From : Hybrid Electric Vehicle Technology. *SAE TECHNICAL PAPER SERIES*, (2004-01-3038), 2012.

[26] B. Bonsen. Efficiency optimization of the push-belt CVT by variator slip control. *Dissertation Abstracts International*, 2006.

[27] A. Boretti. Modeling of Engine and Vehicle for a Compact Car with a Flywheel Based Kinetic Energy Recovery Systems and a High Efficiency Small Diesel Engine. *SAE TECHNICAL PAPER SERIES*, (2010-01-2184), Oct. 2010.

[28] S. Boyd, J. Lee, and D. J. Nelson. A Simplified Battery Model for Hybrid Vehicle Technology Assessment. *SAE TECHNICAL PAPER SERIES*, 2007(2007-01-0301), 2012.

[29] C. Brockbank. Application of a variable drive to supercharger & turbo compounder applications. *Proc. of the SAE conference*, (1), 2009.

[30] C. Brockbank. Development of full-toroidal traction drives in flywheel based mechanical hybrids. *the 6th Int. Conf. on Continuously Variable and Hybrid* , 2010.

[31] C. Brockbank and W. Body. Flywheel based mechanical hybrid system; simulation of the fuel consumption benefits of various transmission arrangements and control strategies. In *Proceedings of the ASME 2010 International Design Engineering Technical Conferences & Computers and Information in Engineering Conference IDETC/CIE 2010*, pages 1–8, 2010.

[32] R. Buchwald and A. Sommer. Laying Out Diesel-Engine Control Systems in Hybrid Drives Hybrid Vehicles and Energy Management. In *Hybrid Vehicles and Energy Management, 6th Symposium 18th and 19th February 2009*, 2007.

[33] E. Cacciatori, B. Bonnet, N. D. Vaughan, M. Burke, and D. Price. Regenerative Braking Strategies for A Parallel Hybrid Powertrain with Torque Controlled IVT. *SAE Technical Paper*, (2005-01-3826), 2005.

[34] C. Chan, E. Lo, and S. Weixiang. The available capacity computation model based on artificial neural network for lead acid batteries in electric vehicles. *Journal of Power Sources*, 87(1-2):201–204, Apr. 2000.

[35] A. Chasse and A. Sciarretta. Supervisory control of hybrid powertrains: An experimental benchmark of offline optimization and online energy management. *Control Engineering Practice*, 19(11):1253–1265, Nov. 2011.

[36] A. Chasse, A. Sciarretta, J. Chauvin, and I. Fran. Online optimal control of a parallel hybrid with costate adaptation rule. In *6th IFAC Symposium Advances in Automotive Contro*, pages 10–15, 2013.

[37] K. Chau and Y. Wong. Overview of power management in hybrid electric vehicles. *Energy Conversion and Management*, 43(15):1953–1968, Oct. 2002.

[38] B. Cho. *Control of A Hybrid Electric Vehicle with Predictive Journey Estimation*. PhD thesis, Cranfield University, 2008.

[39] D. Crolla and Q. Ren. Controller design for hybrid vehicles: state of the art review. *Vehicle Power and* , (since 2000):1–6, 2008.

[40] J. Dailey, R. Plivelich, L. Huston, J. Landi, and M. Klein. The Bipolar Nickel-Metal Hydride Battery for Advanced Transportation and High Voltage Power and Energy Storage Systems. *SAE TECHNICAL PAPER SERIES*, (2006-01-3020), 2006.

[41] M. Dassen. Modelling and control of automotive clutch systems. (July), 2003.

[42] M. Debert and G. Colin. Li-ion battery models for HEV simulator. In *Advances in Hybrid Powertrain*, 2008.

[43] S. Delprat and T. Guerra. Control strategy optimization for an hybrid parallel powertrain. In *American Control Conference (ACC)*, pages 1315–1320, 2001.

[44] S. Delprat, T. Guerra, and J. Rimaux. Control strategies for hybrid vehicles: optimal control. In *In Proceedings of the 56th IEEE Vehicular Technology Conference*, volume 3, pages 1681–1685, Birmingham, AL, USA, Sept. 2002. IEEE.

[45] S. Delprat, J. Lauber, T. Guerra, and J. Rimaux. Control of a Parallel Hybrid Powertrain: Optimal Control. *IEEE Transactions on Vehicular Technology*, 53(3):872–881, May 2004.

[46] O. Dingel, N. Pini, I. Trivic, J. Ross, N. Cavina, A. Cerofolini, and M. Rioli. Benchmarking hybrid concepts: On-line vs. off-line fuel economy optimization for different hybrid architectures. *SAE International Journal of Alternative Powertrains*, 2(3):456–470, 2013.

[47] O. Dingel, J. Ross PhD, I. Trivic, N. Cavina, and M. Rioli. Model-Based Assessment of Hybrid Powertrain Solutions. *SAE International*, (2011-24-0070), Sept. 2011.

[48] C. Donitz. *Hybrid Pneumatic Engines*. Phd thesis, ETH Zurich, 2009.

[49] C. Donitz, I. Vasile, C. Onder, and L. Guzzella. Realizing a Concept for High Efficiency and Excellent Driveability : The Downsized and Supercharged Hybrid. *SAE International*, 4970(2009-01-1326), 2013.

[50] M. Duoba, H. Ng, and R. Larsen. In-Situ Mapping and Analysis of the Toyota Prius HEV Engine. *SAE TECHNICAL PAPER SERIES*, (2000-01-3096), 2000.

[51] S. r. B. Ebbesen. *OPTIMAL SIZING AND CONTROL OF HYBRID ELECTRIC VEHICLES*. PhD thesis, ETH Zurich, 2012.

[52] M. M. Flynn, J. J. Zierer, and R. C. Thompson. Performance Testing of a Vehicular Flywheel Energy System. *SAE TECHNICAL PAPER SERIES*, 2005(2005-01-0809), 2005.

[53] J. a. Francisco and F. Heck. Design of a Pneumatic Regenerative Braking System Design of a Pneumatic Regenerative Braking System. *SAE TECHNICAL PAPER SERIES*, (2005-01-3969), 2011.

[54] L. Fu and U. Ozguner. Real-time energy management and sensitivity study for hybrid electric vehicles. *2011 Control Conference (ACC)*, pages 4–9, 2011.

[55] X. Fu and X. Xie. The control strategy of flywheel battery for electric vehicles. In *Control and Automation, 2007. ICCA 2007. IEEE* , volume 00, pages 492–496, 2007.

[56] Y. Gao, L. Chen, and M. Ehsani. Investigation of the Effectiveness of Regenerative Braking for EV and HEV. *SAE TECHNICAL PAPER SERIES*, (1999-01-2910), 1999.

[57] H. Geering. *Optimal control with engineering applications*. Springer Verlag, 2007.

[58] G. Genta. *Motor vehicle dynamics – modeling and simulation*. World Scientific Publishing Co. Pte. Ltd, 1997.

[59] Q. Gong, Y. Li, and Z. Peng. Trip-based optimal power management of plug-in hybrid electric vehicles. *Vehicular Technology, IEEE* , 57(6):3393–3401, 2008.

[60] O. Grondin, C. Quérel, and Q. C. Grondin, O. Thibault L. Transient torque control of a diesel hybrid powertrain for NOx limitation. In *2012 IFAC*

*Workshop on Engine and Powertrain Control (ECOSIM 2012)*, number October, pages 219–228, 2012.

[61] O. Grondin, L. Thibault, P. Moulin, A. Chasse, and A. Sciarretta. Energy Management Strategy for Diesel Hybrid Electric Vehicle. *Proc. IEEE Vehicle Power and Propulsion Conference (VPPC)*, 2011.

[62] G. Gu, B. Rizzoni. An adaptive algorithm for hybrid electric vehicle energy management based on driving pattern recognition. In *Proceedings of the 2006 ASME International Mechanical Engineering Congress and Exposition*, 2006.

[63] B. O. S. R. G. Guardiola, C. Pla. A new approach to optimally tune the control strategy for hybrid vehicles application. In *2012 IFAC Workshop on Engine and Powertrain Control, Simulation and Modeling (ECOSIM12)*, 2012.

[64] L. Guzzella. Modeling and control of advanced propulsion systems. *Oil & Gas Science and Technology-Revue* , 62(4):585–594, 2007.

[65] L. Guzzella and A. Amstutz. CAE tools for quasi-static modeling and optimization of hybrid powertrains. *IEEE Transactions on Vehicular Technology*, 48(6):1762–1769, 1999.

[66] L. Guzzella and A. Sciarretta. *Vehicle Propulsion Systems*. Springer Verlag, 3d edition, 2012.

[67] H.-W. He, R. Xiong, and Y.-H. Chang. Dynamic Modeling and Simulation on a Hybrid Power System for Electric Vehicle Applications. *Energies*, 3(11):1821–1830, Nov. 2010.

[68] X. He. Battery Modeling for HEV Simulation Model Development. *SAE TECHNICAL PAPER SERIES*, (2001-01-0960), 2012.

[69] T. Hofman and M. Steinbuch. Rule-based equivalent fuel consumption minimization strategies for hybrid vehicles. *Proceedings of the 17th World Congress The International Federation of Automatic Control*, pages 5652–5657, 2008.

[70] T. Hofman, M. Steinbuch, R. van Druten, and A. Serrarens. Rule-based energy management strategies for hybrid vehicles. *Drivetrain Innovations B*, 1(1), 2007.

[71] K. Huang, H. Nam-Nguyen, and K. Quang. Validation of a Dynamic Model of a Hybrid Pneumatic Power System. *SAE Technical Paper*, (2009-01-1304), 2011.

[72] K. Huang and S.-C. Tzeng. Development of a hybrid pneumatic-power vehicle. *Applied Energy*, 80(1):47–59, Jan. 2005.

[73] K. D. Huang, S.-C. Tzeng, and W.-C. Chang. Energy-saving hybrid vehicle using a pneumatic-power system. *Applied Energy*, 81(1):1–18, May 2005.

[74] Y. Huang and K. Wang. A hybrid power driving system with an energy storage flywheel for vehicles. *SAE TECHNICAL PAPER SERIES*, (2007-01-4114), 2007.

[75] H. L. Husted. A Comparative Study of the Production Applications of Hybrid Electric Powertrains. *SAE TECHNICAL PAPER SERIES*, (724), 2003.

[76] R. a. Jackey. A Simple, Effective Lead-Acid Battery Modeling Process for Electrical System Component Selection. *SAE TECHNICAL PAPER SERIES*, (2007-01-0778), Apr. 2007.

[77] R. A. Jackey, G. L. Plett, and M. J. Klein. Parameterization of a Battery Simulation Model Using Numerical Optimization Methods. *SAE TECHNICAL PAPER SERIES*, (2009-01-1381), 2012.

[78] B. Jacobson and M. Spickenreuther. Gearshift sequence optimisation for vehicles with automated non-powershifting transmissions. *International Journal of Vehicle Design*, 32(3/4):187, 2003.

[79] L. Johannesson. Assessing the potential of predictive control for hybrid vehicle powertrains using stochastic dynamic programming. *IEEE TRANSACTIONS ON INTELLIGENT TRANSPORTATION SYSTEMS*, 8(1):71–83, 2007.

[80] V. Johnson. Battery performance models in ADVISOR. *Journal of Power Sources*, 110(2):321–329, Aug. 2002.

[81] V. Johnson, A. Pesaran, T. Sack, and S. America. Temperature-dependent battery models for high-power lithium-ion batteries. Technical Report January, NREL, 2001.

[82] V. H. Johnson, K. B. Wipke, and D. J. Rausen. HEV Control Strategy for Real-Time Optimization of Fuel Economy and Emissions. *SAE Technical Paper*, (724), Apr. 2000.

[83] R. Johri and Z. S. Filipi. Self-Learning Neural Controller for Hybrid Power Management Using Neuro-Dynamic Programming. *SAE International*, (2011-24-0081), Sept. 2011.

[84] K. Kamichi, K. Okasaka, M. Tomatsuri, T. Matsubara, Y. Kaya, and H. Asada. Hybrid System Development for a High-Performance Rear Drive Vehicle. *SAE TECHNICAL PAPER SERIES*, 2006(2006-01-1338), 2008.

[85] E. Karlsson. *Analysis of Hybrid Management Strategies*. Master thesis, Chalmers University of Technology, 2008.

[86] K. J. Kelly, M. Zolot, G. Glinsky, and A. Hieronymus. Test Results and Modeling of the Honda Insight Using ADVISOR Preprint. Technical Report August, NREL, 2001.

[87] S. Kermani, S. Delprat, T. M. Guerra, and R. Trigui. Real time control of hybrid electric vehicle on a prescribed road. In *Proceedings of the 17th World Congress The International Federation of Automatic Control*, pages 3356–3361, 2008.

[88] J. Kessels and M. Koot. Vehicle modeling for energy management strategies. In *AVEC 04*, 2004.

[89] J. Kessels, M. Koot, and P. van den Bosch. Optimal adaptive solution to powersplit problem in vehicles with integrated starter/generator. In *Vehicle Power and Propulsion, IEEE*, 2006.

[90] J. Kessels and P. van den Bosch. Online energy management for hybrid electric vehicles. *IEEE TRANSACTIONS ON VEHICULAR TECHNOLOGY*, 57(6):3428–3440, 2008.

[91] J. Kessels, F. Willems, W. Schoot, and P. van den Bosch. Integrated energy & emission management for hybrid electric truck with SCR aftertreatment. *2010 IEEE Vehicle Power and Propulsion Conference*, pages 1–6, Sept. 2010.

[92] T. V. Keulen, B. D. Jager, and M. Steinbuch. An Adaptive Sub-Optimal Energy Management Strategy for Hybrid Drive-Trains. In *Proc. IFAC World Congress*, pages 102–107, 2008.

[93] T. V. Keulen, D. V. Mullem, B. D. Jager, J. T. Kessels, and M. Steinbuch. Design, implementation, and experimental validation of optimal power split control for hybrid electric trucks. *Control Engineering Practice*, 20(5):547–558, 2012.

[94] H. Khayyam, A. Kouzani, V. Marano, and G. Rizzoni. Intelligent Energy Management in Hybrid Electric Vehicles. *intechopen*, 2006.

[95] D. Kim, H. Peng, S. Bai, and J. M. Maguire. Control of Integrated Powertrain With Electronic Throttle and Automatic Transmission. *IEEE Transactions on Control Systems Technology*, 15(3):474–482, May 2007.

[96] N. Kim, S. Cha, and H. Peng. Optimal Control of Hybrid Electric Vehicles Based on Pontryagin's Minimum Principle. *IEEE Transactions on Control Systems Technology*, 19(5):1279–1287, Sept. 2011.

[97] T. S. Kim, C. Manzie, and R. Sharma. Model Predictive Control of Velocity and Torque Split in a Parallel Hybrid Vehicle. In *Proceedings of the 2009 IEEE International Conference on Systems, Man, and Cybernetics San Antonio, TX, USA - October 2009*, number October 2009, pages 2014–2019, 2014.

[98] T. S. Kim, C. Manzie, and H. Watson. Fuel Economy Benefits of Look-ahead Capability in a Mild Hybrid Configuration. In *Proceedings of the 17th World Congress The International Federation of Automatic Control Seoul, Korea, July 6-11, 2008 Fuel*, pages 5646–5651, 2008.

[99] a. Kleimaier and D. Schroder. An approach for the online optimized control of a hybrid powertrain. *7th International Workshop on Advanced Motion Control. Proceedings (Cat. No.02TH8623)*, pages 215–220, 2002.

[100] A. Kleimarer. *Optimale Betriebsführung von Hybridfahrzeugen*. PhD thesis, Technische Universitaet Muenchen, 2003.

[101] I. Kolmanovsky, I. Siverguina, and B. Lygoe. Optimization of powertrain operating policy for feasibility assessment and calibration: stochastic dynamic programming approach. *Proceedings of the 2002 American Control Conference (IEEE Cat. No.CH37301)*, 2(i):1425–1430, 2002.

[102] M. Koot and B. D. Jager. Energy management strategies for vehicle power nets. *American Control Conference (ACC)*, 2004.

[103] M. Koot and J. Kessels. Fuel reduction potential of energy management for vehicular electric power systems. *International Journal of Alternative Propulsions*, 1(1):112–131, 2006.

[104] M. Koot, J. Kessels, B. DeJager, W. Heemels, P. VandenBosch, and M. Steinbuch. *Energy Management Strategies for Vehicular Electric Power Systems*, volume 54. May 2005.

[105] K. Koprubasi. *MODELING AND CONTROL OF A HYBRID-ELECTRIC VEHICLE FOR DRIVABILITY AND FUEL ECONOMY IMPROVEMENTS*. PhD thesis, Ohio State University, 2008.

[106] M. V. Kothare, P. J. Campo, M. Morari, and C. N. Nett. A Unified Framework for the Study of Anti-windup Designs. *Automatica*, 30(12):1869–1883, 1994.

[107] D. Kum. *Modeling and Optimal Control of Parallel HEVs and Plug-in HEVs for Multiple Objectives*. PhD thesis, University of Michigan, 2010.

[108] D. Kum, H. Peng, and N. K. Bucknor. Supervisory Control of Parallel Hybrid Electric Vehicles for Fuel and Emission Reduction. *Journal of Dynamic Systems, Measurement, and Control*, 133(6):061010, 2011.

[109] S. Kutter. *Eine prädiktive und optimierungsbasierte Betriebsstrategie für autarke und extern nachladbare Hybridfahrzeuge*. Phd thesis, Technische Universität Dresden, 2013.

[110] L. B. Lave and H. L. Maclean. An Environmental-Economic Evaluation of Hybrid Electric and Other Advanced Vehicles. *SAE Technical Paper*, (2001-01-3738), 2001.

[111] M. Lazar. *Model Predictive Control of Hybrid Systems: Stability and Robustness*. PhD thesis, Technische Universiteit Eindhoven, 2006.

[112] D. Le Guen, T. Weck, A. Balihe, and B. Verbeke. Definition of Gearshift Pattern: Innovative Optimization Procedures Using System Simulation. *SAE Int. J. Fuels Lubr.*, 4(1):412–431, Apr. 2011.

[113] H.-d. Lee, S.-k. Sul, H.-s. Cho, and J.-m. Lee. Advanced Gear-shifting and Clutching Strategy for a Parallel-Hybrid Vehicle. *EEE Industry Applications Magazine*, (December):26–32, 2000.

[114] B. Y. Liaw. Fuzzy Logic Based Driving Pattern Recognition for Driving Cycle Analysis.pdf. *Journal of Asian Electric Vehicles*, 3(2):551–556, 2004.

[115] C. Lin and H. Peng. Power management strategy for a parallel hybrid electric truck. *Proceedings of the 10th Mediterranean Conference on Control and Automation - MED2002 Lisbon,*, 2002.

[116] C.-c. Lin, Z. Filipi, Y. Wang, L. Louca, H. Peng, D. Assanis, and J. Stein. Integrated , Feed-Forward Hybrid Electric Vehicle Simulation in SIMULINK and its Use for Power Management Studies. *SAE TECHNICAL PAPER SERIES*, (2001-01-1334), 2012.

[117] C.-c. Lin, H. Pengl, and J. W. Grizzle. A Stochastic Control Strategy for Hybrid Electric Vehicles. In *Proceeding of the 2004 American Control Conference Boston, Massachusetts*, pages 4710–4715, 2004.

[118] N. Lindenkamp. Strategies for Reducing NOX- and Particulate Matter Emissions in Diesel Hybrid Electric Vehicles. In *Hybrid Vehicles and Energy Management, 6th Symposium 18th and 19th February 2009*, number February, pages 20–33, 2009.

[119] J. Liu and H. Peng. Control optimization for a power-split hybrid vehicle. *2006 American Control Conference*, page 6 pp., 2006.

[120] Z. Liu, S. Shi, H. He, and W. Li. Study on Dynamic Shift Schedule of Automated Mechanical Transmission in a Parallel Hybrid Electric Vehicle. *Proceedings of the 2nd International Conference on Electronic and Mechanical Engineering and Information Technology (2012)*, pages 1619–1622, 2012.

[121] K. Loehe. *Optimierung der Ansteuerung verteilter Fahrzeugantriebe für bekannte Fahrzyklen*. Diplomarbeit, Friedrich-Alexander-Universitaet Erlangen-Nuernberg, 2010.

[122] Z. Lu, G. J. Thompson, V. H. Mucino, and J. E. Smith. Simulation of a Continuously Variable Power Split Transmission. *SAE TECHNICAL PAPER SERIES*, (1999-01-0062), 1999.

[123] R. Luus and O. Rosen. Application of dynamic programming to final state constrained optimal control problems. *Industrial & Engineering Chemistry Research*, 1:1525–1530, 1991.

[124] F. Millo, C. V. . Ferraro, and L. Rolando. Analysis of different control strategies for the simultaneous reduction of CO2 and NOx emissions of a diesel hybrid passenger car. *Int. J. Vehicle Design*, 58(2/3/4):427–448, 2012.

[125] S. Molla. SYSTEM MODELING AND POWER MANAGEMENT STRATEGY FOR A SERIES HYDRAULIC HYBRID VEHICLE. (May), 2010.

[126] D. Moro, N. Cavina, I. Trivic, and V. Ravaglioli. Guidelines for Integration of Kinetic Energy Recovery System ( KERS ) based on Mechanical Flywheel in an Automotive Vehicle. *SAE International*, (2010-01-1448), 2011.

[127] C. Musardo and G. Rizzoni. A-ECMS: An Adptive Algorithm for Hybrid Electric Vehicle Management. *Proceedings of the 44th IEEE Conference on Decision and Control, and the European Control Conference 2005*, pages 1816–1823, 2005.

[128] C. Musardo, B. Staccia, S. Midlam-Mohler, Y. Guezennec, and G. Rizzoni. Supervisory Control for NOx Reduction of an HEV with a Mixed-

Mode HCCI/CIDI Engine. *Proc. American Control Conference (ACC)*, (FrA14.6):3877–3881, 2005.

[129] M. Nakano, H. Kumura, and J. Sugihara. Development of a large torque capacity half-toroidal CVT. *SAE transactions*, (724), 2000.

[130] S. Nallabolu. Simulation of Hybrid Vehicle Powertrain with an Advanced Battery Model. *SAE Technical Paper*, (2011-28-0069), 2012.

[131] E. K. Nam and A. Mitcham. Dynamometer and On-board Emissions Testing of the Honda Insight and Toyota Prius. *SAE TECHNICAL PAPER SERIES*, 2005(2005-01-0681), 2005.

[132] H. K. Ng, J. A. Anderson, M. J. Duoba, and R. P. Larsen. Engine Start Characteristics of Two Hybrid Electric Vehicles (HEVs): Honda Insight and Toyota Prius. *SAE TECHNICAL PAPER SERIES*, 2001(2001-01-1335), 2001.

[133] V. Ngo, T. Hofman, M. Steinbuch, and a. Serrarens. Optimal Control of the Gearshift Command for Hybrid Electric Vehicles. *IEEE Transactions on Vehicular Technology*, 61(8):3531–3543, Oct. 2012.

[134] V. D. Ngo, J. a. Colin Navarrete, T. Hofman, M. Steinbuch, and a. Serrarens. Optimal gear shift strategies for fuel economy and driveability. *Proceedings of the Institution of Mechanical Engineers, Part D: Journal of Automobile Engineering*, 227(10):1398–1413, June 2013.

[135] T. Nüesch, P. Elbert, M. Flankl, C. Onder, and L. Guzzella. Convex Optimization for the Energy Management of Hybrid Electric Vehicles Considering Engine Start and Gearshift Costs. *Energies*, 7(2):834–856, Feb. 2014.

[136] T. Nüesch, M. Wang, C. Voser, and L. Guzzella. Optimal Energy Management and Sizing for Hybrid Electric Vehicles Considering Transient Emissions. *2012 IFAC Workshop on Engine and Powertrain Control, Simulation and Modeling*, 2012.

[137] S. Onori and L. Serrao. On Adaptive-ECMS strategies for hybrid electric vehicles. *Les Rencontres Scientifiques, IFP Energies nouvelles Int. Scient. Conf. on hybrid and electric vehicles, RHEVE 2011*, (December):1–7, 2011.

[138] D. Opila, X. Wang, R. McGee, and R. Gillespie. Incorporating Drivability Metrics into Optimal Energy Management Strategies for Hybrid Vehicles Part 2: Real-World Robustness and Constraint Implementation. *eecs.umich.edu*.

[139] D. F. Opila. *Incorporating Drivability Metrics into Optimal Energy Management Strategies for Hybrid Vehicles*. Phd thesis, University of Michigan, 2010.

[140] D. F. Opila, X. Wang, R. McGee, R. B. Gillespie, J. a. Cook, and J. W. Grizzle. An Energy Management Controller to Optimally Trade Off Fuel Economy and Drivability for Hybrid Vehicles. *IEEE Transactions on Control Systems Technology*, 20(6):1490–1505, Nov. 2012.

[141] T. Ott, C. Onder, and L. Guzzella. Hybrid-Electric Vehicle with Natural Gas-Diesel Engine. *Energies*, 6(7):3571–3592, July 2013.

[142] G. Paganelli and S. Delprat. Equivalent consumption minimization strategy for parallel hybrid powertrains. *2002. VTC Spring*, 4:2076–2081, 2002.

[143] G. Paganelli, T. M. Guerra, S. Delprat, J.-J. Santin, M. Delhom, and E. Combes. Simulation and assessment of power control strategies for a parallel hybrid car. *Proceedings of the Institution of Mechanical Engineers, Part D: Journal of Automobile Engineering*, 214(7):705–717, Jan. 2000.

[144] R. Pfiffner and L. Guzzella. Optimal operation of CVT-based powertrains. *International Journal of Robust and Nonlinear Control*, 11(11):1003–1021, Sept. 2001.

[145] R. Pfiffner, L. Guzzella, and C. Onder. Fuel-optimal control of CVT powertrains. *Control Engineering Practice*, 11(3):329–336, Mar. 2003.

[146] S. Piller, M. Perrin, and A. Jossen. Methods for state-of-charge determination and their applications. *Journal of Power Sources*, 96(1):113–120, June 2001.

[147] P. Pisu, K. Koprubasi, and G. Rizzoni. Energy Management and Drivability Control Problems for Hybrid Electric Vehicles. *Proceedings of the 44th IEEE Conference on Decision and Control*, pages 1824–1830, 2005.

[148] P. Pisu and G. Rizzoni. A Comparative Study Of Supervisory Control Strategies for Hybrid Electric Vehicles. *IEEE TRANSACTIONS ON CONTROL SYSTEMS TECHNOLOGY*, 15(3):506–518, 2007.

[149] V. Pop, H. J. Bergveld, P. H. L. Notten, and P. P. L. Regtien. State-of-the-art of battery state-of-charge determination. *Measurement Science and Technology*, 16(12):R93–R110, Dec. 2005.

[150] W. B. Powell. *Approximate dynamic programming*. WILEY, 2 edition, 2011.

[151] J. Pu, C. Yin, and J. Zhang. Fuel optimal control of parallel hybrid electric vehicles. *Frontiers of Mechanical Engineering in China*, 3(3):337–342, May 2008.

[152] K. Pullen and C. Ellis. Kinetic energy storage for vehicles. pages 1–21, 2006.

[153] D. Qin, M. Ye, and Z. Liu. Regenerative braking control strategy in mild hybrid electric vehicles equipped with automatic manual transmission. *Frontiers of Mechanical Engineering in China*, 2(3):364–369, July 2007.

[154] J. Qu and D. Liu. An Optimal Method for Dynamic Three-Parameter Fuel Economy Shift Schedule of AMT. *2009 International Conference on Information Engineering and Computer Science*, pages 1–4, Dec. 2009.

[155] G. Rizzoni, L. Guzzella, and B. Baumann. Unified modeling of hybrid electric vehicle drivetrains. *IEEE/ASME Transactions on Mechatronics*, 4(3):246–257, 1999.

[156] G. Rousseau. Constrained optimization of energy management for a mild-hybrid vehicle. *Oil & Gas Science and Technology, Institut Français du Pétrole*, 62(4):623–634, 2007.

[157] L. Rubino, P. Bonnel, R. Hummel, A. Krasenbrink, U. Manfredi, G. de Santi, M. Perotti, and G. Bomba. PEMS Light Duty Vehicles Application: Experiences in downtown Milan. *SAE Technical Paper*, (2007-24-0113), 2007.

[158] L. Rubino, P. Bonnel, R. Hummel, A. Krasenbrink, U. Manfredi, and G. D. Santi. On-road Emissions and Fuel Economy of Light Duty Vehicles using PEMS: Chase-Testing Experiment. *SAE Int. J. Fuels Lubr.*, 1(1):1454–1468, 2009.

[159] M. Saeedi, R. Kazemi, M. Rafat, and A. Pasdar. Real World Modeling and Nonlinear Control of an Electrohydraulic Driven Clutch. *INTERNATIONAL JOURNAL OF AUTOMOTIVE ENGINEERING*, 2(2), 2012.

[160] H. Sagha, S. Farhangi, and B. Asaei. Modeling and design of a NOx emission reduction strategy for lightweight hybrid electric vehicles. *2009 35th Annual Conference of IEEE Industrial Electronics*, pages 334–339, Nov. 2009.

[161] T. Saito and A. LEWIS. Development of a simulation technique for CVT metal pushing V-belt with feedback control. *SAE transactions*, 2004(724), 2004.

[162] T. Saito and T. OKANO. Development of Metal Pushing V-Belt Stress Simulation for Continuously Variable Transmission. *Honda R&D Technical Review*, 2003(2003-01-0969), 2001.

[163] M. Salman. Learning Energy Management Strategy for Hybrid Electric Vehicles. *2005 IEEE Vehicle Power and Propulsion Conference*, pages 427–432, 2005.

[164] F. R. Salmasi. Control Strategies for Hybrid Electric Vehicles: Evolution, Classification, Comparison, and Future Trends. *IEEE Transactions on Vehicular Technology*, 56(5):2393–2404, Sept. 2007.

[165] a. Sciarretta, M. Back, and L. Guzzella. Optimal Control of Parallel Hybrid Electric Vehicles. *IEEE Transactions on Control Systems Technology*, 12(3):352–363, May 2004.

[166] A. Sciarretta and L. Guzzella. Control of Hybrid Electric Vehicles: Optimal Energy-Management Strategies. *IEEE CONTROL SYSTEMS MAGAZINE*, (April):60–70, 2007.

[167] L. Serrao. *A COMPARATIVE ANALYSIS OF ENERGY MANAGEMENT STRATEGIES FOR HYBRID ELECTRIC VEHICLES*. PhD thesis, Ohio State University, 2009.

[168] L. Serrao, S. Onori, and G. Rizzoni. ECMS as a realization of Pontryagin’s minimum principle for HEV control. *Control Conference, 2009. ACC’*, 2009.

[169] L. Serrao, S. Onori, A. Sciarretta, Y. Guezennec, and G. Rizzoni. Optimal energy management of hybrid electric vehicles including battery aging. In *American Control Conference (ACC)*, number 3, pages 2125–2130, 2011.

[170] L. Serrao, a. Sciarretta, O. Grondin, a. Chasse, Y. Creff, D. Di Domenico, P. Pognant-Gros, C. Querel, and L. Thibault. Open Issues in Supervisory Control of Hybrid Electric Vehicles: A Unified Approach Using Optimal Control Methods. *Oil & Gas Science and Technology, IFP Energies nouvelles*, 68(1):23–33, Mar. 2013.

[171] V. Sezer, M. Gokasan, S. Bogosyan, and S. Member. A Novel ECMS and Combined Cost Map Approach for High-Efficiency Series Hybrid Electric Vehicles. *IEEE TRANSACTIONS ON VEHICULAR TECHNOLOGY*, 60(8):3557–3570, 2011.

[172] E. Shafai. Fahrzeugemulation an einem dynamischen Verbrennungsmotor-Prüfstand. (9080), 1990.

[173] S. Shen and F. Veldpaus. Analysis and Control of a Flywheel Hybrid Vehicular Powertrain. *IEEE Transactions on Control Systems Technology*, 12(5):645–660, Sept. 2004.

[174] D. Sinoquet, G. Rousseau, and Y. Milhau. Design optimization and optimal control for hybrid vehicles. *Optimization and Engineering*, 12(1-2):199–213, Dec. 2009.

[175] M. Sivertsson. Adaptive control of a hybrid powertrain with map-based ECMS. *IFAC World Congress* , 2011.

[176] M. Sniedovich. *Dynamic Programming: Foundations and Principles*. CRC Press, 2 edition, 2011.

[177] J. Srnik and F. Pfeiffer. Dynamics of CVT chain drives: Mechanical model and verification. In *DETC’97*, 1997.

[178] M. Stiegeler. *Entwurf einer vorausschauenden Betriebsstrategie für parallele hybride Antriebsstränge*. Phd thesis, Ulm University, 2008.

[179] O. Sundström. Optimal Hybridization in Two Parallel Hybrid Electric Vehicles using Dynamic Programming. In *Proceedings of the 17th World Congress The International Federation of Automatic Control*, pages 4642–4647, 2008.

[180] O. Sundström. A Generic Dynamic Programming Matlab Function. In *18th IEEE International Conference on Control Applications*, number 7, pages 1625–1630, 2009.

[181] O. Sundström. *OPTIMAL CONTROL AND DESIGN OF HYBRID-ELECTRIC VEHICLES*. PhD thesis, ETH Zurich, 2009.

[182] O. Sundström, D. Ambühl, and L. Guzzella. On Implementation of Dynamic Programming for Optimal Control Problems with Final State Constraints. *Oil & Gas Science and Technology, Institut Français du Pétrole*, 65(1):91–102, Sept. 2009.

[183] M. Sunwoo, W. Lee, and D. Choi. Modelling and simulation of vehicle electric power system. *Journal of Power Sources*, 109(September 2001):58–66, 2002.

[184] E. Surewaard and M. Tiller. A Comparison of Different Methods for Battery and Supercapacitor Modeling. *SAE TECHNICAL PAPER SERIES*, (2003-01-2290), 2012.

[185] E. Tate and S. Boyd. Finding ultimate limits of performance for hybrid electric vehicles. *SAE transactions*, (2000-01-3099), 2000.

[186] J. Theodorus and B. Anna. *Energy Management for Automotive Power Nets*. PhD thesis, TECHNISCHE UNIVERSITEIT EINDHOVEN, 2007.

[187] S. Trajkovic. *The Pneumatic Hybrid Vehicle*. Phd thesis, Lund University, 2010.

[188] I. Trivic. *Comparative Analysis of Alternative Hybrid Systems for Automotive Applications*. Phd thesis, University of Bologna, 2012.

[189] P. Tulpule, S. Stockar, V. Marano, and G. Rizzoni. Optimality assessment of equivalent consumption minimization strategy for PHEV applications. In *Proc. ASME Dynamic Systems and Control Conf. (DSCC)*, 2009.

[190] J. Tzeng, R. Emerson, and P. Moy. Composite flywheels for energy storage. *Composites Science and Technology*, 66(14):2520–2527, Nov. 2006.

[191] United Nations. Regulation No.101. Rev.2/Add. 100. E/ECE/324 E/ECE/TRANS/505, 2005.

[192] T. Universit and N. Lehrstuhl. *Ableitung einer heuristischen Betriebsstrategie für ein Hybridfahrzeug aus einer Online-Optimierung*. PhD thesis, TECHNISCHE UNIVERSITÄT MÜNCHEN, 2010.

[193] T. van Keulen, J. Gillot, B. de Jager, and M. Steinbuch. Solution for state constrained optimal control problems applied to power split control for hybrid vehicles. *Automatica*, Oct. 2013.

[194] N. D. Viet. *Gear Shift Strategies for Automotive Transmissions*. PhD thesis, Eindhoven University of Technology, 2012.

[195] M. Vojtisek-Lom, M. Fenkl, M. Dufek, and J. Mareš. Off-cycle, Real-World Emissions of Modern Light Duty Diesel Vehicles. *SAE Technical Paper*, (2009-24-0148), 2009.

[196] B. Vroemen. *Component control for the zero inertia powertrain*. Phd thesis, TECHNISCHE UNIVERSITEIT EINDHOVEN, 2001.

[197] J. Walters, H. Husted, and K. Rajashekara. Comparative Study of Hybrid Powertrain Strategies. *SAE TECHNICAL PAPER SERIES*, (2001-01-2501), 2001.

[198] F. Wang, X.-J. Mao, B. Zhuo, H. Zhong, and Z.-L. Ma. Parallel hybrid electric system energy optimization control with automated mechanical transmission. *Proceedings of the Institution of Mechanical Engineers, Part D: Journal of Automobile Engineering*, 223(2):151–167, Feb. 2009.

[199] W. Wang. Revisions on the Model of Toyota Prius in ADVISOR 3 . 1. *SAE TECHNICAL PAPER SERIES*, (2002-01-0993), 2002.

[200] W. Wang, Q. Wang, and X. Zeng. Automated Manual Transmission Shift Strategy for Parallel Hybrid Electric Vehicle. *SAE International*, (2009-01-0144), 2009.

[201] M. Weiss, P. Bonnel, R. Hummel, A. Provenza, and U. Manfredi. On-road emissions of light-duty vehicles in Europe. *Environmental Science & Technology*, 45(19):8575–81, Oct. 2011.

[202] M. Weiss, P. Bonnel, R. Hummel, and N. Steininger. A complementary emissions test for light-duty vehicles: Assessing the technical feasibility of candidate procedures. Technical report, European Commission, Joint Research Centre, Ispra, Italy, 2013.

[203] C. Weng and Y. Wang. Optimal control of hybrid electric vehicles with power split and torque split strategies: A comparative case study. *American Control Conference (ACC)*, pages 2131–2136, 2011.

[204] K. Wipke, M. Cuddy, and S. Burch. ADVISOR 2.1: a user-friendly advanced powertrain simulation using a combined backward/forward approach. *IEEE Transactions on Vehicular Technology*, 48(6):1751–1761, 1999.

[205] B. Wu, C. Lin, and Z. Filipi. Optimal power management for a hydraulic hybrid delivery truck. *Vehicle System* , (734), 2004.

[206] W. Xi. *MODELING AND CONTROL OF A HYBRID ELECTRIC DRIVETRAIN FOR OPTIMUM FUEL ECONOMY, PERFORMANCE AND DRIVEABILITY*. Phd thesis, Ohio State University, 2004.

[207] Z. Xiaohua, W. Qingnian, W. Weihua, and C. Liang. Analysis and Simulation of Conventional Transit Bus Energy Loss and Hybrid. *SAE TECHNICAL PAPER SERIES*, 2005(724), 2005.

[208] L. Xu, G. Cao, J. Li, F. Yang, L. Lu, and M. Ouyang. Equivalent consumption minimization strategies of series hybrid city buses. *cdn.intechopen.com*, pages 133–147, 2005.

[209] X. Yin, W. Wang, X. Chen, and H. Lu. Multi-Performance Optimization of the Shift Schedule for Stepped Automatic Transmissions. *SAE International*, (2013-01-0488), Apr. 2013.

[210] Z. Yong and S. Jian. Automatic Transmission Shift Point Control Under Different Driving Vehicle Mass. *SAE TECHNICAL PAPER SERIES*, (2002-01-1258), 2002.

[211] A. T. Zaremba, C. Soto, and M. Jennings. Methodology for Assessment of Alternative Hybrid Electric Vehicle Powertrain System Architectures. *SAE International*, (2012-01-1010), Apr. 2012.

[212] S. Zentner, J. Asprion, C. Onder, and L. Guzzella. An Equivalent Emission Minimization Strategy for Causal Optimal Control of Diesel Engines. *Energies*, pages 1230–1250, 2014.

[213] C. Zhang. *Predictive Energy Management in Connected Vehicles: Utilizing Route Information Preview for Energy Saving*. Phd thesis, Clemson University, 2010.

[214] C. Zhang and A. Vahid. Real-time optimal control of plug-in hybrid vehicles with trip preview. *American Control Conference (ACC), 2010*, pages 6917–6922, 2010.

[215] M. Zolot, A. A. Pesaran, and M. Mihalic. Thermal Evaluation of Toyota Prius Battery Pack. *SAE TECHNICAL PAPER SERIES*, (2002-01-1962), 2002.